UQAC

Université du Québec
à Chicoutimi

Antibacterial Aluminum Surfaces

Par

Henry Agbe

Thèse présentée à l'Université du Québec à Chicoutimi en vue de l'obtention

du grade de doctorat en ingénierie

Québec, Canada

UNIVERSITY OF QUÉBEC AT CHICOUTIMI

A THESIS SUBMITTED TO

THE UNIVERSITY OF QUÉBEC AT CHICOUTIMI

IN PARTIAL FULFILMENT OF THE REQUIREMENTS

FOR THE DEGREE OF DOCTOR OF PHILOSOPHY

IN ENGINEERING

BY

HENRY AGBE

ANTIBACTERIAL ALUMINUM SURFACES

Jury

Prof. Dilip Kumar Sarkar (Director)	**University of Quebec At Chicoutimi**
Prof. Xiao Grant Chen (Co-Director)	**University of Quebec At Chicoutimi**
Prof. Diego Mantovani (Examiner)	**Université Laval**
Prof. Zhan Zhang (Examiner)	**University of Quebec At Chicoutimi**
Prof. Duygu Kocafe (President-Examiner)	**University of Quebec At Chicoutimi**

07-09-2021

Dedicated to the memory of my mom, Ms. Mildred Erskine

RÉSUMÉ

Les infections nosocomiales (associées à soins de santé, IAS) constituent un important problème de santé publique et sont à l'origine d'environ 8000 à 12000 décès par an parmi les Canadiens. Outre les thérapies antibactériennes, antifongiques et antivirales, une stratégie potentielle pour briser la chaîne de transmission des IAS consiste à modifier les surfaces fréquemment touchées ayant des caractéristiques antibactériennes, appelées *surfaces touchées antibactériennes*. Ceci est particulièrement vrai, étant donné que la plupart des microbes pathogènes survivent pendant des jours, des mois, voire des années sur les surfaces fréquemment touchées, incluant les poignées de porte, les tables de lit et les comptoirs, des semaines et même des mois. Ainsi, les surfaces fréquemment touchées peuvent devenir des réservoirs de contamination croisée directe et indirecte. Cependant, les problèmes associés aux revêtements antibactériens existants tels que la durabilité du revêtement, la libération incontrôlée d'agents antibactériens, l'absence de protocoles pour des tests standardisés et les problèmes de résistance antibactérienne, imposent le besoin de disposer de surfaces antibactériennes nouvelles et durables, en plus d'un régime de nettoyage approprié pour la décontamination des surfaces fréquemment touchées.

Dans ce projet de recherche, les revêtements d'alliage d'aluminium AA6061-T6 (alliage Al-Mg-Si) ont été transformées en surface antibactérienne durable via quatre stratégies nouvelles. La première stratégie consiste en une modification de la surface d'aluminium anodisée par argent-polyméthylhydrosiloxane (Ag-PMHS) superhydrophobe, ce qui fournit un oxyde stable d'alumine poreux et nano-rugueux. Cette première modification est suivie d'une seconde modification avec des nanocomposites Ag-PMHS, générant un deuxième degré des motifs nanométriques à partir des nanoparticules d'Ag (Ag-NPs), et rendant la surface superhydrophobe grâce à la passivation d'une surface de faible

énergie PMHS. Les Ag-NP ont été utilisés pour assurer la longévité des propriétés antibactériennes, même après une éventuelle perte de superhydrophobicité à long terme. Ces surfaces présentaient une réduction d'adhérence bactérienne de 99,0%, 99,5% et 99,3% pour les bactéries d'intérêt, à savoir, respectivement, *Pseudomonas aeruginosa (P.A.), Escherichia-coli (E. coli)* et *Staphylococcus aureus (S. A.)*.

La deuxième stratégie implique la fabrication d'une surface originale en aluminium superhydrophobe avec des propriétés antibactériennes et anti-bio-encrassement accordables par gravure chimique et passivation d'octyltriéthoxysilane (OTES) / sel d'ammonium quaternaire (QUAT). Les propriétés superhydrophobes de l'aluminium ayant un revêtement passif d'OTES ont été accordées de manière monotone en optimisant la quantité de molécules QUATs par variation des ratios molaires QUATs / OTES de 0 à 54×10^{-4}. Une propriété antibactérienne ayant une zone d'inhibition de $34 \pm 1,6$, $22 \pm 1,4$ et $25 \pm 0,9$ contre *S.A, P.A.* et *E. coli*, respectivement, ont été obtenues pour la solution d'OTES-QUAT, tandis qu'une propriété anti-encrassement biologique de 99,9, 99 et 99% pour les mêmes bactéries respectivement, a été obtenue pour la surface d'aluminium revêtue d'OTES-QUAT.

La troisième stratégie visait à l'utilisation d'un dépôt de phosphate d'argent (Ag_3PO_4) sur les surfaces d'aluminium anodisées à deux étapes, afin d'obtenir des propriétés antibactériennes durables. Pour cette technique, l'ion d'argent (Ag^+) était premièrement réduit en argent métallique (Ag^0) sur surface d'oxyde d'aluminium anodisée, suivi d'une oxydation de Ag^0 dans un électrolyte d'orthophosphate de sodium pour former un précipité électrochimique Ag_3PO_4 *in situ* sur surface d'aluminium anodisée. L'aluminium anodisée recouvert d'Ag_3PO_4 a une adhérence de recouvrement très élevée et une propriété antibactérienne à 100% contre *E Coli*.

Finalement, un procédé supplémentaire d'anodisation de l'aluminium dur en une étape a également été utilisé pour fabriquer une surface originale d'aluminium antibactérienne. En contrôlant la concentration des différents types d'électrolytes, la densité de courant et le temps d'anodisation, une morphologie de surface optimisée avec des diamètres de 151 ± 37 nm s'est avérée fournir des propriétés antibactériennes excellentes, tuant efficacement 100% des bactéries *E. coli*.

Les résultats de cette thèse démontrent que l'utilisation de nouvelles stratégies d'ingénierie de surface telles que l'anodisation, la passivation à faible énergie de surface et la modification de surface électrochimique sur l'alliage d'aluminium AA6061-T6 s'avère efficace dans les activités antibactériennes ainsi que dans la robustesse et la durabilité. Ces nouvelles surfaces ont montré la capacité de réduire la charge microbienne des pathogènes cliniquement pertinents et impliqués dans les IAS, à savoir, *S.A., P.A.* et *E. coli*.

ABSTRACT

Healthcare-associated infections (HCAI) is a serious public health problem that results in the death of 8,000-12000 Canadians each year. Besides antibacterial, antifungal, and antiviral therapies, one potential strategy for breaking the chain of HCAI transmission is via the modification of frequently touched surfaces with antibacterial characteristics, called *Antibacterial touched surfaces.* This is particularly so, given that most pathogenic microbes survive on frequently touched surfaces including doorknobs, over bed tables and countertops, for days, weeks and even months. Thus, frequently touched surfaces can become reservoirs for subsequent direct and indirect cross contamination events. However, problems associated with existing antibacterial coatings such as lack of durability, uncontrolled release of antibacterial agents, lack of standardized testing protocols and antibacterial resistance issues, have necessitated the need for a novel and durable antibacterial surfaces, in addition to appropriate cleaning regime for decontamination of frequently touched surfaces.

In this research project, surfaces of AA6061-T6 aluminum alloy (Al-Mg-Si alloy) have been transformed into durable antibacterial surface via four different novel strategies. The first strategy consists of fabrication of superhydrophobic silver-polymethylhydrosiloxane (Ag-PMHS) modified aluminum surface by anodization of aluminum, which provides nano-rough, porous, and stable oxide of aluminum, followed by modification with Ag-PMHS nanocomposites, which delivers a second degree of nanorough patterns from the presence of Ag nanoparticles (Ag-NPs), as well as renders the surface superhydrophobic due to the passivation of low surface energy PMHS. Ag-NPs were used to ensure longevity of antibacterial properties even after eventual possible loss of superhydrophobicity in the long-term. These surfaces presented a bacterial adhesion

reduction of 99.0 %, 99.5 %, and 99.3 % for the bacteria of interest, namely, *Pseudomonas aeruginosa (P.A.)*, *Escherichia-coli (E. coli)* and *Staphylococcus aureus (S.A.),* respectively.

The second strategy involves the fabrication of novel superhydrophobic aluminum surface with tunable antibacterial and anti-biofouling properties by chemical etching and octyltriethoxysilane (OTES)–quaternary ammonium salt (QUATs) passivation. The superhydrophobic properties of the OTES passivated aluminum was monotonically tuned by optimizing the quantity of QUATs molecules by varying the molar ratios of QUATs/OTES from 0 to 54×10^{-4}. An antibacterial property with a zone of inhibition of 34 ± 1.6, 22 ± 1.4, and 25 ± 0.9 against *S.A*, *P.A., and E. coli,* respectively were obtained for the solution form of OTES-QUATs, while an anti-biofouling property of 99.9, 99 and 99% for same bacteria respectively, were obtained for the OTES-QUATs coated aluminum surface.

The third strategy aimed at utilizing a two-step electrochemical deposition of silver phosphate (Ag_3PO_4) on anodized aluminum surfaces to obtain durable antibacterial properties. In this technique, ionic silver (Ag^+ ion) was first reduced to metallic Ag^0 on anodized aluminum oxide surface, followed by oxidation of the metallic silver (Ag^0) in an electrolyte of sodium orthophosphate to electrochemically precipitate Ag_3PO_4 in situ on anodized aluminum surface. The Ag_3PO_4 coated anodized aluminum exhibited a remarkably high coating adhesion and a 100% antibacterial property against *E. coli* bacteria.

Finally, an additional one-step hard aluminum anodization process was also employed to fabricate novel antibacterial aluminum surface. Controlling the concentration of different electrolytes, current density and anodization time, optimized surface morphology with diameters 151 ± 37 nm was found to provide excellent antibacterial properties, efficiently killing 100% *E. coli* bacteria.

Results of this dissertation demonstrate that the utilization of novel surface engineering strategies such as anodization, low surface energy passivation and electrochemical surface modification on AA6061-T6 aluminum alloy, proves to be efficient in antibacterial activities as well as in robustness and durability. These novel surfaces have shown the ability of reducing microbial burden of clinically relevant and HCAIs implicated pathogens, namely, *S.A., P.A., and E. coli*.

.

ACKNOWLEDGEMENTS

Finally, one of my aspirations for life, i.e., contributing to the advancement of scientific knowledge has been accomplished. Just like Sir Isaac Newton, if I have successfully completed this project, it is because I stood on the shoulders of Giants. These, I would like to acknowledge here.

Firstly, I would like to thank the Almighty God and Our Lord Jesus Christ, by whose grace I live, have my sustenance, inspiration, and direction for life.

Secondly, I would like to express my deep most appreciation to the director of this thesis, Prof. Dilip Kumar Sarkar for the rare opportunity to work on this exciting, promising, and burgeoning field of research. Your visit to the Materials Chemistry Group, Department of Materials Science and Metallurgy, University of Cambridge, which culminated in my acceptance on this project, will always be remembered. Your supervision, invaluable contributions, scientific insights, suggestions, scientific and technical criticisms, and confidence reposed in me throughout this project; continuously helped shape me into a productive and independent graduate student, a researcher, and a scientist.

Thirdly, I am extremely grateful to my co-director, Prof. X.-Grant Chen, for his invaluable suggestions, counsel, financial support, and scientific comments on my manuscripts.

Fourthly, I would like to thank all the sponsors of this research project, namely, The Fonds de recherche du Québec – Nature et technologies (FRQNT), the Aluminum Research Centre – REGAL, University of Québec at Chicoutimi and the Aluminum anodized antibacterial Surfaces (A3 Surfaces, Chicoutimi). I would also like to appreciate the

invaluable contributions of our collaborators, without which, this project would not have been a success: Prof. Nathalie Faucheux, Prof. Gervais Soucy and Ms Jessica Jann, Department of Chemical Engineering and Biotechnology Engineering, University of Sherbrooke, for the insightful and fruitful scientific discussions we had these years and in particularly, discussions leading to the development of the novel dry seeding protocols in this project. In addition, my heartfelt thanks go to the team at Aluminum anodized antibacterial Surfaces (A3 Surfaces) for providing me training and access to an excellent microbiology laboratory and facilities, where all microbiology investigations were conducted. In this regard, it is appropriate to mention Mr. Jean-Luc Bernier, Mr. Maxime Dumont, Mr. Martin Lambert, Mr. Patrick Asselin-Mullen and Ms Audrey Grenier for their help in providing me the requisite skills and expertise in microbiology, and the strong foundation for future work in this project.

Fifthly, I wish to thank Dr. Saleema Noormohammed, National Research Council of Canada, Saguenay, for taking time off her busy schedule to proofread and to offer useful comments for improving the quality of this thesis. Also, to Dr. Zhang Zhan for training me on the use of Scanning Electron Microscope (SEM). Additionally, I would like to acknowledge Mr. Dave Girard, Mr. Dany Racine, and Mr. Samuel Dessureault for their technical support.

Sixthly, I am extremely grateful to Prof. Diego Mantovani, Director, Laboratory for Biomaterials and Bioengineering, Laval University, Prof. Duygu Kocaefe, UQAC and Dr. Zhang Zhan, UQAC, for taking time off their heavy schedules to serve as members of the jury for the doctoral examination.

Seventhly, I would like to appreciate colleagues at CURAL, University of Quebec at Chicoutimi, namely Dr. Khaled, Dr. Redouane Farid, Dr. Karthikeyan Rajan, Algendy

Ahmed, Elashery Ali, Ramadan, Siamak, Reza, Afia Nuamah, Mani Mohan Tiwari, Amara Belkacem for the friendship and the moments we shared together during the last three years. Not forgetting the help of visiting master's students, namely Nelly, Etienne, and Emely, for their contributions towards some of the preliminary studies on superhydrophobic silver-polymethylhydrosiloxane aluminum surface.

Eighthly, I would like to acknowledge Prof David Arhin-Dodoo, Department of Materials Science and Engineering, University of Ghana, Prof. Vasant Kumar, Department of Materials Science and Metallurgy, University of Cambridge, Dr. Emmanuel Nyankson, Department of Materials Science and Engineering, University of Ghana, Prof. Caterina Ducati, Department of Materials Science and Metallurgy, University of Cambridge, Prof. Richard Amankwah, Vice chancellor, University of Mines and Technology, Ghana, and Dr. Lawrence Darkwah, Head of Department, Chemical Engineering Department, KNUST, Ghana, for their counsel, mentorship, support and encouragement.

Ninthly, to my entire family members in Ghana and abroad, namely: Mr and Mrs Patrick Antwi Kusi, Mrs Geogina Ninson, Mrs Anastacia Praaka-Asante, Mrs Charlotte Adu-Mensah, Mr. Frank Erbah, Celestina Agbe, John Agbe, Ezekiel Antwi-Kusi, Joseph Antwi-Kusi, Emmanuel Antwi-Kusi, Jesse Antwi-Kusi, Charity Ninson, Joycelyne Ninson, Patricia Adu-Mensah, Ms Michelle Boakye and Mr and Mrs Boakye for all their supports, prayers, and encouragement.

"Best for last" to my lovely wife, Dr. Mrs Mercy Agbe and beautiful daughter, Davina Aba Agbe, for all their sacrifices, love and prayers throughout this PhD adventure. I say, May the Almighty God richly bless you.

Finally, to everyone who contributed in diverse way to the successful completion of this thesis, I apologize for my inability to thank you by name.

TABLE OF CONTENT

LIST OF TABLES

LIST OF FIGURES

LIST OF SYMBOLS AND ABBREVIATIONS

α: Porosity

η: Pore density

μ: Reduced mass,

β: Beta

k: Bond strength (dyne. cm^{-1})

ω: Frequency of vibration

B: Barrier layer

D_p: Pore diameter

Dc: Cell diameter

W: Wall thickness

γ_{sl}: Solid-liquid interfacial surface energy (mNm^{-1})

γ_{LG}: Liquid-vapor interfacial surface energy (mNm^{-1})

θ: Contact angle of water on any surface (°)

f_s: Fraction of solid area on the surface

f_G: Fraction of vapor area on the surface

r: Wenzel roughness factor

AST: Active surveillance testing

ATCC: American Type Culture Collection

ASTM: American Society for Testing and Materials

ANOVA: Analysis of variance

AAO: Anodized aluminum Oxide

AMP: Antimicrobial peptides

AFM: Atomic Force Microscope

ATR-FTIR: Attenuated Total Reflectance-Fourier Transform Infrared spectroscopy

CAUTI: Catheter-associated urinary tract infections

CVD: Chemical vapour deposition

CA: Contact angle

CAH Contact angle hysteresis (°)

CLABSI: Central line-associated bloodstream infection

CDC: Centers for Disease Control and Prevention

CAI: Community-associated infection

CFU: Colony-forming units

COVID-19: Coronavirus of 2019

DNA: Deoxyribonucleic acid

DEB: Dey-Engley neutralizing Broth

EDS: Energy dispersive X-ray

EPA: Environmental Protection Agency

E-coli: Escherichia coli

EPS: Extracellular polymeric substance

GLAD: Glancing angle deposition

HCAIs: Healthcare associated infections

HIV: Human immunodeficiency virus

H1N1: Hemagglutinin Type 1 and Neuraminidase Type 1

ICP-MS: Inductively coupled plasma mass spectrometry

MRD: Maximum recovery diluent

MRSA: Methicillin-resistant *Staphylococcus aureus*

MDROs: Multidrug-resistant organisms

MDRA: Multidrug-resistant *Acinetobacter*

MIC: Minimum inhibitory concentration

OTES: Octyltriethoxysilane

PEO: Plasma electrolytic oxidation

PECVD: Plasma-enhanced chemical vapour deposition

PBS: Phosphate buffer solution

PMHS: Polymethylhydrosiloxane-

P.A: *Pseudomonas aeruginosa*

PVD: Physical vapour deposition

QUATs: Quaternary ammonium, salts

QS*:* Quorum sensing

RSV: Respiratory syncytial virus

ROS: Reactive Oxygen Species

RNA: Ribonucleic Acid

RV: Rhinovirus

RTV: Room temperature vulcanized

RBCs: Rotating Biological Contactors

SARS-CoV-2: Severe acute respiratory syndrome coronavirus 2

SEM: Scanning electron microscope

Ag-NPs: Silver nanoparticles

SSI: Surgical site infections

S.A: *Staphylococcus aureus*

TEOS: Tetraethyl orthosilicate

TMOS: Tetramethylorthosilicate

TSB: Tryptic Soy Broth

VRE: Vancomycin-resistant enterococci

VAP: Ventilator-associated pneumonia

XRD: X-ray powder diffraction

ZoI: Zone of inhibition

CHAPTER 1

INTRODUCTION

1   CHAPTER 1: INTRODUCTION

"A hundred times every day, I remind myself that my inner and outer life depended on labours of other men, living and dead, and I must exert myself to give in the same measure as I have received and am still receiving" - Albert Einstein.

This chapter introduces the problem of healthcare associated infections (HCAIs) and the potential solution to overcome these issues via antibacterial aluminum surface technology. Furthermore, the objectives, novelty of the research and methodology employed are provided in the following sections

1.1   Introduction

Microorganisms are very small (10nm-300µm) living organisms that individually cannot be visualized with an unaided eye. They can be classified as bacteria, virus, fungi, protozoa, algae, parasitic helminths, and arthropods. Microorganisms can be found everywhere: in the air, water, soil, on the rock, in plants, animals and on and inside our bodies. Microbes are the largest of all life forms and about 60 % of biomass. They are generally beneficial for our survival; for example, they help in digesting our food and for production of antibiotics, insulin, vitamin (B and K), alcohol, wine, yoghurt etc. While microorganisms are essential for life, they can also be pathogenic [4], that is, they can cause diseases. This is evident in the current coronavirus of 2019 (COVID-19) outbreak, a global pandemic, caused by the *severe acute respiratory syndrome coronavirus 2* (SARS-CoV-2), which has resulted in over 219 million cases and more than 4.5 million deaths

globally [5]. There have been many other such pandemics that have cost lives of millions of people in the past including the Bubonic Plague (1346-1353), the "Spanish Flu" Pandemic (1918-1920), HIV Pandemic (early 1980s), "Swine Flu" or H1N1/09 Pandemic (2009), etc. [5]. In such pandemics, infections can easily spread from the community to healthcare facilities and vice-versa. Healthcare facilities are major venues that need significant protection against infections as the population leans over these facilities for recovery, while it is also at high risk of acquiring additional infections due to the contagious nature of most of these viral or bacterial outbreaks. It becomes, therefore of great significance in the improvement of healthcare hygiene by safe protection measures. Therefore, this dissertation will focus mainly on the healthcare associated infection (HCAI).

1.2   Statement of the problem

Healthcare-associated infection (HCAI) is a serious public health problem [6]. It is the 4th leading cause of death after cancer, heart disease and stroke [8]. In Canada, more than 200,000 patients contract HCAI yearly, out of which 8,000-12000 of the cases result in fatality [9]. Common forms of HCAI include; central line-associated bloodstream infection (CLABSI), surgical site infections (SSI), catheter-associated urinary tract infections (CAUTI) and frequently touched surfaces-mediated infections [10]. Besides antibacterial, antifungal, and antiviral therapies, one potential strategy for breaking the chain of HCAI transmission is to have *Antibacterial touched surfaces* to curb attachment of pathogens such as *Staphylococcus aureus, Pseudomonas aeruginosa and Escherichia coli*. However, problems associated with existing antibacterial solutions such as lack of long term durable antibacterial coating, uncontrolled release

3

of antibacterial agents, lack of standardized testing protocols and antibacterial resistance problems [11], have necessitated the need for novel, stable and durable antibacterial surfaces in addition to appropriate cleaning regime for decontamination of frequently touched surfaces [7].

Aluminum is a very attractive material for engineering constructions and many aluminum components are widely used in medical devices [9, 10, 12] and being explored in fabricating frequently touched surfaces such as doorknobs, push plate, bedrails, over bed tables and countertops. Aluminum has excellent physical, chemical and mechanical properties such as low density, wear and corrosion resistance, high elastic modulus, good tensile and yield strength etc. Aluminum is the third most abundant element in the earth's crust (after oxygen and silicon) and most abundant metal on earth. It is highly reactive metal and exists with a layer of passive aluminum oxide film on its surface. To render aluminum surfaces antibacterial, this passive oxide layer needs to be modified with appropriate technology.

1.3 **Objectives**

In the context of fabricating antibacterial aluminum surfaces capable of reducing bacterial loads of clinically relevant pathogens such as *Staphylococcus aureus, Pseudomonas aeruginosa and Escherichia coli*, the main objective of this dissertation is to obtain durable antibacterial aluminum surfaces for potential application on frequently touched HCAI prone surfaces by applying different fabrication approaches. Specific objectives of this research project, therefore, are as follows:

1. Fabrication of a topography-mediated antibacterial aluminum surface via anodization process.

2. Fabrication of durable antibacterial and anti-biofouling aluminum surfaces by passivating anodized nano-porous topographical patterns with low surface energy silver-polymethylhydrosiloxane molecules.

3. Fabrication of a tunable anti-biofouling and antibacterial aluminum surfaces by passivating nano-porous topographical patterns with low surface energy octyltriethoxysilane molecules.

4. Fabrication of silver-based photo catalysts on aluminum surfaces by electrochemical deposition process.

1.4 **Novelty of the research**

Although many antibacterial surfaces technology have been reported in the literature, most of them have not transitioned laboratory bench to the market, presumably due to lack of durability of these coatings [13]. There is therefore the need for novel stable and durable antibacterial surface. As a commonly used engineering material, aluminum alloy is capable of being transformed into antibacterial surface *by: (i) anodization process to create a nano-porous topographical pattern, which kill bacteria on contact; (ii) as well as passivating the nano-porous topographical pattern to create superhydrophobic properties to repel the initial attachment of bacteria; or (iii) immobilizing antibacterial agents on anodized aluminum to kill bacteria on contacts.* Such anodized pores would provide both chemical adhesion and mechanical anchorage of the antibacterial thin films to enhance durability.

Interestingly, only few studies have reported on antibacterial aluminum surface mediated by topography [14], which relate to chemical etching of aluminum. Admittedly, while desirable nanoscale topography can be achieved by chemical etching, mechanical property of the nanoscale features may not be strong [1]. As such, an alternative surface treatment process with well-known excellent anti-corrosive, tribological and mechanical properties such as anodization [2] appears promising.

Secondly, in spite of significant efforts on superhydrophobic coatings in application of antibacterial surfaces, bacterial-repellent performance has been rather low [3]. Furthermore, the applicability of such coating is limited due to the degradation with time. As Ag and quaternary ammonium, salts (QUATs) have natural properties to kill bacteria, incorporating them in silicone-based superhydrophobic coatings such as polymethylhydrosiloxane (PMHS) and octyltryethoxysilane (OTES) molecules could reduce bacterial adhesion and improve the overall longevity of such coatings. However, fabrication of superhydrophobic Ag-PMHS and OTES-QUATs nano-composite coatings with inherent antibacterial and anti-biofouling properties are yet to be reported in the literature.

Thirdly, to the best of our knowledge, the electrochemically synthesis of Ag_3PO_4 coated anodized aluminum, capable of killing bacteria on contact is yet to be reported in the literature. Thus, the novelty of this project is in three folds:

1. Fabrication of topography-mediated novel antibacterial aluminum surface technology via anodization process.

2. Fabrication of a novel superhydrophobic antibacterial aluminum surface.

3. Fabrication of a novel silver phosphate photocatalytic antibacterial aluminum surfaces.

1.5 **Methodology**

A highlight of the approaches employed to meet the objectives of this research is provided below. However, detailed experimental methods are provided in chapters 3-7 of this thesis.

1. Topography-mediated antibacterial aluminum surfaces were fabricated by optimizing anodization parameters such as concentrations (3%, 15% and 45% wt.) of H_3PO_4, H_2SO_4 and $C_2H_2O_4$, anodization time (30, 60 and 120 minutes) and current densities (10, 20, 30 and 40 mA/cm^2), followed by studying their antibacterial properties.

2. Antibacterial and anti-biofouling aluminum surfaces were fabricated by anodizing AA606-T6 aluminum alloy at optimal anodization parameters of 15% of H_2SO_4, anodization time (30, 60 and 120 minutes) and current density of 40 mA/cm^2, followed by passivating the anodized nano-porous topographical patterns with silver/polymethylhydrosiloxane polymer at an optimal molar ratio.

3. Tunable anti-biofouling and antibacterial aluminum surfaces were fabricated by chemically etching the AA6061-T6 aluminum alloys, followed by passivation with low surface energy octyltriethoxysilane molecules. During the etching process, aluminum alloy was immersed in an etchant solution of diluted HCl for a pre-determined period. During

this time, the top layer of the aluminum substrate was partially removed to create desired micro-nano-porous topographical patterns. Tunable property was achieved by simply dipping the etched aluminum in a mixed solution of octyltriethoxysilane-quaternary ammonium.

4. Silver phosphate photocatalysts aluminum surfaces were fabricated by anodizing AA6061-T6 aluminum alloys at optimal anodization parameters using 3% of H_3PO_4, anodization time of 120 minutes and current density of 40 mA/cm^2, followed by in situ electrochemical deposition of silver phosphate photocatalysts on anodized aluminum.

The remainder of the thesis is organized as follows: Chapter 2 provides detailed literature review on healthcare associated infections, the role surfaces play in healthcare associated infections, antibacterial surfaces, fabrication, and challenges with current antibacterial coatings solutions, among others. Detailed experimental methods used for fabrication of antibacterial aluminum surfaces are provided in Chapter 3. Chapters 4 and 5 describe the results of published articles focusing on antibacterial and anti-biofouling properties of superhydrophobic Ag-polymethylhydrosiloxane nanocomposite aluminum surfaces and tunable anti-biofouling and antibacterial aluminum surfaces, respectively. Chapter 6 sheds light on electrochemical deposition process of silver phosphate on anodized aluminum surfaces and their antibacterial property. The serendipitous discovery of a topography-mediated antibacterial aluminum surface fabricated by a one-step hard anodization process is presented in Chapter 7. Finally, Chapter 8 provides brief discussions on findings of the contributing chapters, overall conclusions, and future recommendations, though each contributing chapter (chapters 4 through 7) is accompanied by its respective conclusions.

1.6 References:

1. McCall, D., D. Stock, and P. Achey, *11th hour: introduction to microbiology*. 2009: John Wiley & Sons.
2. Organization, W.H., *Coronavirus disease (COVID-19): weekly epidemiological update.* 2020.
3. Huremović, D., *Brief history of pandemics (pandemics throughout history)*, in *Psychiatry of pandemics*. 2019, Springer. p. 7-35.
4. Schmidt, M., *The role of antimicrobial surfaces in hospitals to reduce healthcare-associated infections (HAIs)*, in *Decontamination in Hospitals and Healthcare*. 2020, Elsevier. p. 259-299.
5. Anne MacLaurin, Kanchana Amaratunga, Chantal Couris, Charles Frenette, Riccarda Galioto, Gerry Hansen, Jennifer Happe, Kim Neudorf, Linda Pelude, Caroline Quach and Suzanne Rhodenizer Rose., *Measuring and Monitoring Healthcare-Associated Infections: A Canadian Collaboration to Better Understand the Magnitude of the Problem.* Healthcare quarterly (Toronto, Ont.), 2020. **22**(SP): p. 116-128.
6. Linda Bonilla-Gameros., Pascale Chevallier, Andranik Sarkissian, Diego Mantovani, *Silver-based antibacterial strategies for healthcare-associated infections: Processes, challenges, and regulations. An integrated review.* Nanomedicine: Nanotechnology, Biology and Medicine, 2020. **24**: p. 102142.
7. C. Adlhart , J. Verran , N.F. Azevedo , H. Olmez , M.M. Keina¨nen-Toivola ,I. Gouveia , L.F. Melo, F. Crijns, *Surface modifications for antimicrobial effects in the healthcare setting: A critical overview.* Journal of Hospital Infection, 2018. **99**(3): p. 239-249.
8. Cole, M., *Exploring the hand hygiene competence of student nurses: a case of flawed self assessment.* Nurse education today, 2009. **29**(4): p. 380-388.
9. Jafar Hasan , Shubham Jain , Rinsha Padmarajan , Swathi Purighalla , Vasan K. Sambandamurthy, Kaushik Chatterjee, *Multi-scale surface topography to minimize adherence and viability of nosocomial drug-resistant bacteria.* Materials & design, 2018. **140**: p. 332-344.
10. Jafar Hasan, Yanan Xu, Tejasri Yarlagadda, Michael Schuetz, Kirsten Spann, Prasad KDV Yarlagadda, *Antiviral and antibacterial nanostructured surfaces with excellent mechanical properties for hospital applications.* ACS Biomaterials Science & Engineering, 2020.
11. Lumley, R., *Fundamentals of aluminium metallurgy: production, processing and applications*. 2010: Elsevier.
12. Jafar Hasan, Alyssa Pyke, Neelima Nair, Tejasri Yarlagadda, Geoffrey Will, Kirsten Spann, and Prasad K.D.V. Yarlagaddal., *Antiviral Nanostructured Surfaces Reduce the Viability of SARS-CoV-2.* ACS Biomaterials Science & Engineering, 2020.
13. Haobo Shi, Mei Yu, Jianhua Liu, Gang Rong, Rongtao Du, Jie Wang and Songmei Li, *Effect of alkaline etching on microstructure and anticorrosion performance of anodic film on Al-Mg-Si alloy.* Corrosion Science, 2020. **169**: p. 108642.
14. Rungsinee Canyook, Phakaphol Seubsom, Jatupum Sang-ngean, Thotsaphon Trirujirapapong and Kattareeya Taweesup, *Influences of sealing solutions on anodized layer properties of 7075 aluminium alloy.* Materials Today: Proceedings, 2018. **5**(3): p. 9483-9488.
15. Meier, M., V. Dubois, and S. Seeger, *Reduced bacterial colonisation on surfaces coated with silicone nanostructures.* Applied Surface Science, 2018. **459**: p. 505-511.
16. Crick, C.R., et al., *An investigation into bacterial attachment to an elastomeric superhydrophobic surface prepared via aerosol assisted deposition.* Thin Solid Films, 2011. **519**(11): p. 3722-3727.

CHAPTER 2

LITERATURE REVIEW

2   CHAPTER 2: LITERATURE REVIEW

This chapter provides a review on current understanding on healthcare associated infections and recent advances in antibacterial coatings for curbing infections in hygiene critical environment, with particular focus on topography-mediated antibacterial surfaces, superhydrophobic antibacterial coatings and hydrophilic antibacterial coatings.

2.1   Healthcare associated infections

Healthcare-associated infection (HCAI) is an infection acquired in a healthcare facility, long-term care homes, outpatient surgical centres, dialysis centres or ambulatory care clinics that was not present or incubating 48 h prior to admission [5, 6]. Incidence of HCAI predates modern literature, however, it was only recently, in the 1970s that the Center for Disease Control and Prevention (CDC) developed a system to monitor the incidence of HCAIs and their associated risk factors and pathogens [7]. Available information shows that bacteria are the leading cause of HCAI, while virus and fungi contribute to a lesser extent [5]. While HCAIs are acquired in healthcare settings, infections are also acquired in the community. In this case, the infected person may be asymptomatic carrier at the time of admission. If the asymptomatic carrier exhibits symptoms in less than 48 h of admission, such infection is regarded as community-associated infection (CAI). The 48 h is the gold standard for differentiating a community-acquired infection from a healthcare acquired infection [5]. Note that the 48 h is the incubation period required for an asymptomatic host to fully show symptoms of infection. Generally, CAIs are less problematic when compared to HCAI [5], however, in periods of outbreaks or pandemics such as the current

coronavirus disease of 2019 (COVID-19) pandemic, CAIs can be equally devastating. However, for the purpose of this project, only HCAI is presented herein.

As noted previously, HCAI is a global public health problem, and in the USA, more than 2 million patients contract HCAI annually, leading to about 100,000 fatality, and a financial loss of $4.5 billion [8]. In Canada, it is estimated to lead to ~200,000 infections, out of which 8,000-12000 of the cases result in fatality [9] and a financial loss of about $1 billion. According to the European Centre for Disease Prevention and Control, over 2.5 million people in Europe are infected by HCAI annually, leading to 90,000 deaths [10]. In Addition, at any given time, up to 7% of patients in developed countries and 10% of patients in developing countries will be affected by at least one HCAI. [11] Commonly implicated pathogens for HCAIs include Methicillin-resistant *Staphylococcus aureus* (MRSA), Enterobacteriaceae family (including *Escherichia coli* (*E. coli*), *Klebsiella species, Pseudomonas aeruginosa), Clostridium difficile,* coagulase-negative *Staphylococci* (CoNS) *etc.* Note that clinically, HCAIs are classified based on the site of location of these pathogenic bacteria as: Catheter-associated urinary tract infection (CAUTI); Central line-associated bloodstream infection (CLABSI); Surgical site infection (SSI); Ventilator-associated pneumonia (VAP) etc. [5]. However, causative pathogens are not restricted to specific sites; thus, a single bacterium can become causative pathogen for multiple HCAIs as shown in Figure 2.1.
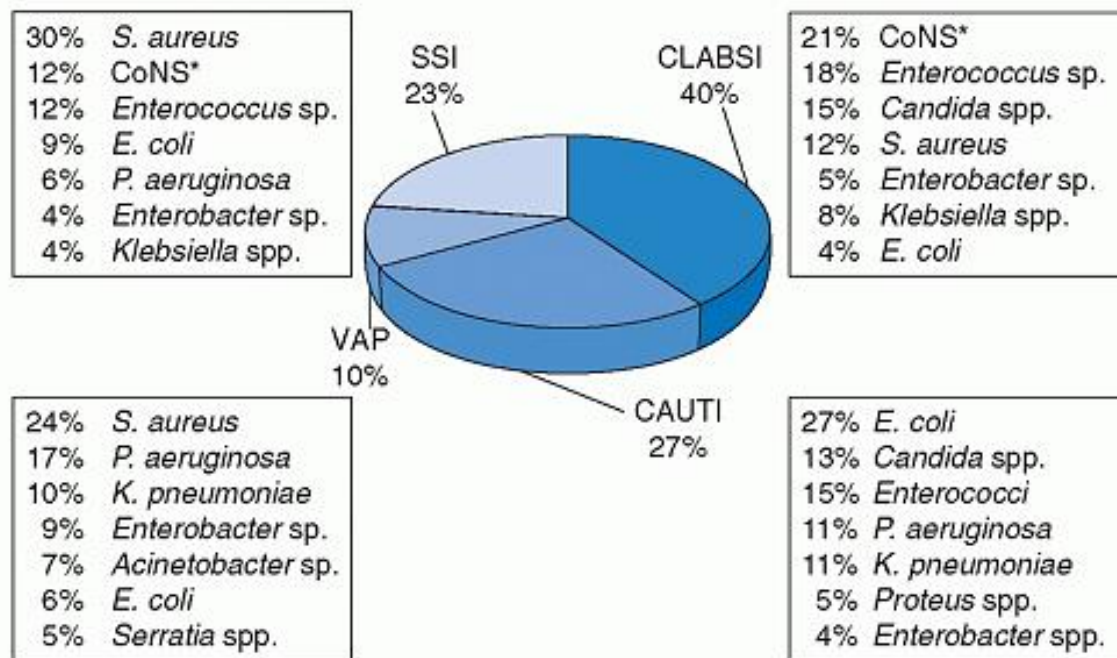
Figure 2-1.Distribution of HCAl pathogens; SSI, surgical site infection; CLABSI, central line-associated bloodstream infection; CAUTI, catheter-associated urinary tract infection; VAP, ventilator- associated pneumonia. Adapted from [1].

Furthermore, the problem of HCAI is compounded by the fact that most causative pathogens have become resistant to conventional antibiotics [12], thus, necessitating the need for novel antimicrobial solutions. This is particularly important, given that 99% of causative pathogens exit as biofilms on either implant devices or frequently touched surfaces [13, 14]. It is interesting to note that bacteria in biofilm require ~500-1000 order of magnitude higher in minimum inhibitory concentration (MIC) of antimicrobial agent than their free floating planktonic forms [15], thus, biofilm provides a safe haven for the spread of HCAIs. Again, causative pathogens are known to survive on frequently touched surfaces (such as doorknobs, overbed table,

faucet handles, and intravenous (IV) poles etc.,) for days, weeks and months [16], hence, contributing to both direct and indirect cross contamination events as discussed below.

2.1.1 The role of environmental surfaces in healthcare associated infections

The majority of healthcare associated infections were thought to originate from the patient's own pathogenic microbial flora [17]. In the 1980s, studies did not implicate pathogens on environmental surfaces as contributing to HCAIs. However, recent epidemiological evidences suggest that significant transmission of microbes from healthcare personnel and contaminated inanimate surfaces, in close proximity to vulnerable patients also greatly contribute to HCAI [18]. This is alarming when one considers that HCAI causative pathogens and in general multidrug-resistant organisms (MDROs) contaminate inanimate surfaces despite terminal hospital rooms cleaning [19]. A recent microbial analysis from a large clinical disinfection study by Kanamori H et al. [20], showed that microbial burden of HCAI causative pathogens, especially multidrug-resistant *Acinetobacter* (MDRA) and vancomycin-resistant enterococci (VRE) persisted on environmental inanimate surfaces such as overbed table and bed rail, despite terminal room disinfection [20]. Furthermore, patients admitted to hospital rooms previously occupied by patients colonized or infected by MDROs, have increased risk of acquiring same pathogens [5, 21]. Thus, due to the inability to eliminate causative pathogens on environmental inanimate surfaces despite terminal cleaning, these surfaces, and in particular, those near patients can become potential reservoirs for both direct and indirect cross contamination events.

Note that for pathogens to propagate, three elements are necessary: *source of pathogen*, *susceptible host,* and *mode of transmission*. If this epidemiology triad were connected, a chain of

14

infection would establish transmission. Pathogen can then be transmitted directly or indirectly. Direct contact transmission occurs when pathogens are transmitted from person to person, without an intermediate person or object. On the contrary, indirect mode of transmission occurs when there are intermediate inanimate contaminated surfaces (Figure 2.2). Typical intermediate contaminated surfaces in close vicinity to susceptible patients include medical equipment and instruments, furniture, bed surfaces, over bed tables, bed rails, floor etc.
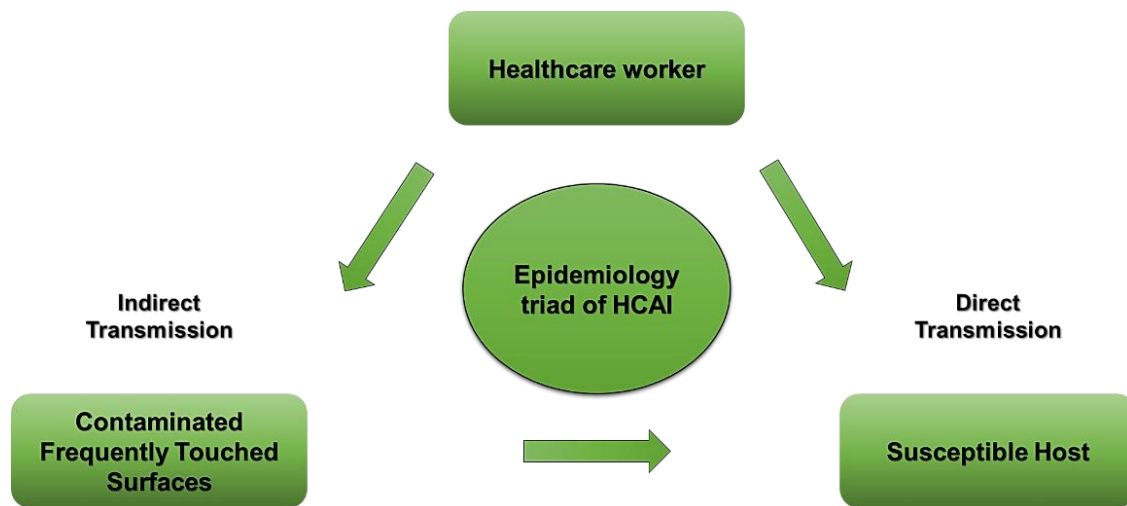
Figure 2-2. Transmission routes for healthcare-associated infections pathogens. Adapted from [27].

Since healthcare workers, patients and visitors, mostly touch inanimate surfaces, these are termed *frequently touched surfaces*. However, contamination of most *frequently touched surfaces* can be attributed to pathogen shedding by patients. It is interesting to note that despite causative pathogens' ability to survive on dry frequently touched surfaces for extended periods (Table 2.1), and at concentrations sufficient for both direct and indirect cross contamination events, attention

has not been given to these surfaces over the years, perhaps the reason for the high incidence of HCAIs.

Table 2-1 Survival times of nosocomial (HCAI) pathogens on environmental surfaces.

Organisms	Range of survival (Inanimate surfaces)	Reference
Clostridium difficile (spores)	5 months (dry surface)	[22]
Clostridium. Difficile (Vegetative form)	15 min (dry surface)	[22]
Escherichia coli	1.5 h to 16 months	[23]
Pseudomonas aeruginosa	6 h up to 16 months	[23]
Staphylococcus aureus including MRSA and MSSA	7 days up to 1 year (In-vitro)	[23]
SARS-CoV-2	3 days stainless and plastic, 1 day on cardboard, 4h on copper	[24]
Candida albicans	1-4 weeks	[25]

2.1.2 **Current prevention strategies of HCAI and challenges**

The prevention of HCAI generally takes two forms: *vertical interventions,* which aim to reduce specific causative pathogen's colonization, infection, and transmission from carriers to other patients, through the use of active surveillance testing (AST); and *horizontal interventions,* which aim to reduce the risk of infections from a broad array of pathogens through implementation of standardized practices that do not depend on patient-specific conditions [26]. In other words, horizontal approach considers holistic interventional strategies such as healthcare staff education for improved hand hygiene; improved disinfection regimens (including hydrogen peroxide vapor (HPV) and no-touch ultra-violet C (UVC) technologies); use of aggressive antimicrobial stewardship programs etc., [27] to combat HCAI. Even so, many challenges still do exist.

Firstly, hand hygiene compliance was a major problem prior to the COVID-19. Though hand hygiene was recognized as the single most effective strategy for preventing the spread of HCAI, compliance by healthcare workers was less than optimal [28]. In fact, a systematic review of 96 studies showed that on average, only ~40%, with (30-40%) for Intensive Care Unit (ICU) and (50-60%) for other settings were attainable [29]. However, due to the current COVID-19 pandemic, there has been an increased interest by healthcare workers not only to practise improved hand-hygiene but also to sanitize inanimate environmental surfaces [30]. Happily, this interest has led to an increased compliance rate of ~100% [31]. It would be in the common good of all that this high momentum for improved hand hygiene is sustained post COVID 19 pandemics.

Another reason HCAI remains a challenge is the complexity of the hospital environment, characterized by different substrata surfaces of metal, plastics, ceramics, textiles etc. This leads to incomplete decontamination of surfaces with available disinfectants (such as hydrogen peroxide

17

aerosols, bleach, quaternary ammonium compound and chlorhexidine) and cleaning agents (such as detergents) [32]. Indeed, rooms with terminal cleaning have shown to harbour about 44 % *Clostridium difficile (C. difficile)* spore even long after cleaning [33]. Furthermore, disinfections such as bleach reacts adversely with inanimate environmental surfaces, and in particular, corrodes metal inanimate surfaces [34].

Additionally, modern medical practice inevitably employs catheterization and other invasive medical implantation procedures to improve quality of life. Unfortunately, surfaces of implant devices are easily colonized by multidrug resistant pathogens in biofilms, hence compounding the problem of HCAI.

Overall, while *horizontal interventions* have significantly lowered the incidence of infections, prevalence of HCAIs is still unacceptably high [35], therefore necessitating the need for self-disinfection antibacterial surface technology, in addition to appropriate cleaning regime for decontamination of the inanimate environment (Figure 2.3).

Current Rigorously Implemented Measures to Reduce HCAI Rate

- Hand washing before and after every contact with a patient or object
- Isolation of infected patient
- Use of disposable and personal protective equipment
- Use of filters and better ventilation management
- Improved hospital cleaning
- Increased personnel per patient
- Increase in infection control personnel
- Aggressive antibiotic control programs

Overlooked and neglected bio-control

of the inanimate environment

HCAI Rate

Years

Figure 2-3. HCAI are not eliminated by the current implemented measures. Adapted from [27].

2.2 Bacteria

Bacteria are single-celled prokaryotic (Greek word, meaning pre-nucleus) microorganisms without membrane-bound organelles. Contrarily, multicellular, or unicellular organisms with membrane-bound organelles are known as *Eukaryotic cells* (Greek word, meaning true nucleus). Bacterial cell structure consists typically of cytoplasm, ribosomes, a plasma membrane, a nucleoid, plasmid, flagellum, pili etc. Since they do not have nucleus, their DNA (a singular circularly arranged chromosome) is loosely located within the cytoplasm. The size of bacteria ranges from

19

0.2-2.0 μm in diameter and about 2.0-8.0 μm in length. Depending on the way individual bacterium aggregates, bacteria can colonize as singular rounded form (*coccus*), cluster-like form (*staph(ylo)*), chain-like form (*strep(to)*), double-rounded (*diplo*), quadruple (*tetrad*) or as a cluster of bacilli bending at the points of cell division (*palisades*). They reproduce very fast by constant cell division through a process called *binary fission*. Under optimal conditions, bacteria and in particular, HCAI causative pathogens such as *Escherichia coli* (*E.coli*) and *Staphylococcus aureus* (*S. aureus),* double every 20 and 30 minutes, respectively [14, 36].

One unique feature of prokaryotic bacterial cell is the presence of cell wall structure. Bacterial cell walls are mainly composed of carbohydrate and protein complex called *peptidoglycan.* Based on how staining dyes bond and react with the *peptidoglycan* cell wall, bacteria can be classified as either a *gram-positive* or a *gram-negative* bacterium. *Gram-positive* bacteria have thicker *peptidoglycan* cell wall of about 30-100 nm compared to *gram-negative* bacteria with thinner cell wall of 2-10nm. When stained with crystal violet dye, *gram-positive* cells retain the dye and remain purple whilst *gram-negative* bacteria remain colourless until counterstained with safranin dye to show a red colouration [14]. Clinically, the cell wall is very important, as it is the target site for most conventional antibiotics and modern antibacterial agents. A detailed structure of both *gram-positive* and *gram-negative* bacteria is presented in Figure 2.4
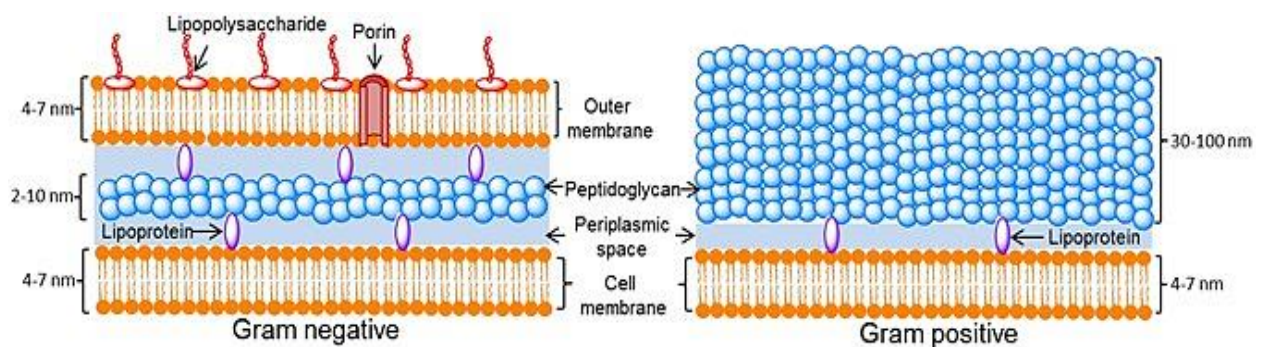
Figure 2-4. Cell wall structure of Gram-negative and Gram-positive bacteria. Adopted from [1].

2.2.1 **Formation of biofilms**

Bacteria exist in two states: free-floating *planktonic* and *sessile cell forms*. Single cell bacterium proliferating to colonize different niches, constitutes the free-floating *planktonic cells*, whereas the slowly growing cells that prefer to adhere to substrata surfaces are called the *sessile cells*. The sessile cells constitute the community of cells called biofilms. Biofilms are three-dimension cluster of sessile bacterial cells embedded in an extracellular polymeric substance (EPS) on either biotic or abiotic surfaces. Over 99% of the world's bacteria live in biofilms [37], therefore it is likely such environment might be beneficial for bacterial survival.

Biofilm formation begins with colonization of substratum surface, which in turn is affected by many factors, including type of bacteria species, bacteria's surface composition, nature and surface chemistry of substratum, nutrient availability, hydrodynamics, cell-to-cell communication, and global regulatory networks [38]. Generally, the attachment of bacteria on surfaces goes through five main processes, as shown in Figure 2.5: 1) *Reversible Attachment*; at this stage, cell-substratum interaction is weak and reversible. Initial bacterial attachment differs depending on type of bacteria and substratum surface (that is either biotic or abiotic). For *S. aureus,* bacterial attachment on biotic surface (such as tissue) is mediated by a specific peptidoglycan-anchored protein mechanism such as lectin or adhesin docking mechanisms [39]. Contrarily, *P. aeruginosa* on substrata is by flagella, type-IV pili chemotaxis and non-specific interactions such as electrostatic, hydrophobic, or van der Waals forces [38]. 2) At the *Irreversible attachment and cell-cell adhesion* stage, bacteria produce diffusible signalling molecules in a process called *quorum sensing,* which among other things, induce bacteria to secrete the EPS [40], leading to a strong cell-substratum interaction and a stable bacterial attachment. 3 and 4) During the *Proliferation and Maturity* stage, bacteria proliferate and mature within the EPS, which is

composed of polysaccharides, protein and nucleic acids (extracellular DNA) [13]. The EPS cements both the cluster of bacteria and the substrata surface together and provide a three-dimensional mechanically stable biofilm. Prior to the cementation process, *quorum sensing* (QS) molecules synchronizes alterations in the genetic expression of all bacteria population to coordinate and to form the biofilm [41]. 4) At the *Dispersion* stage, bacteria proliferation within biofilm reaches a critical mass, where the biofilm loses essential nutrient, water, and oxygen. As a result, they disperse to release free-floating planktonic cells, which is capable of re-colonizing other substrata surfaces.
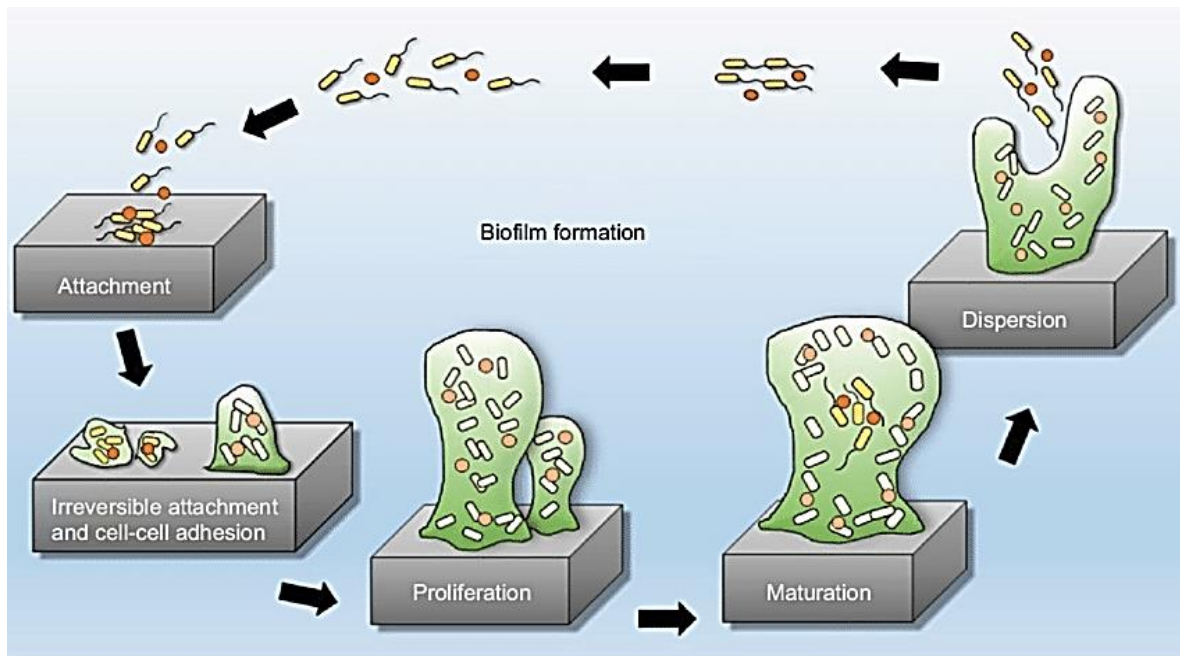
Figure 2-5. Formation of biofilms on surfaces. Adopted from [39].

2.2.2 **Role of biofilms in healthcare associated infections**

Though formation of biofilms may be beneficial for metabolizing recalcitrant compounds such as phenols, cyanides, thiocyanides in applications such as Rotating Biological Contactors (RBC) technologies, they generally pose challenges in food processing, marine and healthcare industries. In fact, it is well acknowledged that about 65% of all HCAIs are mediated by biofilm-associated infections of implantable medical devices [42]. Formation of biofilm is a natural selection self-defense strategy bacteria use to protect themselves from external threats such as nutrient-deficient conditions, antimicrobial regimen, clearance by both humoral and cellular host defense mechanisms, and dynamic environments [43]. As such, bacteria in biofilm have some advantages such as an ability to acquire resistant strains, undertake intercellular communication via *quorum sensing* (QS), and evade antimicrobial regimen [44]. Biofilm also provides a safe haven for the spread of HCAIs [45]. Within biofilms, bacteria are significantly less susceptible, making them difficult to be diagnosed and treated, and unfortunately, often necessitating removal of infected implants [40].

Common orthopaedic and indwelling prostheses implicated in HCAIs include urinary catheters, intravascular catheters, heart valves, pacemakers, stents, endotracheal tubes, artificial kneel and hip joints [46]. Common causative pathogen in biofilms of indwelling prostheses include coagulase-negative staphylococci (CoNS), *S. aureus*, *Enterococcus faecalis*, *E.coli*, *Klebsiella pneumoniae*, Staphylococcus epidermidis (*S. epidermidis), Proteus mirabilis*, *Candida* spp. etc. [38]. Among these CoNS*, S. aureus* and *Candida* spp. lead to prosthetic valve endocarditis, while *S. epidermidis* and *S. aureus* account for more than 90% of prosthetic joint infections [47]. Overall,

biofilm has major implications for both patients and healthcare systems in terms of prolonged hospital stay and increased healthcare costs [48, 49].

Note that biofilm-mediated HCAI, in wet conditions has extensively been studied, however little is known about their counterparts of dry surface conditions [4]. As discussed earlier under section 2.1.1, MDROs, which lead to HCAIs, can persist on environmental inanimate surfaces for months even after terminal discharge room cleaning. This is presumably due to their persistence as dry biofilms, which shield them against traditional disinfections and desiccation processes. In fact, a recent study of dry biofilms occurrence, persistence, and diversity on hospital surfaces by Ledwoch, K. et al. [4], revealed that both gram-positive and gram-negative bacteria could persist as dry biofilms on patients' folders, chairs and computer keyboard keys, in spite of terminal cleaning with chlorine-based disinfectants (Figure 2.6).
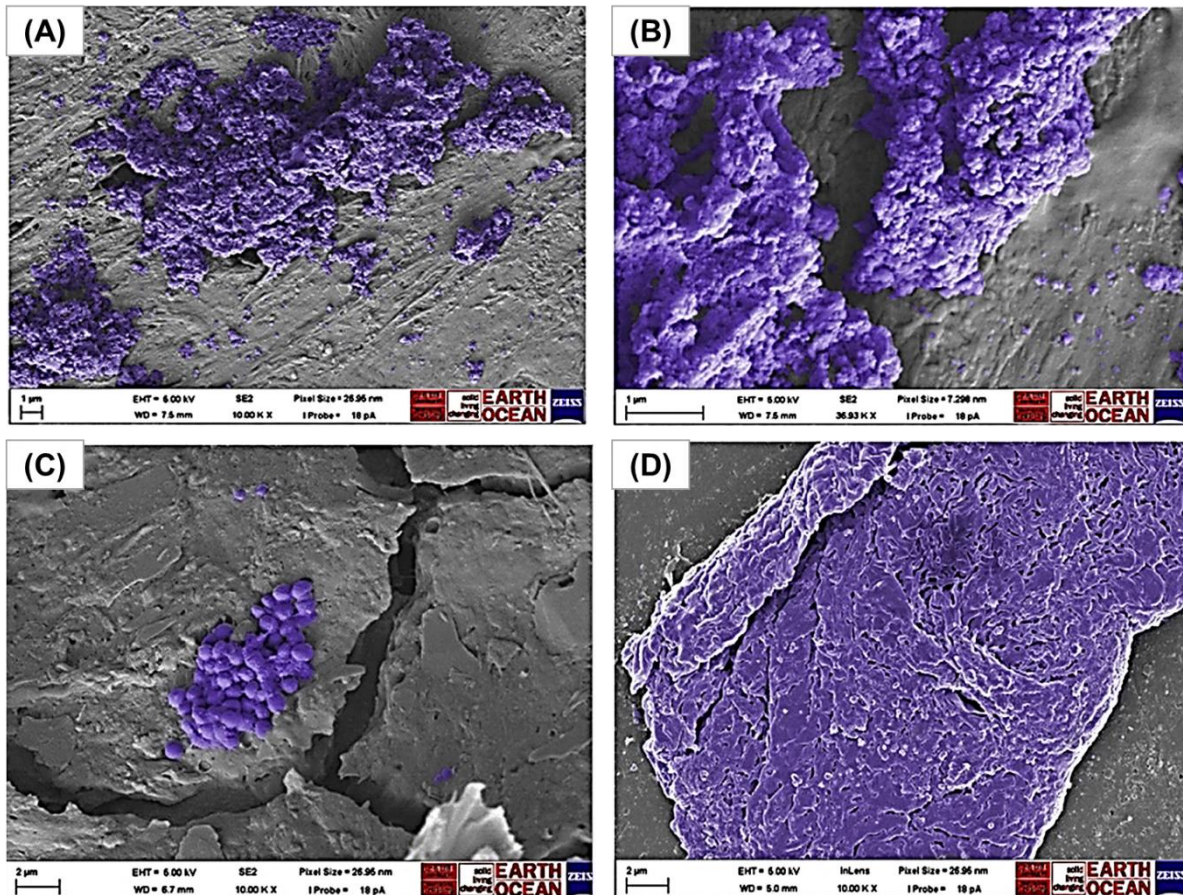
Figure 2-6. Examples of 'dry' biofilms recovered from surfaces; magnification X 10,000. (A, B) Patient folders, (C) Patient chair, (D) Keyboard key. Images of biofilms were coloured in purple to help visualization and contrast using GNU (GNU's Not Unix) image manipulation program (GIMP2.8) software. Images were not otherwise altered. Adapted from [3].

2.3   Antimicrobial resistance

Antimicrobial resistance describes the inability of natural antibiotics, synthetic or semi-synthetic antimicrobial agents to inhibit microbial growth or kill microorganisms. Most available

antibiotics such as vancomycin, methicillin, tetracycline, cephalosporin, gentamycin, carbapenem, rifampicin, etc., have now become less effective at inhibiting or killing HCAI pathogens [5]. It is even feared that with widespread use of antimicrobial drugs and antibiotics in the current COVID-19 pandemic, antimicrobial resistance problem will be exacerbated post COVID 19 [50].

Many bacteria produce enzymes capable of chemically degrading, blocking, or inactivating antimicrobial agents ((Figure 2.7 (1-4)). Bacteria secrete *beta (β)-lactamases* that degrade the beta lactam ring of penicillin family of antibiotics long before the latter reach the target sites. Furthermore, through several gene transfer mechanisms such as *conjugation*, *transformation*, and *transduction*, bacteria can transfer resistant *plasmid* genes to otherwise susceptible cells, making the latter also resistant. In addition, bacteria can actively pump out antimicrobial agents using their efflux pump mechanism, to increase the minimum inhibitory concentration (MIC) of antimicrobial agents necessary to kill them.
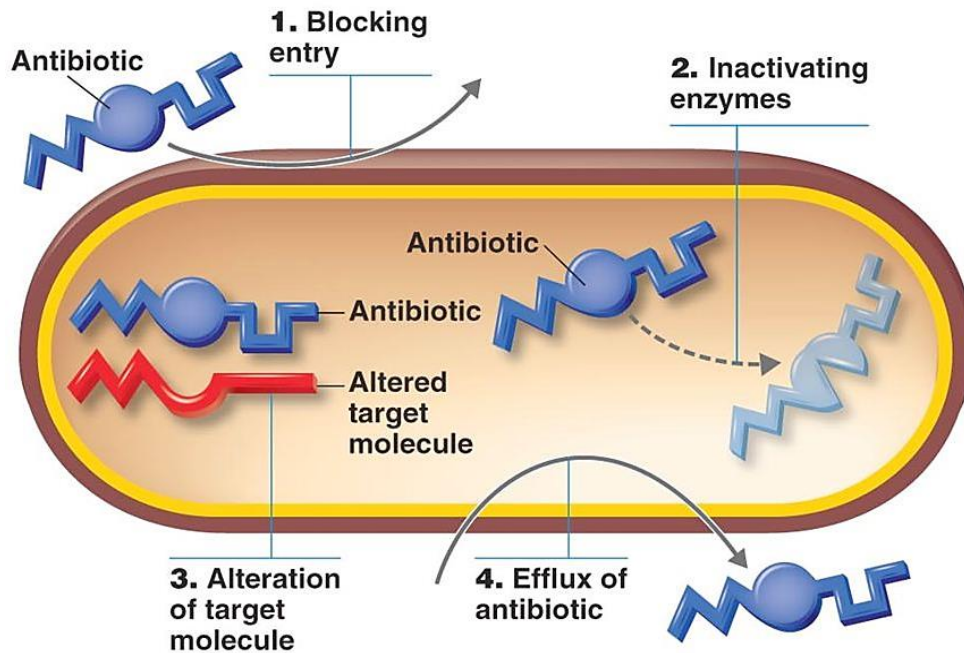
Figure 2-7. Schematic diagram showing mechanisms of microbial resistance to antimicrobial agents: (1) Blocking the antibiotics' entry into the cell, (2) Inactivation of the antibiotics by enzymes, (3) Alteration of the antibiotics' target site, (4) Efflux pumps transport out antibiotics from the cell. Adopted from [14] with permission.

2.4 Antimicrobial agents

Antimicrobial agents are synthetic or semi-synthetic agents that inhibit the growth or kill microorganisms such as viruses, fungi, bacteria, and protozoa, herein referred as *antiviral, antifungal, antibacterial and antiprotozoal*, respectively. For this thesis, only synthetic antibacterial agents are discussed further. Commonly synthesized antibacterial agents include: (a) *Cationic compounds antibacterial agents*, including quaternary ammonium salts (QUATs); and (b) *Inorganic antibacterial agents*, which include silver and copper nanoparticles, and metal oxides photo catalysts materials (Table 2.2).

27

Table 2-2 Major antibacterial coatings.

Substrates	Representative antibacterial coating	Bacterial type	Ref
glass	tetraethoxysilane (TEOS) and Q_4N^+ Si $(OR)_3^-$	*S. Aureus* and *E. coli*	[51]
glassware	CuS-NPs	S. Aureus and *E. coli*	[52]
5L carbon steel	TiO_2/ZnO ceramic coatings	*E. coli*	[53]
316L stainless steel	*Ag*-NPs	*E. coli*	[54]
hydroxyapatite	Ag–TiO_2	*E. coli*	[55]

2.4.1 **Quaternary ammonium salts (QUATs)**

QUATs are amphiphilic nitrogen (N^+) containing compounds covalently attached to four different functional groups. QUATs has a general formula of $N^+R_1R_2R_3R_4X^-$, where R is a hydrogen atom, a plain, aryl or an alkyl hydrophobic tail substituted with other functionalities, and X, as halide anion [56]. QUATs is a first-line antiseptics for managing pathogenic infections in

hospitals [57]. Their use as disinfectants in healthcare settings date back to the 1930s due to: their prolonged antimicrobial activities; non-toxic and non-irritant properties; non-reactive nature; and low antibacterial resistance [58]-[56]. QUATs are effective against most pathogens, including *S. aureus, Klebsiella pneumonia*, *Acinetobacter baumannii, P. aeruginosa,* etc., [59]. Though, antibacterial mechanism of QUATs is still under investigation, it is generally accepted that the electrostatic interactions between the positively charged moiety (N^+) and negatively charged phospholipid bilayer of bacteria lead to its antibacterial effects. Once anchored within the negatively charged phospholipid bilayer, the hydrophobic portion of the molecule intercalate into the membrane, disrupting membrane diffusive forces and ion gradients, leading to bacterial cell death [60]. However, the bioactivity of QUATs can be limited by the action of efflux pump resistance mechanism (Figure 2.8).
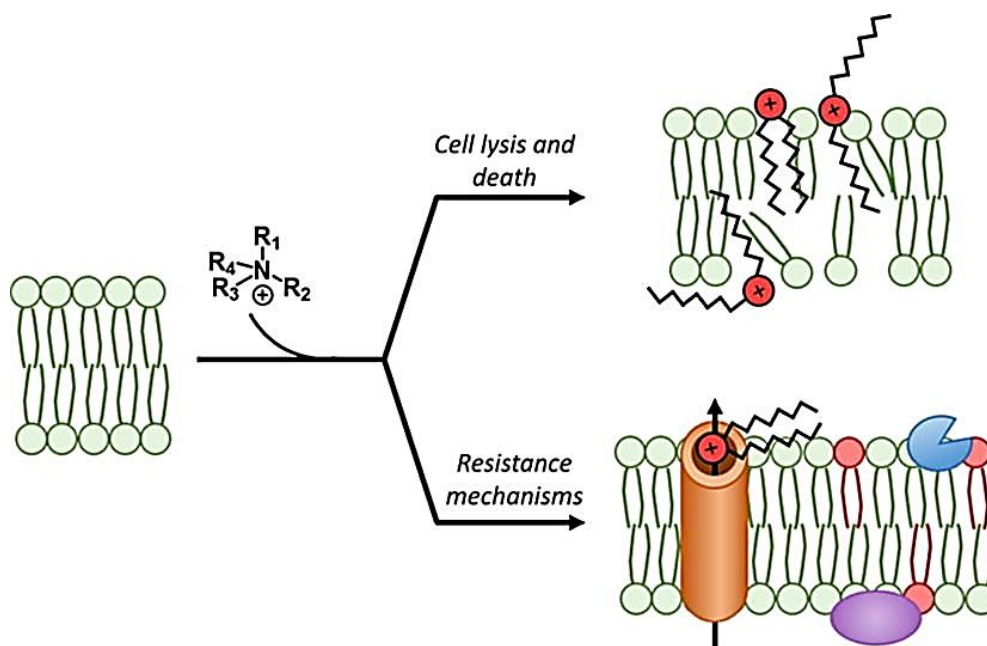
Figure 2-8. Antibacterial mechanism of QUATs. Adopted from [60] with permission.

2.4.2　**Silver-based antimicrobial agents.**

Silver-based antimicrobial agents, along with copper have been used to fight infectious disease throughout history. For example, the ancient Chaldean used silver as cutleries as early as 4000 B.C, before the discovery of microbes [61]. The ancient Greeks and Romans also used to store water in silver vessels to keep it fresh. Again, the Mediterranean and Asiatic cultures used silver flasks and storage containers to prevent spoilage of liquids, and placed silver foil into wounds to prevent infection [62]. Additionally in 1880s, Americans travelling west used to put silver coins in water barrels as a tradition, as well as to inhibit the growth of bacteria and algae [63].

Silver has broad-spectrum antimicrobial activity against a wide variety of pathogens such as bacteria, fungus, yeast, virus, and protozoa. In fact, metallic silver was used for many applications and by 20th century, silver had become the main antimicrobial agent or material. However, the use of silver was limited after the discovery of penicillin by Sir Alexander Fleming in 1928 and the advent of antibiotics due to the high costs associated with silver production [64]. Note that prior to the 21st century, silver was utilized in many domestic products such as needles, vessels, plates, cutleries, and silver fillings due to its antimicrobial properties (Figure 2.9) [65].
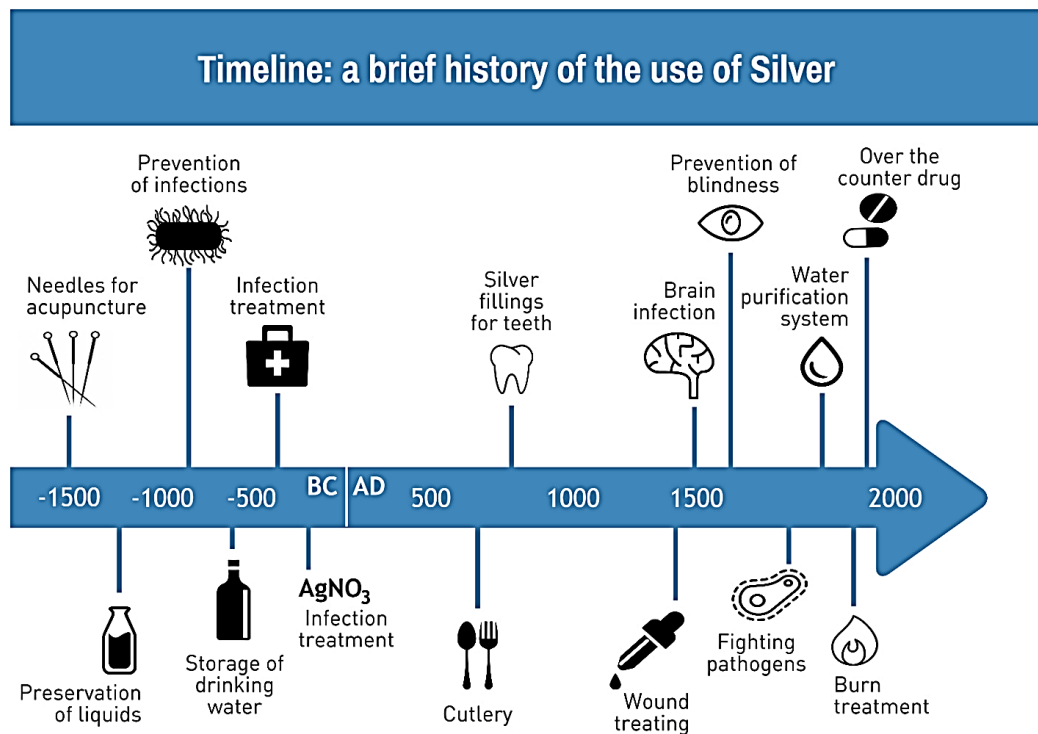
Figure 2-9. Exemplary applications of silver related products along the course of human history. Adopted from [65] with permission.

2.4.2.1 **Antimicrobial properties of silver nanoparticles**

Properties such as silver particles size, morphology and facets, strongly affect how bacteria attach to silver and subsequent destruction [66]. Therefore, considerable effort has been devoted to tunable silver particle size studies (Figures 2.10 (A-F)) [67].

As silver particle reduces in size, active reaction site increases. Microorganisms that adhere to such active reactive sites can be inactivated. For example, biocidal activity of silver nanoparticles (Ag-NPs) with diameter of 5-100 nm, are found to be effective at killing bacteria due to the good interaction with bacterial cell membrane [68]. In particular, smaller diameter such

as 5 nm, shows better biocidal activity (Figure 2.6 G) [69]. Again, the presence of sharp edges, kinks, steps and defects (on exposed facets) result in high surface energy, high adsorption rate and arguably improve biocidal activity. In recent work by Zheng, K. et al [68], truncated triangular (bipyramids) Ag-NPs with (1 1 1) lattice plane exhibited a higher antimicrobial activity against *E. coli* as compared to the spherical and rod-shaped Ag-NPs. In particular, triangular Ag-NPs containing high atom-density (1 1 1) facets, showed highest antimicrobial activity [68]. Again, comparing morphologies of silver antimicrobial agents against both gram-positive and gram-negative microbes, Ag nanoplates (Ag-NPls) (with two-dimensional (2D) structure) showed the highest antimicrobial activity towards *S. aureus* and *E. coli*, when compared to Ag nanorods (Ag-NRds) and Ag nanospheres (Ag-NPs) (figure 2.11 H). It was postulated that the presence of high surface area Ag-NPls resulted in excellent interaction with the bacterial cell wall and subsequently damaged the cell walls [70].
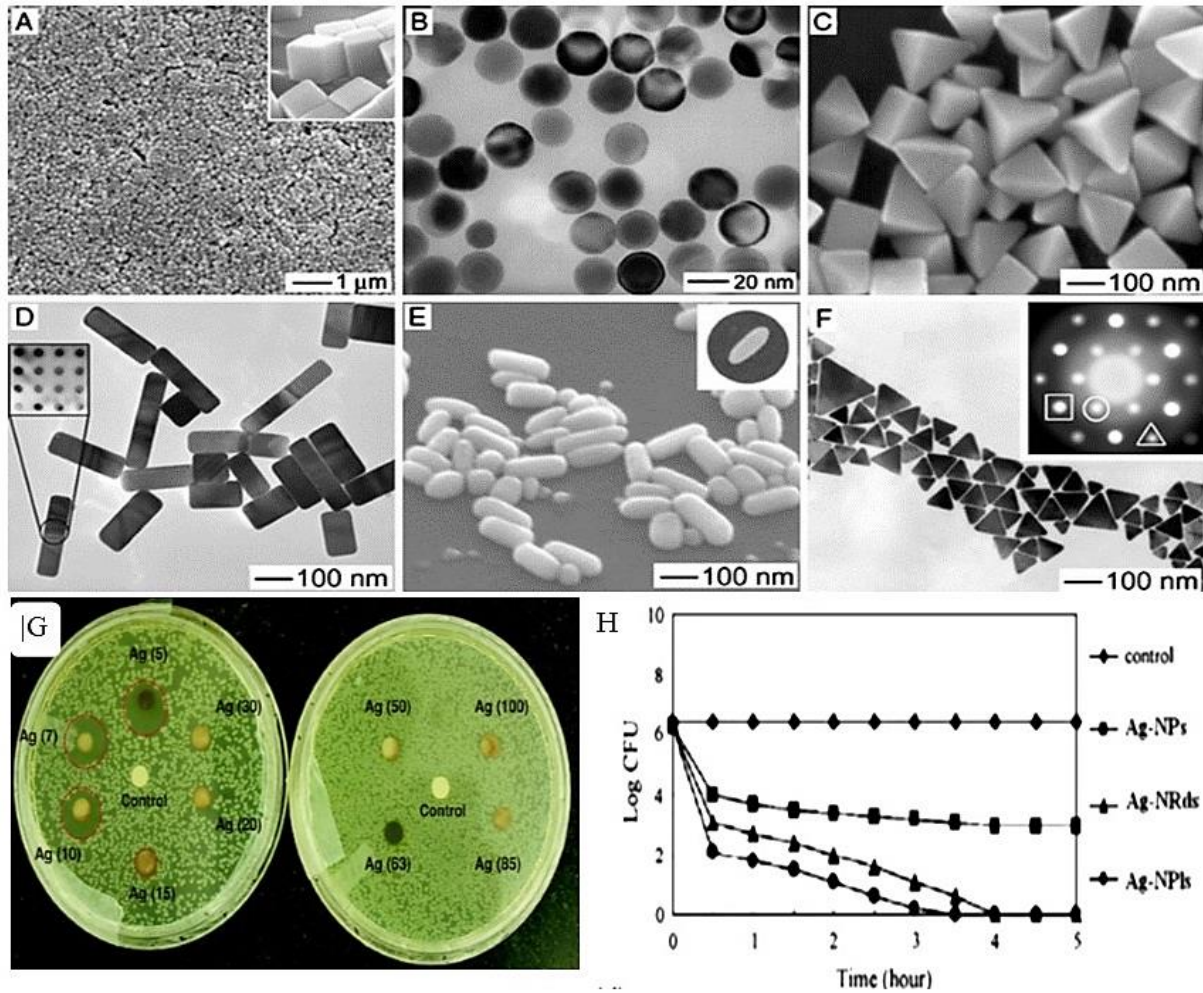
Figure 2-10. Electron microscope images of silver nanoparticles in different shapes. (A), (C) and (E): The scanning electron micrograph of Ag nanocubes, bipyramids, nanorice, respectively. (B), (D) and (F): Transmission electron micrograph of nanospheres, nanobars and nanoplates, respectively. (G) Disc diffusion tests for different sized Ag-NPs against *E. coli* MTCC 443 strains. (H) Growth inhibition curves of *E. coli* in LB medium treated with the Ag-NPs of different shapes. Adopted from [66, 68] with permission.

Silver shows excellent antibacterial property and is effective at inactivating implant mediated HCAIs pathogens. Therefore, silver antimicrobial coating has gained much attention due

to: (1) its broad spectrum antibacterial property and high chemotherapeutic ratio [71]; (2) its non-toxicity to human cell in low concentration (10 ppm (0.01 mg/ml)) [72]; (3) its multifunctional antimicrobial mechanism [73]; (5) its strong oligo dynamic effects (especially against "super-bugs") and low tendency for antimicrobial resistance [72, 74, 75].

2.4.2.2 **Antimicrobial mechanisms of silver-based antimicrobial agents**

The current scientific understanding on antimicrobial mechanism of silver is that upon bacteria-silver contact, Ag^0 is oxidized into Ag^+ by respiratory enzymes [78]. Subsequently, the released Ag^+ ion binds to the thiol functional groups of proteins and other intracellular structures including, phospholipid bilayer of the plasma membrane, ribosome, DNA etc. Indeed, it has been found that Ag^+ ion bonds to Deoxyribonucleic acid (DNA), thiol groups and the other organelles to effect its antibacterial activity [76-77]. The general mode of action is described as shown in Figure 2.11 [79], below:

1. Destabilisation of ribosome and prevention of protein synthesis.
2. Cell wall disruption of the peptidoglycan complex.
3. Formation of Reactive Oxygen Species (ROS), to mediate bacterial death through lipid peroxidation and membrane destabilization.
4. Intercalation between DNA bases, leading to subsequent DNA molecule destruction.
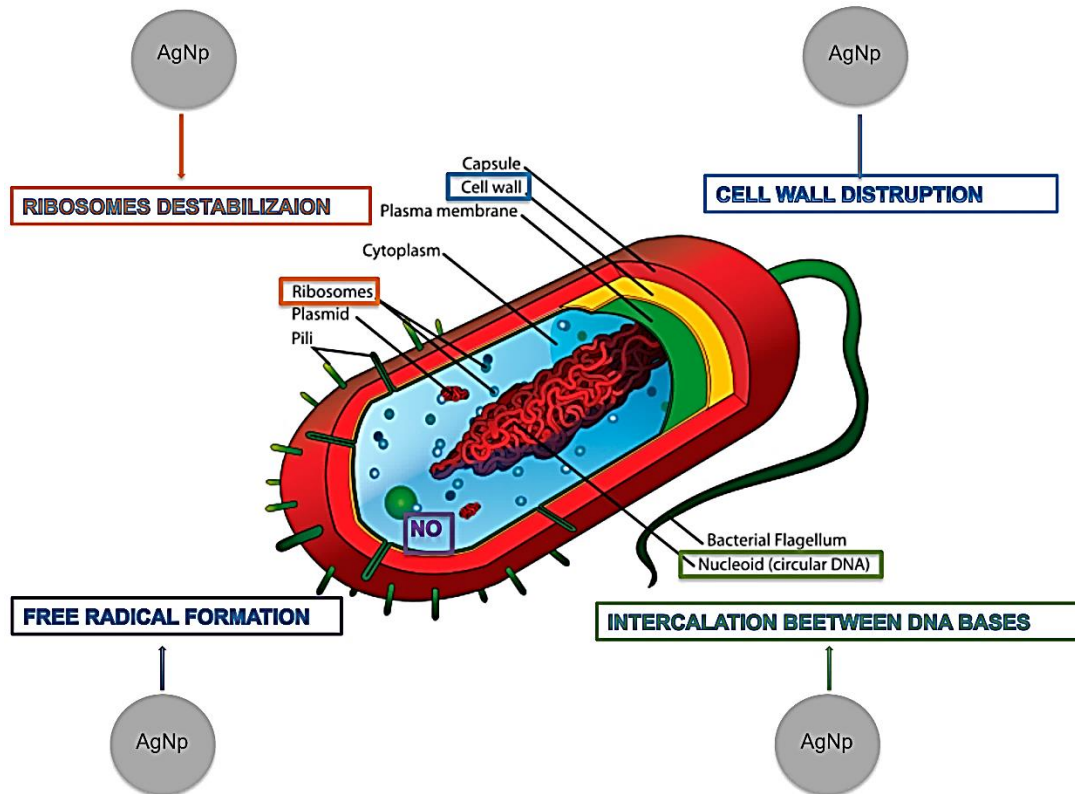
Figure 2-11. Mechanisms of antibacterial action of Ag-NPs. Adopted from [79].

2.4.3 Copper

The discovery of copper alloys (> 60% copper) as solid antimicrobial material capable of destroying microorganisms is considered a great innovation in antimicrobial surfaces technology [80-82]. Solid Copper alloy has since 2008 been registered by US Environmental Protection Agency (EPA) as solid antimicrobial copper surfaces. As a further development, Cu and Cu alloys now show great potential for use as antimicrobial-touched surfaces in hospitals and healthcare facilities. For instance, compared to stainless steel surfaces, copper alloys exhibited good antibacterial property and effectiveness at reducing bioburden of HCAI pathogens such as *E. coli O157, methicillin-resistant S. aureus* (MRSA)*, C. difficile, influenza A virus, adenovirus,* and *fungi*

[83, 84]. A recent study by Chatterjee, P. et al. [85] on copper-impregnated solid material surfaces in patient rooms, showed a 58% reduction in aerobic bacteria colonies compared to standard hospital laminated stainless steel surfaces.

2.4.4 **Photocatalytic antimicrobial agents**

Photo catalysis is defined as the acceleration of a chemical transformation by catalyst in the presence of solar irradiation [86]. Photocatalysis is generally observed for semiconducting materials, and for large band-gap semiconductors like titanium dioxide (TiO_2), zinc oxide (ZnO) and cerium oxide (CeO_2). Fujishima and Honda, reported in the early 1970s the photocatalytic splitting of water on TiO_2 electrodes [87] and since then, there has been great interest in TiO_2-based photocatalysis for renewable energy, environmental, and healthcare applications such as antibacterial coatings, disinfection of water, water splitting, organic pollutant degradation etc. Compared to standard chemical approaches, photocatalysis exhibits key advantage of using sunlight to activate and drive the degradation processes and is therefore, energetically sustainable, and more eco-compatible. Photocatalytic antimicrobial agents generate free radicals when activated by light irradiation. The commonly used photocatalytic antimicrobial agents are zinc oxide (ZnO), titanium dioxide (TiO_2), silver phosphate (Ag_3PO_4), etc. Under photon irradiation, metal oxide is catalyzed to generate Reactive Oxygen Species (ROS). These ROS such as singlet oxygen molecules ($^1O_2$), superoxide anion radicals ($*O_2^-$), hydroxyl radicals ($*OH^-$) etc., have strong oxidizing ability and can destroy pathogens. These free radicals can interact with outer cell

membrane and decomposing them into CO_2, H_2O, N_2 and S. In the process, DNA and other biomolecules are annihilated, leading to bacterial cell death (Figure 2.12).
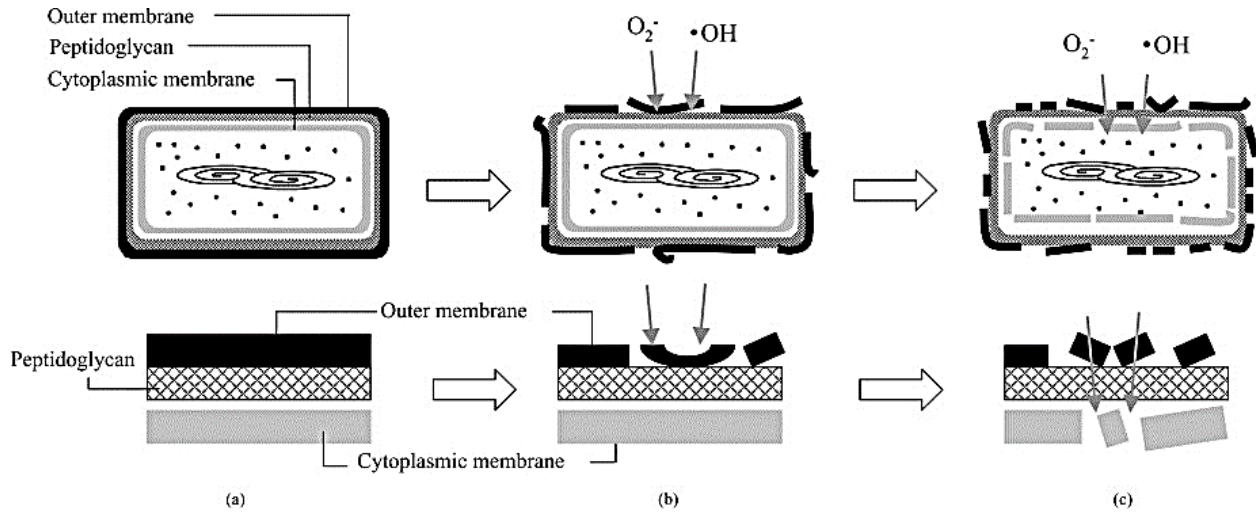
Figure 2-12. (a–c) Schematic representation of photo killing mechanism in *E. coli* on TiO_2 film. Adopted from [89].

2.5 Fabrication of antibacterial coatings

Antibacterial coatings are surfaces fabricated from build-up thin films of antibacterial agents on substratum surfaces [88]. Antibacterial coatings or surfaces used interchangeably can reduce the extent of attachment and proliferation of bacteria. Antibacterial coatings are generally classified into two main categories (Figure 2.13): *Anti-biofouling surfaces* that repel initial bacterial attachment by steric, electrostatic repulsion and low energy surfaces; and *bactericidal surfaces* that kill bacteria by releasing biocides or by physical topography [89]. An example of steric repulsive anti-biofouling surface is polyethylene glycol (PEG) coating. An example of electrostatic repulsive surface is *antimicrobial peptides* (AMP). On the other hand, *Low energy surfaces* are self-cleaning, the so-called superhydrophobic surfaces. *Bactericidal surfaces* disrupt

37

cell membrane to result in bacterial death [90]. *Bactericidal surfaces* can be grouped into those that inactivate bacteria by releasing biocides (such as metallic silver and copper) or inactivate by topography.

Typically, antibacterial surfaces are fabricated by chemical, biological and physico-mechanical surface modification strategies [13]. Chemical and biological modifications include, surface functionalization, polymerization, plasma-assisted surface treatment etc., whereas physical modification may include fabrication of surface topography [91]. For this thesis, attention is focused on chemical and physical modification methods, which lead to topography-mediated antibacterial surfaces, superhydrophobic antibacterial surfaces and hydrophilic antibacterial surfaces.
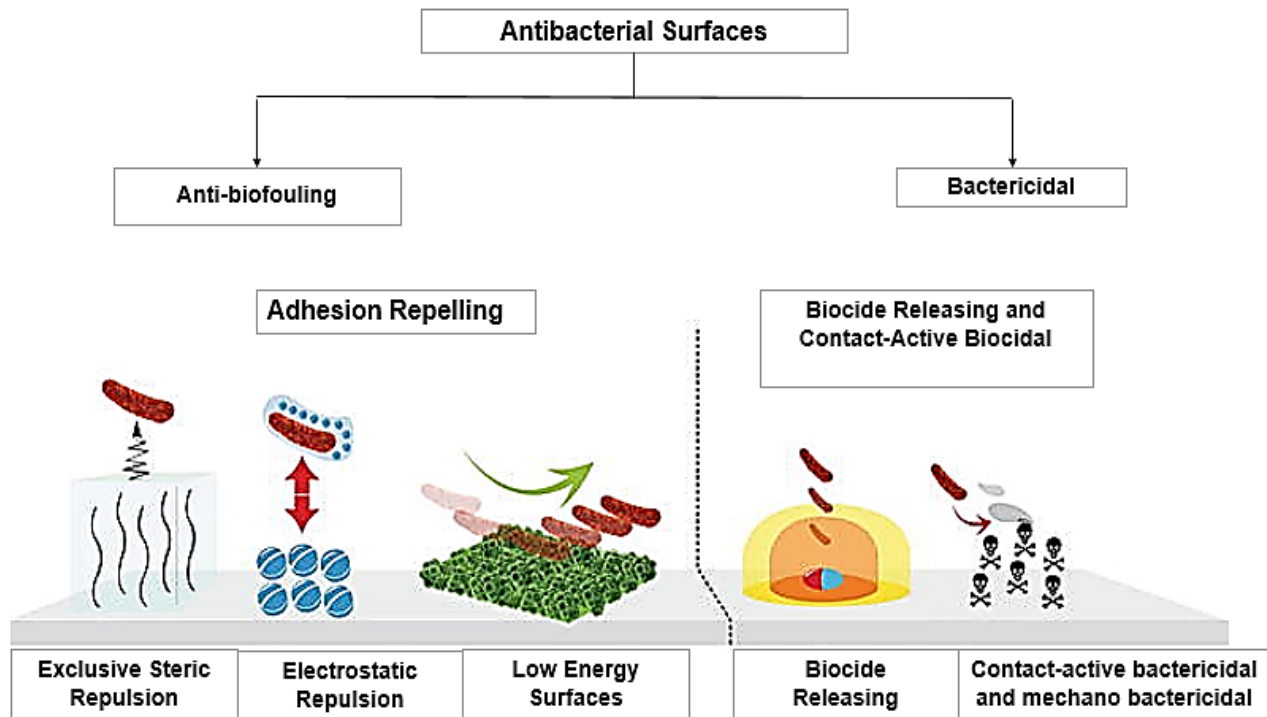
Figure 2-13. Classification of antibacterial surfaces. Adapted from [91] with permission.

2.5.1 **Fabrication of topography-mediated antibacterial surfaces.**

In nature, many living things such as insects, plants, sharks and geckos have developed protective mechanisms towards pathogens, despite the latter's ability to employ complex adaptive mechanisms to colonize surfaces [92]. The former on the other hand, exploit their micro- and nano-topographical features to induce antibacterial activity. These surfaces that kill bacterial cells by topography are called Mechano-bactericidal surfaces [92]. The first mechano-bactericidal surfaces mediated by nano topography of cicada wings was reported by Ivanova and co-workers [93]. In this work, Ivanova et al, showed that by pure physical contact of *P. aeruginosa* (gram -ve) bacterium on topographical rough surface of cicada's wings, *P. aeruginosa* died in 30 minutes. As a result, various report on other wings, such as dragonfly and skin of geckos etc., and their synthetic analogues have been fabricated on metals, ceramics and polymers [94] (Figure 2.14).
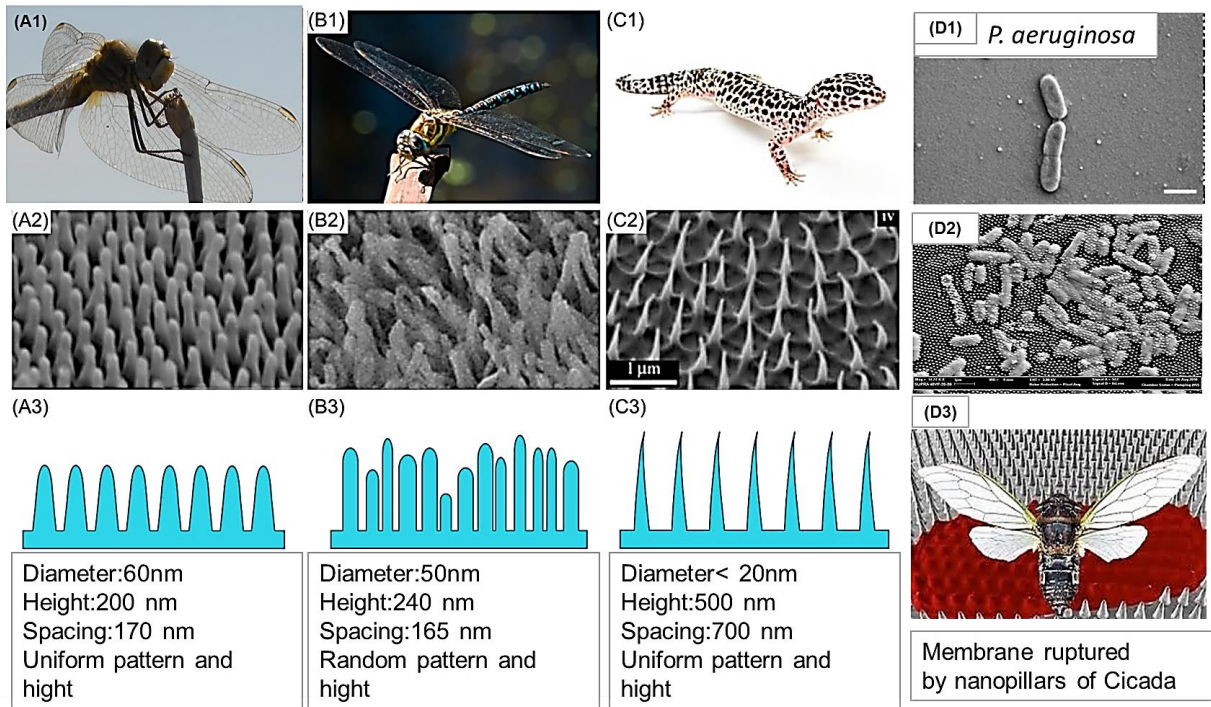
Figure 2-14. Naturally occurring mechano-bactericidal surfaces: (A1–C1), psaltoda claripennis, dragonfly and gecko, respectively; (A2–C2), Scanning electron microscopy (SEM) images of cicada wing, dragonfly wing and gecko skin; (A3–C3), Schematic of the representative nano topographies found on the cicada wing, dragonfly wing and gecko skin, to illustrate the differences between each nano-topography; (D1-D3), *Pseudomonas aeruginosa* ruptured by cicada wings. Adapted from [3].

Mechano-bactericidal surfaces can be fabricated by chemical and physical surface modification processes, such as alkaline hydrothermal process, reactive ion etching (RIE), thermal oxidation, anodization, chemical etching and glancing angle deposition (GLAD) [3]. Hydrothermal process can be used to fabricate nanostructures of varied topography on titanium and other substrates. Typically, the micro-nanoscale patterns of the metal are fabricated from the aqueous precursor in a sealed stainless steel autoclave above ambient temperature and atmospheric pressure (Figure 2.15 (A), Top). For instance, alkaline hydrothermal has been used to fabricate

TiO$_2$ topographical nanostructures on titanium alloy, Ti-6Al-4V [95]. By controlling experimental parameters such as temperature, reaction time, concentration of the reaction media (e.g., acids or bases) various topographical nanostructures similar to dragonfly were fabricated, as shown in figure 2.10 (A), Bottom) [3].

Another common technique is thermal oxidation. This involves the oxidation of substrate to grow nanostructures by controlling the temperature within a range of 400 to 900 °C in a carbon-containing atmosphere (Figure 2.15 (B), Top) [3]. Thermal oxidation can generate nanostructures analogue to the topographical features of the wings of dragonfly (Figure 2.15 (B), Bottom) [3]. Anodization is like thermal oxidation process except that the oxidation process is achieved by electrochemical means (see Section 2.7.1). Anodization process can also generate such topographical features, however, to the best of our knowledge, bactericidal property achieved purely by anodization for touched surfaces application is yet to be reported in the literature.

Regarding physical modification process, glancing angle deposition (GLAD) and Reactive ion etching (RIE) are the most commonly used fabrication techniques [91]. During conventional physical vapour deposition, a stream of vapour-phase atom strikes and condenses upon a perpendicular substrate to form a dense, solid film. Contrarily, for GLAD, the substrate can be tilted to a glancing angle or rotated such as to create an oblique deposition geometry [96]. Typically, GLAD involves an oblique angle deposition and manipulation of substrate (by tilting and rotating) to engineer columnar architectures nanostructured on surfaces (Figure 2.15 (C), Top) [97]. The main feature of GLAD is the "shadowing effect" or line-of-sight.
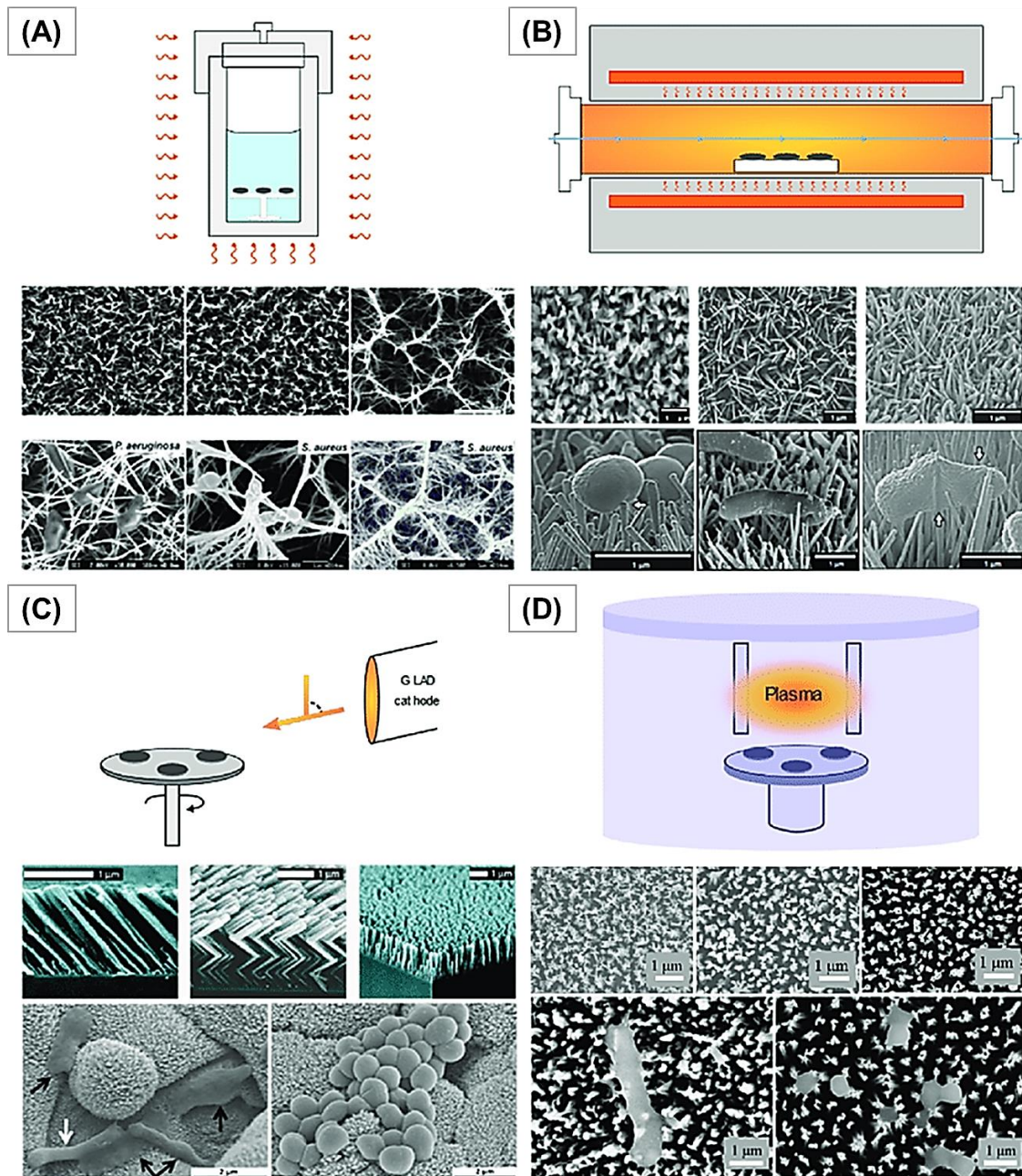
Figure 2-15. Nanofabrication techniques and surface topographies generated: (A) Alkaline hydrothermal (AH); (B) Thermal oxidation (TO); (C) Glancing angle deposition (GLAD) and (D) Reactive ion etching (RIE). Each panel shows a basic schematic of the technique, an example of the topographical nanostructured surfaces generated by each technique and evidence of bactericidal activity. Adapted from [2] with permission.

Thus, the "shadowing effect" prevents incoming vapour from condensing into regions behind the nuclei, causing the nuclei to develop into columns that tilt towards the vapour source [96]. GLAD method has been used to fabricate highly and precisely controlled micro and nanostructures (Figure 2.15 (C) Bottom) [3]. Reactive ion etching (RIE) involves the partial removal of a top layer of substrate to create desired micro-nano-porous topographical patterns from a reaction plasma in a low vacuum system (Figure 2.15 (D), Top). RIE was utilized by Ishak, Mohd I et al. to fabricate micro-nano topographical features (Figure 2.15 (D) Bottom) [3].

Overall, mechano-bactericidal surface is promising, innovative and environmentally friendly antibacterial surface technology when compared to traditional antibacterial coating since the former is durable, do not leach out toxic ions or lead to antibacterial resistance problem [13]. Thus, mechano-bactericidal surface is more eco-sustainable and has great potential for biomedical and general healthcare applications.

2.5.2   **Fundamentals of superhydrophobicity**

Wettability defines the tendency for a liquid droplet to wet or spread over solid surface. The wettability of a solid surface plays an important role in our daily lives, marine and biomedical industry. The contact angle a droplet makes with a solid surface is a function of its surface free energy or the energy required to break an intermolecular bond [98]. Contact angle is the angle between the liquid-vapor and liquid-solid interface. For an ideal rigid, chemically homogeneous, non-reactive smooth solid surface, its contact angle at thermodynamic equilibrium condition is predicted based on the Young model, (Figure 2.16 (A)) given by equation 2.1.

$$\cos \theta = \frac{(\gamma_{SG} - \gamma_{SL})}{\gamma_{LG}} \qquad\qquad (2.1)$$

where the θ is contact angle, (γ_{SL}), is the solid-liquid interfacial surface energy, (γ_{LG}) is the liquid-vapor interfacial surface energy and (γ_{SG}) is the solid-vapor interfacial surface energy. However, in practice, surfaces are rough and chemically heterogeneous. To compensate for roughness, Wenzel proposed a model to explain the relationship between surface roughness and the apparent contact angle, where a liquid droplet completely fills the surface structures [99] (Figure 2.16 (B)).
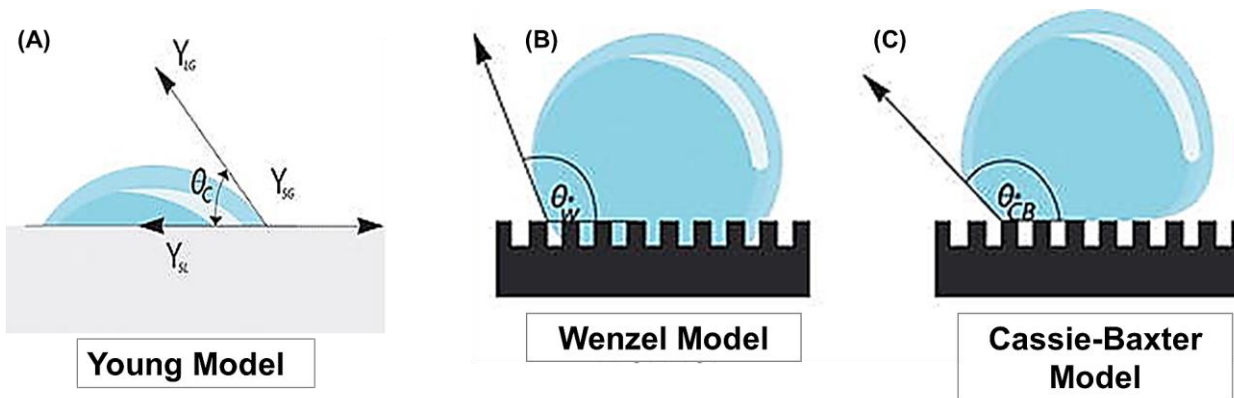
Figure 2-16. Liquid droplet on solid surfaces, representing the Young (A), The Wenzel (B) and The Cassie-Baxter models (C). Adopted from [103].

By introducing a roughness factor, the apparent contact angle at equilibrium, can be expressed as equation 2.2.

$$\cos\theta^* = r cos\theta \qquad\qquad\qquad\qquad\qquad\qquad\qquad\qquad\qquad (2.2)$$

where the Wenzel roughness factor, r is defined as the Roughness r of the material and can be expressed as a ratio of the actual surface area to the apparent surface area and θ^* and θ represent the liquid contact angles on rough and ideal smooth surfaces, respectively. By increasing the roughness (a bigger height difference between the posts and grooves, and the density of posts), super hydrophobicity can be achieved for such homogeneous surfaces [100].

However, for heterogeneous surfaces with different chemical compositions and contact angles, Cassie and Baxter [101] proposed that if the heterogeneous surfaces are sufficiently hydrophobic, the air phase between the solid-liquid micro-nano groove interface will remain entrapped, providing a lower surface area between droplet and underlying solid rough surface, and thus, become liquid repellent (Figure 2.16 (C)). Cassie and Baxter contact angle can be modelled according to equation 2.3

$$\cos\theta^* = f_s cos\theta_s + f_G cos\theta_G \qquad\qquad\qquad\qquad\qquad\qquad (2.3)$$

where f_s and f_G are the fractions of the solid and vapor areas on the surface, respectively. Also, θ^*, θ_s and θ_G constitute the composite contact angle of the heterogeneous surface, and the contact angles of the components of the micro-nano hierarchical surface structures and the entrapped air, respectively. Furthermore, micro-nano hierarchical surface structures and the entrapped air constitute the f_s and f_G area fractions, respectively. Assuming the contact angle of the air or vapor is 180°, and $f_G = 1 - f_s$, then the equation 2.3 can be further modified as:

45

$$\cos\theta^* = f_s(\cos\theta + 1) - 1 \qquad\qquad\qquad (2.4)$$

Thus, according to agreed definitions, surfaces can be classified into one of four categories [13]:

1. Surfaces with a water contact angle $> 150°$ and a contact angle hysteresis $< 10°$, are considered superhydrophobic and self-cleaning.

2. Surfaces with a water contact angle between $90°$ and $150°$, are hydrophobic.

3. Surfaces with a water contact angle between $10°$ and $90°$, are hydrophilic.

4. Whereas those with a water contact angle $< 10°$ can be considered super hydrophilic. From Cassie-Baxter model, super hydrophobicity is due to the combined effects of low surface energy molecules (26 mJ/m^2) and the entrapped air within the micro-nano hierarchical surface structures.

2.5.2.1 Fabrication of superhydrophobic antibacterial surfaces

Scientists have discovered the unique water roll-off property in several plants, such as lotus leaves. These plants utilize their surface micro-nanoscale structures to adapt, inhibit colonization and as evolutionary surviving strategy [102]. The micro-nanostructures are made of long chain palmitic (hexadecanoic) and stearic (octadecanoic) fatty acids [103], which render them superhydrophobic. Inspired by nature, scientists now fabricate superhydrophobic surfaces in the lab by patterning micro-nano structures, followed by passivation with low surface energy molecules.

Various strategies such as photolithography, sol–gel, plasma etching, anodization and chemical etching [104], have been employed to fabricate superhydrophobic surfaces, which find applications as self-cleaning-fabrics, anticorrosion, drag reduction and anti-biofouling surface [105]. Of particular interest is in anti-biofouling application, as superhydrophobic surfaces have the potential of preventing initial bacterial attachment and subsequent biofilm formation. However, superhydrophobic surfaces fail under long-term exposure in humid environments [106]. Thus, incorporating bactericides in superhydrophobic coating holds promise not only in inducing both anti-biofouling and antibacterial properties, but also for improving their longevity. Chung et al. [107] fabricated silver-perfluorodecanethiolate coatings on silicon wafer with both superhydrophobic and antibacterial properties via precipitation method, using perfluorodecanethiol (PFDT) and silver as fluorinated and metal-thiolate complexes precursors, respectively (Figure 2.17 (A)). This silver-perfluorodecanethiolate superhydrophobic surface exhibited bacterial adhesion reduction factor of 77%. In a related work, Wang et al. [108] fabricated superhydrophobic diamond films with both antibacterial and anti-biofouling properties using both hot filament chemical vapor deposition and sol-gel perfluorodecyltrichlorosilane (PFTS) process (Figure 2.17 (B)). The perfluorodecyltrichlorosilane superhydrophobic diamond films showed a bacterial adhesion reduction of 90-99%.
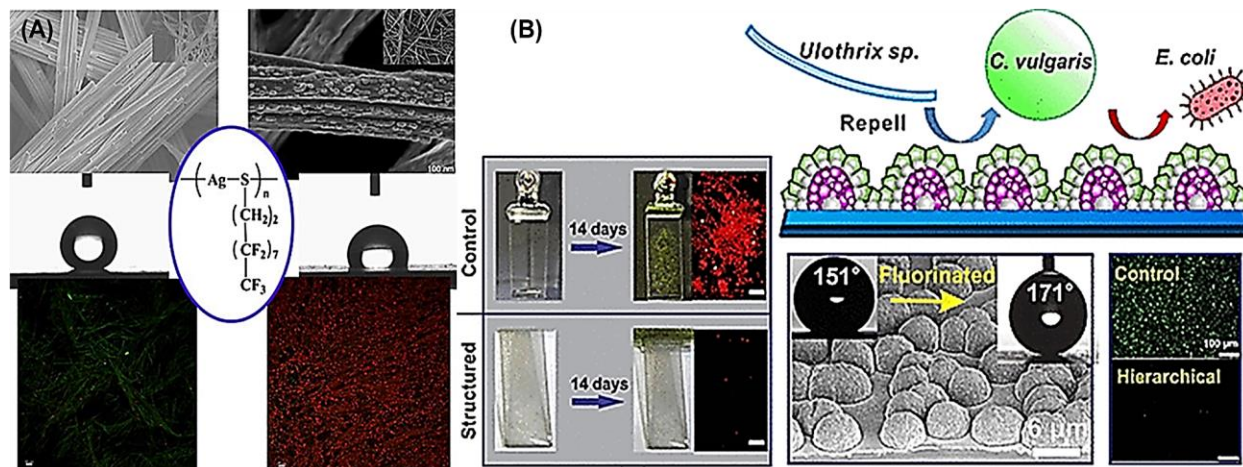
Figure 2-17. (A) Silver-perfluorodecanethiolate superhydrophobic coatings; (B) Hierarchical structured diamond superhydrophobic films with Anti-biofouling, self-cleaning and antibacterial properties. Adopted from [107, 108] with permission.

2.5.3 Fabrication of hydrophilic antibacterial surfaces

Hydrophilic antibacterial coatings are surfaces with contact angle between 10° and 90°. Like superhydrophobic antibacterial surfaces, fabrication of hydrophilic antibacterial surfaces involves physical, chemical and biological processes. These surfaces are particularly useful for orthopaedic and medical implants device as they enhance protein conditioning and cell tissue integration [109]. Various hydrophilic antibacterial agents such as TiO_2, ZnO, Ag and Cu nanoparticles are commonly fabricated on metals and other substrates. However, for the purpose of this thesis, silver-based hydrophilic antibacterial coatings fabricated by chemical and electrochemical reduction processes are discussed further.

2.5.3.1 **Chemical and electrochemical reduction**

Silver nanoparticle is commonly synthesized from $AgNO_3$ using various reducing agents including citrate, sodium borohydride, $(NaBH_4)$, hydroquinone, Tollen's reagent, N,N-dimethyl formamide (DMF), poly (ethylene glycol) (PEG), ascorbic acids, ethylene glycol etc., [110]. However, chemical reduction method results in agglomeration of large-sized particles. To overcome this problem, morphological controlling agents such as polymers and surfactants are normally used, in particular, polyvinylpyrrolidone (PVP), polyvinyl alcohol (PVA), cationic Cetyl trimethylammonium bromide (CTAB), and anionic dioctyl sulfosuccinate (DOSS) surfactants. Chemical reduction is by far the most widely used because: (a) it is relatively cheap and an efficient synthesis method; (b) different morphologies (cube with (100), trigonal with (111), rhombdodecahedron and spherical) can be produced; and (c) is amenable to large-scale production [111]. However, disadvantages with chemical reduction tend to be toxicity concerns and difficulty with separating capping agent from Ag-NPs after synthesis.

To overcome the toxicity concerns, biocompatible green silver synthesis processes such as plant extracts, micro-organisms and sol-gel processes are gaining interest in recent times [54, 112, 113]. In particular, sol-gel process has advantage of being a low temperature synthesis process, which facilitates easy synthesis of inorganic and hybrid composite materials of organic moieties [114]. The most common precursors are tetraethyl orthosilicate (TEOS) and tetramethylorthosilicate (TMOS). Sol-gel process generally involves the simultaneous hydrolysis and condensation of organic and inorganic moiety [115]. The colloidal suspension (sol) subsequently evaporates to form a 3 dimension network in a continuous liquid phase (gel) [116] (Figure 2.18). This can subsequently be coated on substrate by dipping, casting, spinning, or spraying processes. For instance, Agbe et al [117], recently deployed a sol-gel process to fabricate

silver-polymethylhydrosiloxane (PMHS) nanocomposites, followed by dip coating on anodized aluminum. The Ag-PMHS nanocomposite coating on anodized Al showed excellent anti-biofouling property with an adhesion reduction of 99.0 %, 99.5 %, and 99.3 % for *P. aeruginosa*, *E-coli* and *S. aureus (*S.A), respectively.
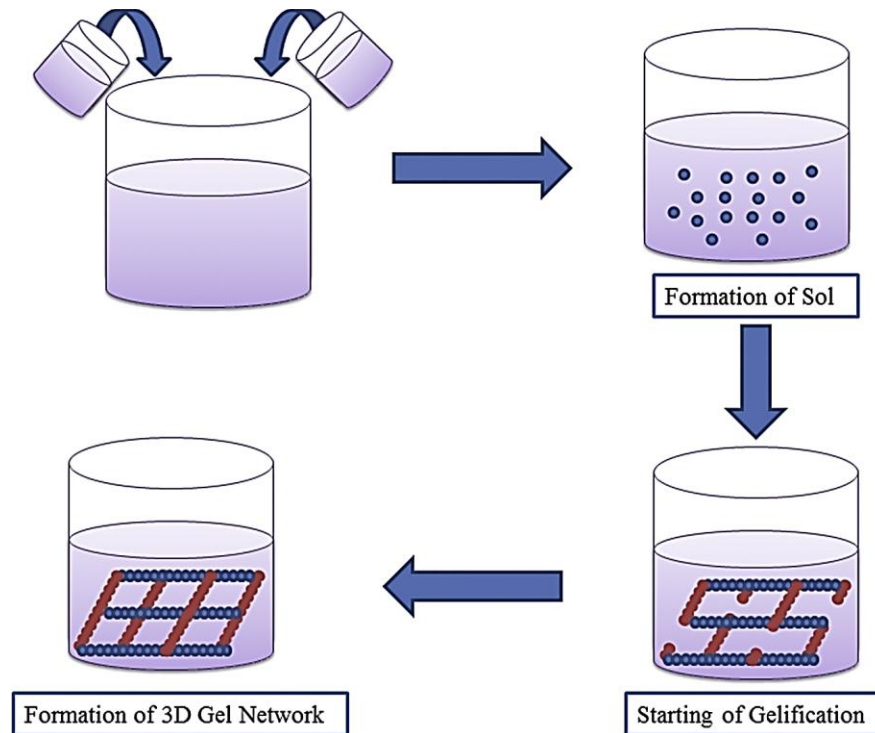
Figure 2-18. General reaction scheme of sol–gel technique. Adopted from [116]), with permission.

Another commonly used method is electrochemical reduction process. In this process, silver is deposited on the cathode from a solution of its salt. As the reduction of Ag^+ ion to Ag^0 is thermodynamically non-spontaneous, an external driving force (Direct current (DC), or alternative current (AC) power supply) is required to drive the electrolytic chemical reduction process.

Contrarily, in a galvanic cell, chemical reaction converts electrical energy to drive an external load. A complete electrolytic cell consists of: (a) two conducting anode and cathode electrodes; (b) an electrolyte, containing ions of the metal or solid to be deposited; and (c) a DC, AC, or pulse current mode. Typical electrodeposition process is shown in figure 2.19.
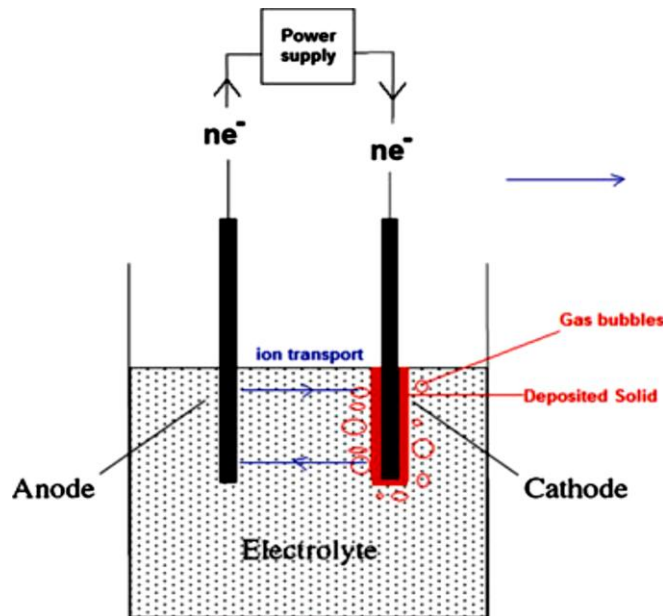
Figure 2-19. Schematic of electrodeposition process. Adopted from [121].

As an engineering material, aluminum has become one of the commonly used substrates for electrodeposition of metallic coatings such as silver. For electrodeposition of silver on anodized aluminum oxide (AAO/Al), AC power source is ideal [118, 119]. In a typical AC electrodeposition process, the barrier oxide layer acts as a rectifying p-n junction source. Therefore, AAO/Al templates can be used directly as the cathode during an electrodeposition process. Thus, the barrier layer becomes preferentially conductive during the cathodic half-cycle. This rectifying property allows reduction of metal ions in the pore while decreasing the oxidation rate of the deposited metal [119]. Chir, *et al.* [118] deployed AC electrodeposition to deposit Ag for antibacterial

application. Their results showed a 95% antibacterial efficiency for *E. coli*, *P. aeruginosa*, *Streptococcus faecalis* and *S. aureus.* However, for DC electrodeposition, it is necessary to separate the AAO/Al templates by chemically etching to separate the base aluminum metal, followed by metallization of the AAO/Al [120]. However, this may be challenging and increase complexity of the overall electrodeposition process.

2.6 Challenges of antibacterial coatings for touched surfaces application

An ideal antibacterial coating for frequently touched surface application should be fabricated with simple and low-cost process. It must be adaptable to large-scale production, possess ability for broad-spectrum effectiveness, mechanically stable, and non-toxic. However, despite the many efforts, most antibacterial coatings have not been able to transition from the laboratory bench to the market [13]. There are four main challenges in designing safe antibacterial coatings including: *lack of durability* (*the long-term stability of coating), leaching and toxicity*, *antibacterial resistance problem* and *the lack of standardized* testing protocols [121].

While antibacterial surfaces have the potential to contribute to reducing HCAIs, antibacterial surfaces cannot be a stand-alone solution. It must therefore be included as an adjunct to existing protocols in a horizontal multi-interventional approach to fighting HCAIs. Despite the promising role of antibacterial coatings, most of them are unstable and mostly temporary solution. To overcome this challenge however, polymeric viscous matrix such as poly(methacrylic acid) (PMMA), polyacrylic acid (PAA) and resins, have become common to covalently tether antibacterial agents to substrates for enhanced coating stability [122]. However, it is important

mechanical testing, such as hardness, tribology, scratch, and anti-adhesion studies are performed on these coatings.

Another challenge with existing antibacterial coatings for touched surfaces is the uncontrolled release kinetics of coatings with leachable antimicrobial agents, leading to possible toxicity concerns. Even with the well-established implant device applications, coating with leachable antibacterial agents that maintain release kinetics within the therapeutic window (that is release kinetics sufficient to kill bacteria but low enough to limit cytotoxicity toward eukaryotes) remains a significant challenge [122]. Thus, the health and environmental impacts of nanoparticles in leachable antibacterial agents of existing frequently touched antibacterial coatings are not clear. A promising technique to tackle this problem is the concept of *Safe by Design* (SbD). SbD is a generic concept with an ultimate goal of eliminating potential health and safety risks associated with products or processes during the early design phase [121]. Thus, the next generation antibacterial coatings must comply with regulations by incorporating health and safety risks that might be difficult to deal with after products get to the market [121].

Another issue worthy of consideration is antibacterial resistance problem. Pathogens implicated in HCAIs can develop various clever pathways to develop resistance to antibiotics. The natural tendency of bacteria to mutate due to selection pressure and the indiscriminate use of antibiotics for both human and veterinary medicine have given rise to multiple-drug resistant pathogens. It is estimated that more than 40 % of *S. aureus* strains collected from hospitals are resistant to methicillin antibiotics [68]. Thus, given the massive report of antibacterial coatings in the literature, coupled with widespread use of antimicrobial agents and disinfectants for sanitizing frequently touched surfaces in the current COVID-19 pandemic, it is feared antimicrobial resistance may exacerbate, post-COVID-19 pandemic [50]. The rationale behind adding an

antimicrobial agent to a specific surface should be a balance between the potential impact of the antimicrobial agent on the emergence of resistant microbial strains and the impact of preventing the spread of the pathogen within the healthcare environment [121]. Therefore, there is an urgent need for developing novel topography-mediated antibacterial surfaces to minimize the risk of antimicrobial resistance.

Finally, since antibacterial coatings for frequently touched surfaces is a new line of research, the field lacks *standardized* testing protocols. This makes it impossible to establish a proper comparison between antibacterial coatings with different antimicrobial agents and processing technologies that are both in the market and in the research and development phase [121]. It should be mentioned that existing protocols such as the ASTM 2180 [123], Japanese Standard JIS Z2801 [124] and ISO 22196 [125] stipulate conditions of high liquid medium ($> 90\%$ humidity) and temperature up to 37°C, to allow for diffusion of antimicrobial agents. However, these do not necessarily reflect the near dry surface conditions around patients, requiring comfortable humidity and temperature [126]. Thus, these protocols may not truly predict the efficacy of antibacterial surfaces under realistic conditions [126]. The USA Environmental Protection Agency's (EPA's) protocol on non-porous hard surfaces [127], is yet another common antimicrobial testing method. Though it attempts to simulate typical contaminated clinical environment, it does not completely mimic the near dry conditions of typical high touch surfaces contaminated by the human skin [128]. Also, a number of other evaluation methods such as Agar zone of inhibition assay, Adhesion-based assay, Live and Dead staining, MTT (based on the reduction of MTT dye 3-(4,5-dimethylthiazol-2-yl)-2,5-diphenyl tetrazolium bromide to purple formazan by NAD(P)H), Bioluminescent strains etc., do exist [129]. However, each of these methods have their limitations, for instance, the Live/dead staining (e.g. LIVE/DEAD Bacterial

Viability Kit (BacLightTM)), which demonstrates the presence or absence of cell wall damage, following bacterial contact with antibacterial coating may not always be valid since damaged cell walls (red fluorescent bacteria-usually presumed dead) may sometimes be culturable [130]. Again, the Bioluminescence and MTT assays, which rely on metabolic activity to demonstrate cell viability, may be flawed since an absence of metabolic activity may not necessarily mean bacterial death [129]. Thus, in the absence of *standardized* testing protocols for evaluating effectiveness antibacterial touched surfaces, it is hoped that many of the above assays would be complemented to evaluate promising candidates to enable transition from laboratory bench to the market.

.

2.7 Aluminum as an antibacterial surface

Traditionally, stainless steel has been the most common metallic alloy for fabricating frequently touched surfaces. However, despite its aesthetic appeal and ease of cleaning, it offers no antimicrobial effect and therefore not the most suitable material for high-touch surface fabrication [131-134]. Thus, alternative material with inherent antibacterial property such as copper is becoming of interest. However, problems with solid metallic copper such as long-term corrosion, poor aesthetic appeal, difficulty in machining, and relative high cost [135], necessitate the need for other novel, durable and mechanically stable alternatives.

Aluminum is a very attractive material for engineering constructions and many aluminum components are widely used in medical devices [136]. Aluminum can be transformed into antibacterial surface via simple wet chemistry and electrochemical processes. Even so, only few studies on antibacterial aluminum surfaces have been reported in the literature. Hasan et al [137], utilized 0.2 M NaOH to chemically etch aluminum Al 6063 to fabricate antibacterial aluminum

surface against the *severe acute respiratory syndrome coronavirus 2* (SARS-CoV-2). This topography-mediated antibacterial surface resulted in a 5-log reduction in viral load after 6 h of contact [137]. In a related study by same group [136], 0.2 M NaOH was employed to chemically etch aluminum Al 6063 to fabricate topography-mediated antibacterial surface. This surface was successful in inactivating multi-drug resistant bacterial (MDR) pathogens such as *P. aeruginosa* and *S. aureus* and common respiratory viruses such as respiratory *syncytial virus* (RSV) and *rhinovirus* (RV). The surface resulted in a 92 % and 87 % reduction of P. *aeruginosa* and *S. aureus* bacteria, respectively under 3 h. Similarly, a 3−4 log reduction in RV viral load was achieved under 24 h. In another study by Valiei et al [138], silver-quaternary ammonium salt was dipped coated unto anodized aluminum to fabricate antibacterial aluminum surface which inactivated the growth of MDR bacteria such as *S. aureus*, *P. aeruginosa*, *E-coli and E. faecalis*. Their antibacterial aluminum surfaces exhibited excellent bacterial killing between 2-15 minutes of contact.

Thus, through surface modification strategy such as anodization, aluminum can be optimized to create nano-porous topographical pattern, which kill bacterial on contact; or passivating the nano-porous topographical pattern with low surface energy molecules, to create superhydrophobic coatings capable of repelling bacterial adhesion; or immobilizing the nano-porous topographical patterns with antibacterial agents to kill bacteria on contacts. Not only can the anodized pores aid in chemical adhesion but also mechanical anchorage to enhance coating durability. Again, the anodized oxide layer protects aluminum from corrosion and wear, thus improving overall longevity of the antibacterial coating.

2.7.1 **Anodization of aluminum**

Anodization involves formation of close-pack hexagonal nanostructures with a periodic arrangement of nanopore arrays by controlling electrochemical parameters such as electrolytes, potential, current density, temperature, and anodization time. By optimizing these parameters, a self-organized densely close-pack aluminum porous template can be fabricated that can serve as paint primers and glues for decorating aluminum surface, as anticorrosive surface or templates for synthesizing functional nanomaterials for various applications in rechargeable batteries, memories, water splitting and antimicrobial surfaces [139-142]. Though anodization of aluminum has been in existence since the 1920s [143], it was only after the discovery of the two-step anodization process by Masuda and Fakuda in 1995 [144] that truly self-organized densely hexagonal anodized aluminium oxide (AAO) templates were achieved.

2.7.2 **Structure and morphological features of anodic porous alumina**

Control of anodization conditions produce morphological features that can serve as porous template for subsequent applications. The most important porous oxide features include pore size (pore diameter) D_p, cell diameter (inter-pore distance) Dc, wall thickness W, barrier layer B, porosity (a) and pore density (η), as shown in Figure 2.20.
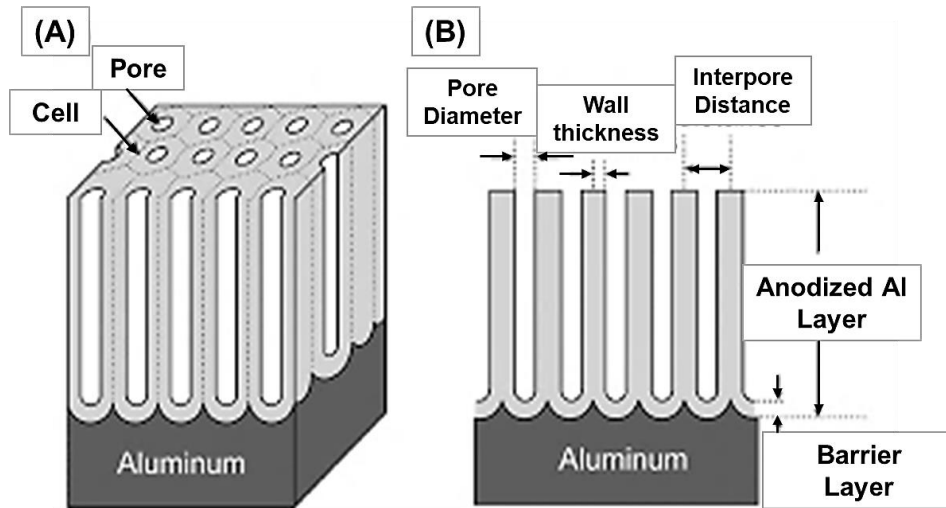
Figure 2-20. Idealized structure of anodic porous alumina (A) and a cross-sectional view of the anodized layer (B). Adapted from [146], with permission.

.

The pore diameter, D_p defines the diameter of pores created at the porous oxide layer under controlled electric field. It varies linearly with applied potential (V) as proposed by O'Sullivan and Wood [145], according to equation 2.5.

$$D_p = \lambda_p \times V \tag{2.5}$$

As expected, the rate of porous structure formed depends on anodization conditions such as voltage and pH (concentration of electrolyte) [146]. For H_2SO_4 electrolyte, a potential of 25 V and concentration > 5 M (27 wt.%) at acidic pH, are ideal conditions for producing small size pore diameter, whilst high potential 45 V, produces larger pore size [146]. Similar trend has been observed for H_3PO_4 and organic electrolytes [145].

The cell diameter D_c can be defined as the inter-pore distance between two pores. It varies linearly with applied potential, according to equation 2.6, where D_c is cell diameter; V is the applied potential and λ_c, a proportionality constant of ~ 1.29 nmV^{-1}. Anodization of aluminum in electrolyte of H_2SO_4 with an applied potential of 12.5 V and 24 V was found to produce cell diameters of 32.7 ± 2.8nm and 45.4 ± 8nm, compared to 65.1 ± 6.5nm and 80.5 ± 3nm for high potentials such as 30 V and 40 V [147].

$$D_c = \lambda_c \text{ x } V \tag{2.6}$$

The wall thickness is usually calculated as the difference between cell diameter and pore diameter. Since both cell diameter and pore diameters are circular, wall thickness W, can be calculated from equation 2.7.

$$W = \frac{Dc - Dp}{2} \tag{2.7}$$

The larger the pore diameter at constant cell diameter, the smaller the wall thickness. According to O'Sullivan and Wood, the cell wall thickness is ~ 71% of the barrier layer (B) [145]. Other morphological features of interest are pore density and porosity. The pore density n, defines the number of pores occupying a single square centimetre area (number of pores/cm^2), and represented by equation (2.8).

$$n = \frac{2.14\char`^14}{\sqrt{3\lambda^2 \text{ U}^2}} \tag{2.8}$$

where n = pore density, λ is a proportionality constant and U, the applied potential. An ideal pore density ranges between 10^9 to 10^{10} per cm^2 [146]. Like pore density, the porosity α, is the ratio of the pore surface area to entire area of the AAO surface. It is given by equation 2.9.

$$\alpha = \frac{S_{pores}}{S_h} = \frac{S_p}{S_h} \tag{2.9}$$

Assuming each pore as a perfect circle, the following equations hold.

$$Sp = \pi \left(\frac{D_p}{2}\right)^2 \tag{2.10}$$

$$Sh = \frac{D_c^2 \sqrt{3}}{2} \tag{2.11}$$

By substitution equations. (2.10) and (2.11) into (2.9), gives the expression for porosity of a porous oxide layer as:

$$\alpha = \frac{\pi}{2\sqrt{3}} \left(\frac{D_p}{D_c}\right)^2 = 0.907 \left(\frac{D_p}{D_c}\right)^2 \tag{2.12}$$

Nielsch et al [148] have reported 10 % as ideal porosity attainable under optimal conditions of temperature, applied voltage, current density and anodization time.

2.7.3 Anodization process parameters

The growth of the porous AAO requires control of operational parameters such as electrolyte, applied voltage, current density, temperature, and anodization time to achieve the required morphological features described under section 2.7.2.

2.7.3.1 Electrolytes

Several types of acidic electrolytes such as sulphuric acid, phosphoric acid, oxalic acid and chromic acid are commonly used for anodization [149-151]. However, the choice of acid depends on the desired features' size. While strong inorganic acids are the main electrolytes for anodizing aluminum, other organic acids such as oxalic acid, malonic acid, squaric acid, selenic acid, acetic acid, citric acid, tartaric acid, glutaric acid and glycolic acids have been explored [152-154]. Table 2.3 [155] shows lists of some major acids and their concentration.

Table 2-3 Acid components of typical electrolyte types used to produce porous oxide layer on an aluminum substrate

.

Electrolyte	Molecular Formula	Concentration (M)	Pore Size Range (nm)	Ref
Sulphuric acid	H_2SO_4	0.18 to 2.5	12 to 100	[146, 156, 157]
Oxalic acid	$C_2H_2O_4$	0.2 to 0.5	20 to 80	[158-160]
Phosphoric acid	H_3PO_4	0.04 to 2.0	30 to 235	[161, 162]
Malonic acid	$CH_2(CO_2H)_2$	0.1 to 5	Not specified	[158, 163, 164]

In a bid to expand the range of electrolyte, neutral aqueous solutions, and non-acidic solutions (pH = 5 - 7) are also gaining attention. Neutral aqueous solution is ideal for growing the barrier layer. The barrier layer, (which defines the thickness between the metallic aluminum and the porous oxide layer) does not only serve as protective layer against corrosion but also as electrical insulators. Examples of neutral aqueous solutions are: boric acid, ammonium borate, ammonium tartrate and aqueous phosphate solutions [165]. Apart from the type of electrolytes, concentration is equally important. Generally, high concentration increases barrier layer thickness

but decreases both porous oxide layer and the inter-pore distance [166]. Ideal concentrations for commonly used electrolytes are shown Table, 2.3.

2.7.3.2 **Applied potential, time and temperature**

In addition to selecting optimal electrolytes, applied voltage is also a critical parameter that must be controlled. This is important as each electrolyte has critical applied voltage that gives required morphology. For mild anodization, critical applied voltage for the three main electrolytes are: 25V, 40V, and 160 V, for sulphuric acid, oxalic acid and phosphoric acids, respectively [139]. Also, anodization time and temperature vary linearly with both dissolution and formation of the AAO and the resulting morphological features (such as pore and cell diameters) [167]. Thus, control of these parameters is very critical. Table 2.4 summarizes applied voltage, temperature, anodization times and pore diameters, achieved for the three main electrolytes.

Table 2-4 Effect of anodization parameters on pore diameter.

Acid	Concentration (M)	Voltage (V)	Time (min)	Temperature (ºC)	Pore Diameter (nm)	Ref
Sulphuric	0.5	45	60	0	35-40	[168]
	0.3	15-35	120	-1	30-50	[169]
	0.3	25	11	-	20-63	[170]
	12	40	30	0	70	[170]
Phosphoric	0.3	120	30	0	300	[170]
	0.3	45	60	45	45	[171]
	0.6	30-60	30-45	60-80	50-130	[172]
	Not specified	195	15	3	180	[174]
Oxalic	0.3	40	160	0	67 ± 6 and 99 ± 8	[144]
	0.3	-	300	5-15	50-130	[172]
	0.3	40	22	5-8	40	[173]
	0.3	60	35	17	70	[167]

2.8   **Kinetics and mechanism of self-organized anodic porous alumina formation**

The natural formation of oxide layer on aluminum surface in the presence of air is thermodynamically favourable. Consequently, aluminum can be anodized to form desired porous

oxide layer. During anodization, the growth and dissolution of the oxide layer follows simultaneous oxidation-reduction reactions at the anode and cathode respectively, according to equations 2.13 to 2.16.

Anodic reactions

$$2Al_s \rightarrow Al^{3+} + 6e^-$$ (2.13)

$$6OH^- \rightarrow 3H_2O + O^{2-} + 4e^- + O_2 \uparrow$$ (2.14)

$$2Al^{3+} + 3O^{2-} \rightarrow Al_2O_3$$ (2.15)

Cathodic reaction

$$6H^+ + 6e^- \rightarrow 3H_2$$ (2.16)

Assuming no complex anions formation, the Nernst equation equals:

$$E = E_0 - \left(\frac{RT}{ZF}\right) In \left(\left[\frac{Red}{Ox}\right]\right)$$ (2.17)

where R is the universal gas constant, 8.314 J.K^{-1}.mol^{-1}, T is the absolute temperature in Kelvin, z is number of electrons transferred in the cell reaction, and F is the Faraday constant (96,500 C mol^{-1}). The electrode potential E of the anodized Al electrode can be written as:

$$E = -1.66 - 0.059pH$$ (2.18)

where E^0 (V) of Al = -1.66V. According to the equation 2.18, formation of an anodic porous alumina depends on potential and the pH of electrolyte, which changes with anodization conditions.

The kinetics for the formation of self-organized anodic porous oxide alumina depends on the type of oxide formation-time transient modes. This is either in constant current (galvanostatic) or in constant voltage (potentiostatic) modes (Figure 2.21 (A) and (B)). For galvanostatic anodization, potential increases sharply at initial stage (Figure 2.21 (A-a)). The sharp increase in potential is due to high resistance induced by the compact barrier oxide layer. The potential continues to increase linearly with time until it reaches a local maximum, called the *breakdown potential* ((Figure 2.21 (A-b)). Because of the breakdown of the otherwise compact barrier oxide layer, the potential drop accordingly (Figure 2.21 (A-c)), thus, resulting in a gradual potential decrease until reaching the *steady state-forming potential* [139] ((Figure 2.21 (A-d)). At *the state-forming potential*, the rate of dissolution of oxide equals the formation of the porous oxide alumina with anodization time [139].
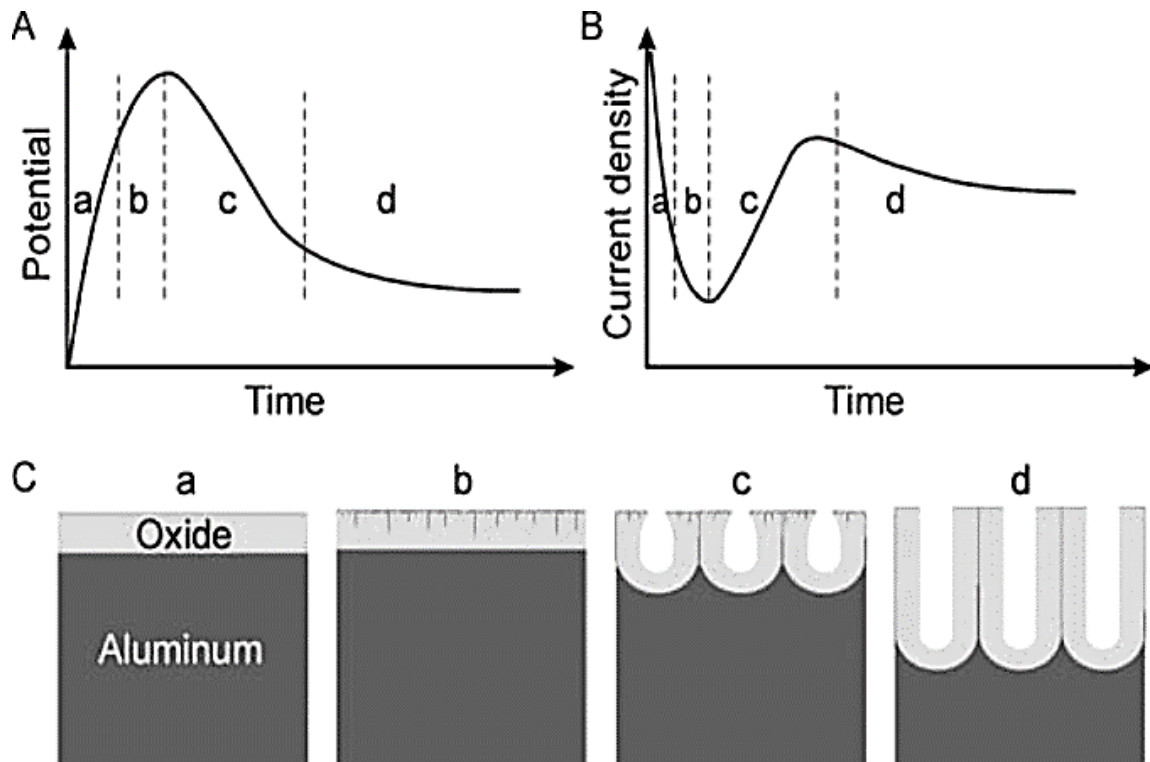
Figure 2-21. Schematic illustration of the kinetics of porous oxide growth in galvanostatic (A) and, potentiostatic (B) regimes, together with stages of anodic porous oxide development (C). Adopted from [139] with permission.

Similar kinetics occurs for potentiostatic mode, except that current density decreases sharply at the initial stage ((Figure 2.21 (B-a)); until breakdown of the compact barrier oxide ((Figure 2.21 (B-b)), followed by gradual increase in the steady state-forming potential ((Figure 2.21 (B-c-d)). Whereas both modes provide a well self-organized close-packed hexagonal porous structure, the potentiostatic mode appears to be common in the literature [169, 174, 175]. For example, Wojciech J. S et al [176], produced a well self-organized hexagonal close-packed porous structure with uniform features in potentiostatic mode for subsequent fabrication of copper nanowires. However, few researchers have also reported excellent features and nanostructure

morphologies in galvanostatic mode [149, 177]. While the choice of either modes is the prerogative of the researcher, galvanostatic mode appears to have many benefits compared to potentiostatic mode. For example, (a) it provides an efficient method for controlling anodization parameters; (b) oxide thickness and anodization time could be predicted with the "720 rules"; and (c) produces faster anodization process, which is ideal for industrial application [149, 152, 178].

The mechanism for formation of the self-organised porous nanostructures is complex and therefore various theories have been proposed [179-181]. However, current understanding is based on the field-assisted mechanism [165]. Under this hypothesis, the porous structure anodic alumina film develops from the barrier-type film at the start of the anodization process. The barrier layer is relatively homogeneous, however due to surface imperfections; localized current variations initiate nucleation for subsequent dissolution and formation of the self-organized anodic porous oxide alumina (Figure 2.21 (C a-d)). This surface heterogeneity may arise from surface roughness, defects, impurities, grain boundaries or presence of pre-treatment remnants (ridges and troughs from mechanical or electrochemical polishing or etching) [182]. Specifically, the growth of the barrier layer occurs due to the migration of ions (Al^{3+}, OH^-, O^{2-}) across the electrical double layer (metal/electrolyte interface) as results of constant electric field. This causes a uniform growth of film across the entire barrier layer (Figure 2.22 (A)). However, surface irregularity provides regions of potential difference for local galvanic corrosion. Localized current density and temperature fluctuation induce nucleation for enhanced field and or temperature-assisted oxide dissolution and formation (Figure 2.22 (B)). Since the oxide layer grown above ridges (made of flaw sites with impurities and scratches) are susceptible to highly localized stress, successive cracking of the film and rapid healing could occur [183] (Figure 2.22 (C) and (D)).
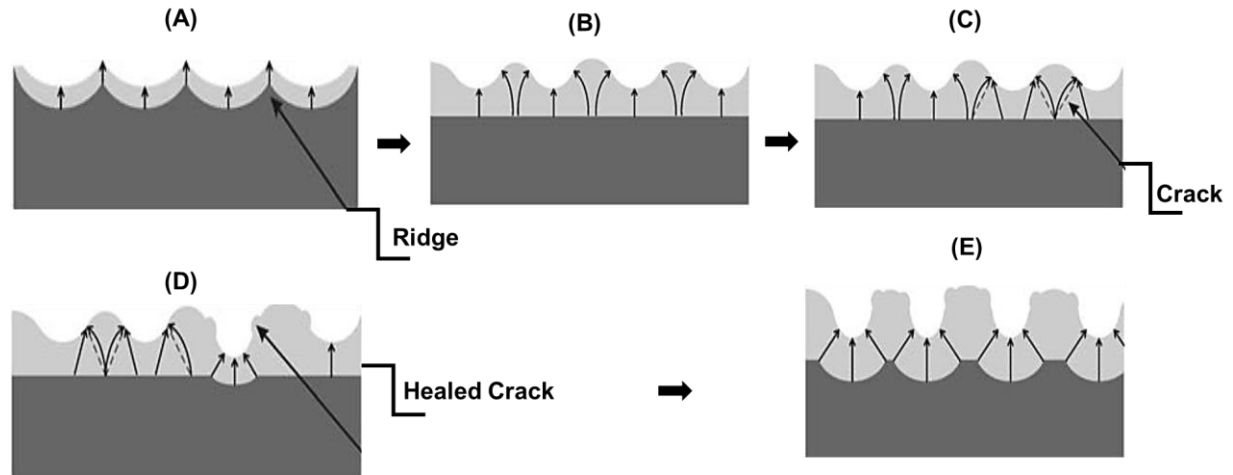
Figure 2-22. Schematic diagram showing current distribution during pore initiation and development of pores on anodized alumina. Adapted from [139]

As the cracking and healing process continues, there is a gradual increase in the rate of oxide dissolution and formation. Thus, the growth of oxide and dissolution of the metal at the oxide/Al metal base interface and electrolyte/oxide interface respectively continue, resulting in a subsequent steady-state growth of the porous oxide layer (Figure 2.22 (E)).

Similar mechanism has been proposed by Keller et al [179], according to this, the passage of current leads to increased local electrolyte temperature and subsequent oxide dissolution and current breakdown in the oxide layer [144]. However, Baumman [180], proposed the presence of vapour film at the active sites, located at the bottom of the pores (at the oxygen/electrolyte interface) to be responsible. Accordingly, these active sites serve as nucleation sites for subsequent simultaneous growth of the porous oxide structure, following dissolution [180].

Contrarily, Murphy and Michelson [150], argued that there exist hydroxide and hydrated compounds from a reaction between the barrier outer layer and water in the electrolyte. Hence, these compounds adsorb more water and anion to form a gel-like matrix at the outer layer (electrolyte/metal interface) with a simultaneous build-up of dense oxide at the inner layer

(oxide/metal interface) [150]. Thus, potential drop between the outer hydrated barrier layer and the continuous dense oxide inner layer causes oxidation of aluminium and the subsequent anodic porous oxide formation.

In summary, current understanding on healthcare associated infections and advances in antibacterial surfaces and coating technology with particular focus on topography-mediated antibacterial surfaces, superhydrophobic antibacterial coatings and hydrophilic antibacterial coatings have been discussed. The potential for transforming a general-purpose aluminum alloy into antibacterial surfaces capable of reducing microbial burden of clinically relevant pathogens has also been presented. However, problems associated with current antibacterial solutions, such as lack of long-term durable antibacterial coating, uncontrolled release of antibacterial agents, lack of standardized testing protocols and antibacterial resistance problems; need to be overcome to enable promising candidates to transition from laboratory bench to the market.

2.9   **References:**

1.   Shirly Berezin, Yaron Aviv, Hagit Aviv, Elad Goldberg, Yaakov R. Tischler., *Replacing a century old technique–modern spectroscopy can supplant Gram staining.* Scientific reports, 2017. **7**(1): p. 1-7.
2.   McCall, D., D. Stock, P. Achey, *11th hour: introduction to microbiology.* 2009: John Wiley & Sons.
3.   Mohd I. Ishak, Xiayi Liu, Joshua Jenkin, Angela H. Nobbs and Bo Su., *Protruding nanostructured surfaces for antimicrobial and osteogenic titanium implants.* Coatings, 2020. **10**(8): p. 756.
4.   K Ledwoch, S J Dancer, J A Otter, K Kerr, D Roposte, L Rushton, R Weiser, E Mahenthiralingam, D D Muir and J-Y Maillard., *Beware biofilm! Dry biofilms containing bacterial pathogens on multiple healthcare surfaces; a multi-centre study.* Journal of Hospital Infection, 2018. **100**(3): p. e47-e56.
5.   Jarvis, W.R., *Bennett & Brachman's hospital infections.* 2013: Lippincott Williams & Wilkins.
6.   Escobar, D. and D. Pegues, *Healthcare-associated infections: where we came from and where we are headed.* BMJ Publishing Group Ltd.
7.   T G Emori, D H Culver, T C Horan, W R Jarvis, J W White, D R Olson, S Banerjee, J R Edwards, W J Martone, R P Gaynes, *National nosocomial infections surveillance system (NNIS): description of surveillance methods.* American journal of infection control, 1991. **19**(1): p. 19-35.

8.   Organization, W.H., *Report on the burden of endemic health care-associated infection worldwide.* 2011.

9.   Anne MacLaurin, Kanchana Amaratunga, Chantal Couris, Charles Frenette, Riccarda Galioto, Gerry Hansen, Jennifer Happe, Kim Neudorf, Linda Pelude, Caroline Quach, Suzanne Rhodenizer Rose, *Measuring and Monitoring Healthcare-Associated Infections: A Canadian Collaboration to Better Understand the Magnitude of the Problem.* Healthcare quarterly (Toronto, Ont.), 2020. **22**(SP): p. 116-128.

10.   Alessandro Cassini, Diamantis Plachouras, Tim Eckmanns, Muna Abu Sin, Hans-Peter Blank, Tanja Ducomble, Sebastian Haller, Thomas Harder, Anja Klingeberg, Madlen Sixtensson, Edward Velasco, Bettina Weiß, Piotr Kramarz, Dominique L. Monnet, Mirjam E. Kretzschmar, Carl Suetens, *Burden of six healthcare-associated infections on European population health: estimating incidence-based disability-adjusted life years through a population prevalence-based modelling study.* PLoS medicine, 2016. **13**(10): p. e1002150.

11.   Organization, W.H., *Guidelines on core components of infection prevention and control programmes at the national and acute health care facility level.* 2016.

12.   Friedrich, A.W., *Control of hospital acquired infections and antimicrobial resistance in Europe: the way to go.* Wiener Medizinische Wochenschrift, 2019. **169**(1): p. 25-30.

13.   Ivanova, E.P. and R. Crawford, *Antibacterial surfaces*. 2015: Springer.

14.   Tortora, G.J., B.R. Funke, and C.L. Case, *Microbiology: an introduction.* 2010.

15.   Ramos, *Susceptibility of the Candida haemulonii Complex to Echinocandins: Focus on Both Planktonic and Biofilm Life Styles and a Literature Review.* Journal of Fungi, 2020. **6**(4): p. 201.

16.   Ziad W Jaradat, Qutaiba O Ababneh, Sherin T Sha'aban, Ayesha A Alkofahi, Duaa Assaleh, Anan Al Shara, *Methicillin Resistant Staphylococcus aureus and public fomites: a review.* Pathogens and Global Health, 2020: p. 1-25.

17.   Borkow, G., *Use of biocidal surfaces for reduction of healthcare acquired infections*. 2014: Springer.

18.   Suleyman, G., G. Alangaden, A.C. Bardossy, *The role of environmental contamination in the transmission of nosocomial pathogens and healthcare-associated infections.* Current infectious disease reports, 2018. **20**(6): p. 12.

19.   Weber, D.J., H. Kanamori, W.A. Rutala, *'No touch' technologies for environmental decontamination: focus on ultraviolet devices and hydrogen peroxide systems.* Current opinion in infectious diseases, 2016. **29**(4): p. 424-431.

20.   Hajime Kanamori, William A Rutala, Maria F Gergen, Emily E Sickbert-Bennett, Lauren P Knelson, Deverick J Anderson, Daniel J Sexton, David J Weber, *Microbial assessment of healthcare-associated pathogens on various environmental sites in patient rooms after terminal room disinfection*. in *Open Forum Infectious Diseases*. 2021.

21.   B G Mitchell, S J Dancer, M Anderson, E Dehn., *Risk of organism acquisition from prior room occupants: a systematic review and meta-analysis.* Journal of Hospital Infection, 2015. **91**(3): p. 211-217.

22.   David J Weber, William A Rutala, Melissa B Miller, Kirk Huslage, Emily Sickbert-Bennett, *Role of hospital surfaces in the transmission of emerging health care-associated pathogens: norovirus, Clostridium difficile, and Acinetobacter species.* American journal of infection control, 2010. **38**(5): p. S25-S33.

23.   Kramer, A., I. Schwebke, G. Kampf, *How long do nosocomial pathogens persist on inanimate surfaces? A systematic review.* BMC infectious diseases, 2006. **6**(1): p. 130.

24.   Van Doremalen, N, *Aerosol and surface stability of SARS-CoV-2 as compared with SARS-CoV-1.* New England Journal of Medicine, 2020. **382**(16): p. 1564-1567.

25. Ozlem Koca, Ulku Altoparlak, Ahmet Ayyildiz and Hasan Kaynar, *Persistence of nosocomial pathogens on various fabrics.* The Eurasian journal of medicine, 2012. **44**(1): p. 28.

26. Abbas, S.M., M. Doll, M.P. Stevens, *Vertical versus horizontal infection control interventions*, in *Infection Prevention*. 2018, Springer. p. 173-179.

27. Borkow, G., *Use of biocidal surfaces for reduction of healthcare acquired infections*. Springer.

28. Kathryn Ann Lambe, Sinéad Lydon, Caoimhe Madden, Akke Vellinga, Aoife Hehir, Mary Walsh, Paul O'Connor, *Hand hygiene compliance in the ICU: a systematic review.* Critical Care Medicine, 2019. **47**(9): p. 1251-1257.

29. Xiao Zhong, Dong-Li Wang, Li-Hua Xiao, Lan-Fang Mo, Qing-Fei Wu, Yan-Wei Chen and Xiao-Feng Luo, *Comparison of two electronic hand hygiene monitoring systems in promoting hand hygiene of healthcare workers in the intensive care unit.* BMC Infectious Diseases, 2021. **21**(1): p. 1-10.

30. Giulio Toccafondi, Francesco Di Marzo, Massimo Sartelli, Mark Sujan, Molly Smyth, Paul Bowie, Martina Cardi, Maurizio Cardi, *Will the COVID-19 pandemic transform infection prevention and control in surgery? Seeking leverage points for organizational learning.* International Journal for Quality in Health Care, 2021. **33**(Supplement_1): p. 51-55.

31. Wong, S.-C., *Is it possible to achieve 100 percent hand hygiene compliance during the COVID-19 pandemic?* Journal of Hospital Infection, 2020.

32. Ali, S., G. Moore, and A. Wilson, *Spread and persistence of Clostridium difficile spores during and after cleaning with sporicidal disinfectants.* Journal of Hospital Infection, 2012. **80**(2): p. 186.

33. Brittany C Eckstein, Daniel A Adams, Elizabeth C Eckstein, Agam Rao, Ajay K Sethi, Gopala K Yadavalli and Curtis J Donskey, *Reduction of Clostridium difficile and vancomycin-resistant Enterococcus contamination of environmental surfaces after an intervention to improve cleaning methods.* BMC infectious diseases, 2007. **7**(1): p. 61.

34. Kevin Tyan, Jason Kang, Katherine Jin, Aaron M Kyle., *Evaluation of the antimicrobial efficacy and skin safety of a novel color additive in combination with chlorine disinfectants.* American journal of infection control, 2018. **46**(11): p. 1254-1261.

35. Cole, M., *Exploring the hand hygiene competence of student nurses: a case of flawed self assessment.* Nurse education today, 2009. **29**(4): p. 380-388.

36. Gibson, B, *The distribution of bacterial doubling times in the wild.* Proceedings of the Royal Society B: Biological Sciences, 2018. **285**(1880): p. 20180789.

37. Li, Y.-H. and X.-L. Tian, *Microbial interactions in biofilms: impacts on homeostasis and pathogenesis*. 2016: IntechOpen.

38. Pace, J.L., M.E. Rupp, and R.G. Finch, *Biofilms, infection, and antimicrobial therapy*. 2005: CRC Press.

39. Dunne, W.M., *Bacterial adhesion: seen any good biofilms lately?* Clinical microbiology reviews, 2002. **15**(2): p. 155-166.

40. Karen Vickery, Honghua Hu, Anita Simone Jacombs, David AlanBradshaw, Kumar Deva, *A review of bacterial biofilms and their role in device-associated infection.* Healthcare infection, 2013. **18**(2): p. 61-66.

41. F Boyen, V Eeckhaut, F Van Immerseel, F Pasmans, R Ducatelle, F Haesebrouck, *Quorum sensing in veterinary pathogens: mechanisms, clinical importance and future perspectives.* Veterinary microbiology, 2009. **135**(3-4): p. 187-195.

42. Steven Percival David Williams Tracey Cooper Jacqueline Randle., *Biofilms in infection prevention and control: A healthcare handbook*. 2014: Academic Press.

43. Tiwari, A., *Handbook of antimicrobial coatings*. 2017: Elsevier.

44. Ammar Algburi, Nicole Comito, Dimitri Kashtanov, Leon M T Dicks, Michael L Chikindas, *Control of biofilm formation: antibiotics and beyond.* Appl. Environ. Microbiol., 2017. **83**(3): p. e02508-16.

45. Rabih, O.D., *Device-Associated Infections: A Macroproblem That Starts with Microadherence.* Clinical Infectious Diseases, 2001. **33**(9): p. 1567-1572.

46. Steven L Percival, Louise Suleman, Claudia Vuotto, Gianfranco Donelli, *Healthcare-associated infections, medical devices and biofilms: risk, tolerance and control.* Journal of medical microbiology, 2015. **64**(4): p. 323-334.

47. Ehrlich, G.D., *Intelligent implants to battle biofilms.* Asm News, 2004. **70**(3): p. 127-133.

48. Palmer, L.B., *Ventilator-associated infection.* Current opinion in pulmonary medicine, 2009. **15**(3): p. 230-235.

49. Strom, M., T. Crowley, and S. Shigdar, *Novel Detection of Nasty Bugs, Prevention Is Better than Cure.* International Journal of Molecular Sciences, 2021. **22**(1): p. 149.

50. Razzaque, M.S., *Exacerbation of antimicrobial resistance: another casualty of the covid-19 pandemic?* Expert Review of Anti-infective Therapy, 2021.

51. Mitra S Ganewatta, Kristen P Miller, S Parker Singleton, Pegah Mehrpouya-Bahrami, Yung P Chen, Yi Yan, Mitzi Nagarkatti, Prakash Nagarkatti, Alan W Decho, Chuanbing Tang, *Antibacterial and biofilm-disrupting coatings from resin acid-derived materials.* Biomacromolecules, 2015. **16**(10): p. 3336-3344.

52. Chiara Gargioni, Mykola Borzenkov, Laura D'Alfonso, Paola Sperandeo, Alessandra Polissi, Lucia Cucca, Giacomo Dacarro, Pietro Grisoli, Piersandro Pallavicini, Agnese D'Agostino and Angelo Taglietti, *Self-assembled monolayers of copper sulfide nanoparticles on glass as antibacterial coatings.* Nanomaterials, 2020. **10**(2): p. 352.

53. Yusliza Yusuf, Mariyam Jameelah Ghazalia, Yuichi Otsukac, Kiyoshi Ohnumad, Sarita Morakule, Susumu Nakamuraf, Mohd Fadzli Abdollah, *Antibacterial properties of laser surface-textured TiO2/ZnO ceramic coatings.* Ceramics International, 2020. **46**(3): p. 3949-3959.

54. ShuaiZhang, XinjinLiang,Geoffrey MichaelGadd, QiZhao, *A sol–gel based silver nanoparticle/polytetrafluorethylene (AgNP/PTFE) coating with enhanced antibacterial and anti-corrosive properties.* Applied Surface Science, 2021. **535**: p. 147675.

55. Reddy, M.P., A. Venugopal, M. Subrahmanyam, *Hydroxyapatite-supported Ag–TiO2 as Escherichia coli disinfection photocatalyst.* Water research, 2007. **41**(2): p. 379-386.

56. Yang Jiao, Li-Na Niu, Sai Ma, Jing Li, Franklin R Tay, Ji-Hua Chen, *Quaternary ammonium-based biomedical materials: State-of-the-art, toxicological aspects and antimicrobial resistance.* Progress in Polymer Science, 2017. **71**: p. 53-90.

57. Megan C Jennings, Bettina A Buttaro, Kevin P C Minbiole, William M Wuest, *Bioorganic investigation of multicationic antimicrobials to combat QAC-resistant Staphylococcus aureus.* ACS infectious diseases, 2015. **1**(7): p. 304-309.

58. Domagk, G., *A new class of disinfectants.* Deut. Med. Wochenschr., 1935. **61**: p. 829-832.

59. Helen W Boucher, George H Talbot, John S Bradley, John E Edwards, David Gilbert, Louis B Rice, Michael Scheld, Brad Spellberg, John Bartlett, *Bad bugs, no drugs: no ESKAPE! An update from the Infectious Diseases Society of America.* Clinical infectious diseases, 2009. **48**(1): p. 1-12.

60.   Kelly R Morrison, Ryan A Allen, Kevin P C Minbiole, William M Wuest, *More QACs, more questions: Recent advances in structure activity relationships and hurdles in understanding resistance mechanisms.* Tetrahedron letters, 2019. **60**(37): p. 150935.

61.   Hill, W.R. and D.M. Pillsbury, *Argyria: the pharmacology of silver*. 1939: Williams & Wilkins.

62.   Oppermann, R., *Silver in industry: edited by Lawrence. Addicks. 636 pages, illustrations, tables, 16× 24 curs. New York, Reinhold Publishing Corporation, 1940. Price $10.00*. 1941, Pergamon.

63.   Barillo, D.J. and D.E. Marx, *Silver in medicine: A brief history BC 335 to present.* Burns, 2014. **40**: p. S3-S8.

64.   Paweł Kowalczyk, Mateusz Szymczak, Magdalena Maciejewska, Łukasz Laskowski, Magdalena Laskowska, Ryszard Ostaszewski, Grzegorz Skiba and Ida Franiak-Pietryga, *All That Glitters Is Not Silver—A New Look at Microbiological and Medical Applications of Silver Nanoparticles.* International Journal of Molecular Sciences, 2021. **22**(2): p. 854.

65.   Jasper S Möhler, Wilson Sim, Mark A T Blaskovich, Matthew A Cooper, Zyta M Ziora, *Silver bullets: A new lustre on an old antimicrobial agent.* Biotechnology advances, 2018. **36**(5): p. 1391-1411.

66.   Claire M. Cobley, Sara E. Skrabalak, Dean J. Campbell, Younan Xia, *Shape-Controlled Synthesis of Silver Nanoparticles for Plasmonic and Sensing Applications.* Plasmonics, 2009. **4**(2): p. 171-179.

67.   Henry Agbe, Nadeem Raza, David Dodoo-Arhin, Aditya Chauhan, Ramachandran Vasant Kumar, *H2O2 rejuvenation-mediated synthesis of stable mixed-morphology Ag3PO4 photocatalysts.* Heliyon, 2018. **4**(4): p. e00599.

68.   Kaiyuan Zheng, Magdiel Inggrid Setyawati, David Tai Leong, Jianping Xie, *Antimicrobial silver nanomaterials.* Coordination Chemistry Reviews, 2018. **357**: p. 1-17.

69.   Agnihotri, S., S. Mukherji, and S. Mukherji, *Size-controlled silver nanoparticles synthesized over the range 5100 nm using the same protocol and their antibacterial efficacy.* RSC Advances, 2013. **4**(8): p. 3974-3983.

70.   Babak Sadeghi, Farshid S.Garmaroudi, M.Hashemi, H.R.Nezhad, A.Nasrollahi, Sima Ardalan, Sahar Ardalan, *Comparison of the anti-bacterial activity on the nanosilver shapes: Nanoparticles, nanorods and nanoplates.* Advanced Powder Technology, 2010. **23**(1).

71.   J.M.Schierholz, L.J.Lucas, A.Rump, G.Pulverer, *Efficacy of silver-coated medical devices.* Journal of Hospital infection, 1998. **40**(4): p. 257-262.

72.   Ang Gao, Ruiqiang Hang, Xiaobo Huang, Lingzhou Zhao, Xiangyu Zhang, Lin Wang, Bin Tang, Shengli Ma, Paul K Chu, *The effects of titania nanotubes with embedded silver oxide nanoparticles on bacteria and osteoblasts.* Biomaterials, 2014. **35**(13): p. 4223-4235.

73.   Singha, P., J. Locklin, and H. Handa, *A review of the recent advances in antimicrobial coatings for urinary catheters.* Acta biomaterialia, 2017. **50**: p. 20-40.

74.   Shenglin Mei, Huaiyu Wang, Wei Wang, Liping Tong, Haobo Pan, Changshun Ruan, Qianli Ma, Mengyuan Liu, Huiling Yang, Liang Zhang, Yicheng Cheng, Yumei Zhang, Lingzhou Zhao, Paul K Chu, *Antibacterial effects and biocompatibility of titanium surfaces with graded silver incorporation in titania nanotubes.* Biomaterials, 2014. **35**(14): p. 4255-4265.

75.   Hui Qin, Huiliang Cao, Yaochao Zhao, Guodong Jin, Mengqi Cheng, Jiaxin Wang, YaoJiang, Zhiquan An, Xianlong Zhang, Xuanyong Liu, *Antimicrobial and osteogenic properties of silver-ion-implanted stainless steel.* ACS applied materials & interfaces, 2015. **7**(20): p. 10785.

76.   Jai Prakash, Shuhui Sun, Hendrik C.Swart, Raju Kumar Gupta, *Noble metals-TiO2 nanocomposites: From fundamental mechanisms to photocatalysis, surface enhanced Raman scattering and antibacterial applications.* Applied Materials Today, 2018. **11**: p. 82-135.

77.   Q L Feng, J Wu, G Q Chen, F Z Cui, T N Kim, J O Kim, *A mechanistic study of the antibacterial effect of silver ions on Escherichia coli and Staphylococcus aureus.* Journal of biomedical materials research, 2000. **52**(4): p. 662-668.

78.   Banerjee, S.L., P. Potluri, and N.K. Singha, *Antimicrobial cotton fibre coated with UV cured colloidal natural rubber latex: A sustainable material.* Colloids and Surfaces A: Physicochemical and Engineering Aspects, 2019. **566**: p. 176-187.

79.   Franci, G., et al., *Silver Nanoparticles as Potential Antibacterial Agents.* Molecules, 2015. **20**(5): p. 8856-8874.

80.   Mehtar, S., I. Wiid, and S. Todorov, *The antimicrobial activity of copper and copper alloys against nosocomial pathogens and Mycobacterium tuberculosis isolated from healthcare facilities in the Western Cape: an in-vitro study.* Journal of Hospital Infection, 2008. **68**(1): p. 45-51.

81.   Bryant, C., S.A. Wilks, and C.W. Keevil, *Rapid inactivation of SARS-CoV-2 on copper touch surfaces determined using a cell culture infectivity assay.* bioRxiv: p. 2021.01. 02.424974.

82.   Cortes, A.A. and J.M. Zuñiga, *The use of copper to help prevent transmission of SARS-coronavirus and influenza viruses. A general review.* Diagnostic microbiology and infectious disease, 2020: p. 115176.

83.   Grass, G., C. Rensing, and M. Solioz, *Metallic copper as an antimicrobial surface.* Applied and environmental microbiology, 2011. **77**(5): p. 1541-1547.

84.   Noyce, J., H. Michels, and C. Keevil, *Potential use of copper surfaces to reduce survival of epidemic meticillin-resistant Staphylococcus aureus in the healthcare environment.* Journal of Hospital Infection, 2006. **63**(3): p. 289-297.

85.   Chatterjee, P., et al. *Effectiveness of copper-impregnated solid surfaces on lowering microbial bio-burden levels in an acute care hospital*. in *Open forum infectious diseases*. 2020. Oxford University Press US.

86.   Haque, M.M., D. Bahnemann, and M. Muneer. *Photocatalytic degradation of organic pollutants: Mechanisms and kinetics*. in *Organic Pollutants Ten Years after the Stockholm Convention–Environmental and Analytical Update*. 2012.

87.   Fujishima, A. and K. Honda, *Electrochemical photolysis of water at a semiconductor electrode.* nature, 1972. **238**(5358): p. 37-38.

88.   Hasan, J., R.J. Crawford, and E.P. Ivanova, *Antibacterial surfaces: the quest for a new generation of biomaterials.* Trends in biotechnology, 2013. **31**(5): p. 295-304.

89.   Siedenbiedel, F. and J.C. Tiller, *Antimicrobial polymers in solution and on surfaces: overview and functional principles.* Polymers, 2012. **4**(1): p. 46-71.

90.   Jafar Hasan, Russell J Crawford, Elena P Ivanova, *Antibacterial surfaces: the quest for a new generation of biomaterials.* Trends in biotechnology, 2013. **31**(5): p. 295-304.

91.   Glocker, D. and S. Ranade, *Medical Coatings and Deposition Technologies*. 2016: John Wiley & Sons.

92.   Nicholas Lin, Paula Berton, Christopher Moraes , Robin D. Rogers , Nathalie Tufenkji, *Nanodarts, nanoblades, and nanospikes: Mechano-bactericidal nanostructures and where to find them.* Advances in colloid and interface science, 2018. **252**: p. 55-68.

93.   Jafar Hasan, Hayden K Webb, Vi Khanh Truong, Sergey Pogodin, Vladimir A Baulin, Gregory S Watson, Jolanta A Watson, Russell J Crawford, Elena P Ivanova, *Selective bactericidal activity of nanopatterned superhydrophobic cicada Psaltoda claripennis wing surfaces.* Applied microbiology and biotechnology, 2013. **97**(20): p. 9257-9262.

94.   Mary Nora Dickson, Elena I Liang, Luis A Rodriguez, Nicolas Vollereaux, Albert F Yee, *Nanopatterned polymer surfaces with bactericidal properties.* Biointerphases, 2015. **10**(2): p. 021010.

95.   Laila Damiati, Marcus G Eales, Angela H Nobbs, Bo Su, Penelope M Tsimbouri, Manuel Salmeron-Sanchez and Matthew J Dalby, *Impact of surface topography and coating on osteogenesis and bacterial attachment on titanium implants.* Journal of tissue engineering, 2018. **9**: p. 2041731418790694.

96.   Hawkeye, M.M., M.T. Taschuk, and M.J. Brett, *Glancing angle deposition of thin films: engineering the nanoscale*. 2014: John Wiley & Sons.

97.   Robbie, K., J. Sit, and M. Brett, *Advanced techniques for glancing angle deposition.* Journal of Vacuum Science & Technology B: Microelectronics and Nanometer Structures Processing, Measurement, and Phenomena, 1998. **16**(3): p. 1115-1122.

98.   Nosonovsky, M. and B. Bhushan, *Patterned nonadhesive surfaces: superhydrophobicity and wetting regime transitions.* Langmuir, 2008. **24**(4): p. 1525-1533.

99.   Wenzel, R.N., *Resistance of solid surfaces to wetting by water.* Industrial & Engineering Chemistry, 1936. **28**(8): p. 988-994.

100.   Morán, G. and R. Méallet-Renault, *Superhydrophobic Surfaces Toward Prevention of Biofilm-Associated Infections*, in *Bacterial Pathogenesis and Antibacterial Control*. 2017, IntechOpen.

101.   Cassie, A. and S. Baxter, *Wettability of porous surfaces.* Transactions of the Faraday society, 1944. **40**: p. 546-551.

102.   Jafar Hasan, Anindo Roy, Kaushik Chatterjee, Prasad KDV Yarlagadda, *Mimicking insect wings: The roadmap to bioinspiration.* ACS Biomaterials Science & Engineering, 2019. **5**(7): p. 3139-3160.

103.   Elena P. Ivanova, Song Ha Nguyen, Hayden K. Webb, Jafar Hasan, Vi Khanh Truong, Robert N. Lamb, Xiaofei Duan, Mark J. Tobin, Peter J. Mahon, Russell J. Crawford, *Molecular organization of the nanoscale surface structures of the dragonfly Hemianax papuensis wing epicuticle.* PLoS One, 2013. **8**(7): p. e67893.

104.   Safaee, A., D.K. Sarkar, and M. Farzaneh, *Superhydrophobic properties of silver-coated films on copper surface by galvanic exchange reaction.* Applied Surface Science, 2008. **254**(8): p. 2493-2498.

105.   Brassard, J.-D., D.K. Sarkar, and J. Perron, *Synthesis of monodisperse fluorinated silica nanoparticles and their superhydrophobic thin films.* ACS applied materials & interfaces, 2011. **3**(9): p. 3583-3588.

106.   Shuhao Liu, Jeremy Zheng, Li Hao, Yagmur Yegin, Michael Bae, Beril Ulugun, Thomas Matthew Taylor, Ethan A. Scholar, Luis Cisneros-Zevallos, Jun Kyun Oh, Mustafa Ak, *Dual-Functional, Superhydrophobic Coatings with Bacterial Anticontact and Antimicrobial Characteristics.* ACS Applied Materials & Interfaces, 2020.

107.   Jae-Seung Chung, Byoung Gak Kim, Soojin Shim, Seong-Eun Kim, Eun-Ho Sohn, Jeyong Yoon, Jong-Chan Lee, *Silver-perfluorodecanethiolate complexes having superhydrophobic, antifouling, antibacterial properties.* Journal of colloid and interface science, 2012. **366**(1): p. 64-69.

108.   Tao Wang, Lei Huang, Yuzhi Liu, Xingxing Li, Chunhua Liu, Stephan Handschuh-Wang, Yang Xu, Ying Zhao, Yongbing Tang, *Robust Biomimetic Hierarchical Diamond Architecture with a Self-Cleaning, Antibacterial, and Antibiofouling Surface.* ACS applied materials & interfaces, 2020. **12**(21): p. 24432-24441.

109.   H Chouirfa, H Bouloussa, V Migonney, C Falentin-Daudré, *Review of titanium surface modification techniques and coatings for antibacterial applications.* Acta Biomaterialia, 2018.

110. Sharma, V.K., R.A. Yngard, and Y. Lin, *Silver nanoparticles: Green synthesis and their antimicrobial activities.* Advances in Colloid and Interface Science, 2009. **145**(1): p. 83-96.

111. Sharma, V.K., R.A. Yngard, and Y. Lin, *Silver nanoparticles: green synthesis and their antimicrobial activities.* Advances in colloid and interface science, 2009. **145**(1-2): p. 83-96.

112. Simin Wei, Yinghui Wang, Zhishu Tang, Hongbo Xu, Zhe Wang, Tian Yang and Taiyan Zou, *A novel green synthesis of silver nanoparticles by the residues of Chinese herbal medicine and their biological activities.* RSC Advances, 2021. **11**(3): p. 1411-1419.

113. Aparna Banerjee, Debasis Das, Rodrigo Andler and Rajib Bandopadhyay, *Green Synthesis of Silver Nanoparticles Using Exopolysaccharides Produced by Bacillus anthracis PFAB2 and Its Biocidal Property.* Journal of Polymers and the Environment, 2021: p. 1-9.

114. Iqbal, S. and S. Ahmad, *Recent development in hybrid conducting polymers: synthesis, applications and future prospects.* Journal of industrial and engineering chemistry, 2018. **60**: p. 53-84.

115. Schubert, U., N. Hüsing, and A. Lorenz, *Hybrid inorganic-organic materials by sol-gel processing of organofunctional metal alkoxides.* Chemistry of materials, 1995. **7**(11): p. 2010-2027.

116. Hench, L.L. and J.K. West, *The sol-gel process.* Chemical reviews, 1990. **90**(1): p. 33-72.

117. Henry Agbe, Dilip Kumar Sarkar, X.-Grant Chen, Nathalie Faucheux, Gervais Soucy, Jean-Luc Bernier, *Silver–Polymethylhydrosiloxane Nanocomposite Coating on Anodized Aluminum with Superhydrophobic and Antibacterial Properties.* ACS Applied Bio Materials, 2020. **3**(7): p. 4062-4073.

118. G.JChj, S.WYao, JFan, W.GZhang, H.ZWang, *Antibacterial activity of anodized aluminum with deposited silver.* Surface and Coatings Technology, 2002. **157**(2-3): p. 162-165.

119. Wojciech J. Stepniowski, Marcin Moneta, Krzysztof Karczewski, Marta Michalska-Domanska, Tomasz Czujko, Johannes M.C. Mol, Josephus G. Buijnsters, *Fabrication of copper nanowires via electrodeposition in anodic aluminum oxide templates formed by combined hard anodizing and electrochemical barrier layer thinning.* Journal of Electroanalytical Chemistry, 2018. **809**: p. 59-66.

120. Ghaddar, A., J. Gieraltowski, and F. Gloaguen, *Effects of anodization and electrodeposition conditions on the growth of copper and cobalt nanostructures in aluminum oxide films.* Journal of applied electrochemistry, 2009. **39**(5): p. 719-725.

121. C.Adlhart, J.Verran, N.F.Azevedo, H.Olmez, M.M.Keinänen-Toivola, I.Gouveia, L.F.Melo, F.Crijns, *Surface modifications for antimicrobial effects in the healthcare setting: A critical overview.* Journal of Hospital Infection, 2018. **99**(3): p. 239-249.

122. Cloutier, M., D. Mantovani, and F. Rosei, *Antibacterial coatings: challenges, perspectives, and opportunities.* Trends in biotechnology, 2015. **33**(11): p. 637-652.

123. ASTM, E. *2180-07.".* in *ASTM E*. 2012.

124. Association, J.S., *Antimicrobial products: test for antimicrobial activity and efficacy.* Japanese Industrial Standard 2000; JIS Z 2801, 2000.

125. Cornelia Wiegand, Andrea Völpel, Andrea Ewald, Markko Remesch, Jan Kuever, Janine Bauer, Stefanie Griesheim, Carolin Hauser, Julian Thielmann, Silke Tonndorf-Martini, Bernd W Sigusch, Jürgen Weisser, Ralf Wyrwa, Peter Elsner, Uta-Christina Hipler, Martin Roth, Carolin Dewald, Claudia Lüdecke-Beyer, Jörg Bossert, *Critical physiological factors influencing the outcome of antimicrobial testing according to ISO 22196/JIS Z 2801.* PloS one, 2018. **13**(3): p. e0194339.

126. Johannes Karl-Mark Knobloch, Sabrina Tofern, Wladimir Kunz, Sara Schütze, Michael Riecke, Werner Solbach, Thomas Wuske, *"Life-like" assessment of antimicrobial surfaces by a new touch*

transfer assay displays strong superiority of a copper alloy compared to silver containing surfaces. Plos one, 2017. **12**(11): p. e0187442.

127.   Association, C.D. *TEST 3 Continuous Reduction of Bacterial Contaminants*. 2012; Available from: https://cuverro.com/tested-proven-trusted/scientific-proof/epa-tests.

128.   Christophe Espírito Santo, Nadine Taudte, Dietrich H. Nies, and Gregor Grass, *Contribution of copper ion resistance to survival of Escherichia coli on metallic copper surfaces.* Appl. Environ. Microbiol., 2008. **74**(4): p. 977-986.

129.   Jelmer Sjollema, Sebastian A J Zaat, Veronique Fontaine, Madeleine Ramstedt, Reto Luginbuehl, Karin Thevissen, Jiuyi Li, Henny C van der Mei, Henk J Busscher, *In vitro methods for the evaluation of antimicrobial surface designs.* Acta biomaterialia, 2018. **70**: p. 12-24.

130.   Lei Shi, Susanne Günther, Thomas Hübschmann, Lukas Y Wick, Hauke Harms, Susann Müller, *Limits of propidium iodide as a cell viability indicator for environmental bacteria.* Cytometry Part A: the Journal of the International Society for Analytical Cytology, 2007. **71**(8): p. 592-598.

131.   Noyce, J., H. Michels, and C. Keevil, *Use of copper cast alloys to control Escherichia coli O157 cross-contamination during food processing.* Appl. Environ. Microbiol., 2006. **72**(6): p. 4239-4244.

132.   Robine, E., L. Boulangé-Petermann, and D. Derangère, *Assessing bactericidal properties of materials: the case of metallic surfaces in contact with air.* Journal of Microbiological Methods, 2002. **49**(3): p. 225-234.

133.   Wilks, S.A., H.T. Michels, and C.W. Keevil, *Survival of Listeria monocytogenes Scott A on metal surfaces: implications for cross-contamination.* International journal of food microbiology, 2006. **111**(2): p. 93-98.

134.   Wilks, S., H. Michels, and C. Keevil, *The survival of Escherichia coli O157 on a range of metal surfaces.* International journal of food microbiology, 2005. **105**(3): p. 445-454.

135.   Augustin, A., K.R. Udupa, and K.U. Bhat, *Characterization of DC Magnetron Sputtered Copper Thin Film on Aluminium Touch Surface.* Transactions of the Indian Institute of Metals, 2019. **72**(6): p. 1683-1685.

136.   Jafar Hasan, Yanan Xu , Tejasri Yarlagadda , Michael Schuetz, Kirsten Spann, Prasad KDV Yarlagadda, *Antiviral and antibacterial nanostructured surfaces with excellent mechanical properties for hospital applications.* ACS Biomaterials Science & Engineering, 2020.

137.   Jafar Hasan, Alyssa Pyke, Neelima Nair, Tejasri Yarlagadda, Geoffrey Will, Kirsten Spann, and Prasad K.D.V. Yarlagadda, *Antiviral Nanostructured Surfaces Reduce the Viability of SARS-CoV-2.* ACS Biomaterials Science & Engineering, 2020.

138.   Amin Valiei, Mira Okshevsky, Nicholas Lin, and Nathalie Tufenkji, *Anodized Aluminum with Nanoholes Impregnated with Quaternary Ammonium Compounds Can Kill Pathogenic Bacteria within Seconds of Contact.* ACS applied materials & interfaces, 2018. **10**(48): p. 41207-41214.

139.   Alkire, R.C., Y. Gogotsi, and P. Simon, *Nanostructured materials in electrochemistry*. 2008: John Wiley & Sons.

140.   Yasser Abdelrhman, Sengo Kobayashi, Satoshi Okano, Takeaki Okamoto, Mohamed Abdel-Hady Gepreel, *Biocompatibility of Anodized Low-Cost Ti-4.7 Mo-4.5 Fe Alloy*. in *Materials Science Forum*. 2021. Trans Tech Publ.

141.   Janaina Soares Santos, Patrícia dos Santos Araújo, Yasmin Bastos Pissolitto, Paula Prenholatto Lopes, Anna Paulla Simon, Mariana de Souza Sikora, and Francisco Trivinho-Strixino, *The Use of Anodic Oxides in Practical and Sustainable Devices for Energy Conversion and Storage.* Materials, 2021. **14**(2): p. 383.

142.   Fei Cheng, Guo Chen, Zhenfei Lv, Chen Yang, Zhaohui Huang, Minghao Fang, Yan'gai Liu, Xiaowen Wu, Xin Min, *A novel nano-porous aluminum substrate with anodizing treatment to encapsulate*

1-tetrapropanol as composite phase change materials for thermal energy utilization. Chemical Engineering Journal, 2021. **404**: p. 124588.

143. Poinern, G.E.J., N. Ali, and D. Fawcett, *Progress in nano-engineered anodic aluminum oxide membrane development.* Materials, 2011. **4**(3): p. 487-526.

144. Masuda, H. and K. Fukuda, *Ordered metal nanohole arrays made by a two-step replication of honeycomb structures of anodic alumina.* science, 1995. **268**(5216): p. 1466-1468.

145. O'Sullivan, J.P. and G.C. Wood, *The Morphology and Mechanism of Formation of Porous Anodic Films on Aluminium.* Proceedings of the Royal Society of London. Series A, Mathematical and Physical Sciences (1934-1990), 1970. **317**(1531): p. 511-543.

146. Wojciech J. Stepniowski, Marcin Moneta, Krzysztof Karczewski, Marta Michalska-Domanska, Tomasz Czujko, Johannes M.C. Mol, Josephus G. Buijnsters, *Fabrication of copper nanowires via electrodeposition in anodic aluminum oxide templates formed by combined hard anodizing and electrochemical barrier layer thinning.* Journal of Electroanalytical Chemistry, 2018. **809**: p. 59-66.

147. P CHOWDHURY, K RAGHUVARAN, M KRISHNAN, HARISH C BARSHILIA, K S RAJAM, *Effect of process parameters on growth rate and diameter of nano-porous alumina templates.* Bulletin of Materials Science, 2011. **34**(3): p. 423-427.

148. Kornelius Nielsch, Jinsub Choi, Kathrin Schwirn, Ralf B. Wehrspohn, Ulrich Gösele, *Self-ordering Regimes of Porous Alumina: The 10 Porosity Rule.* Nano Letters, 2002. **2**(7): p. 677-680.

149. Y. Nazarkina, K. Kamnev, A. Dronov, A. Dudin, A. Pavlov, S. Gavrilov, *Features of porous anodic alumina growth in galvanostatic regime in selenic acid based electrolyte.* Electrochimica Acta, 2017. **231**: p. 327-335.

150. Fontana, M.G. and W. Stactile, *Corrosion Science and Technology.* Plenum Press, London, 1970. **1**: p. 149.

151. G. Knörnschild, A.A. Poznyak, A.G. Karoza, A. Mozalev, *Effect of the anodization conditions on the growth and volume expansion of porous alumina films in malonic acid electrolyte.* Surface & Coatings Technology, 2015. **275**: p. 17-25.

152. Tatsuya Kikuchi, Akimasa Takenaga, Shungo Natsui, Ryosuke O. Suzuki, *Advanced hard anodic alumina coatings via etidronic acid anodizing.* Surface and Coatings Technology, 2017. **326**: p. 72-78.

153. Nakajima, Daiki; Kikuchi, Tatsuya; Natsui, Shungo; Suzuki, Ryosuke O., *Growth behavior of anodic oxide formed by aluminum anodizing in glutaric and its derivative acid electrolytes.* Applied Surface Science, 2014. **321**: p. 364-370.

154. Ying-dong Li, You ZHANG, Song-mei LI, Pi-zhi ZHAO, *Influence of adipic acid on anodic film formation and corrosion resistance of 2024 aluminum alloy.* Transactions of Nonferrous Metals Society of China, 2016. **26**(2): p. 492-500.

155. Poinern, G., N. Ali, and D. Fawcett, *Progress in Nano-Engineered Anodic Aluminum Oxide Membrane Development*, in *Materials*. 2011. p. 487-526.

156. W.M. de Azevedo, D.D. de Carvalho, H.J. Khoury, E.A. de Vasconcelos, E.F. da Silva, *Spectroscopic characteristics of doped nanoporous aluminum oxide.* Materials Science and Engineering: B, 2004. **112**(2-3): p. 171-174.

157. Prasad, S. and J. Quijano, *Development of nanostructured biomedical micro-drug testing device based on in situ cellular activity monitoring.* Biosensors and Bioelectronics, 2006. **21**(7): p. 1219-1229.

158. Li, S.-Y., J. Wang, and Y. Li, *Photoluminescence properties of anodic aluminum oxide formed in a mixture of ammonium fluoride and oxalic acid.* Optical Engineering, 2017. **56**(6): p. 067107.
159. Kushwaha, M.K., *A comparative Study of Different Electrolytes for Obtaining Thick and Well-ordered nano-porous Anodic Aluminium Oxide (AAO) Films.* Procedia Materials Science, 2014. **5**: p. 1266-1273.
160. Maximilian Sieber, Roy Morgenstern, Ingolf Scharf, Thomas Lampke, *Effect of nitric and oxalic acid addition on hard anodizing of AlCu4Mg1 in sulphuric acid.* Metals, 2018. **8**(2): p. 139.
161. Akiya, Shunta; Kikuchi, Tatsuya; Natsui, Shungo; Suzuki, Ryosuke O., *Nanostructural characterization of large-scale porous alumina fabricated via anodizing in arsenic acid solution.* Applied surface science, 2017. **403**: p. 652-661.
162. A. Jagminienė, G. Valinčius, A. Riaukaitė, A. Jagminas, *The influence of the alumina barrier-layer thickness on the subsequent AC growth of copper nanowires.* Journal of crystal growth, 2005. **274**(3-4): p. 622-631.
163. G. Knörnschild, A.A. Poznyak, A.G. Karoza, A. Mozalev., *Effect of the anodization conditions on the growth and volume expansion of porous alumina films in malonic acid electrolyte.* Surface and Coatings Technology, 2015. **275**: p. 17-25.
164. Ono, S., M. Saito, and H. Asoh, *Self-ordering of anodic porous alumina formed in organic acid electrolytes.* Electrochimica Acta, 2005. **51**(5): p. 827-833.
165. Eftekhari, A., *Nanostructured materials in electrochemistry*. 2008, Weinheim : [Chichester: Wiley-VCH , John Wiley, distributor. xxv, 463 p.
166. Patermarakis, G., J. Chandrinos, and K. Moussoutzanis, *Interface physicochemical processes controlling sulphate anion incorporation in porous anodic alumina and their dependence on the thermodynamic and transport properties of cations.* Journal of Electroanalytical Chemistry, 2001. **510**(1-2): p. 59-66.
167. Hideki Masuda, Haruki Yamada, Masahiro Satoh,Hidetaka Asoh, *Highly ordered nanochannel-array architecture in anodic alumina.* Applied Physics Letters, 1997. **71**(19): p. 2770-2772.
168. Wojciech J. Stępniowski, Agata Nowak-Stępniowska, Adam Presz, Tomasz Czujko, Robert A. Varin, *The effects of time and temperature on the arrangement of anodic aluminum oxide nanopores.* Materials characterization, 2014. **91**: p. 1-9.
169. Marta Michalska-Domańska, Małgorzata Norek, Wojciech J.Stępniowskj, Bogusław Budner, *Fabrication of high quality anodic aluminum oxide (AAO) on low purity aluminum—A comparative study with the AAO produced on high purity aluminum.* Electrochimica Acta, 2013. **105**: p. 424-432.
170. Yanagishita, T. and H. Masuda, *Facile preparation of porous alumina through-hole masks for sputtering by two-layer anodization.* AIP Advances, 2016. **6**(8): p. 085108.
171. Zaraska, L., M. Jaskuła, and G.D. Sulka, *Porous anodic alumina layers with modulated pore diameters formed by sequential anodizing in different electrolytes.* Materials Letters, 2016. **171**: p. 315-318.
172. P CHOWDHURY, K RAGHUVARAN, M KRISHNAN, HARISH C BARSHILIA, K S RAJAM, *Effect of process parameters on growth rate and diameter of nano-porous alumina templates.* Bulletin of Materials Science, 2011. **34**(3): p. 423-427.
173. Loïc Assaud, Sebastian Bochmann, Silke Christiansen, Julien Bachmann, *A large electrochemical setup for the anodization of aluminum towards highly ordered arrays of cylindrical nanopores.* Review of Scientific Instruments, 2015. **86**(7): p. 073902.

174. Kondo, Ryunosuke; Kikuchi, Tatsuya; Natsui, Shungo; Suzuki, Ryosuke O, *Fabrication of self-ordered porous alumina via anodizing in sulfate solutions.* Materials Letters, 2016. **183**: p. 285-289.

175. Fengnan Yang, Lu Huang, Tao Guo, Changzheng Wang, Liyan Wang, Pengxiang Zhang, *The precise preparation of anodic aluminum oxide template based on the current-controlled method.* Ferroelectrics, 2018. **523**(1): p. 50-60.

176. Stepniowski, W.J., Moneta, Marcin, Karczewski, Krzysztof, Michalska-Domanska, Marta, Czujko,Tomasz, Mol, J.M.C., Buijnsters, J.G., *Fabrication of copper nanowires via electrodeposition in anodic aluminum oxide templates formed by combined hard anodizing and electrochemical barrier layer thinning.* Journal of Electroanalytical Chemistry, 2017.

177. Patermarakis, G. and K. Moussoutzanis, *Transformation of porous structure of anodic alumina films formed during galvanostatic anodising of aluminium.* Journal of electroanalytical chemistry, 2011. **659**(2): p. 176-190.

178. Yi Li, Yuyan Qin, Shiyu Jin, Xing Hu, Zhiyuan Ling, Qihong Liu, Jinfu Liao, Cheng Chen, Yanhua Shen, Ling Jin, *A new self-ordering regime for fast production of long-range ordered porous anodic aluminum oxide films.* Electrochimica Acta, 2015. **178**: p. 11-17.

179. Keller, F., M. Hunter, and D. Robinson, *Structural features of oxide coatings on aluminum.* Journal of the Electrochemical Society, 1953. **100**(9): p. 411-419.

180. Baumann, W., *Wechselstromuntersuchungen an anodisch oxydiertem Aluminium.* Zeitschrift für Physik, 1936. **102**(1-2): p. 59-66.

181. Patermarakis, G., *The origin of nucleation and development of porous nanostructure of anodic alumina films.* Journal of Electroanalytical Chemistry, 2009. **635**(1): p. 39-50.

182. O'sullivan, J. and G. Wood, *The morphology and mechanism of formation of porous anodic films on aluminium.* Proc. R. Soc. Lond. A, 1970. **317**(1531): p. 511-543.

183. K. Shimizu, K. Kobayashi, G. E. Thompson, G. C. Wood, *Development of porous anodic films on aluminium.* Philosophical Magazine A, 1992. **66**(4): p. 643-652.

CHAPTER 3

EXPERIMENTAL PROCEDURE

3   CHAPTER 3: EXPERIMENTAL PROCEDURES

In this chapter, the materials, synthesis techniques and characterization procedures employed to fabricate antibacterial aluminum surfaces are discussed. The chapter is divided into two sections: (3.3) Fabrication methods for antibacterial aluminum surfaces and (3.4) Physicochemical and in-vitro biological characterization.

3.1   Materials

A general-purpose AA6061-T6 aluminum alloy was utilized as substrate material in this study. AA6061-T6 aluminum alloy is commonly used in automobiles, marine structures, aerospace, food processing equipment and frequently touched surface applications (such as doorknobs, bedrails, countertop etc.) due to its low density, good corrosion resistance, high elastic modulus, tensile strength and yield stress [1]. The metallurgical composition of the AA6061-T6 aluminum alloy (Al-Mg-Si alloy) is listed in Table 3.1. A flat aluminum substrate was used in this research project to model flat geometries of bedside tables, walls, floor tiles, push plates, over bed tables and countertops.

Table 3-1. The chemical composition of AA6061-T6 aluminum alloy.

Elements	Al	Mg	Si	Fe	Cu	Mn	Ti	Zn
Composition (wt.%)	95.85-98.56	0.8-1.2	0.04-0.8	0.0-0.7	0.15-0.40	0.0-0.55	0.0-0.15	0.0-0.25

3.2   Aluminum surface pre-treatments for micro-nanoroughening

Surface of valve metals such as aluminum, titanium, niobium, zirconium, tungsten etc., can be modified to achieve micro-nanorougheness by various techniques including physical vapour deposition (PVD) (sputtering and ion implantation), chemical vapour deposition (CVD) (plasma reactive ion etching), sol-gel process, chemical etching process and electrochemical methods for diverse applications including biomedical field and semi-conductors. Among these fabrication methods, electrochemical method and in particular, anodization appears widely preferred due to its ability to grow mechanically stable and durable anti-corrosive micro-nanoporous oxide layers, serve as templates for synthesizing nanomaterials, its reproducibility and cost effectiveness [2]. Anodization is an electrochemical process employed for growing a self-organized close-pack porous oxide alumina by anodic oxidation of aluminum.

3.2.1   Surface pre-treatment of aluminum by anodization

The aluminum anodization process involves a pre-treatment sequence of aluminum substrates, which include cleaning to remove surface contamination, alkaline etching to remove native oxide layer, rinsing to prevent further oxidation, desmutting in dilute HNO_3 and rinsing in deionized water. Anodization is then performed on this final surface. The following sub-sections briefly describe the pre-treatment sequence involved in aluminum anodization.

3.2.1.1 Cleaning of aluminum substrates

AA6061-T6 aluminum alloy substrates of laboratory scale dimensions $1'' \times 2''$ was ultra sonically cleaned in a 1 vol. % Liquinox anionic liquid detergent (Sigma Aldrich) for 15 minutes, followed by distilled water rinsing ultrasonically for additional 15 minutes. Finally, the cleaned aluminum substrates were dried at 70 ˚C in an electric oven (VWR) for 24h to remove excess water prior to further processing.

3.2.1.2 Alkaline etching of aluminum substrate

Alkaline etching is an important pre-treatment process prior to anodization of aluminum alloys. Alkaline etching not only removes passive aluminum oxide layer, residual lubricant, intermetallic phases and sub-surface defects, but also creates smooth surfaces necessary for providing uniform current distribution and porous oxide growth [3, 4]. This step also helps remove intermetallic Mg_2Si precipitates that affect the quality of morphological features of the anodized aluminum surface. Hence, cleaned AA6061-T6 aluminum alloy substrates were etched in a 1 M sodium hydroxide (NaOH) etchant at 55°C for a duration of 3 minutes. Subsequently, the etched aluminum substrates were washed in distilled water by ultra sonication for 15 minutes to remove any debris resulted from etching. The aluminum alloy substrates were further immersed in a 10 vol.% HNO_3 solution at room temperature for desmutting for 1.5 minutes, where the smooth dark aluminum substrate turned silvery and bright. Finally, the desmut aluminum substrates were further rinsed in distilled water for additional 15 minutes to remove other impurities, followed by drying at 70 ˚C in an electric oven (VWR) for 24h to remove excess water.

3.2.1.3 **Anodization of aluminum**

Anodization of aluminum typically takes place in two steps. The first step usually serves the purpose of creating nucleation sites for subsequent growth of a well-ordered close-packed hexagonal porous alumina oxide during the second step. Whilst this two-step anodization process produces desirable morphological features, the two steps involved render the process long and tedious. Therefore, a one-step hard anodization process that produces a well-ordered porous and uniform aluminum oxide structure with desirable morphological features in short time was employed in this project.

The one-step anodization process was performed by optimizing operation parameters such as electrolytes (phosphoric acid, sulphuric acid, and oxalic acid), current density and anodization time. The electrolyte (acid) concentration was varied between 3 wt. %, 15 wt. % and 45 wt. %, whilst the current density and anodization time varied were 7 mA/cm^2, 10 mA/cm^2, 20 mA/cm^2 and 40 mA/cm^2; and 30, 60 and 120 minutes, respectively. Anodization was performed in a galvanostatic (constant current) mode using a 600 W direct current power system (Ametek Sorensen DCS 100-12E, Chicoutimi, QC, Canada). The etched aluminum substrate, to be anodized was made the anode, whereas the as-received aluminum was used as cathode. These two electrodes were separated in parallel by 1.5 cm. To ensure uniform distribution of heat and to prevent electrolyte over-heating, the electrochemical cell was equipped with circulating cold-water coolant (5 °C) bath and magnetic Teflon® stirrer in the beaker containing the electrolyte, constantly rotating at 2000 rpm. Figure 3.1 shows the schematic of the anodization set-up. At the end of each anodization process, anodized samples were ultra-sonicated for 30 minutes in distilled water to remove residual electrolytes to stop any further reaction, followed by drying at 70 °C in an electric oven (VWR) for 24h.
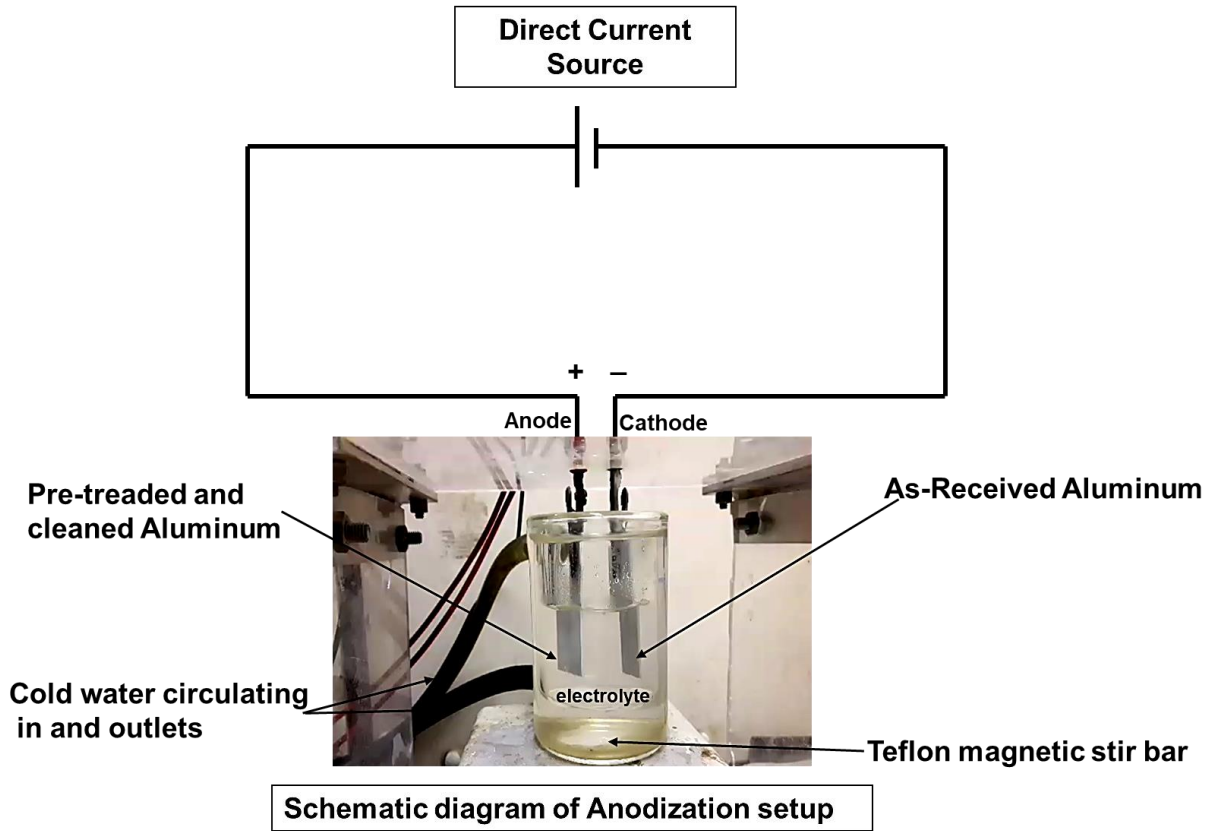
Figure 3-1. Schematic representation of the anodization process of aluminum alloy substrates.
© Henry Agbe, 2021

3.3 Fabrication methods for antibacterial aluminum surfaces

To fabricate antibacterial aluminum surfaces with superhydrophobic, photocatalytic and topography-mediated antibacterial properties, the following procedures were followed.

3.3.1 Fabrication of superhydrophobic silver-polymethylhydrosiloxane coating on anodized aluminum

Superhydrophobic silver-polymethylhydrosiloxane (Ag-PMHS) coating was fabricated by firstly, anodizing aluminum substrate to achieve a surface nano-roughness, and secondly, synthesizing and incorporating Ag-PMHS nanocomposites in the anodized porous structure, which provided both surface nano-roughness and low surface energy for surface passivation to result in reduced affinity to water.

Anodization was performed in the galvanostatic mode at a current density of 40 mA/cm^2, electrolyte concentration of 15 wt. % H_2SO_4 (VWR) and anodization time of 30, 60 and 120 minutes. A simple sol-gel process was employed to synthesize the Ag-PMHS nanocomposite as shown in Figure 3.2. Sol-gel process is a low cost and low temperature synthesis approach for fabricating inorganic networks of silicon or metal alkoxide monomer precursors. Though, sol-gel synthesis was first discovered in the late 1800s, it was only in the early 1970s that the process gained attention for forming monolithic inorganic gels and glass at low temperature [5]. Sol-gel generally involves the simultaneous hydrolysis and condensation of metal alkoxides network through the formation of a colloidal suspension (sol) and gelation of the sol to form a network in a continuous three-dimensional liquid phase (gel). As an organofunctional siloxane source, PMHS acts as an effective reducing agent due to the active Si–H moiety at the siloxane backbone [6].

CH₃ structures — reaction schemes:

Hydrolysis ... + ROH   3.1

Water Condensation ... + HOH   3.2

Alcohol Condensation ... + ROH   3.3

$n\text{Ag}^+$ + ... $\xrightarrow[55°C]{NH_4OH}$ ... + $nH_2 \uparrow$ 3.4
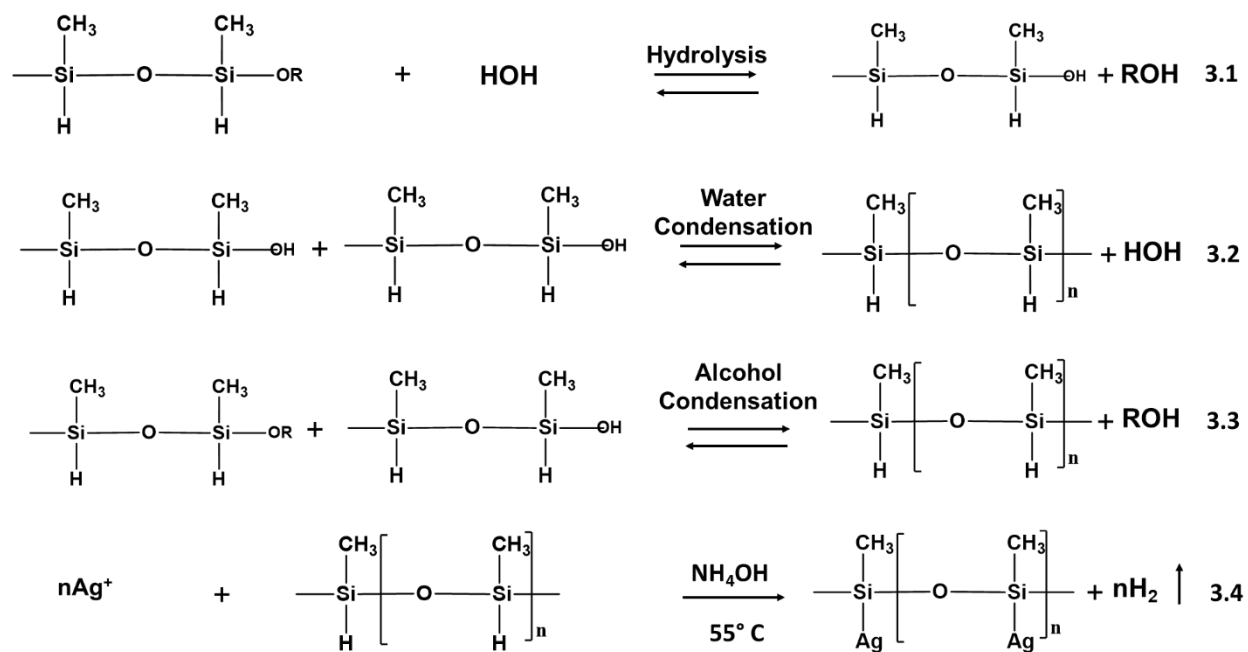
Figure 3-2. Schematic representation of reaction steps of polymethylhydrosiloxane sol-gel process. © Henry Agbe, 2021

To synthesize the Ag-PMHS nanocomposites, 0.08 M PMHS ($\geq$ 97%, VWR) was dispersed in ethanolic solution under sonication (Branson® Ultrasonic Bath, 230 Vac, 50 Hz) for 15 minutes. Subsequently, the 0.08 M PMHS was added to mineral spirit while stirring using a magnetic Teflon stirrer rotating at a speed of 500 rpm at 55 °C for 30 minutes. A 11.2 M ammonium hydroxide (VWR) was added dropwise to the reaction suspension to achieve a pH of 11 for catalysis to occur. In the hydrolysis process, a nucleophilic attack of water on the silicon atom allows the substitution of alkoxide groups (–OR) with the hydroxyl groups (–OH) as shown in the reaction scheme (equation 3.1) of Figure 3.2. At the condensation reaction, siloxane bonds (Si–O–Si) condense to form a three-dimensional network of (Si–O–Si) polymer with the elimination of water and alcohol as seen in the reaction schemes in equations 3.2 and 3.3 of Figure 3.2. Finally, at the gel point, which was achieved after 24 h, a viscous, stable, and elastic gel network was observed. However, for the purpose of obtaining thin film coatings of Ag-PMHS

nanocomposite on AAO/Al, the ageing process was limited to 30 minutes. Subsequently, a 0.08 M $AgNO_3$ (VWR) solution was added dropwise to the above suspension, where Ag^+ was reduced by active Si–H moiety of PMHS, with the formation of Ag^0 in-situ and H_2 gas evolution, as shown in equation 3.4 of Figure 3.2. Ammonium hydroxide (NH_4OH) accelerates the reduction process, where liquid ammonia forms a silver ammonia complex ($Ag(NH_3)_2^+$aq) similarly to how saccharides reduces Ag^+ ions in a Tollens Ag synthesis [7, 8]. The as-synthesized product was stirred vigorously using a magnetic Teflon® stirrer rotating at 700 rpm at 55 °C for an additional 15 minutes.

The as-synthesized Ag-PMHS nanocomposite was then loaded with premium room-temperature vulcanized (RTV) adhesive silicone. The RTV silicone-loaded Ag-PMHS nanocomposite was then ultrasonicated to obtain a homogeneously dispersed polymeric solution, which was then used for coating on the anodized aluminum substrate via a 5-min dip coating deposition process. The dip coating process typically consisted of dipping the anodized aluminum coupons at a rate of 0.5 cm/s, a dwelling time of 5 minutes, withdrawal rate of 0.1 cm/s and a room temperature drying for 24 h as shown in Figure 3.3.
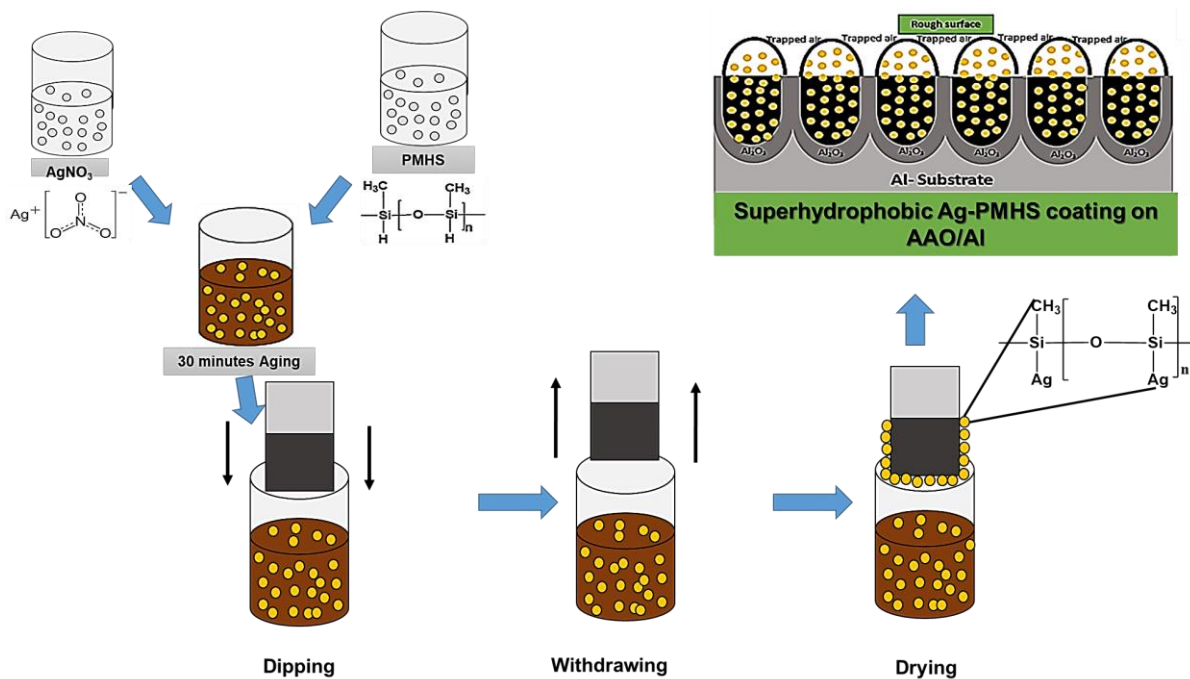
Figure 3-3. Schematic representation of in situ synthesis of silver polymethylhydrosiloxane (Ag-PMHS) by sol – gel process. © Henry Agbe, 2021

3.3.2   **Fabrication of tunable superhydrophobic aluminum surfaces**

Tunable superhydrophobic aluminum surfaces were fabricated by creating a micro-nano surface roughness using hydrochloric acid (HCl) etching, followed by passivation with low surface energy octyltriethoxysilane (OTES) molecules in a chemical bath deposition (CBD) process. Chemical bath deposition is a simple low-cost wet chemical coating technique, where atomic, molecular, or ionic species of the precursor solution precipitate and bond to the substrate surface to form desirable thin films on substrates. Typically, AA6061-T6 aluminum alloy coupons of

laboratory scale dimensions 1″ × 2″ were ultrasonically degreased in a soap solution, followed by chemical etching in a 30 wt. % HCl at 55 °C for 3 minutes. During the etching process, the material from the topmost layers of the aluminum substrates surfaces was partially removed to create random micronano-porous topographical patterns. The hydrochloric acid etching process enhances formation of random pattern appropriate for mechanical interlocking of coating material, enhancing adhesion of coatings [9]. Subsequently, the hydrochloric acid etched, and ultrasonically cleaned aluminum substrates were immersed in a chemical bath consisting of 50 ml ethanol, 1mL of 3.0 M OTES and 0.01 M quaternary ammonium (QUAT) molecules for 30 minutes. Figure 3.4 shows the schematic representation of the fabrication process. The QUAT was added dropwise in such as way that the molar ratio of QUAT/OTES varied between 0 to 54×10^{-4} to tune the wettability property from superhydrophobic to hydrophilic state. On addition of QUAT, the alkyl group of nitrogen, $(N^+)-(CH_3)_3$ covalently binds with the octyl chains of the OTES molecules through a non-hydrolysable reaction [10], shown in Figure 3.4. Finally, the tunable superhydrophobic surfaces were dried in the oven at 100 ˚C, in air atmosphere for 2 h to remove residual solvents.
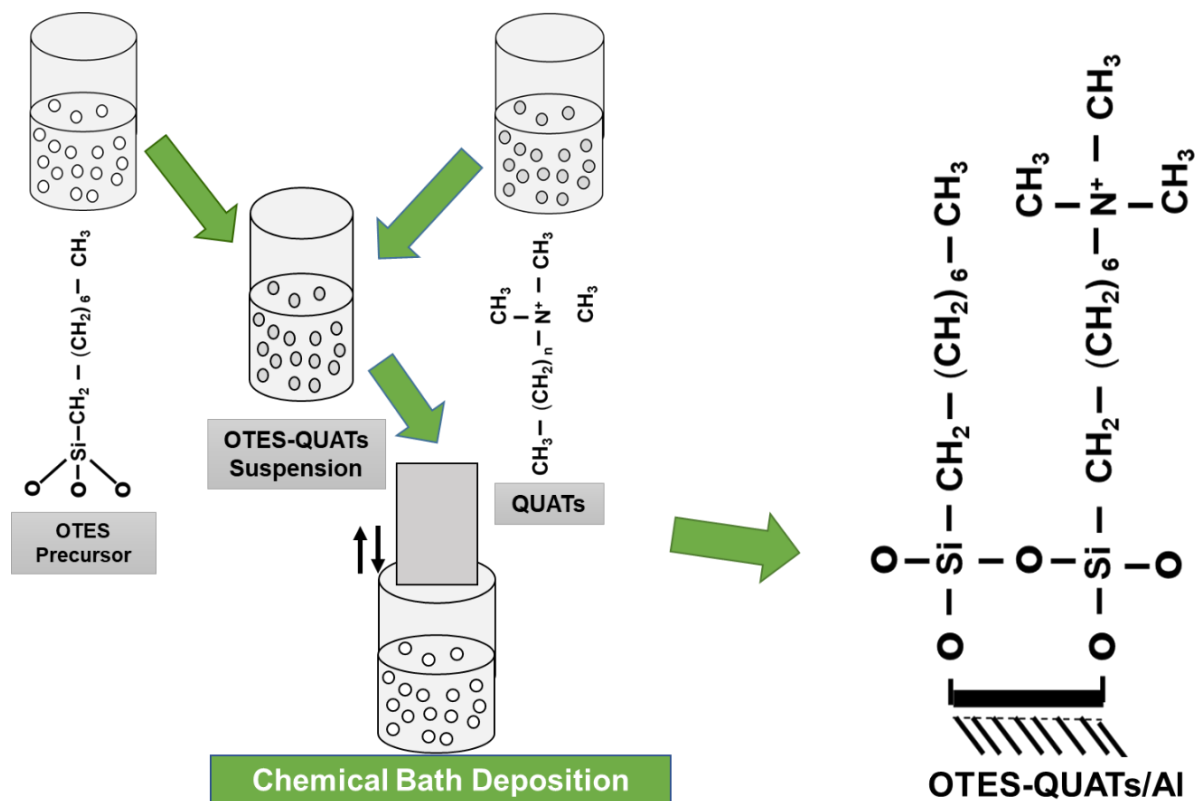
Figure 3-4. Schematic representation of fabrication of a tunable superhydrophobic aluminum surface. © Henry Agbe, 2021

3.3.3 Synthesis of silver phosphate photocatalyst

Synthesis of silver phosphate (Ag_3PO_4) nanoparticles was achieved by two main methods: (a) Ion-exchange precipitation method, and (b) Electrochemical synthesis on anodized aluminum

a) **Ion-exchange precipitation method of Ag_3PO_4**: In this method, 1.2 g of 0.12 M silver nitrate ($AgNO_3$) was dissolved in 60 ml distilled water under constant magnetic

stirring. Further, 0.12 M aqueous solution of sodium phosphate (Na_2HPO_4) was added dropwise under continuous stirring for 15 minutes turning the clear solution to yellowish in color confirming the formation of Ag_3PO_4. The yellowish Ag_3PO_4 was collected by centrifugation and washed several times with deionised water, followed by drying in an oven (VWR) at 100 ˚C for 2 h to remove residual solvents.

b) **Electrochemical synthesis of Ag_3PO_4 nanoparticles on anodized aluminum**: Generally, electrochemical synthesis of coatings on anodized aluminum is achieved from three main power sources: direct current (DC), alternating current (AC) and pulse current (PC) deposition. Of these, DC source is rarely utilized for electrodeposition of coatings on anodized aluminum due to the presence of the barrier oxide layer, which provides high resistance for electron tunnelling, necessitating a separation of the barrier oxide layer for successful electrodeposition [11]. However, in this project, an optimal reduction potential of 1.0V was found adequate to deposit Ag_3PO_4 nanoparticle in-situ on anodized aluminum by DC electrochemical process. Typically, by applying -1.0 V potential at a temperature of 65 ± 1 °C to a 0.12 M $AgNO_3$ in a two-electrode electrolytic cell, Ag^+ ion is reduced into metallic Ag^0 in a reduction reaction process. Electrochemical deposition times in the current study were varied to 15, 30 and 60 minutes. On the other hand, by applying a 10 V DC potential to a 0.12 M sodium orthophosphate (Na_2HPO_4) electrolyte for 60 seconds at 65 ± 1 °C, metallic silver was oxidized from the Ag^0 state to Ag^+ state, where Ag^+ react with PO_4^{3-} to electrochemically precipitate Ag_3PO_4 [12], in-situ on the anodized aluminum

3.4   Physicochemical and in-vitro biological characterization

The physical and chemical methods employed to characterize the antibacterial aluminum surfaces in terms of morphology and chemistry, along with in-vitro assays utilized to evaluate efficiency of the antibacterial aluminum surfaces are discussed here.

3.4.1   Microstructural characterization by scanning electron microscopy

Morphological features of anodized aluminum including the pore and cell diameters of the anodized porous oxide layer, chemical composition and particles sizes of nanocomposites were characterized using a Scanning Electron Microscope (SEM, JEOL JSM 6480LV), equipped with energy dispersive X-ray spectroscopy (EDS), as shown in Figure 3.5. SEM is a very important and a versatile tool for topological study and surface chemical analysis in material science and engineering. In this technique, electrons are ejected from an electron gun via either a field emission or thermionic emission process in a high vacuum system. The vacuum system prevent electron scattering by gas molecules and reduce contamination of the gun. The electrons are focused and accelerated toward the sample by an applied voltage, (typically ~20 KV) and a set of electromagnetic field-controlled condenser and objective lenses. The sample is raster scanned by the impinging electron beam, controlled by strong scanning coils. The surface-electron interaction produces topography and compositional information of the sample. The secondary and backscattered electrons are used for sample imaging, while the X-rays provide the elemental compositional information. Prior to each SEM analyses, samples were metalized with a thin

coating of gold (~8 nm) using an Edwards Scancoat Six Sputter Coater to enhance conductivity, prevent charging and improve resolutions.

Figure 3-5. Digital image of scanning electron microscope (model SEM JEOL JSM 6480LV), CURAL, UQAC. © Henry Agbe, 2021

3.4.2 **Fourier transformed infrared spectroscopy**

Chemical composition of the samples was analyzed with an Attenuated Total Reflectance-Fourier Transform Infrared spectroscopy (ATR-FTIR, Agilent Technologies Cary 630) in the

wavenumber range of 4000-450 cm^{-1}, shown in Figure 3.6. FTIR is a chemical analytical technique, which measures the infrared intensity versus wavenumber (cm^{-1}) of light. FTIR is useful for elucidating the molecular structure of organic and inorganic functional groups. When the frequency of impinging infrared radiation on a sample matches the normal vibrational stretching or bending modes of the molecules in the sample, the bonds absorb some of the impinging IR, while the remaining get transmitted, in transmission mode FTIR spectroscopy. Since vibrational frequency varies linearly with the bonding force (k) and inversely with reduced mass of atom, μ as shown in Equation 3.5 [13], the resulting signal detected is a molecular 'fingerprint' for specific molecules within the sample.

$$\omega = \frac{1}{2\pi} \sqrt{\frac{k}{\mu}}$$

3.5

where ω is the frequency of vibration, (cm^{-1}) and k is the bond strength (dyne. cm^{-1}).

Thus, based on vibrational frequency, molecules absorb IR radiation at specific wavelengths, which enables identification of specific functional groups of interest in a sample, such as Si–O–Si, Si−CH$_3$, Ag−O or Si-O-CH$_2$CH$_3$ in this study. Contrary to transmission mode FTIR, in ATR-FTIR, the IR beam is totally reflected. Typically, a high refractive index (RI) diamond micro-ATR crystal (RI = 2.41) is used in ATR mode. Due to the high refractive index of the crystal, IR beam is totally reflected at the sample-crystal interface within the crystal. However, because of the wave-like property, the IR penetrates the few micron layers of the sample (depth of penetration, dp) resulting in an evanescent wave. The intensity of the evanescent wave decays exponentially, therefore, the attenuated total reflected IR signals, carrying absorption information of the samples is collected at the detector. The signal is then subsequently Fourier transformed and recorded as ATR-FTIR spectra.

Figure 3-6. Digital image of Fourier transform infrared spectroscopy instrument (ATR-FTIR) Cary 630 Agilent Technologies, CURAL, UQAC. © Henry Agbe, 2021

3.4.3   X-Ray diffraction (XRD)

X-radiation diffraction technique utilizes electromagnetic X radiation of wavelength range 0.1-100Å to identify and quantify phases by comparison with data from known structures, characterize lattice parameters and crystal lattice structures among others. Typically, monochromatic X-rays beams are incident at an angle to the crystallographic planes. The internal crystal planes reflect the incident beam constructively or destructively, depending on whether they satisfy Bragg's law, in equation 3.6.

$$n\lambda = 2d\sin\theta$$

where λ is the wavelength of the monochromatic X-ray beam incident on the crystallographic planes, n is an integer, d is the atomic spacing and θ is the angle of incidence of X-rays on the crystallographic planes. If the wavelength of the impinging X-ray beam is approximately comparable to the interspace distance of the internal crystal planes and the Bragg's law is satisfied, the impinging X-rays will be in phase and be diffracted, leading to constructive interference, as shown in Figure 3.7. On the contrary, if the impinging X-rays are out of phase, they will cancel out and lead to destructive interference with no diffraction. The diffraction patterns obtained from constructive interferences are unique for individual crystal structures and are therefore "fingerprints" for identifying phases and crystallinity of synthesized samples.
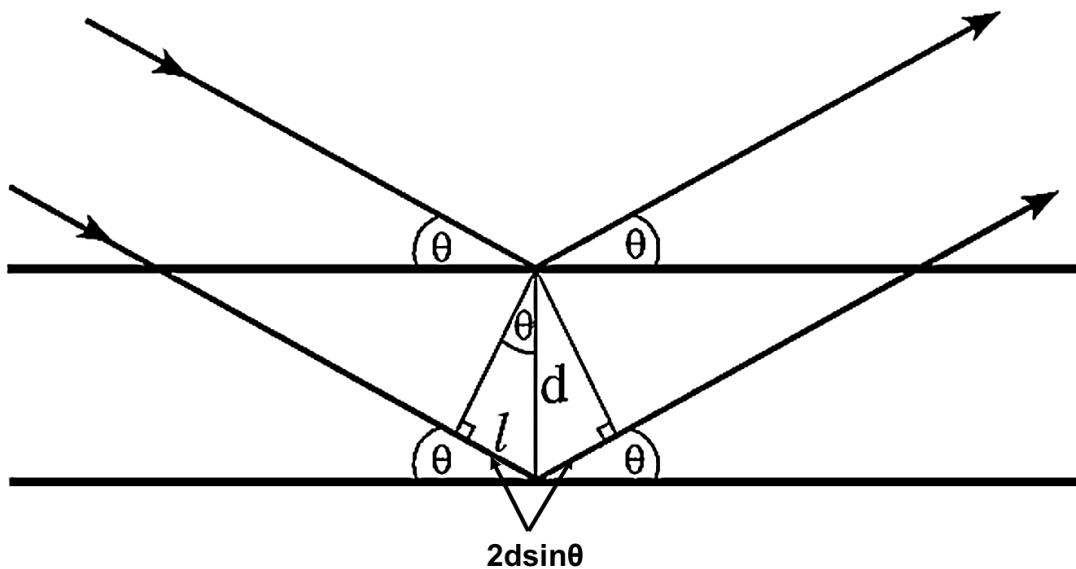
Figure 3-7. The condition for Bragg's law. Adopted from [30].

The crystalline structure of the aluminum coatings and nanocomposites studied in this project were analyzed using X-ray powder diffraction (XRD, Bruker D8 Discover system) shown in figure 3.8.

Figure 3-8. Digital image of X-ray diffractometer, Bruker D8 Discover system, CURAL, UQAC. © Henry Agbe, 2021

3.4.4 **Optical profilometry**

Generally, surface roughness is characterized by mechanical profilometry such as atomic force microscopy (AFM) and stylus profiler or by optical profilometry. Atomic Force Microscope (AFM) is part of a group of scanning probe microscopes (SPM) that is versatile for imaging and manipulating both physical and biological nanostructures at the micro to nanometre scale [14]. While AFM demonstrates the ability to measure surface roughness and map interaction forces on an atomic scale, stylus profilers suffer some disadvantages such as poor lateral resolution and tendency to damage sample due to the contact mode operation. On the contrary, optical, or non-contact mode profilometry are non-destructive and possess faster processing speed. Optical profilometry uses a high-resolution optical probe to sense peaks and valleys on the surfaces to produce a quantitative $Z(X)$ profile of the surface topography [15]. Because surface roughness is very important parameter in substrates surface-cells interaction, an optical profilometry (MicroXAM-100 HR 3D, NANOVEA, Irvine, USA), shown in Figure 3.9, was utilized to characterize surface roughness of the various surfaces fabricated in this research. The instrument extracts topography data from peaks and valleys in both points and lines by raster scanning and converts the data into a three-dimensional image using an in-built image processing software, scanning probe image processor (SPIP). An in-built MapVue software also processes the surface roughness, which is measured in both arithmetic and root mean square (*RMS*) roughness.

Figure 3-9. Digital image of the optical profilometer, CURAL, UQAC. © Henry Agbe, 2021

3.4.5 Superhydrophobic – water contact angle measurements

Superhydrophobic surfaces possess water contact angle (WCA) greater than 150º and contact angle hysteresis (CAH) of less than 10º. While WCA is a measure of the angle of contact the water drops make with a surface upon contact with it, CAH provides the sliding angle, which is determined by taking the difference between the advancing and receding WCAs of the water drops while the drops are in motion in one direction. For real-life applications of repellent surfaces,

it is important that the dynamic movement of droplet be considered by way of investigating the CAH, along side the static WCA [16]. Thus, in the present work, surface wettability characteristics of samples were studied by measuring both static and dynamic contact angles (CA) using a First Ten Angstrom Contact angle FTA200 goniometer, shown in Figure 3.10. The FTA200 goniometer consists of a measurement platform, a frame grabber (video capture) card, and a computer. With the help of a computerized syringe pump, drops of a desired deionized water (10 µL) were cast at least five different positions on each substrate and the image captured using the high-resolution camera for a predetermined time. The contact angles were recorded and analyzed using the image analysis software. The dynamic contact angle was measured by using a method where the water drop is held with a stationary needle in contact with the sample surface and moving the goniometer stage in one direction. This method was adopted instead of tilting the stage to move the drops as the drops were easily rolling off due to high WCAs on the prepared superhydrophobic surfaces making it impossible to control the drops on a stage.
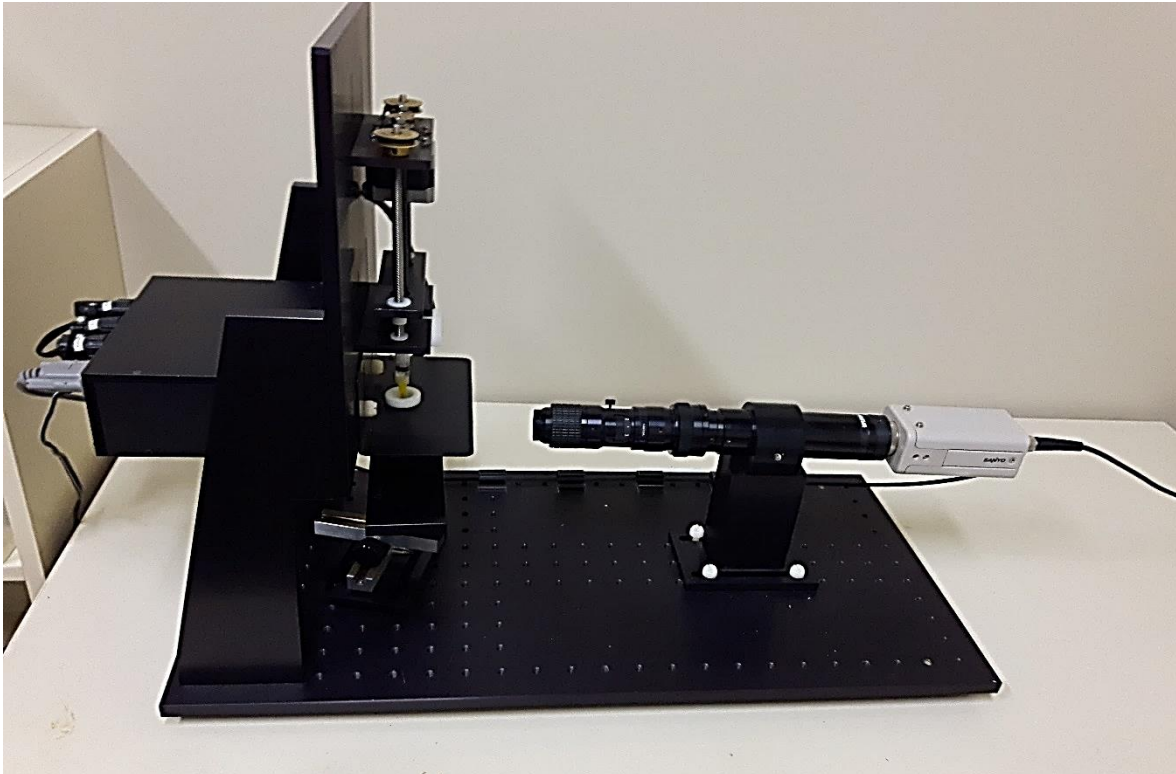
Figure 3-10. Digital image of a contact angle goniometer, Parc technologique,

UQAC. © Henry Agbe, 2021

3.4.6 UV-accelerated weathering study of superhydrophobic coatings

To meet the requirements on superhydrophobic antibacterial coatings for outdoor environmental applications, it is essential that the effects of ultra-violet (UV) radiation on their stability and durability be investigated. In this regard, UV-accelerated weathering tests were conducted on the sample surfaces. UV-accelerated weathering test is a standard method to simulate natural solar irradiation and to quantify the effects of weathering conditions (UV irradiation) on

coating degradation. Typically, the fabricated superhydrophobic coatings were subjected to a 15-watt UV irradiation of 365λ wavelength, using a homemade benchtop lamp device (UV-Blak-Ray XX-15BLB), shown in Figure 3.11. Water roll-off property of the superhydrophobic coatings were monitored and WCAs were measured at the end of each week for a period of 5 weeks to determine stability and longevity of the superhydrophobic coatings.
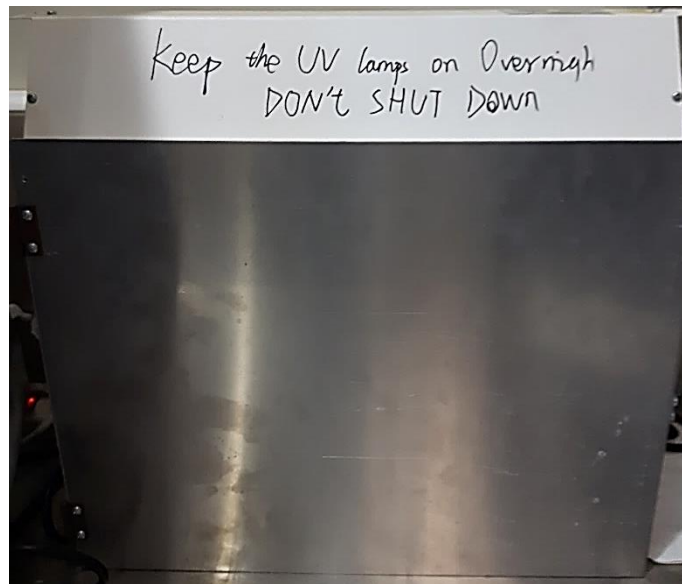
Figure 3-11. Digital image of a homemade benchtop UV lamp device for accelerated weathering test, CURAL, UQAC. © Henry Agbe, 2021.

3.4.7 Coating adhesion evaluation

The quality of coatings' adhesion on aluminum substrate surfaces and hence their mechanical robustness was investigated using an Elcometer 107 Cross Hatch Cutter. This is a simple and effective technique used for assessing the adhesion of coating or resistance to

separation of coatings on substrates' surfaces. Typically, two cuts at 90° angle to each other were made through the coating to the underlying substrate, resulting in a grid of small squares as shown in the images in the third column of Table 3.2. An American Society for Testing and Materials (ASTM-3359) recommended adhesive tape was gently pressed on the two-crosscut lattice, followed by smoothening to ensure that the tape was firmly in place. Then, within 90 seconds of application, the adhesive tape was removed by pulling in a single smooth action at an angle of 180° to the coating surface. Subsequently, the coating was accessed visually by viewing the lattice of cuts. The lattice of cuts is finally compared with ASTM standard rating to evaluate durability of the coating. The ASTM standard rating to evaluate the coating adhesion levels is presented in Table 3.2. According to ASTM-D3359 testing protocol, coatings with highest adhesion to substrates is rated grade 5B while those with lowest adhesion is rated 0B [17].

Table 3-2 ASTM D-3359 standard adhesion rating for coatings on substrates surfaces (Adopted from [31]).

Classification	% of Area Removed	Surface of Cross-cut Area From Which Flaking has Occured for 6 Parrallel Cuts & Adhesion range by %	
5B	0% None		
4B	Less than 5%		
3B	5 - 15%		
2B	15 - 35%		
1B	35 - 65%		
0B	Greater than 65%		
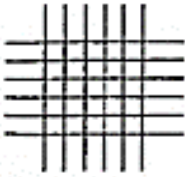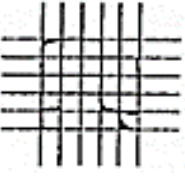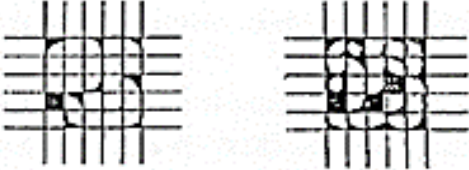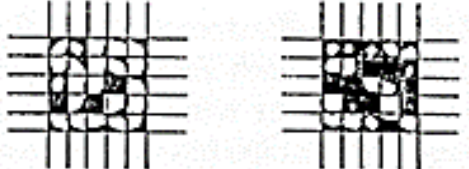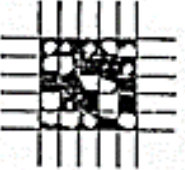
3.4.8   **In-vitro biological characterization**

The in-vitro antibacterial assays employed to evaluate efficiency of the antibacterial surfaces are discussed in this sub-section.

3.4.8.1 **Bacterial strains and culture conditions**

The model bacterial strains, i.e., Gram-positive *Staphylococcus aureus*-S.A (ATCC 6538), Gram-negative *Pseudomonas aeruginosa*-P.A (ATCC 9027), and Gram-negative *Escherichia coli-E.coli* (ATCC 8739-Hardy Diagnostics, USA) were grown overnight from a frozen (-80 °C) stock in Tryptic Soy Broth (TSB), (Hardy Diagnostics, USA) at 37 °C, and then passaged on fresh pre-warmed Tryptic Soy Broth (TSB) or Mueller Hinton (MH) Broth at (37 °C) to OD_{625} 0.1 at exponential growth phase. The bacteria strains were selected since they are among the leading nosocomial pathogens of relevance in inanimate touch surface-mediated nosocomial infections as discussed in Chapter 2, section 2.11 of this thesis. TSB is a general-purpose medium for isolating and culturing most bacteria. It contains digests of soybean meal and casein, providing amino acids and other nitrogenous substances for variety of organisms. On the other hand, MH Broth contains beef infusion, casamino acids, and starch, and is ideal for preparing bacterial suspensions for disk diffusion sensitivity assays.

3.4.8.2 Neutralization and assessment of non-toxicity of Dey-Engley neutralizer

To validate the accuracy of data on antibacterial efficiency, it is important to avoid "carry-over" of active bactericides to recovery media, which may result in biostasis of organism due to activity of residual bactericides [18]. The presence of such in-culture media may hinder the growth of microorganisms, resulting in misleading and inaccurate findings [19]. Thus, it is important that the antibacterial material or bactericide be quenched or neutralized during experiments intended to evaluate antibacterial efficiency. Additionally, it is essential that the neutralizing broth fulfils the following conditions: (1) the neutralizer must effectively inhibit the action of the bactericide, (2) the neutralizer must not itself be unduly toxic to the challenge organisms, and finally (3) the neutralizer and active agent must not combine to form a toxic compound [18]. Therefore, in this work, Dey-Engley Neutralizing Broth (D/EB) was utilized for this purpose, since it is non-toxic and a broad-spectrum neutralizing broth [18].

In this study, a 50 µL bacterial suspension was mixed with 50 µL of Dey-Engley Neutralizing Broth (D/EB) [20, 21]. The mixture was then evenly spread on sterile coupons using sterile bent disposable pipette tips (Mettler-Toledo). These coupons were then air-dried in airflow (Class II cabinet) at ambient conditions of 25 °C and (50 ± 10%) relative humidity (RH) for 1 h, followed by viable bacterial cell count (approximately 30–300 colonies per plate). Similar procedure was followed for control experiments, where a 50 µL bacterial suspension was mixed with 50 µL of sterile physiological saline (0.85 wt. % NaCl in water). For the D/E neutralizer's non-toxicity test, 900 µL of neutralizer was mixed thoroughly with 100 µL of bacterial suspension, followed by incubation at 36 ± 1°C for 1 h to yield countable viable bacteria colonies.

3.4.8.3   **Kirby Bauer disk diffusion or zone-of-inhibition assays**

Kirby Bauer disk diffusion assay is a preliminary technique for determining susceptibility of bacteria to antimicrobial agent based on zone-of-inhibition (ZOI) assays. Usually, when a bacterium is inoculated onto nutritious agar plates, it tends to form continuous colonies. If antimicrobial agent is placed in the media, colony formation will be inhibited around that area due to the leaching of the antimicrobial agent [22]. The region surrounding antimicrobial agent, where microbial growth is inhibited is called the Zone of inhibition (ZOI). The larger the ZOI, the better and effective the antimicrobial agent. In this research, the Kirby Bauer disk diffusion was performed using a modified version of the clinical and laboratory standards institute protocol, *M02-A12—Performance Standards for Antimicrobial Disk Susceptibility Tests; approved standard- 13th edition* [23]. Bacterial culture (which was grown as described in section 3.4.8.1 above) was inoculated on Mueller Hinton Agar using a sterile swab. Bacterial inoculum was further streaked gently on agar plates to obtain a film of bacterial lawn. Subsequently, a 5-20 µL of antibacterial agents such as silver-polymethylhydrosiloxane, silver phosphate or quaternary ammonium salts were dropped onto a sterile 6-mm diameter Whatman filter papers. The antibacterial soaked Whatman filter papers were seeded on the agar media. Finally, these agar plates were aerobically incubated at 37 °C for 24 h. The ZOI are then visualised and measured using a calibrated measuring instrument. Figure 3.12 shows the schematic representation of Kirby Bauer disk diffusion assay.
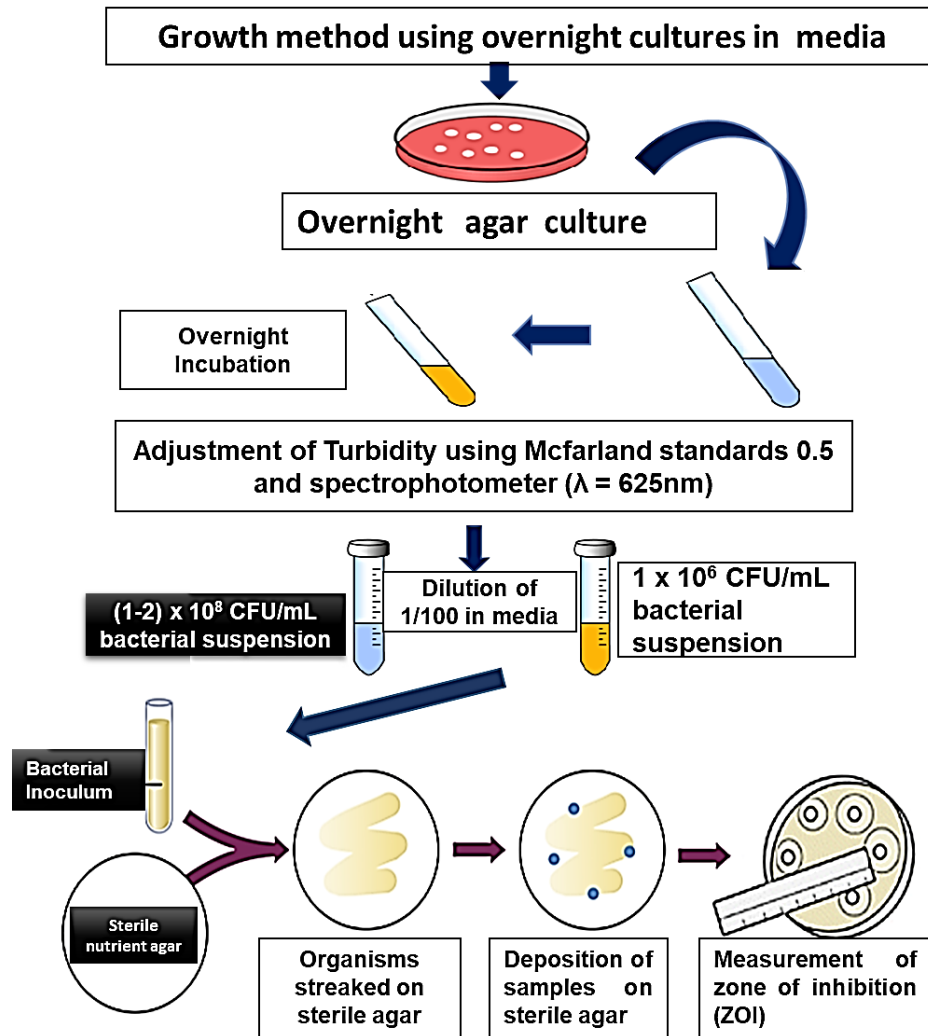
Figure 3-12. Schematic representation of Kirby Bauer disk diffusion assayy sequence. © Henry Agbe, 2021.

3.4.8.4 Static bacterial adhesion or anti-biofouling assays

Bacterial attachment on substrates surface is a prerequisite for biofilm formation. Therefore, designing anti-biofouling surfaces that repels initial bacterial attachment and subsequent biofilm formation is therefore of great interest. Generally, methods to study initial bacterial adhesion involve adhesion of bacteria from a static or flowing fluid suspension [24].

111

However, for frequently touched surfaces application, static bacterial adhesion assay is ideal. The static bacterial adhesion experiment was conducted following a prescribed static adhesion protocol with some modification [25]. Briefly, two 250 mL sterile beakers were filled with 99 mL 10 mM phosphate buffer solution (PBS) (pH 7.5 +/- 0.3 at 25°C.) and 1 mL bacterial culture. Subsequently, sterile test coupons of either Ag-PMHS superhydrophobic anodized aluminum alloys (Ag-PMHS/AAO/Al) or OTES-QUATs passivated etched aluminum alloys and control coupons were placed separately in two sterile beakers and incubated for 3 h at 37 °C. These coupons were rinsed in PBS to remove non-adherent bacteria and subsequently transferred into a 50 mL PBS and ultra sonicated on ice for 10 minutes to remove adherent bacteria. Finally, bacterial suspensions were serially diluted and plated on tryptic soy agar TSA, followed by an aerobic incubation at 37 °C for 24 h, as elaborated in Figure 3.13. Positive controls were performed for t = 0 and t = 3 h to ascertain bacterial viability.
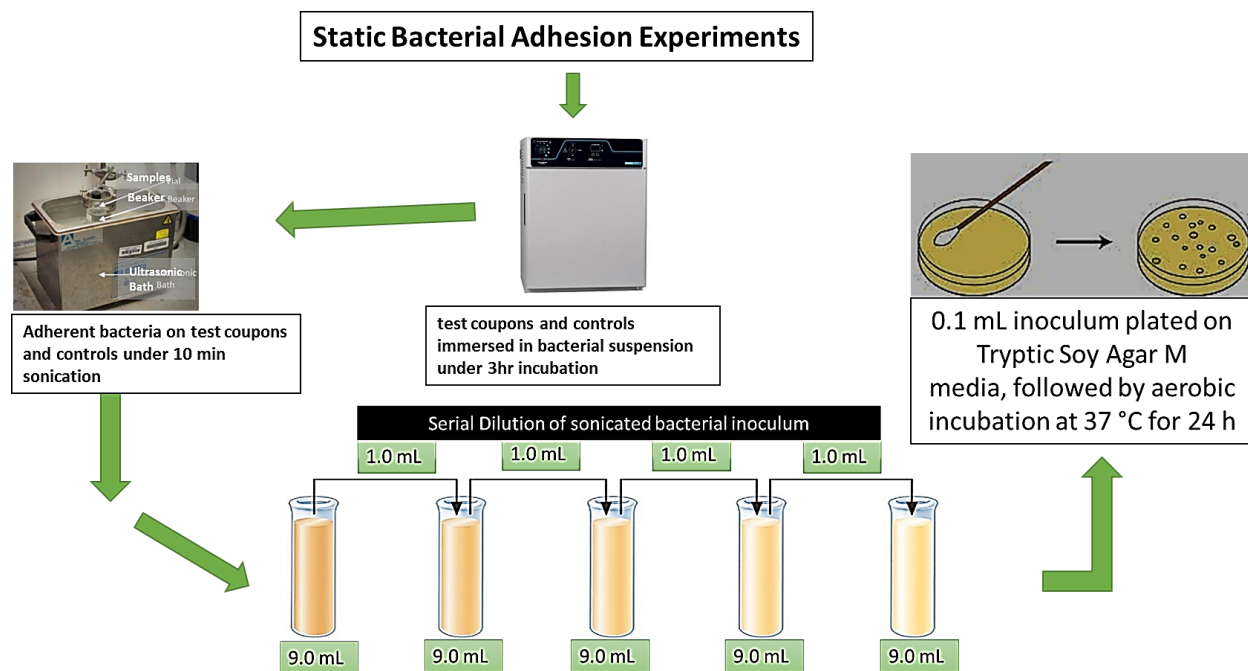
Figure 3-13. Schematic representation of static bacterial adhesion assay sequence.
© Henry Agbe, 2021.

3.4.8.5 **Bactericidal activity of self-sterilizing surfaces.**

Bactericidal efficacy studies were conducted using a modified version of the United States of America's Environmental Protection Agency (EPA)'s standard protocol for testing efficacy of copper alloy surfaces as a sanitizer [26]. Test culture was adjusted to OD_{625} 0.1 and grown to exponential phase in a maximum recovery diluent (MRD) (ThermoFisher) to give a bacterial concentration of 1.5×10^8 colony-forming units/millilitre (CFU) mL^{-1}. The MRD contained 9.5 g/L peptone, which contributes to soiling [27]. Tests were conducted on both sterile test and control coupons, which were inoculated with 5 µL bacterial test culture. To ensure test culture covers the entire coupons and edges, inoculum volume was evenly spread using sterile bent disposable pipette tips (Mettler-Toledo). The coupons were then air-dried in airflow (Class II cabinet) at ambient conditions of 25 °C and (50 ± 10%) relative humidity (RH) for pre-determined times (2, 6, 12, 18 and 24 h) to simulate conditions in hospital environments, followed by neutralization in 20mL D/E neutralizer (ThermoFisher) under 5 minutes sonication [21]. These coupons were inoculated 1, 2, 4, 6 and 8 times, respectively. Further, ten-fold serial dilutions of the neutralizer solutions were plated using standard spread plate method on Tryptic Soy Agar plates. Finally, the plates were incubated at 36 ± 1°C and 50 ± 10 % RH for 24 ± 4 h to yield countable viable bacterial colonies. Bacterial percentage reduction was calculated using the following equation:

% reduction = [(a-b) / a] × 100 % [28]   (3.7)

where, a = geometric mean of the number of CFU/cm^2 recovered on control coupons; and b = geometric mean of the number of CFU/cm^2 recovered on the test coupons.

3.4.8.6 **Novel dry seeding assay**

A novel dry seeding assay was developed to mimic near dry conditions of frequently touched surfaces in hospital settings. Briefly, 5 μL of bacterial inoculum, grown to exponential phase (1.5×10^8 colony-forming units/millilitre (CFU) mL^{-1}) in a physiological saline buffer (0.85% wt. NaCl) was seeded on a sterile $1'' \times 1''$ area of both test and control coupons. Next, coupons were incubated at ambient conditions of 25 °C and $50 \pm 10\%$ RH in a cell culture plates for pre-determined contact times (60, 180 and 240 minutes). Subsequently, using sterile swabs, bacteria were transferred into a 10 mL maximum recovery diluent (MRD) (ThermoFisher), followed by serial dilutions, and plating on tryptic soy agar (TSA). The plates were then incubated at 37 °C for 24 h to yield countable viable bacterial colonies. For continuous bacterial loading assay, same procedure was followed except that the quantitative recovery was performed after 24, 48, 72 and 96 h. The anodized aluminum coupons were inoculated 1, 2, 3 and 4 times. Positive controls were performed for t = 0 and t = 4 h to ascertain bacterial cell viability. Antibacterial efficiency was calculated from [(A-B)/A] ×100 %, where A = CFU/cm^2 of viable bacteria on test coupons and B = CFU/cm^2 of viable bacteria on control coupons. Figure 3.14 shows a schematic representation of dry seeding assay.
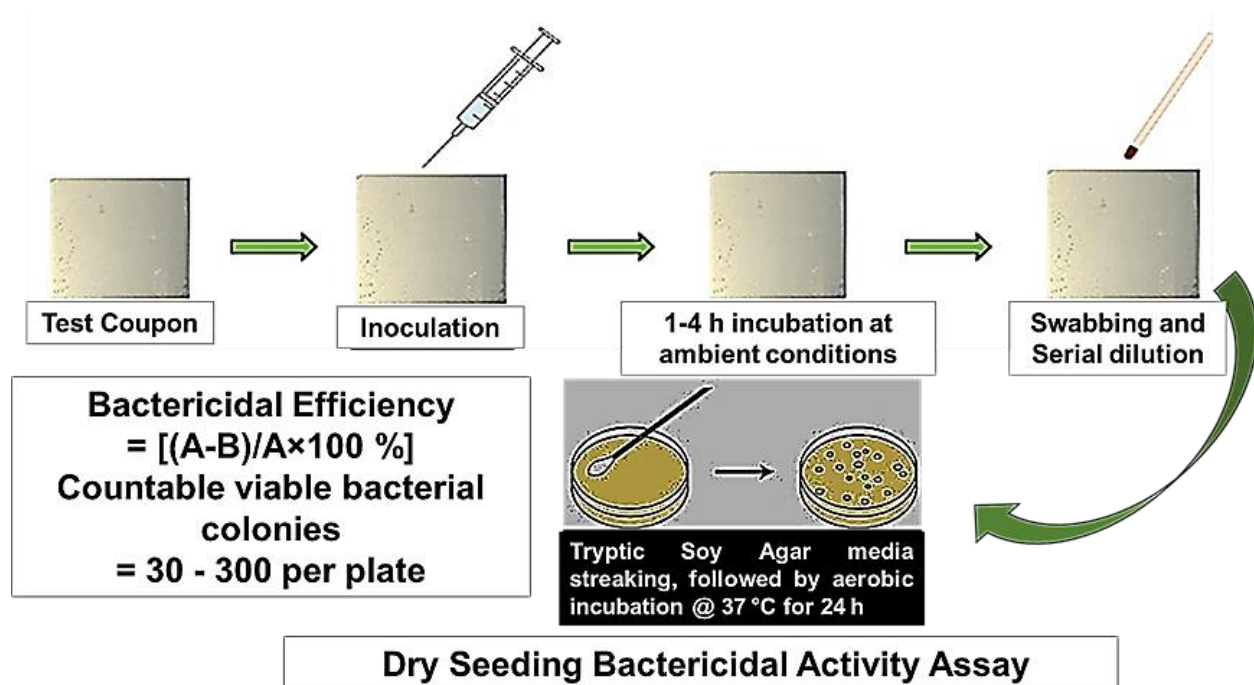
Figure 3-14. Schematic representation of dry seeding assay sequence. © Henry Agbe, 2021

3.4.8.7 **Photocatalysis-mediated bacterial inactivation**

Photocatalytic antimicrobial agents generate free radicals when they react with moisture and oxygen after light irradiation. Under the action of light, photocatalysts can act as catalytically active centers, activate oxygen in humid condition and air producing hydroxyl radicals and active oxygen ions. Active oxygen ions have strong oxidizing ability and can destroy microbe's reproductive ability, causing death through cell lysis. While photocatalysis has traditionally been dominated by TiO_2-based material and limited to UV light irradiation, recent advances in photocatalysis has been focused on visible-light photocatalysis [29]. The latter would enable

115

deployment of visible light induced-catalysis for both outdoor and indoor environmental applications, in particular, for photocatalysis-mediated inactivation of bacteria in hygiene critical environment. Hence, visible light induced catalysis of bacterial strains was investigated in this research project. Briefly, 2g/L visible light active photocatalyst was dispersed in physiological saline, containing bacterial inoculum. Next, the reactor flasks were either exposed to visible light (25-watt table lamp, 17.3 W/m^2) or UV-A light (30-watt UV-A lamp, 259 nm, 21 W/m^2) under constant stirring, with 1 ml aliquots withdrawn for pre-determined time to determine bacteria concentration by serial dilution, followed by streaking to obtain a bacterial lawn. Bacteria were then incubated at 37C° for 24 h to determine viable cells. Bacterial inactivation rate was calculated using the formula:

$$R\% = \left[\frac{C_0 - C_T}{C_0} \right] * 100\% \qquad (3.8)$$

where, C_0 is the initial bacteria concentration, C_T is bacteria concentration at time T and R %, is the inactivation rate. All laboratory supplies, as well as coupons were sterilized at 121 °C for 30 minutes in autoclave prior to antibacterial study. Figure 3.15 shows the schematic of representation of the photocatalysis process.
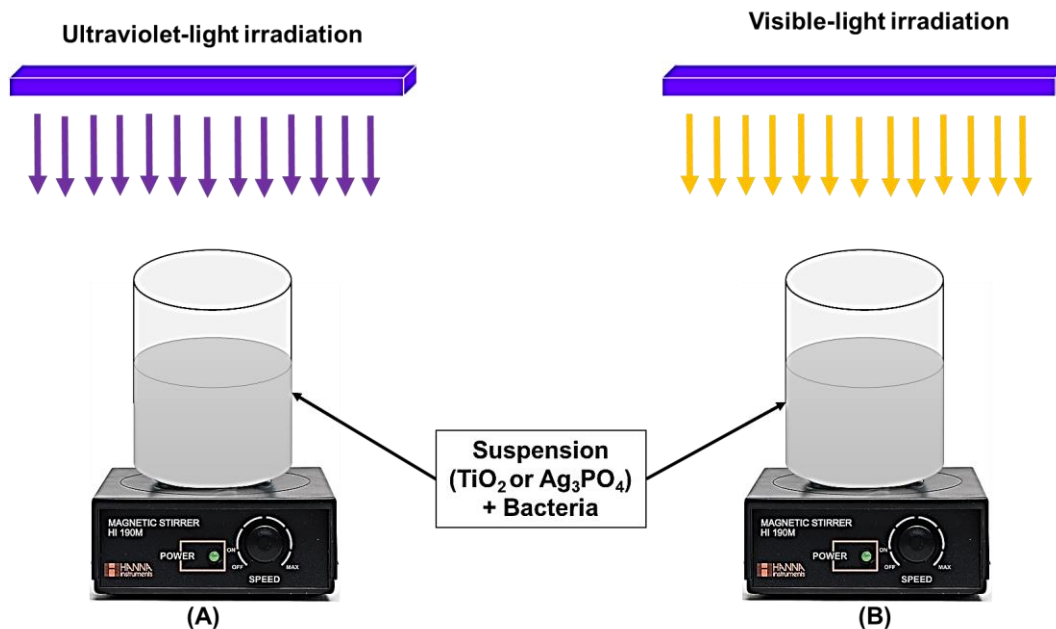
Figure 3-15. Schematic representation of photocatalysis-mediated bacterial inactivation under (A) ultraviolet light irradiation; (B) visible light irradiation.

© Henry Agbe, 2021

3.4.8.8 Statistical analysis

For quality control and reproducibility, all experiments were repeated in triplicates. Data were expressed as the average ± standard deviation (SD). For Bacteria studies, at least three independent experiments were performed and in duplicate on fresh bacterial cell suspension. A one-way analysis of variance (ANOVA) and Tukey's multiple comparison tests were further used to evaluate statistical differences between sample groups. Differences were considered statistically significant for probability or $p < 0.05$.

117

3.4.8.9 **References:**

1. Lumley, R., *Fundamentals of aluminium metallurgy: production, processing and applications*. 2010: Elsevier.

2. Liaoyong Wen, Rui Xu, Yan Mi, Yong Lei, *Multiple nanostructures based on anodized aluminium oxide templates.* Nature nanotechnology, 2017. **12**(3): p. 244-250.

3. Haobo Shi, Mei Yu, Jianhua Liu, GangRong, Rongtao Du, JieWang, Songmei Li, *Effect of alkaline etching on microstructure and anticorrosion performance of anodic film on Al-Mg-Si alloy.* Corrosion Science, 2020. **169**: p. 108642.

4. Zelong Jin, Changrun Cai, Teruo Hashimoto, Yudie Yuan, DaeHoonKang, JohnHunter, Xiaorong Zhou, *Alkaline etching and desmutting of aluminium alloy: The behaviour of Mg2Si particles.* Journal of Alloys and Compounds, 2020. **842**: p. 155834.

5. Myers, P., *David Levy and Marcos Zayat (Eds.): The Sol–Gel Handbook: Synthesis, Characterization and Applications. 3-Volume Set*. 2016, Springer.

6. Zuo-Yi Xiao, Shu-Xian Huang, Shang-Ru Zhai, Bin Zhai, Feng Zhang, Qing-Da An, *PMHS-reduced fabrication of hollow Ag–SiO 2 composite spheres with developed porosity.* Journal of Sol-Gel Science and Technology, 2015. **75**(1): p. 82-89.

7. Sharma, V.K., R.A. Yngard, and Y. Lin, *Silver nanoparticles: green synthesis and their antimicrobial activities.* Advances in colloid and interface science, 2009. **145**(1-2): p. 83-96.

8. Santipanusopon, S. and S.-A. Riyajan, *Effect of field natural rubber latex with different ammonia contents and storage period on physical properties of latex concentrate, stability of skim latex and dipped film.* Physics Procedia, 2009. **2**(1): p. 127-134.

9. B. A. Ezekoye, V. A. Ezekoye, F. I. Ezema, *Chemical bath deposition technique of thin films: a review.* International Journal of Scientific Research, 2013. **2**(8): p. 452-456.

10. Poberžnik, M. and A. Kokalj, *Implausibility of bidentate bonding of the silanol headgroup to oxidized aluminum surfaces.* Applied Surface Science, 2019. **492**: p. 909-918.

11. Nasirpouri, F., *Electrodeposition of nanostructured materials*. Vol. 62. 2017: Springer.

12. Zhiguo Yi, Jinhua Ye, Naoki Kikugawa, Tetsuya Kako, Shuxin Ouyang, Hilary Stuart-Williams, Hui Yang, Junyu Cao, Wenjun Luo, Zhaosheng Li, Yun Liu & Ray L. Withers, *An orthophosphate semiconductor with photooxidation properties under visible-light irradiation.* Nature materials, 2010. **9**(7): p. 559-564.

13. Berthomieu, C. and R. Hienerwadel, *Fourier transform infrared (FTIR) spectroscopy.* Photosynthesis research, 2009. **101**(2): p. 157-170.

14. Agbe, H. and C. Ducati, *THE STRANGE WORLD OF THE NANOSCALE.*

15. Ali, S.H., *Advanced nanomeasuring techniques for surface characterization.* International Scholarly Research Notices, 2012. **2012**.

16. Morán, G. and R. Méallet-Renault, *Superhydrophobic Surfaces Toward Prevention of Biofilm-Associated Infections*, in *Bacterial Pathogenesis and Antibacterial Control*. 2017, IntechOpen.

17. Milionis, A., E. Loth, and I.S. Bayer, *Recent advances in the mechanical durability of superhydrophobic materials.* Advances in colloid and interface science, 2016. **229**: p. 57-79.

18. Scott V W Sutton, David W Proud, Stephen Rachui, Daniel K Brannan, *Validation of microbial recovery from disinfectants.* PDA Journal of Pharmaceutical Science and Technology, 2002. **56**(5): p. 255-266.

19. MEHREGAN HADI, ELMI F., FAZELI M.R., SHAHVERDI A.R., SAMADI NASRIN, *Evaluation of neutralizing efficacy and possible microbial cell toxicity of a universal neutralizer proposed by the CTPA.* 2006.

20. Dey, B. and F. Engley Jr, *Neutralization of antimicrobial chemicals by recovery media.* Journal of microbiological methods, 1994. **19**(1): p. 51-58.

21. L J Wheeldon, T Worthington, P A Lambert, A C Hilton, C J Lowden, T S J Elliott, *Antimicrobial efficacy of copper surfaces against spores and vegetative cells of Clostridium difficile: the germination theory.* Journal of Antimicrobial Chemotherapy, 2008. **62**(3): p. 522-525.

22. Cioffi, N. and M. Rai, *Nano-antimicrobials: progress and prospects*. 2012: Springer Science & Business Media.

23. The Clinical and Laboratory Standards Institute. *Performance Standards for Antimicrobial Disk Susceptibility Tests, 13th Edition*. 2018,January 11; Available from: https://clsi.org/standards/products/microbiology/documents/m02/.

24. Jelmer Sjollema, Sebastian A J Zaat, Veronique Fontaine, Madeleine Ramstedt, Reto Luginbuehl, Karin Thevissen, Jiuyi Li, Henny C van der Mei, Henk J Busscher, *In vitro methods for the evaluation of antimicrobial surface designs.* Acta biomaterialia, 2018. **70**: p. 12-24.

25. Meier, M., V. Dubois, and S. Seeger, *Reduced bacterial colonisation on surfaces coated with silicone nanostructures.* Applied Surface Science, 2018. **459**: p. 505-511.

26. Association, C.D. *TEST 3 Continuous Reduction of Bacterial Contaminants*. 2012; Available from: https://cuverro.com/tested-proven-trusted/scientific-proof/epa-tests.

27. M Ojeil, C Jermann, J Holah, S P Denyer, J-Y Maillard, *Evaluation of new in vitro efficacy test for antimicrobial surface activity reflecting UK hospital conditions.* Journal of Hospital Infection, 2013. **85**(4): p. 274-281.

28. G. Sauvet, S. Dupond, K. Kazmierski, J. Chojnowski, *Biocidal polymers active by contact. V. Synthesis of polysiloxanes with biocidal activity.* Journal of Applied Polymer Science, 2000. **75**(8): p. 1005-1012.

29. Henry Agbe, Emmanuel Nyankson, Nadeem Raza, David Dodoo-Arhin, Aditya Chauhan, Gabriel Osei, Vasant Kumar, Ki Hyun Kim, *Recent advances in photoinduced catalysis for water splitting and environmental applications.* Journal of Industrial and Engineering Chemistry, 2019. **72**: p. 31-49.

30. University of Cambridge, *Protein Crystollography course.* 2009; Available from: https://www-structmed.cimr.cam.ac.uk/Course/Basic_diffraction/Diffraction.html.

31. Hinhu Colour Power coating, *Classification of Adhesion Test Results-ASTM-D3359-02.* 2019; Available from: https://www.chinapowdercoating.com/test-results-astm-d3359/.

CHAPTER 4

4   CHAPTER 4

This chapter has been published in ACS Applied BioMaterials (ACS *Appl. Bio Mater.* 2020, 3, 7, 4062–407), and was authored by Henry Agbe, Dilip Sarkar Kumar, X-Grant Chen, Nathalie Faucheux, Gervais Soucy and Jean-Luc Bernier. As a first author, I conceived, designed, and performed all experiments, analyzed and interpreted the results, as well as wrote both initial and final manuscripts.

4.1   Abstract

Biofilm formation on both animate and inanimate surfaces serves as an ideal bacterial reservoir for the spread of nosocomial infections. Designing surfaces with both superhydrophobic and antibacterial properties can help reduce initial bacterial attachment and subsequent biofilm formation. In the present study, a two-step approach is deployed to fabricate silver-polymethylhydrosiloxane (Ag-PMHS) nanocomposites, followed by a simple dip-coating deposition on anodized Al. Ag-nanoparticles (Ag-NPs) are synthesized in-situ within a PMHS polymeric matrix. Morphological features of Ag-PMHS coating observed by scanning electron microscopy shows heterogeneous micro–nano structures. The chemical compositions of these coatings were characterized using X-ray diffraction and attenuated total reflection-Fourier Transform infrared spectroscopy, which indicate the presence of a low-energy PMHS polymer. The as-synthesized Ag-PMHS nanocomposite demonstrated excellent antibacterial properties against clinically relevant planktonic bacteria, with zone of inhibition values of 25.3 ± 0.5, 24.8 ± 0.5, and 23.3 ± 3.6 mm for *Pseudomonas aeruginosa* (P.A) (gram -ve), *Escherichia coli* (*E-coli*)

(gram -ve), and *Staphylococcus aureus* (S.A) (gram +ve), respectively. The Ag-PMHS nanocomposite coating on anodized Al provides an anti-biofouling property with an adhesion reduction of 99.0 %, 99.5 %, and 99.3 % for P.A, *E-coli,* and S.A, respectively. Interestingly, the coating maintained a stable contact angle of 158° after 90 days of immersion in saline water (3.5 wt.% NaCl, pH = 7.4). The Ag-PMHS nanocomposite coating on anodized Al described herein demonstrates excellent antibacterial and anti-biofouling properties, owing to its inherent superhydrophobic property.

4.2 Introduction

Bacteria colonize material surfaces and develop into a community (in extracellular polymeric substance (EPS) matrix), herein referred to as a biofilm [1]. The pathogenicity of bacteria in a biofilm differs from their free-floating planktonic cells. A biofilm offers bacteria certain advantages such as the ability to acquire resistant strains [2], intercellular communication ability to regulate gene expression via quorum sensing (QS) [3], and the ability to evade antimicrobial attacks [4]. Furthermore, a biofilm provides a safe haven for the spread of nosocomial infections [5]. It is believed that multidrug-resistant (MDR) bacteria in biofilms (*Staphylococcus aureus* (S.A)*, Pseudomonas aeruginosa* (P.A), *and Escherichia-Coli* (*E-coli*)) are the leading cause of nosocomial infections or healthcare-associated infections [6, 7]. Therefore, designing anti-biofouling surfaces for preventing initial bacterial attachment and subsequent biofilm formation using superhydrophobic coatings has recently gained significant interest [8-10]. However, the ability of superhydrophobic coatings to repel bacterial adhesion in humid environments is limited, mainly due to the loss of property of water repellency [11-14]. To achieve

a robust and long-term anti-biofouling surface, it is desirable to incorporate bactericides such as Ag. Hence, fabricating superhydrophobic coatings with inherent antibacterial properties may serve as an ideal strategy to prevent initial bacterial adhesion and subsequent biofilm formation.

Few studies have reported the fabrication of anti-biofouling surfaces (utilizing superhydrophobicity) with inherent antibacterial properties [15-17]. Wang, Z. et al. [17] fabricated mussel-inspired polydopamine superhydrophobic Ag coatings via a facile Ag mirror reaction and evaluated both the antibacterial and superhydrophobic properties against S.A and *E-coli*. They demonstrated that the superhydrophobic Ag coating exhibited antibacterial properties with a zone of inhibition (ZOI) of ~3.0 ± 0.3 mm and stability of 60 days. Meanwhile, Zhang, M. et al. [15] fabricated a Ag/Cu bimetallic hierarchical architecture coating on a copper substrate with both superhydrophobic and antibacterial properties using a facile galvanic replacement reaction, followed by a simple thermal oxidation process. The study indicated both antibacterial and superhydrophobic properties but failed to report the anti-biofouling property. Furthermore, Ozkan, E. et al. [18] engineered a superhydrophobic antibacterial copper coating via aerosol-assisted chemical vapor deposition (AACVD) with antibacterial properties against *E. coli* and S.A. Even though the superhydrophobic coatings of these studies were well above 150° in contact angle (CA), the antibacterial efficiency was low. Moreover, synthesis methods such as AACVD are expensive. For practical applications, a simple, cost-effective, and scalable process would be the sol–gel synthesis of superhydrophobic Ag nanocomposite coatings on metals such as Al.

It has been reported that polymethylhydrosiloxane (PHMS) can be utilized to synthesize silver nanoparticles (Ag-NPs) via the sol–gel process owing to its ability to reduce Ag^+ to Ag^0 in-situ, due to the (Si–H) moiety on the siloxane backbone [19, 20]. Several groups have explored the synthesis of Ag-NPs via PMHS reduction [19-22]. For example, Shang, R. et al. [21], reported

the synthesis of an Ag-NP-embedded PMHS hybrid material with high surface area, good mesoporosity, and narrow size distribution. Similarly, Zuo,Y. et al. [19] synthesized hollow Ag–SiO$_2$ composite spheres that exhibited high catalytic performance. Additionally, our research group has recently fabricated superhydrophobic coatings on Al using a TiO$_2$/PMHS sol–gel process.

In spite of significant efforts on silicone-based superhydrophobic coatings in applications of antibacterial properties, the adhesion reduction performance of bacteria has been rather low (79 - 95 %)[23, 24]. Furthermore, the applicability of such coating is limited due to the degradation with time. As Ag has natural properties to kill bacteria, incorporating it in silicone-based superhydrophobic coatings such as polymeric PMHS could reduce the bacterial adhesion (anti-biofouling) and improve the overall longevity of such coatings even after the loss of superhydrophobicity. Surprisingly, fabrication of superhydrophobic Ag-PMHS nano-composite coatings with inherent antibacterial and anti-biofouling properties is yet to be reported in the literature.

The objective of this study is to fabricate a novel coating of Ag-PMHS nanocomposites on anodized Al via the sol–gel process for antibacterial and anti-biofouling applications. We hypothesize that the in-situ synthesis of Ag-NPs within a PMHS polymeric matrix, anchored within an anodized Al oxide (AAO) substrate, could enhance the adhesion, durability, and stability of superhydrophobic Ag-PMHS nanocomposites. PMHS not only serves as a reducing agent, but also a morphological controlling agent for holding and presumably triggering controllable Ag$^+$ release. The excellent antibacterial and antibiofouling properties, owing to the inherent superhydrophobicity of the Ag-PMHS nanocomposite coating on anodized Al, are demonstrated.

4.3   Experimental section

Synthesis of Ag–PMHS nanocomposite. Ethanoic polymethylhydrosiloxane (PMHS) ($\geq$ 97%, VWR) stock solution was sonicated (Branson® Ultrasonic Bath, 230 Vac, 50 Hz) for 15 min for dispersion. Subsequently, 0.08 M PMHS was added to mineral spirit while stirring using a magnetic Teflon stirrer rotating at 500 rpm at 55 °C for 30 min. Next, Ammonium hydroxide 11.2 M (28 – 30 wt.% of NH_3, -VWR) was added dropwise to the suspension to achieve a pH of 11. The sol–gel reaction was allowed to age briefly for 30 min. Subsequently, 0.08 M $AgNO_3$ (VWR) solution was added dropwise to the above suspension according to the Ag^+/Si–H molar ratio (Table 4. 1). The as-synthesized product was stirred vigorously using a magnetic Teflon stirrer rotating at 700 rpm at 55 °C for an additional 15 min.

Table 4-1 Ag-PMHS molar ratio.

Samples	Ag^+/Si-H molar ratio	Volume of Mineral Spirit (mL)
1	50:1	15
2	50: 2	15
3	50:30	15
4	50: 40	15
5	50:50	15
6	2: 50	15
7	1 :50	15

Fabrication of Ag-PMHS nanocomposite coating on AAO substrates. The as-synthesized Ag-PMHS nanocomposite was loaded with premium room-temperature vulcanized (RTV) adhesive silicone. The RTV silicone (0.0 % (w/v), 0.4 % (w/v), 2.0 % (w/v), 4.0 % (w/v), 6.0 % (w/v), and 8.0 % (w/v))-loaded Ag-PMHS nanocomposite was sonicated to obtain a homogeneous dispersion. The Ag-PMHS polymeric solution above was coated on an AAO substrate through a 5-min dip coating deposition process, followed by room-temperature drying for 24 h. The anodization process was performed as follows: A $1'' \times 2''$ Al (AA6061) was ultrasonically degreased in a soapy solution and cleaned in deionized water, followed by 1 M NaOH (VWR) chemical etching at 55 °C to remove a superficial oxide layer. Then the etched substrate was further sonicated in distilled water. Afterward, etched Al substrate was subsequently immersed in HNO_3 solution (10 wt.%, VWR) for desmutting, followed by rinsing in distilled water. Next, both etched-and as-received Al substrates were used as anode and cathode, respectively. The electrochemical cell was equipped with a 600 W direct current power supply (Ametek Sorensen DCS 100-12E, Chicoutimi, QC, Canada), a quartz-jacketed beaker with cold circulating water (5 °C), and a small magnetic Teflon stirrer, rotating at 2000 rpm. Anodization was performed in the galvanostatic mode at a current density of 40 mA/cm^2 and electrolyte concentration of (H_2SO_4 -15 wt.%, -VWR), with varying times of 30, 60, and 120 min. During anodization, the two electrodes were separated in parallel by 1.5 cm. For quality control and reproducibility, each experiment was triplicated.

Sample characterization. The surface morphology and elemental analysis of the Ag-PMHS nanocomposite were performed using scanning electron microscopy (SEM, JEOL JSM-6480 LV), equipped with energy dispersive X-ray spectroscopy (EDS). The crystalline structure and chemical composition of the synthesized Ag-PMHS nanocomposite were analyzed with X-ray

powder diffraction (XRD) (a Bruker D8 Discover system) and attenuated total reflection-Fourier transform infrared (ATR-FTIR, Agilent Technologies Cary 630 FTIR), respectively. Static CA was measured with a First Ten Angstorm CA goniometer using 10 μL of deionized water drops. The roughness of the Ag-PMHS nanocomposite coating on anodized Al was measured using a MicroXAM-100 HR 3D surface profilometer.

Antibacterial susceptibility assay. The model bacterial strain, i.e., S.A (ATCC 6538), P.A (ATCC 9027), and *E-coli* (ATCC 8739-Hardy Diagnostics) were grown overnight from a frozen (-80 °C) stock in tryptic soy broth (TSB-Hardy Diagnostics) at 37 °C, re-inoculated in fresh TSB (37 °C), and grown to 10^8 colony forming units (CFU)/mL, as determined by their optical density at 625 nm and verified by both replicate plating on nutrient agar [25] and the 0.5 McFarland standard. An antibacterial assay was studied using the Kirby Bauer disk diffusion assay on S.A (gram +ve), P.A. (gram -ve), and *E-Coli* (gram -ve) [26]. Briefly, bacteria were inoculated in physiological saline (0.85% wt NaCl-Sigma–Aldrich). Sterile swab was used to inoculate isolates over the agar surface, followed by streaking to obtain a bacterial lawn. Next, 5 μL of Ag-PMHS nanocomposite was carefully seeded onto a 6 mm agar disk. Finally, the plates were aerobically incubated at 37 °C for 24 h in an incubator. Subsequently, the results were analyzed by measuring the ZOI. Three independent experiments were triplicated.

Anti-biofouling and biofilm inhibition assay. Bacterial strain was grown overnight to obtain 10^8 CFU/mL. Anti-biofouling experiment was conducted using a protocol described elsewhere [23] with minor modifications. Briefly, two staining jars were filled with 99 mL physiological saline (0.85% wt NaCl) and 1 mL bacterial culture. Subsequently, both 2.54 cm × 2.54 cm anodized Al (Al/AAO, used as control) and superhydrophobic AAO/Al sample (04Sil-AgP-NcAAO), were placed in two separate jars. The staining jars were incubated for 3 h at 37 °C.

The substrates were subsequently removed and gently immersed in physiological saline to rinse non-adherent bacteria. Next, the substrates were transferred into a set of 80 mL sterile beakers containing physiological saline and sonicated on ice for 10 min to remove adherent bacteria. Finally, the bacterial suspensions were serially diluted and then plated on tryptic soy agar, followed by an aerobic incubation at 37 °C for 24 h. Positive controls were performed for t = 0 and t = 3 h to ascertain the bacterial viability. Three independent experiments were performed in triplicate to determine the number of adherent bacteria. Relative bacterial adhesion reduction was calculated using the following formula: Relative bacterial adhesion reduction = [(A-B)/A×100 %], where A = CFU/cm^2 of adherent bacteria on anodized Al (AAO/Al) and B = CFU/cm^2 of adherent bacteria on superhydrophobic AAO/Al sample (04Sil-AgP-NcAAO). Biofilm inhibition study was also performed on *E-coli* bacterium for 48 h to evaluate the ability of superhydrophobic AAO/Al sample (04Sil-AgP-NcAAO) at inhibiting *E-coli* bacterium colonization. Test culture was diluted with physiological saline (0.85% wt. NaCl) (Sigma–Aldrich) to achieve a bacterial inoculum concentration of 1.0×10^7 colony-forming units/millilitre (CFU) mL$^{-1.}$ Next, 22.5 mL tryptic soy broth was added to 2.5 mL bacterial inoculum in separate sterile petri dishes. Both the test sample (04Sil-AgP-NcAAO) and the control sample (AAO/Al) were then immersed in these petri dishes, followed by 48 h incubation for biofilm growth. Subsequently, samples were rinsed with the physiological saline, followed by air-drying in airflow Class II cabinet at ambient conditions of 25 °C and (50 ± 10 %) relative humidity (RH) for 1 h. Samples were finally metalized with gold coating and imaged in a high vacuum SEM. Data were analyzed by a one-way analysis of variance (ANOVA) with the Tukey–Kramer multiple comparison test. Results were considered significant at p < 0.05.

4.4   Results and discussion

Synthesis of Ag–PMHS nanocomposites. PMHS is a linear organofunctional polysiloxane, in which the active moiety, (Si–H) reacts with metallic salts to form the corresponding metallic particles owing to the strong reducing ability of the PMHS [19]. In particular, when silver salts such as $AgNO_3$ react with the PMHS, the Si–H bond is oxidized into Si–O–Si species with H_2 gas evolution and hydridic hydrogen replaced by Ag-NPs [20] as seen in Equation. 4.1.

$$nAg^+ + \begin{array}{c} H_3C \\ | \\ -Si \\ | \\ H \end{array} \begin{bmatrix} O - \begin{array}{c} CH_3 \\ | \\ Si \\ | \\ H \end{array} \end{bmatrix}_n \xrightarrow[55°\,C]{NH_4OH} \begin{array}{c} H_3C \\ | \\ -Si \\ | \\ Ag \end{array} \begin{bmatrix} O - \begin{array}{c} CH_3 \\ | \\ Si \\ | \\ Ag \end{array} \end{bmatrix}_n + nH_2 \uparrow \qquad (4.1)$$
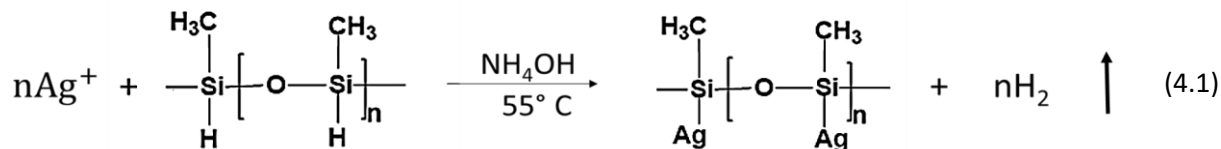
The polymeric PMHS matrix is an ideal template for in-situ Ag-NPs synthesis, similar to the typical host–guest redox reaction [19]. It is noteworthy that such a host–guest structure might exhibit interesting antibacterial properties, in which PMHS acts as a polymeric matrix for holding and presumably triggering controllable Ag^+ release for killing or inhibiting bacterial growth.

To ascertain the amount of Ag^+ ions required to react with the active Si–H moiety, the Ag^+/Si–H molar ratio was varied from 1:50 to 50:1 (Table 4.1). Figure 4.1 shows the ATR-FTIR spectra of PMHS before and after reaction with $AgNO_3$ for different molar ratios of Ag^+/Si–H. Figure 4.1 (III) shows the ATR-FTIR spectrum of liquid PMHS. The single peak at 2939 cm^{-1} at the high-frequency region can be assigned to the asymmetric stretching mode of −CH$_3$ groups in the PMHS molecule [27]. At the lower frequency region, the two peaks at 1270 and 764 cm^{-1} correspond to Si−CH$_3$ groups [28]. Similarly, the peak at 1100 cm^{-1} can be linked to the

asymmetrical stretching vibration of the Si−O−Si mode [29], while that around 800 cm^{-1} can be attributed to the symmetric bending mode of the Si–O–Si bonds [30]. The peak at 2162 cm^{-1} at the mid-frequency region is assigned to the Si−H stretching mode. Notably, at a lower molar ratio of Ag$^+$/Si–H, such as 2:50 (Figure 4.1.(II)), the intensity of the Si–H group marginally decreases by ~10 % compared with the as-received PMHS, suggesting that less amount of Si−H species are consumed. However, at higher molar ratios of Ag$^+$/Si–H such as 50:2, the Si−H group is no longer observed (Figure 4.1 (I)), signifying that all the Si−H species are consumed. A similar observation was made by Omer D. et al. [20], however, their Si–H peak intensity at a higher Ag$^+$/Si-H molar ratio (1:1) decreased by 90 % compared with ours of 100 %, owing to the total consumption of the Si–H species in our case. Our high Ag$^+$/Si–H molar ratio was necessary due to the intended antibacterial application.
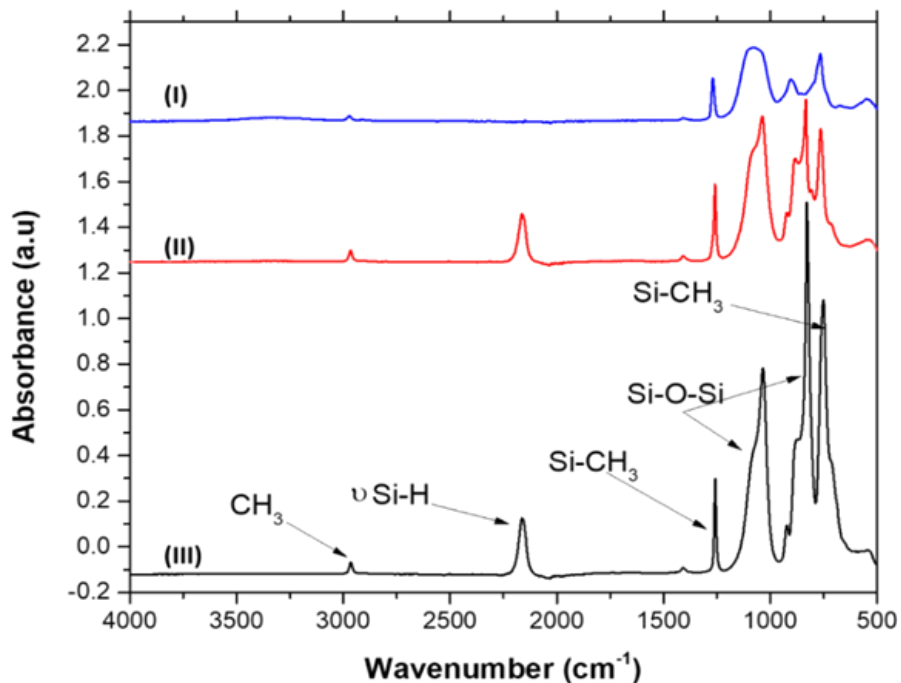
Figure 4-1. ATR-FTIR spectra of PMHS before and after reaction with AgNO$_3$ at different mole ratios: (I) (Ag+/Si–H of 50:2); (II) (Ag+/Si–H of 2:50); and (III) liquid PMHS. © Henry Agbe, 2021.

In addition to Ag, other metal nanoparticles, such as those of Au, Pt, Ta, and Nb can be synthesized by PMHS [31]. In fact, the active Si–H moiety arranged periodically on the siloxane backbone in the PMHS matrix, provides intrinsic sites to synthesize and integrate these metal nanoclusters [20]. Ag-PMHS nanocomposites exhibit a surface plasmonic resonance phenomenon, which is like other chemical reduction syntheses of Ag-NPs. This surface plasmon resonance is due to the collective oscillation of conducting electrons of Ag-NPs, characteristically observed by a color change in Ag-PMHS solutions. Notably, when $AgNO_3$ is added to the PMHS gel, a redox reaction begins immediately with a color change from colorless to yellow, orange, brown, and black (nucleation, nanoparticles, nanoclusters, and growth of controlled aggregates, respectively), as well as, the corresponding formation of different Ag species [20]. In fact, it has been reported that using NH_3 (aq) as a catalyst, $Si^{\delta+}$–$H^{\delta-}$ bonds are polarized via the intermediate formation of hyper coordinated silicon species to increase the sol–gel reaction rate [32]. At the gel point (achieved after 24 h), a viscous, stable, and elastic gel network was observed. Note that typical sol-gel process without NH_3 (aq) can last for ~1000 h [33]. In deed, the NH_3 (aq) does not only catalyze the hydrolysis process but also forms a complex ion with Ag^+ ($Ag (NH_3)_2^+$aq) to accelerate the reduction of Ag^+ ions by PMHS. This is similar to saccharides reduction of Ag^+ ions (in the presence of NH_3 (aq)) in a typical modified Tollens Ag synthesis [34, 35]. However, for the purpose of obtaining a thin Ag-PMHS nanocomposite coating on AAO/Al, the ageing process was limited to 30 min in our experiment.

Figure 4.2 (A) shows the energy dispersive X-ray spectroscopy (EDS) spectrum of elements in the Ag–PMHS nanocomposite (Ag+/Si–H of 50:2 mole ratio), which comprises C, O, and Si with their respective K_α peaks at 0.28, 0.52, and 1.73 keV respectively, and an L_α peak of Ag at 2.98 keV. Similarly, the XRD pattern is shown in Figure 4.2 (B). The XRD pattern matched

well with the JCPDS card (89-3722) standard data of Ag, characterized by a face-centered cubic crystalline silver, with corresponding prominent peaks for 2θ at 38.17°, 44.31°, and 64.44 °. Both the EDS and XRD spectra confirm the formation of Ag-NPs in the PMHS siloxane polymer.
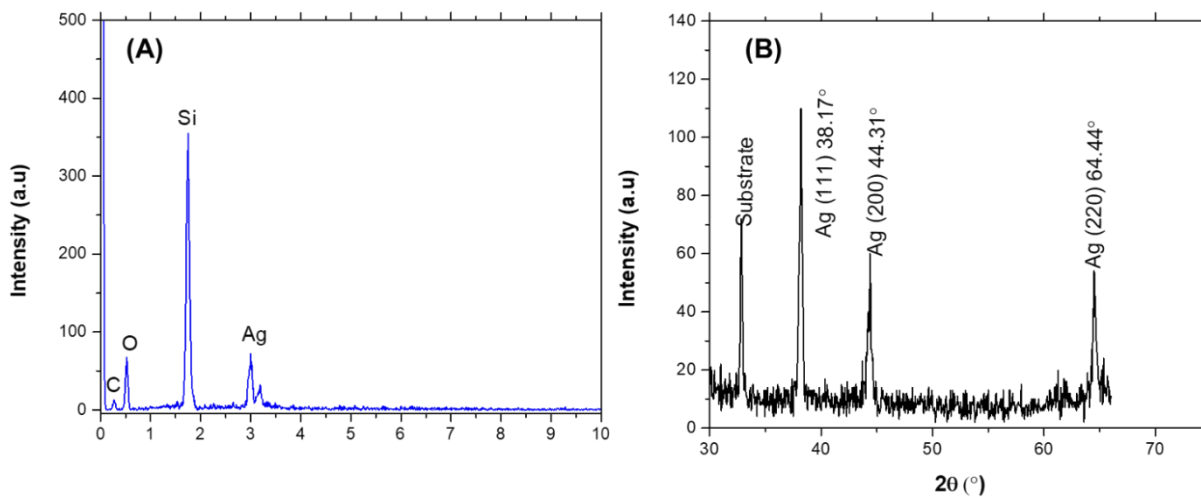
Figure 4-2. (A) EDS spectrum and (B) XRD pattern of as-synthesized Ag-PMHS nanocomposite having a Ag+/Si–H molar ratio of 50:2. © Henry Agbe, 2021.

Anodization. In the present study, anodization was performed to engineer an Al substrate to achieve a high surface topography for coating the Ag-PMHS nanocomposite. Anodization is ideal because it is technologically scalable and offers abrasion and corrosion resistance [36]. In a typical galvanostatic anodization process, potential increases linearly with anodization time [37]. The process begins with nucleation and the subsequent growth of porous structures (Figure 4.3 (A)). As oxide dissolution begins, porous structures are formed. Finally, a steady state of oxide dissolution and formation equilibrium is attained. Notably, for the 120 min sample, the potential increased linearly with time, and beyond the critical voltage (49 V) after 60 min of anodization

(Figure 4.3 (B)). This rise was due to the high resistance of the oxide barrier layer. Beyond the critical voltage, the potential decreased marginally (a decrease of ~4 V) with anodization time, until the rate of oxide dissolution was equivalent to the rate of porous oxide layer formation [38]. However, for both the 60 min and 30 min samples, incomplete anodization was observed. Hence, the 120 min anodized sample was selected for the remainder of the study.
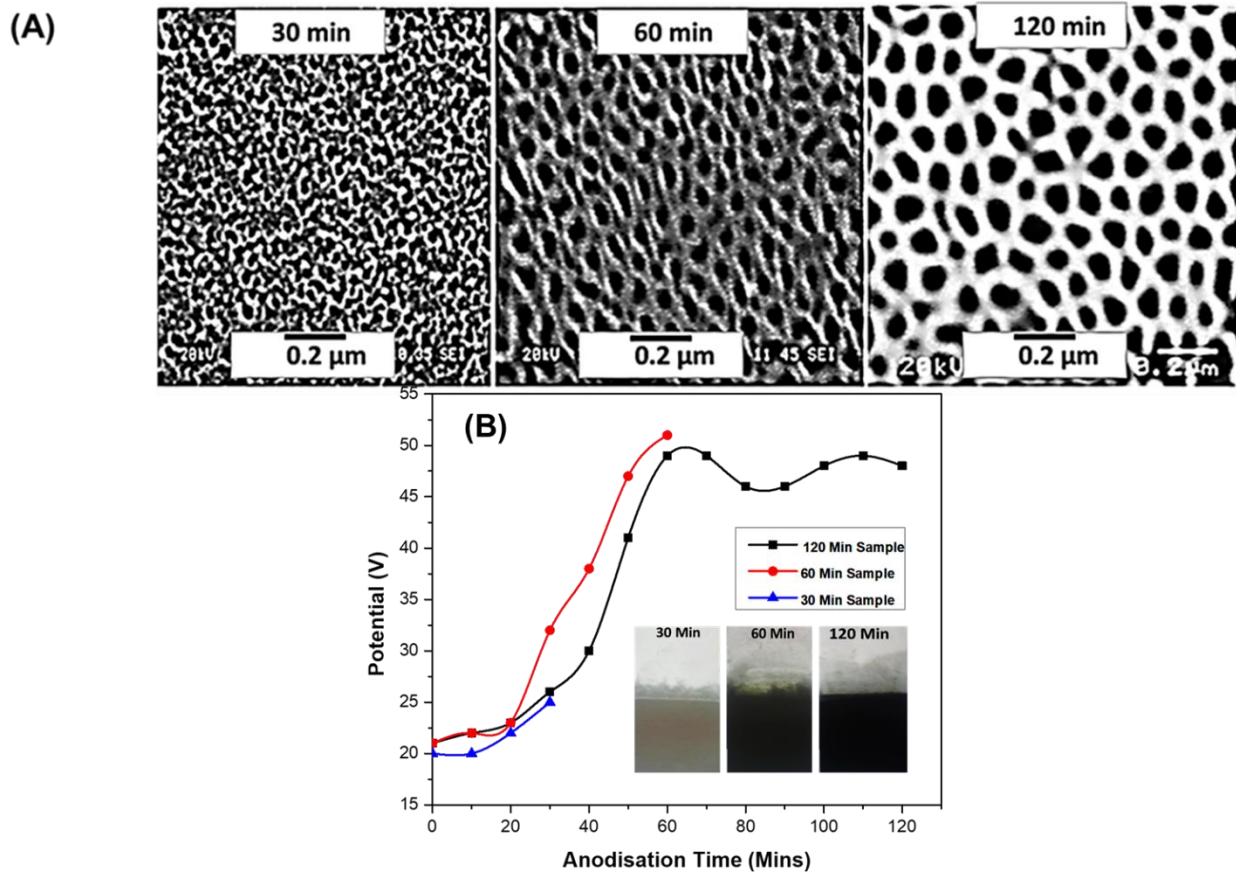
Figure 4-3. (A) SEM image of anodized aluminum oxide (AAO) after a 30 min anodization (left); 60 min (middle); and 120 min (right): (B) Kinetics of anodization process for the three samples above (where ■ 120 min; ● 60 min; and ▲ 30 min). Inset: Digital image of the three samples. © Henry Agbe, 2021.

To engineer a superhydrophobic Ag–PMHS nanocomposite coating on Al with inherent antibacterial property, the Ag–PMHS nanocomposite with a Ag^+/Si–H molar ratio of 50:2 was coated on the 120 min anodized Al (herein referred to as AgP–NcAAO) and used for the remainder of the study. Both the XRD (Figure 4.4 (A)) and EDS spectra (Figure 4.4 (B)) show that the chemical composition of the fabricated AgP–NcAAO sample comprises Al and O; and Ag, Si, and C; from Al_2O_3 (owing to anodization) and the Ag–PMHS nanocomposites, respectively. The broad peak at 10.0° is typical for amorphous SiO_2 [39], which arises from the reaction of PMHS with $AgNO_3$. Notably, the Al peaks ((111), (200), (220), and (311) from the underlying Al substrate), overlap with the Ag peaks ((111), (200), (220), and (311)). The overlapping of diffraction peaks of Al (111) and Ag (111) is due to their similar lattice parameters (Figure 4.4 (A), inset). The presence of sulfur in the EDS spectra of Figure 4.4 (B) can be ascribed to sulfuric acid from anodization. It is noteworthy that an optimal wt.% RTV silicone was used to improve the adhesive bonding of the AgP–NcAAO sample (herein referred to as 04Sil-AgP–NcAAO) (Figure 4.4 (B (III))).
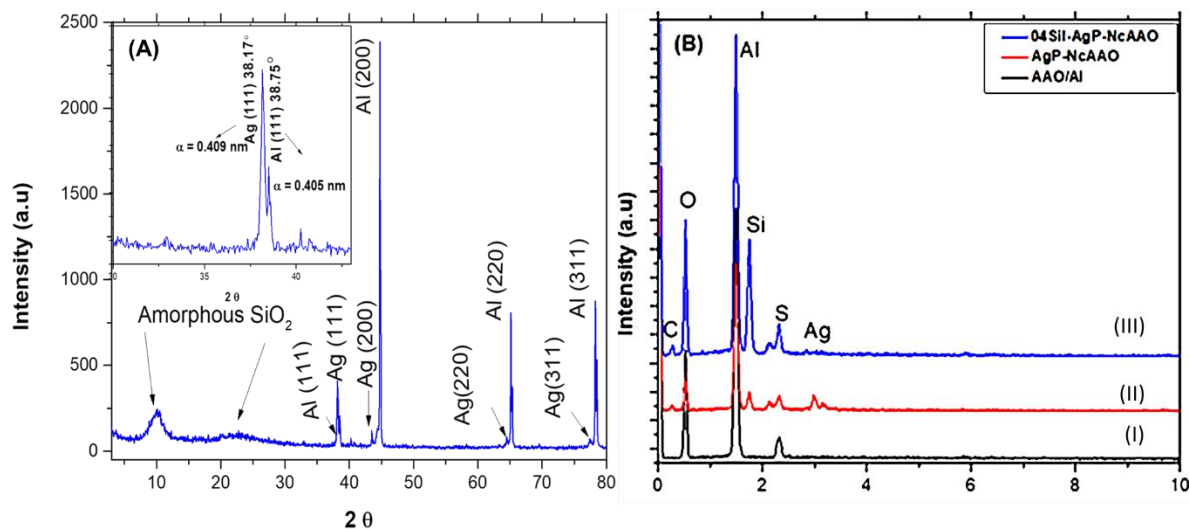
Figure 4-4. (A) XRD pattern of Ag–PMHS nanocomposite having a Ag+/Si–H molar ratio of 50:2.0 coated on AAO/Al (AgP–NcAAO); (B) EDS spectra of: (I) AAO/Al; (II) AgP-NcAAO; (III) 0.4% w/v silicone incorporated in AgP–NcAAO (04Sil-AgP–NcAAO). (Inset: high magnification of Ag and Al (111) planes with their lattice parameters). © Henry Agbe, 2021.

Superhydrophobic property. The two well-known conditions for fabricating superhydrophobic surfaces are the combined effects of low surface energy and geometrical surface structure [40]. In the present study, the desired topography was achieved through the combined effects of Al anodization and presence of silver nanoparticles (Ag-NPs), while low surface energy, by passivation with PMHS molecules. Though, two-step anodization process produces self-organised densely hexagonal AAO templates [41], the process is somehow complex and time consuming, hence we have deployed a one-step constant current hard anodization process to achieve desired surface topography. The surface roughness and CA of the as-received Al substrate were $0.4 \pm 0.02\,\mu m$ and $94 \pm 1.2°$, respectively. CA of $113 \pm 1.5°$ was observed for the Ag–PMHS nanocomposite coating on this surface (as shown in supplementary information, Table S 4.13). Table 4.2 and Figure 4.5 provide information regarding the surface roughness and SEM

micrograph. After a 120 min anodization, uniformly distributed nanopores of average pore diameter and cell diameter 60 ± 11 nm and 121 ± 19 nm, respectively, were observed (Table 4.3). The surface roughness and CA of 9.1 ± 0.9 µm and $8 \pm 0.2°$, respectively, were obtained for 120 min AAO (Figure 4.5 B). This shows that anodization affected the superhydrophilic property on the Al alloy surface. According to the Wenzel model [42], this is due to the increase wettability of the anodized surface. By contrast, the surface roughness of 9.7 ± 1.0 µm and CA of $159 \pm 1.2°$ were achieved for the Ag–PMHS nanocomposite coating on the 120 min AAO sample (AgP–NcAAO) (Figure 4.5 C). The combined effects of the low surface energy PMHS and the empty space by micro-nanostructures, induced by both Ag-cluster and AAO lead to superhydrophobicity that can be explain by Cassie-Baxter model [43]. The change in surface wettability from superhydrophilic to superhydrophobic can be attributed to both the nano-micro surface roughness (induced by both Ag-NPs and anodization) and the presence of low surface-energy organosilicon (long $Si–CH_3$ chain). The presence of Ag-NPs, presumably increase the nano-micro roughness of the Ag-PMHS nanocomposite. We have observed a linear relationship between the CA of the coatings on AAO and Ag:PMHS molar ratio (supplementary information can be found in Table S4-4, describing contact angle measurements of Ag-PMHS nanocomposites at different molar ratio on Al substrates). However, in the absence of Ag-NPs, a lower CA of $123 \pm 3.1°$ was obtained for PMHS coated on AAO. Indeed, we have shown in our previous contribution that a high water CA (~152°) could only be achieved after appropriate combination of PMHS molecule and nano-micro roughness, induced by colloidal TiO_2 NPs [28]. To improve the adhesive property of the AgP–NcAAO sample, RTV-silicone, a well-known adhesive and hydrophobic silicone copolymer with water CA < 120° [44], was loaded into the Ag–PMHS nanocomposites. Consequently, the CA increased to above 150° (Figure 4.5 D).

Table 4-2. The surface topography of samples

Samples	Surface Roughness (rms) /μm
As-received Al Alloy	0.4 ± 0.02
120 min AAO	9.1 ± 0.9
AgP-NcAAO	9.7 ± 1.0
04Sil-AgP-NcAAO	8.9 ± 2.0

Table 4-3 Morphological features of anodized samples at varied anodization time

.

Samples	Pore Diameter: D_p (nm)	Cell Diameter: D_c (nm)	Wall Thickness: W (nm)	Oxide Thickness (μm)	Pore Density: n (Pore/cm^2)	Porosity: α (%)
120 min	60 ± 11	121 ± 19	31 ± 4	75 ± 2.0	7.9×10^9	22
60 min	39 ± 18	90 ± 20	26 ± 2	56 ± 1.0	1.4×10^{10}	39
30 min	26 ± 6	59 ± 14	17 ± 4	36 ± 0.7	3.3×10^{10}	40
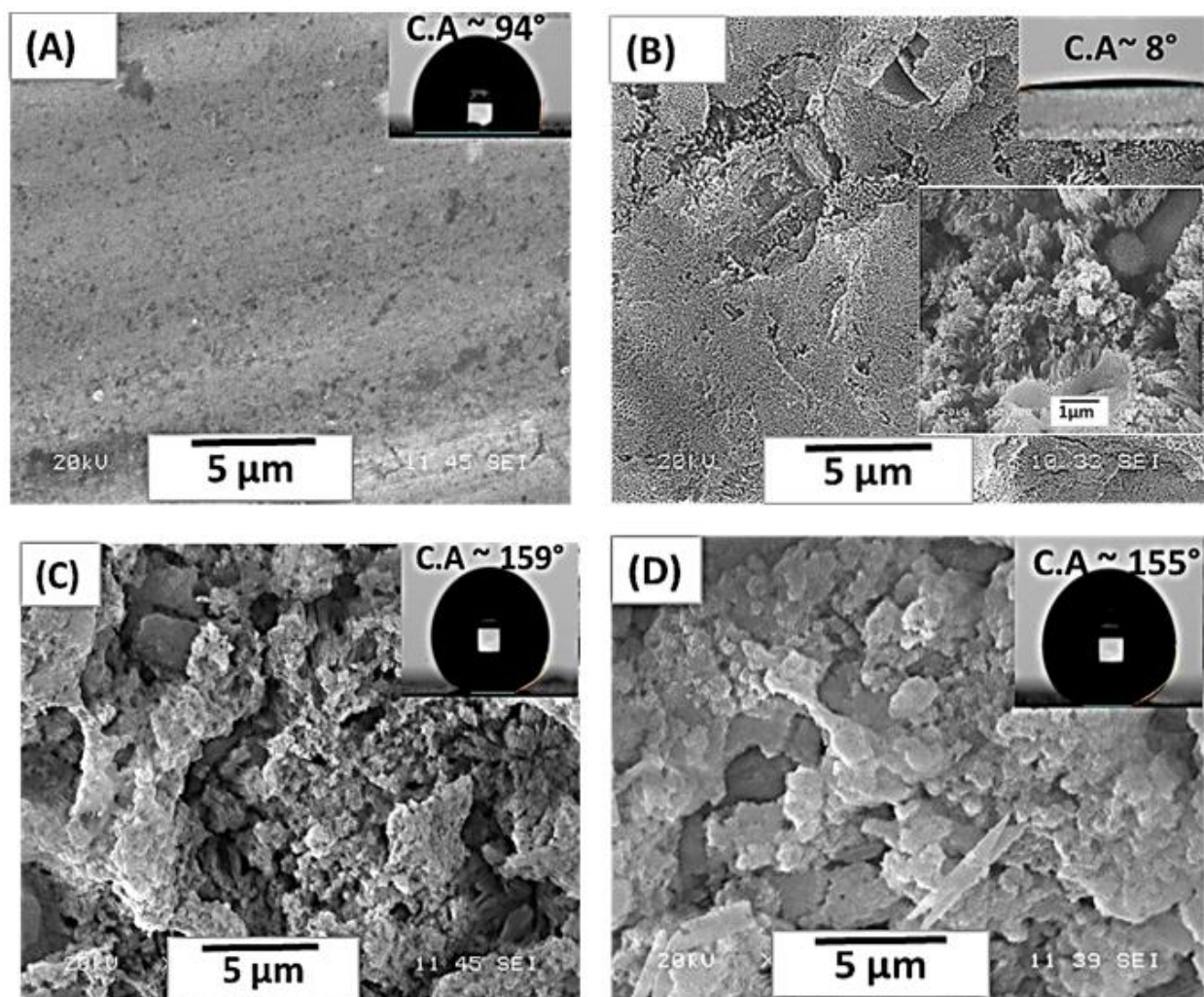
Figure 4-5. SEM images of (A) as-received Al; (B) AAO/Al; (C) Ag–PMHS nanocomposite having a Ag+/Si-H molar ratio of 50:2 coated on AAO/Al (AgP–NcAAO); (D) 0.4 % w/v silicone incorporated in AgP–NcAAO (04Sil-AgP–NcAAO); The insets show 5 μL water drops deposited on the surface along with 1 and 5 μm scale bars. © Henry Agbe, 2021.

In particular, we observed that after silicone loading, the Water contact angle (WCA) increased from 8 ± 0.2° for 120 min AAO, to 155 ± 0.4 ° for 04Sil-AgP–NcAAO. Interestingly, increasing the silicone wt.% resulted in an 8° decrease in CA (Figure. 4.6). This trend is similar to our previous observation when silicone wt.% was deposited on etched Al [45]. The decrease in CA

following the continuous silicone loading can be attributed to the filling-in of the AAO micro- and nanostructures, which results in the smoothening the rough surface. However, the AgP–NcAAO sample resulted in a higher surface roughness of 9.7 ± 1.0 µm and CA of $159 \pm 0.5°$, compared with surface roughness of 8.9 ± 2.0 µm and CA of $155 \pm 0.4°$, for the 04Sil-AgP–NcAAO sample. It must be re-emphasized that the high CA value for the AgP–NcAAO, relative to 04Sil-AgP–NcAAO, is attributed to the partial filling of the entrapped air in the micro–nanoporous structures by RTV-silicone, in accordance with the Cassie–Baxter model [43].
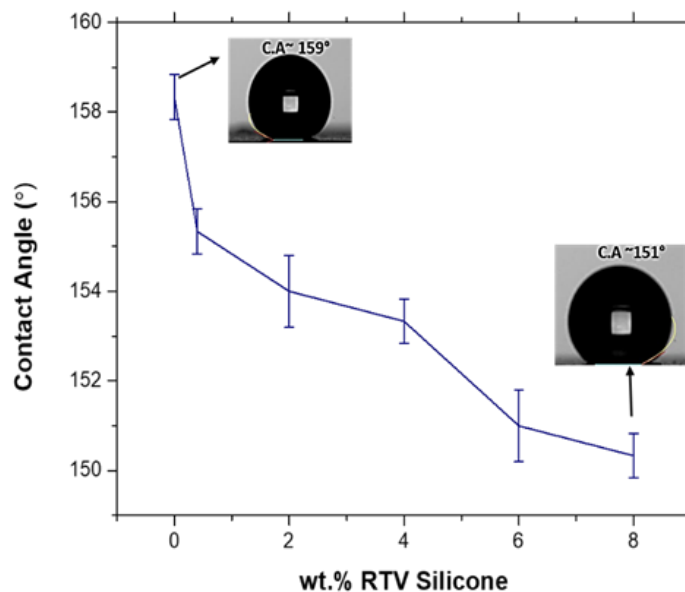
Figure 4-6. Water contact angle on the surface of Ag–PMHS nanocomposites having a Ag+/Si–H molar ratio of 50:2 as a function of wt.% of incorporated silicone. © Henry Agbe, 2021.

According to the Cassie–Baxter model, a rough surface would repel liquid droplets owing to the entrapped air in the nano- and/or microstructural features [43]. The anodization of Al, results

in the formation of porous nano- and/or microstructural Al_2O_3 features. The OH group in Al_2O_3 can form a strong monodentate or bidentate bonding with the Si–O–Si group of Ag–PMHS. In particular, the silanol molecule replaces the OH group, resulting in the formation of water molecules and a strong a SiO−Al monodentate bonding on the Al_2O_3 surface [46]. Such a strong chemical bonding, coupled with AAO's ability to mechanically anchor PMHS, can increase the adhesion bonding of PMHS coatings.

Note that 0.4% (w/v) silicone was deemed optimal for adhesive bonding studies. A test was performed using the American Standard Test Method (ASTM D-3359) on four samples (Figure 4.7 and supplementary information, Table S4-5 A-D, show grade of adhesive bonding on tested samples). The Ag–PMHS nanocomposite coating on the as- received Al, exhibited the lowest grade of 0B, while the Ag–PMHS nanocomposite coating on AAO exhibited grades between 4B and 5B. Interestingly, after 90 days of saline immersion, the Ag–PMHS nanocomposite coating on AAO was still resistant to scratch and exhibited a WCA > 150° (supplementary information can be found in Figure S 4.14 and Table S 4.5D, showing grade of adhesive bonding of Ag–PMHS nanocomposite coating on AAO after 90 days of saline immersion). According to ASTM D-3359, coatings with 5B grade exhibit the highest adhesion bonding, whereas those with grade 0B exhibit the lowest adhesion [47]. Notably, anodization provides an optimal surface topography that affords high abrasive resistance to Ag–PMHS nanocomposite coating. The high adhesive bonding observed can be attributed to both chemical and physical phenomena. Chemically, the RTV-silicone increases the monodentate bonding of the Si–O–Si group and the Al_2O_3. This is confirmed by the increased intensity of siloxane groups in the FTIR peaks of the 04Sil-AgP–NcAAO (as shown in supplementary information, figure S 4.13 (I)). Physically, anodization provides additional support for anchoring the Ag–PMHS nanocomposite coating. In fact, the 04Sil-AgP–

NcAAO sample maintains the superhydrophobic property (More details can be found in Video S 4.1, as a movie demonstration of water roll-off property of the superhydrophobic surface) albeit with a 4° decrease in CA with increased adhesion bonding; therefore, it is ideal for practical applications.
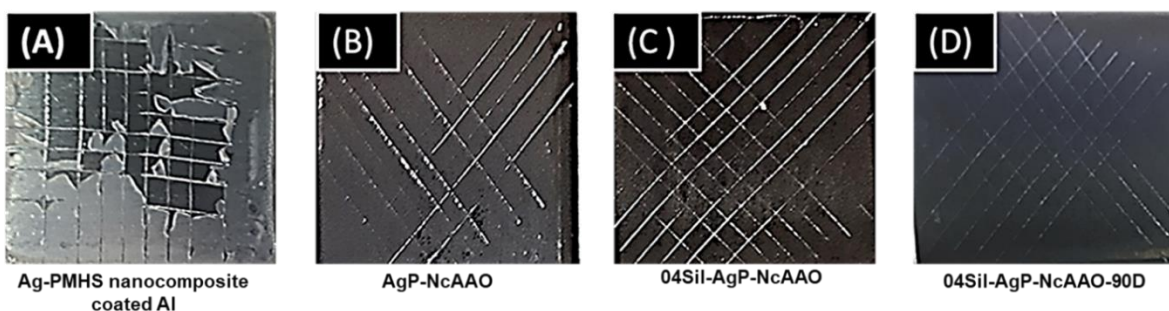
Figure 4-7. Digital images of scratch test based on American Standard Test Method (ASTM D 3359-02) showing the adhesion of Ag–PMHS nanocomposite coatings having a Ag+/Si–H molar ratio of 50:2 on: (A) as-received Al; (B) AAO/Al (AgP-NcAAO); (C) 0.4 % w/v silicone incorporated in AgP–NcAAO (04Sil-AgP–NcAAO); and (D) 04Sil-AgP–NcAAO in 90 days of immersion (04Sil-AgP–NcAAO-90D). © Henry Agbe, 2021.

Furthermore, Ag–PMHS nanocomposite coating on anodized aluminum subjected to UV accelerated weathering test, revealed that WCA was still $> 150°$ after 35 days of UV irradiation (Figure S 4.15), signifying that superhydrophobic AAO/Al sample (04Sil-AgP-NcAAO) was not only mechanically stable but chemically durable and ideal for practical application.

Because the chemical nature of the Ag-NPs' surface is crucial for Ag^+ release kinetics, a representative portion of the superhydrophobic AAO/Al sample (04Sil-AgP-NcAAO) was examined through EDS analysis for elemental mapping. Among three different locations of the elemental mapping, Figure 4.8 (A) shows the SEM micrograph of the representative sites, while

Figures 4.8 (B, C, and D) show the elemental mapping of Ag, Al, and Si, respectively. Dispersed Ag is distributed on the entire area, as shown in Figure 4.8 (B). However, clusters of Ag are visible, as marked in the same figure. Conversely, Al surrounds Ag (dark region) in the Al mapping, as shown in Figure 4.8 (C). Figure 4.8 (D) shows that Si, from the PMHS molecules, is distributed uniformly across the entire sample. Therefore, the elemental mapping demonstrates that elemental Ag is distributed over the entire range of the randomly selected area.
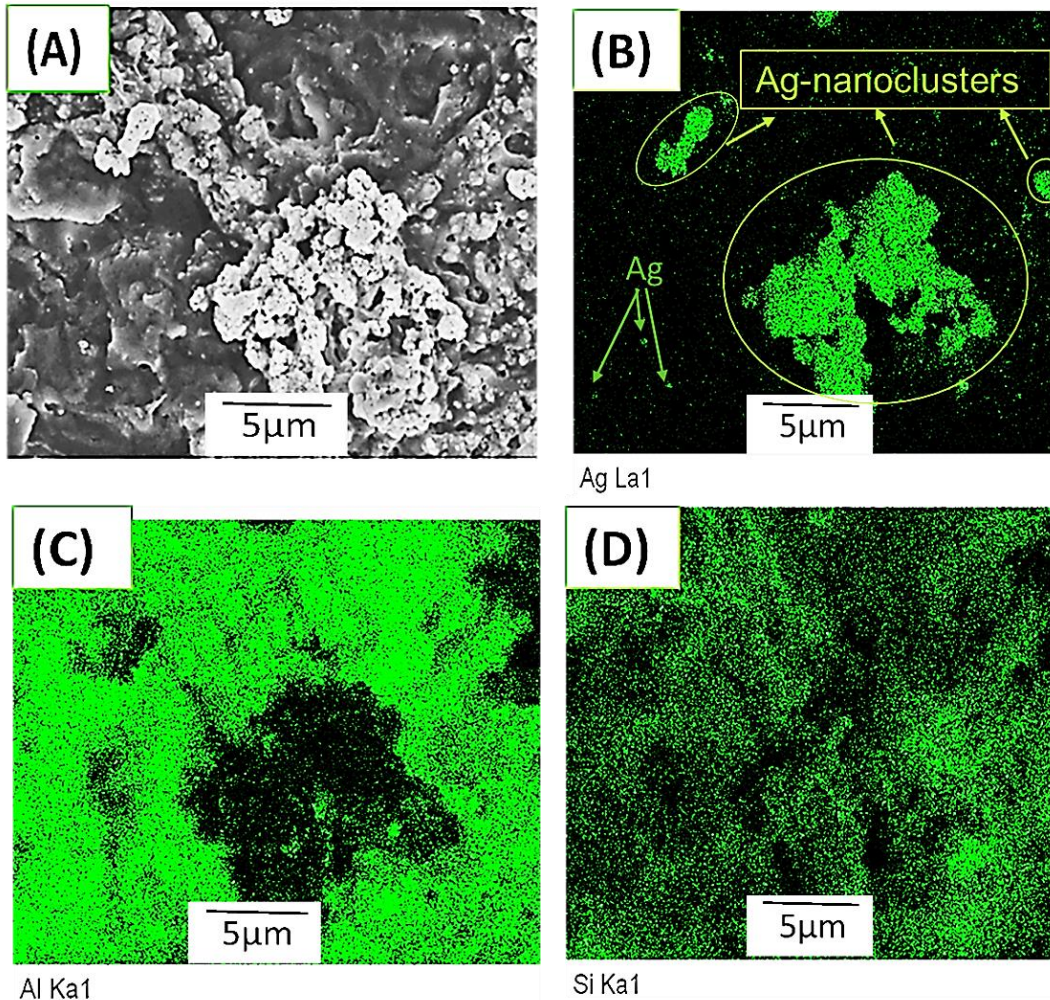
Figure 4-8. EDS mapping of 0.4% w/v silicone incorporated in Ag–PMHS nanocomposites having a Ag+/Si–H molar ratio of 50:2 coated on AAO/Al(04Sil-AgP-NcAAO); (A) SEM image (B) Silver; (C) Al; and (D) Silicon. © Henry Agbe, 2021.

Bacterial susceptibility study. Antibacterial study was performed using two methods. First, antibacterial activity of the Ag–PMHS nanocomposites by the Kirby Bauer disk diffusion assay; second, anti-biofouling study. As model microbes, *S.Aureus*, *P.Aeruginosa*, and *E-coli* were used. It is noteworthy that these bacteria are among the 12 families of the most dangerous

antibiotic-resistant bacteria or "superbugs," of clinical significance [48]. The Kirby Bauer assay utilizes the ZOI to describe regions around the antimicrobial agent, where bacteria colony or growth is inhibited owing to the former's ability to diffuse. Figure 4.9 shows the results of the disk diffusion assay.
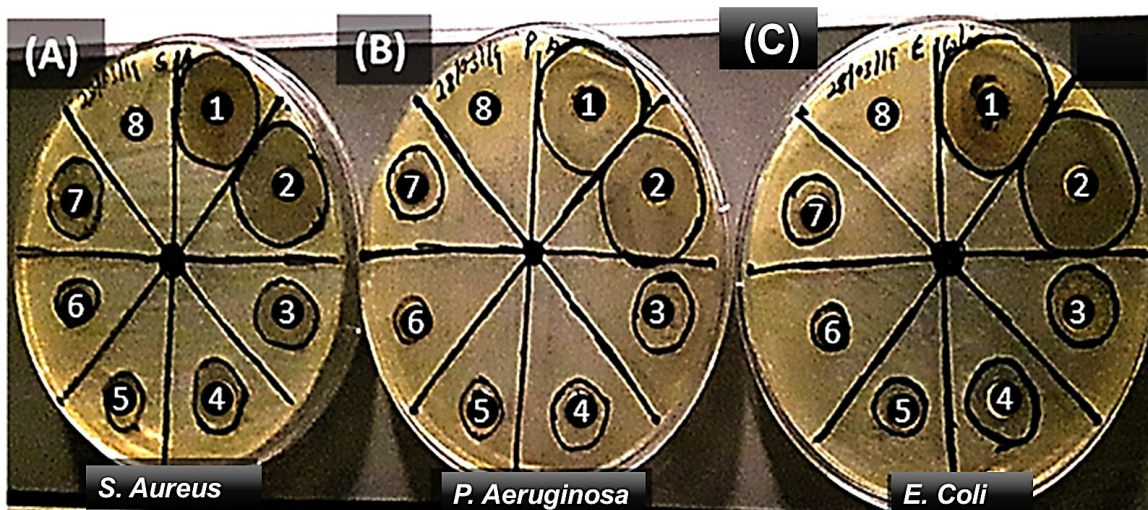
Figure 4-9. Antibacterial activity of Ag–PMHS nanocomposites against: (A) *S.Aureus*; (B) *P.Aeruginosa*; and (C) *E-coli*. Region 1 (Ag+/Si–H of 50:1); region 2 (Ag+/Si–H of 50:2); region 3 (Ag+/Si–H o of 50:30); region 4 (Ag+/Si–H of 50: 40); region 5 (Ag+/Si–H of 50:50); region 6 (Ag+/Si–H of 2:50); region 7 (Ag+/Si–H of 1:50); region 8 represents the Control (mineral spirit + PMHS) (Disk diffusion assay, represents three independent experiments. © Henry Agbe, 2021.

Notably, the Ag^+/Si–H molar ratio of 50:2 was the most effective, followed by 50:1, and the least being 2:50. The relatively high ZOI value for the Ag^+/Si-H molar ratio (1:50), may be due to the antibacterial and anti-biofouling synergistic effect. The mean and standard deviation values of the ZOI for *S.Aureus*, *P.Aeruginosa*, and *E-coli* are 23.3 ± 3.6, 25.3 ± 0.5, and 24.8 ± 0.5

144

mm, respectively. These ZOI values are well within the acceptable range (8–30 mm) for standard antibiotics against *S.Aureus*, *P.Aeruginosa*, and *E-coli*, per the Clinical and Laboratory Standards Institute standards [49]. This shows that the Ag–PMHS nanocomposite at a higher $Ag^+/Si–H$ molar ratio such as 50:2, is an effective antibacterial agent, particularly for gram negative bacteria compared with the gram-positive bacterium *S.Aureus*. However, at a lower $Ag^+/Si–H$ molar ratio such as 2:50, the Ag–PMHS nanocomposite was less effective at inhibiting all the bacteria, with ZOI values of 9.0 ± 0.8, 8.5 ± 0.6, and 6.8 ± 0.5 mm for *S.Aureus* (gram +ve), *P.Aeruginosa*, (gram - ve), and *E-coli* (gram -ve), respectively (Figure 4.10). This can be explained by the fact that as Ag-NPs are locked up at the Si–H reducing sites (Equation. 4.1), less Ag^+ ions effectively leach out to interact with bacteria to induce their lethal effects. Contrarily, at higher molar ratios of $Ag^+/Si–H$ such as 50:2, excess amounts of Ag-NPs are available to leach out a high amount of Ag^+ ions to induce an increased antibacterial effect. The difference in bioactivity between the two classes of bacteria (gram-ve and gram+ve) may be ascribed to the difference in their cell wall composition and structure. Gram (+ve) bacteria have a thicker peptidoglycan layer (30-100 nm) composed of short peptides along with a linear polysaccharide chain cross-linking network. This rigid structure inhibits the penetration of Ag-NPs. By contrast, gram (-ve) bacteria have a relatively thinner peptidoglycan layer (2-10nm), overlaid with an outer lipid cell membrane.

Although the antibacterial mechanism of Ag-NPs is still a scientific debate, the generally held view is that, upon bacterial/Ag-NPs contact, Ag-NPs are oxidized into Ag^+ by respiratory enzymes [50]. It is the released Ag^+ ions that cause the biocidal effect [50]. The Ag^+ ion is electrostatically attracted to the negatively charged cell wall. In particular, the Ag^+ ion binds with the purine and pyrimidine base pairs, rapturing the H-bonds in the base pairs, which results in denaturing and Deoxyribonucleic acid (DNA) disruption [50]. Such Ag^+ ion-cell membrane

interactions prevent DNA replications [51] and subsequently lead to bacterial death [52]. Additionally, Ag-NPs can induce toxicity via reactive-oxygen-species (ROS) -mediated free radical release, which leads to oxidative stresses and possible bacterial death. Therefore, the PMHS molecule may offer a polymeric matrix for holding and presumably triggering controllable Ag^+ release to kill microorganisms via the oligo dynamic effect. It should be noted that Ag^+ ion of concentrations, 1-10 ppm (commonly measured by Inductively coupled plasma mass spectrometry (ICP-MS)) are known to impact antibacterial property without adverse effect on mammalian cell [53-55]. However, Ag^+ release kinetics and cytotoxic impact studies, for example on fibroblasts cell lines, are beyond the scope of this thesis and therefore not reported here.
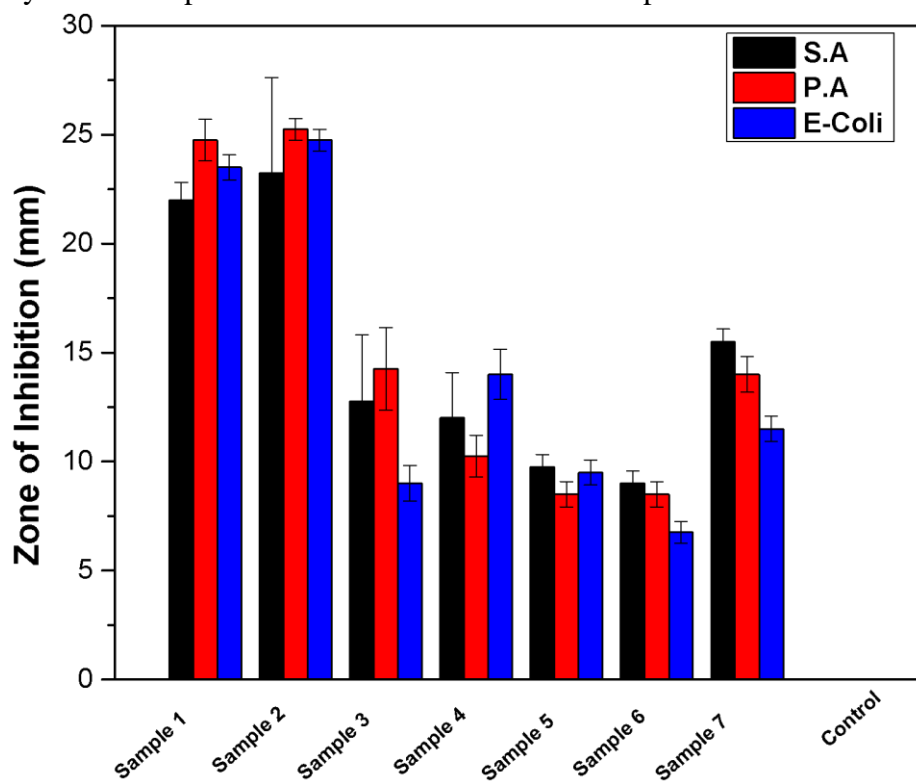
Figure 4-10. Graphical representation of zone of inhibition of Ag–PMHS nanocomposite against model bacteria. Sample 1 (Ag+/Si–H of 50:1); sample 2 (Ag+/Si–H of 50:2); sample 3 (Ag+/Si–H of 50:30); sample 4 (Ag+/Si–H of 50:40); sample 5 (Ag+/Si–H of 50:50); sample 6 (Ag^+/Si–H of 2:50); sample 7 (Ag^+/Si–H of 1:50); control (mineral spirit + PMHS). (Error bars represent SD (standard deviations), and data are from three independent experiments). © Henry Agbe, 2021.

146

Anti-biofouling and biofilm inhibition assay: Bacterial adhesion reduction was performed by two methods. First, by anti-biofouling study; and second, by biofilm inhibition study. Note that limited incubation time was used for the anti-biofouling study. It appears water repellency of most of the superhydrophobic surfaces are lost over time, due to fragility of the surface micro/nano structures and fast surface chemistry degradation [56]. For example, the water roll-off property of a bioresin-based superhydrophobic coating was lost within 6-24 h, leading to colonization by *S.Aureus*, *P.Aeruginosa*, and *E-coli* bacteria. Similarly, gram (+ve) *S.Aureus* cells completely colonized superhydrophobic titanium surface after 18 h incubation period [13]. By contrast, it seems reports on limited incubation time (30 min- 3 h), have demonstrated effectiveness of superhydrophobic coating at inhibiting bacterial attachment [23-25, 57, 58].

Anti-biofouling performance was evaluated by determining the relative bacterial adhesion reduction using the following equation [59].

$$R (\%) = \left[\frac{(A-B)}{A} \right] \times 100 \tag{4.2}$$

where R is the bacterial reduction (%), A the number of bacteria colonies/cm^2 on anodized Al substrate ((AAO/Al), used as control sample), and B the number of bacteria colonies/cm^2 on superhydrophobic AAO/Al sample (04Sil-AgP–NcAAO) having CA of $155 \pm 0.4°$. It must be reiterated that the most promising sample (having Ag+/Si–H molar ratio of 50:2), which exhibited both superhydrophobic and high adhesive properties, was used as test sample for the anti-biofouling study. Such dual action superhydrophobic–biocide, is likely to possess excellent bacterial repellency and inhibits bacterial attachment, even after loss of superhydrophobicity. Figure 4.11 shows the graphical representation of bacterial adhesion/cm^2 reduction for the model bacteria of *S.Aureus*, *P.Aeruginosa*, and *E-coli*. The number of *S.Aureus* colonies on AAO/Al and the superhydrophobic AAO/Al sample (04Sil-AgP–NcAAO) were 6.5×10^7 and 4.5×10^5,

147

respectively. It is worthy of note that bacteria colonies on the superhydrophobic AAO/Al sample (04Sil-AgP-NcAAO) are two orders less than those on the control sample surfaces (AAO/Al), representing a 2.2 log and 99.3 % *S.Aureus* reduction. Similar trend was observed for both gram (-ve) P.A and E-coli bacteria. The number of *P.Aeruginosa*, bacterium that colonized the control sample (AAO/Al), was 5.0×10^6, compared to 5.0×10^4, on superhydrophobic AAO/Al sample (04Sil-AgP-NcAAO). Representing a two order of magnitude lower, a 2-log reduction and 99.0 % P.A bacterium reduction. In the case of *E- coli,* 5.0×10^6 colonies were observed on control sample (AAO/Al), as against 2.5×10^4 bacterial colonies on the superhydrophobic AAO/Al sample (04Sil-AgP–NcAAO). Clearly, superhydrophobic AAO/Al sample (04Sil-AgP–NcAAO) was most effective at inhibiting *E-coli* colonies compared to the other bacteria, with a 2.3 log reduction factor and a 99.5 % adhesion reduction efficiency. However, PMHS alone on AAO/Al did not lead to any significant bacterial reduction. Furthermore, it should be mentioned that less bacterial adhesion reduction is observed for non Ag-based superhydrophobic coatings in the literature. For example, in the work of Meier, M et al [23], superhydrophobic filamented silicone (having CA~ $164 \pm 5°$) exhibited E-coli bacterium adhesion reduction of 84 ± 5 %, under 3 h incubation, while superhydrophobic rod-like silicone (having CA~ $168 \pm 4°$) showed *E-coli* bacterium reduction of 79 ± 7 %, under same condition. Similar trend was also observed for gram (+ve) *S. epidermidis*. Superhydrophobic filamented silicone, exhibited adhesion reduction of 95 $\pm$ 3 %,while superhydrophobic rod-like silicone showed a reduction of 88 $\pm$ 7 % [23]. In a related study by Crick. C.R., et al [24], superhydrophobic silicone elastomer (with CA~ 168°), resulted in 79 % and 58 % adhesion reduction for both gram (-ve) *E-coli*, and gram (+ve) *S.Aureus*, respectively. Interestingly, in our case, the incorporation of Ag in the superhydrophobic surface that provided a CA of $155 \pm 0.4°$, showed bacterial reduction efficiency of 99.3 %, 99.0 % and 99.5 % for the

S.Aureus, *P.Aeruginosa*, and *E-coli* bacteria respectively. However, while direct comparison of different reported results must be treated with caution, as differences may arise owing to experimental conditions, these results somehow corroborate our hypothesis that antibacterial Ag-NPs incorporated in superhydrophobic coatings, can enhance the over all effectiveness of bacterial adhesion reduction.

Note that gram (-ve) bacteria such as *E-coli* and *P.Aeruginosa* are ubiquitous pathogens in biofilms even on dry inanimate surfaces [60-62]. Therefore, evaluating the superhydrophobic AAO/Al sample (04Sil-AgP–NcAAO)'s ability to inhibit biofilm growth is essential. Consequently, SEM was utilized to study the biofilm formation [63]. It has been reported that biofilm maturation begins after 24 h of incubation [64], hence 48 h incubation time was utilized to evaluate biofilm growth. As shown in Figure 4.11 (inset), the entire surface area of AAO/Al (uncoated AAO) is covered by the biofilm. By contrast, the biofilm is not observed on the superhydrophobic AAO/Al sample (04Sil-AgP–NcAAO), except a few bacteria scattered over the surface.
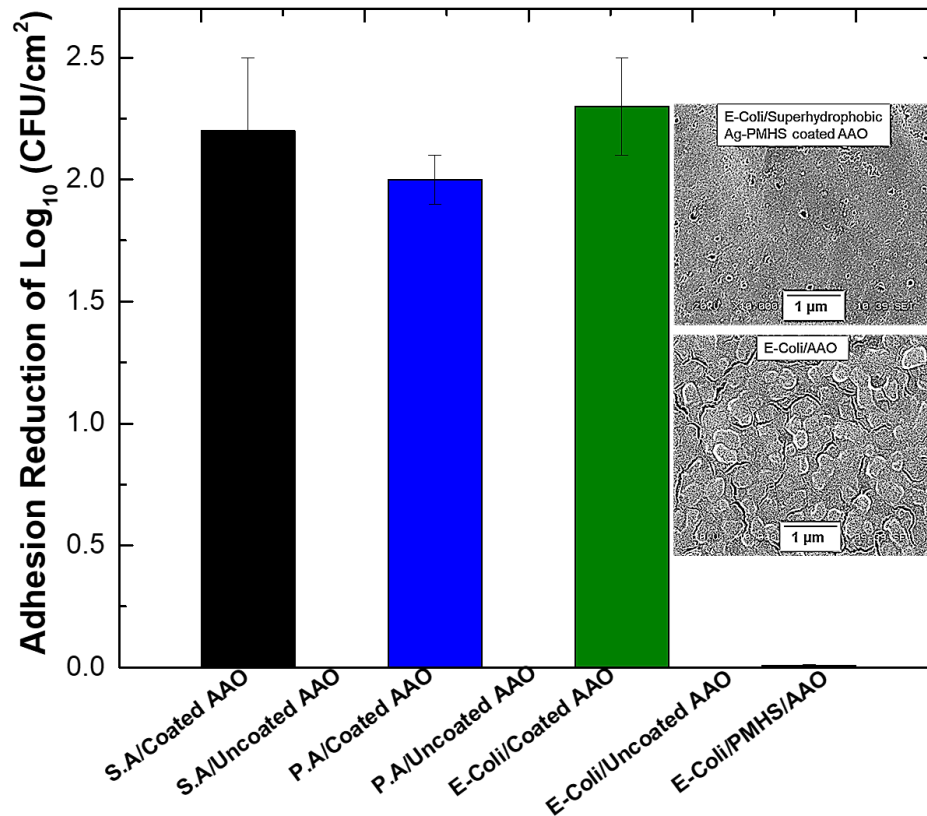
Figure 4-11. Adhesion reduction of bacteria (S.A, P.A, or *E-coli*) on superhydrophobic AAO/Al sample (04Sil-AgP–NcAAO); and control samples (AAO/Al and PMHS/AAO/Al). Data represent multiple independent experiments. Inset: SEM micrograph of *E-coli* biofilm on superhydrophobic AAO/Al sample (Top); and control sample (AAO/Al) (Bottom). © Henry Agbe, 2021.

It is noteworthy that the superhydrophobic AAO/Al sample (04Sil-AgP–NcAAO) lost its water roll-off property after 3 h of being in contact with bacteria. The complex mechanism for bacterial attachment on superhydrophobic coatings, comprising cell adhesion, Van der Waals interactions and activation of quorum sensing molecules, are well acknowledged [64]. This necessitates the need for further detailed studies to establish the correlations between bacteria type, surface chemistry and surface morphology [65]. Nevertheless, it is very likely, bacteria in contact

with Ag–PMHS nanocomposites release bacterial secretions (biopolymers, ß lactamases, and other enzymes) [47] composed of hydrophilic ligands and proteins (N–H, O–H, and C=O) that alter the surface chemistry of the superhydrophobic AAO/Al sample (04Sil-AgP–NcAAO). Interestingly, the sample regained its water roll-off property (with an average CA of $155 \pm 5.0°$) after 3 days of air exposure, presumably due to the evaporation of the hydrophilic ligands. It is likely that 04Sil-AgP–NcAAO exists in the Wenzel wetting state at a high hydrophilic ligand concentration but in the Cassie-Baxter wetting state at a lower hydrophilic ligand concentration. Therefore, the bacterial adhesion reduction observed on superhydrophobic AAO/Al sample, may presumably be facilitated by leachable Ag^+ ions during the Wenzel state. However, for frequently touched surface applications, where the evaporation of the hydrophilic ligand is possible owing to excess dry air, the Cassie–Baxter state can be re-established to facilitate superhydrophocity. Note that PMHS coated on 120 min anodized Al exhibited a lower WCA of $123 \pm 3.1°$ and did not lead to any significant bacterial adhesion reduction.

To further explore the stability of the superhydrophobic sample, a 3-month saline water (3.5 wt.% NaCl, pH = 7.4) immersion study was performed. As shown in Figure 4.12, the WCA was well above 150° after 90 days of saline water immersion. This signifies that the coating has a long-lasting stability in a physiological solution (pH 7.4), typically found in Mammalia cells.
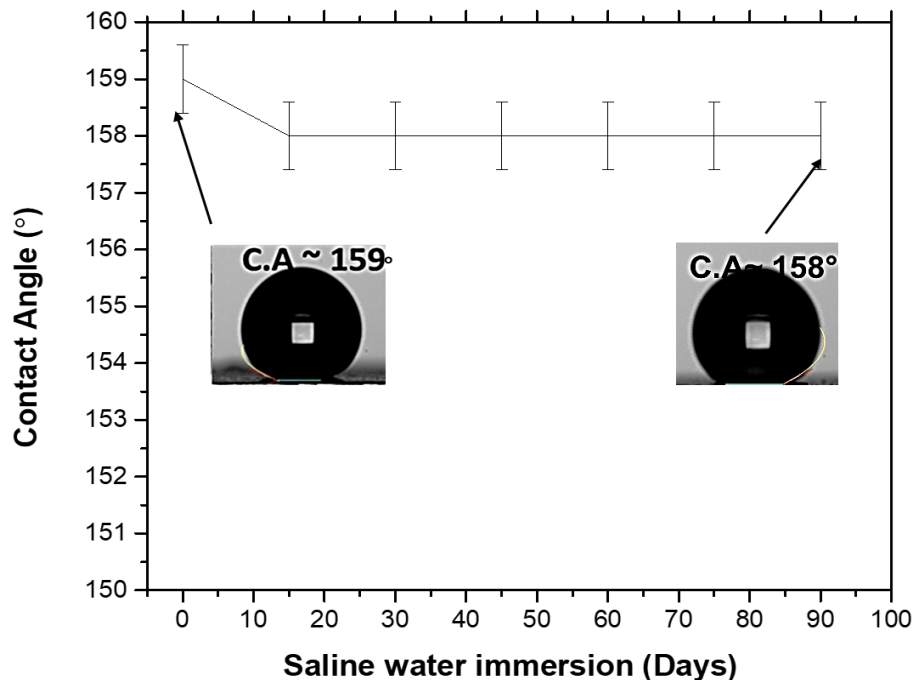
Figure 4-12. Water contact angle of the superhydrophobic sample with time of immersion in 3.5 wt.% NaCl solutions. WCA was measured after drying samples for 2 h at 55 °C. © Henry Agbe, 2021.

In general, the superhydrophobic sample exhibits both bactericidal and anti-biofouling properties. The bactericidal effect is observed owing to the possible release of Ag^+ ions that electrostatically interact with the negatively charged cell wall of bacteria, to inactivate it. The anti-biofouling effect is achieved owing to the superhydrophobic property, induced by the combined effects of nano-micro roughness (achieved by Ag-NPs and anodization) and the presence of –CH$_3$ ligand from PMHS. Due to the superhydrophobicity, water has a minimum contact area with the surface, hence a weaker bacterial interaction would be expected on such surfaces. Therefore, it would be favorable for bacteria to remain in solution and roll off the surface when tilted rather than adhere to the superhydrophobic surface [66].

4.5   Conclusion

In this study, a simple two-step approach was deployed to fabricate Ag–PMHS nanocomposite coatings on anodized Al. The as-synthesized Ag–PMHS nanocomposite coating demonstrated excellent antimicrobial properties against clinically relevant planktonic bacteria, with ZOI values of 25.3 ± 0.5, 24.8 ± 0.5, and 23.3 ± 3.6 mm for *P. Aeruginosa*, *E-coli*, and *S. Aureus*, respectively. The Ag–PMHS nanocomposite coating exhibited a water CA of $159 \pm 0.5°$, providing an excellent anti-biofouling property with bacterial adhesion reductions of 99.0 %, 99.5 %, and 99.3 % for P. *Aeruginosa*, *E-coli*, and *S. Aureus*, respectively. Stability study demonstrated a stable water CA of 158° after 90 days of immersion in saline water (3.5 wt.% NaCl, pH = 7.4). Remarkably, the superhydrophobic Ag–PMHS nanocomposite coating on anodized Al exhibited excellent scratch resistance, strong adhesion property and stability under UV-light irradiation. Overall, Ag–PMHS nanocomposite coating on anodized Al provides a promising and excellent candidate for potential use as antimicrobial touch surfaces to reduce the prevalence of nosocomial infections.

4.6 Supporting information
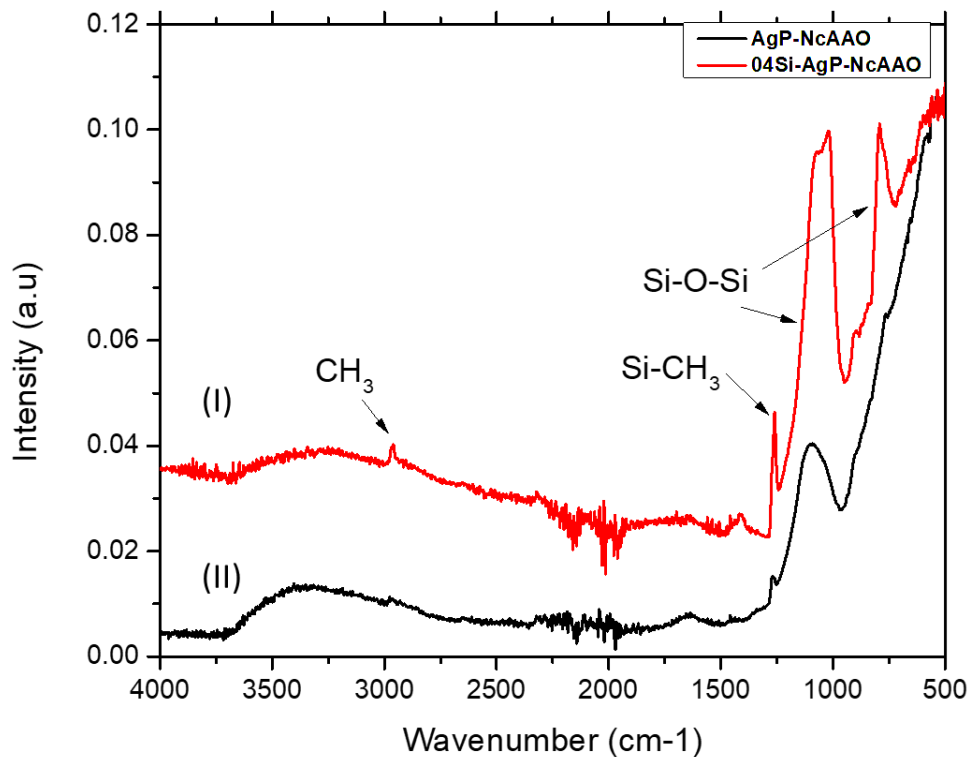
Figure S 4-13. ATR- FTIR spectra of Ag-PMHS nanocomposite having a molar ratio of Ag+/Si-H of 50:2.0 coated on AAO/Al (AgP-NcAAO); and 0.4 % w/v silicone incorporated in AgP-NcAAO (04Sil-AgP-NcAAO), respectively. The increased intensity of siloxane groups in the FTIR peaks for 04Sil-AgP–NcAAO compared to AgP-NcAAO signify the role of RTV siloxane in increasing the monodentate bonding between the Si–O–Si group and the AAO/Al. © Henry Agbe, 2021.

Table S 4-4 Contact angle measurements of Ag-PMHS nanocomposites at different molar ratio on various Al substrates

.

Sample	Ag:PMHS Molar Ratio	Substrate	Contact Angle (°)
1	50:1	120 min AAO	160 ± 2.1
2	50:2	120 min AAO	159 ± 1.2
3	50:30	120 min AAO	154 ± 2.1
4	50:40	120 min AAO	153 ± 1.5
5	50:50	120 min AAO	152 ± 0.6
6	2:50	120 min AAO	149 ± 1.2
7	1:50	120 min AAO	148 ± 1.5
8	50:2	60 min AAO	145 ± 1.0
9	50:2	30 min AAO	128± 2.0
10	50:2	As received Al	113 ± 1.5
11	0:50	120 AAO	123 ± 3.1

Table S 4-5 Grade of adhesive bonding on tested samples- Ag–PMHS nanocomposite coatings having a Ag^+/Si–H molar ratio of 50:2.0 on: (A) as-received Al; (B) AAO/Al; (C) 0.4% w/v silicone incorporated in AgP–NcAAO; and (D) 04Sil-AgP–NcAAO in 90 days of immersion.

Samples	Name	Adhesive bonding (Grade)
A	Ag-PMHS coated aluminum	0B
B	AgP-NcAAO	4B
C	04Sil-AgP-NcAAO	5B
D	04Sil-AgP-NcAAO-90D	5B

The Ag–PMHS nanocomposite coating on the as- received Al, exhibited the lowest grade of 0B, while the Ag–PMHS nanocomposite coating on AAO exhibited grades between 4B and 5B.

Interestingly, after 90 days of saline immersion, the Ag–PMHS nanocomposite coating on AAO (Table S 4.2D) was still resistant to scratch with adhesive bonding Grade 5B.
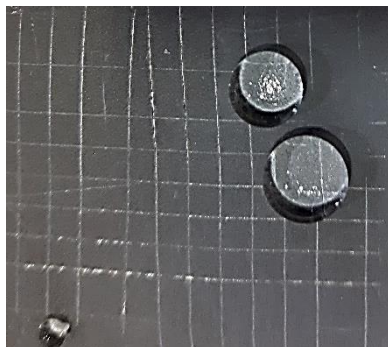
Figure S4-14. Digital image of superhydrophobic Ag–PMHS having Ag+/Si–H molar ratio of 50:2 on AAO/Al, subjected to 90 days immersion (04Sil-AgP–NcAAO-90D) and scratch test. © Henry Agbe, 2021.

Video S 4.1: Demonstration of water roll-off property of superhydrophobic AAO/Al sample (04Sil-AgP–NcAAO); AgP–NcAAO maintains its superhydrophobic property even after loading with 0.4% w/v RTV silicone (04Sil-AgP–NcAAO):

(https://pubs.acs.org/doi/suppl/10.1021/acsabm.0c00159/suppl_file/mt0c00159_si_002.mp4).
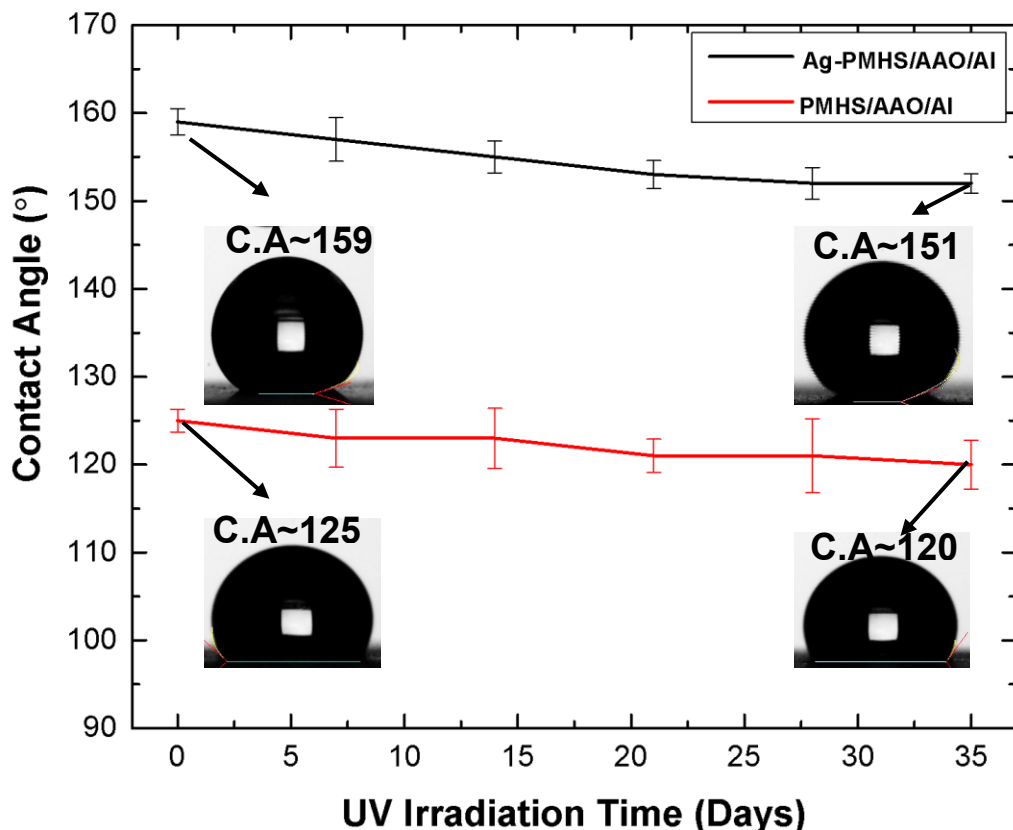
Figure S4-15. Variation of water contact angle as a function of UV irradiation time. © Henry Agbe, 2021.

4.7 **References:**

1. O'Toole, G., H.B. Kaplan, and R. Kolter, *Biofilm formation as microbial development.* Annual Reviews in Microbiology, 2000. **54**(1): p. 49-79.
2. Jafar Hasan, Russell J Crawford, Elena P Ivanova., *Antibacterial surfaces: the quest for a new generation of biomaterials.* Trends in biotechnology, 2013. **31**(5): p. 295-304.
3. Aditi Taunk, Renxun Chen, George Iskander, Kitty K. K. Ho, David StClair Black, Mark D. P. Willcox, Naresh Kumar, *Dual-Action Biomaterial Surfaces with Quorum Sensing Inhibitor and Nitric Oxide To Reduce Bacterial Colonization.* Acs Biomaterials Science & Engineering, 2018. **4**(12): p. 4174-4182.
4. Ammar Algburi, Nicole Comito, Dimitri Kashtanov, Leon M T Dicks, Michael L Chikindas, *Control of biofilm formation: antibiotics and beyond.* Appl. Environ. Microbiol., 2017. **83**(3): p. e02508-16.
5. Rabih, O.D., *Device-Associated Infections: A Macroproblem That Starts with Microadherence.* Clinical Infectious Diseases, 2001. **33**(9): p. 1567-1572.
6. Fair, R.J. and Y. Tor, *Antibiotics and bacterial resistance in the 21st century.* Perspectives in medicinal chemistry, 2014. **6**: p. PMC. S14459.

7.   Asad Bashir Awan, Juliane Schiebel, Alexander Böhm, Jörg Nitschke, Yasra Sarwar, Peter Schierack, Aamir Ali, *Association of biofilm formation and cytotoxic potential with multidrug resistance in clinical isolates of Pseudomonas aeruginosa.* EXCLI journal, 2019. **18**: p. 79.

8.   Shirin Alexander, Julian Eastoe, Alex M. Lord, Frédéric Guittard, Andrew R. Barron, *Branched hydrocarbon low surface energy materials for superhydrophobic nanoparticle derived surfaces.* ACS applied materials & interfaces, 2015. **8**(1): p. 660-666.

9.   Kiduk Han, Tae Yoon Park, Kijung Yong, Hyung Joon Cha, *Combinational Biomimicking of Lotus Leaf, Mussel, and Sandcastle Worm for Robust Superhydrophobic Surfaces with Biomedical Multifunctionality: Antithrombotic, Antibiofouling, and Tissue Closure Capabilities.* ACS applied materials & interfaces, 2019. **11**(10): p. 9777-9785.

10.   M Carmen Morán, Guillem Ruano, Francesca Cirisano, Michele Ferrari, *Mammalian cell viability on hydrophobic and superhydrophobic fabrics.* Materials Science and Engineering: C, 2019. **99**: p. 241-247.

11.   Cláudia Sousa, Diana Rodrigues, Rosário Oliveira, Wenlong Song, João F Mano, Joana Azeredo, *Superhydrophobic poly (L-lactic acid) surface as potential bacterial colonization substrate.* AMB express, 2011. **1**(1): p. 34.

12.   Ellinas, K., A. Tserepi, and E. Gogolides, *Durable superhydrophobic and superamphiphobic polymeric surfaces and their applications: A review.* Advances in colloid and interface science, 2017. **250**: p. 132-157.

13.   Elena Fadeeva, Vi Khanh Truong, Meike Stiesch, Boris N Chichkov, Russell J Crawford, James Wang, Elena P Ivanova, *Bacterial retention on superhydrophobic titanium surfaces fabricated by femtosecond laser ablation.* Langmuir, 2011. **27**(6): p. 3012-3019.

14.   Periklis Papadopoulos, Lena Mammen, Xu Deng, Doris Vollmer, and Hans-Jürgen Butt, *How superhydrophobicity breaks down.* Proceedings of the National Academy of Sciences, 2013. **110**(9): p. 3254-3258.

15.   Mei Zhang, Ping Wang, Hongyan Sun, Zuankai Wang, *Superhydrophobic surface with hierarchical architecture and bimetallic composition for enhanced antibacterial activity.* ACS applied materials & interfaces, 2014. **6**(24): p. 22108-22115.

16.   S Heinonen, E Huttunen-Saarivirta, J-P Nikkanen, Mari Raulio, Outi Priha, J Laakso, Erna Storgårds, E Levänen, *Antibacterial properties and chemical stability of superhydrophobic silver-containing surface produced by sol–gel route.* Colloids and Surfaces A: Physicochemical and Engineering Aspects, 2014. **453**: p. 149-161.

17.   Zhile Wang, Junfei Ou, Ying Wang, Mingshan Xue, Fajun Wang, Bing Pan, Changquan Li, Wen Li, *Anti-bacterial superhydrophobic silver on diverse substrates based on the mussel-inspired polydopamine.* Surface and Coatings Technology, 2015. **280**: p. 378-383.

18.   Ekrem Ozkan, Colin C. Crick, Alaric Taylor, Elaine Allan, Ivan P. Parkin, *Copper-based water repellent and antibacterial coatings by aerosol assisted chemical vapour deposition.* Chemical science, 2016. **7**(8): p. 5126-5131.

19.   Zuo-Yi Xiao, Shu-Xian Huang, Shang-Ru Zhai, Bin Zhai, Feng Zhang Qing-Da An, *PMHS-reduced fabrication of hollow Ag–SiO 2 composite spheres with developed porosity.* Journal of Sol-Gel Science and Technology, 2015. **75**(1): p. 82-89.

20. Omer Dag, Eric J. Henderson, Wendong Wang, Jennifer E. Lofgreen, Srebri Petrov, Peter M. Brodersen, Geoffrey A. Ozin, *Spatially Confined Redox Chemistry in Periodic Mesoporous Hydridosilica–Nanosilver Grown in Reducing Nanopores.* Journal of the American Chemical Society, 2011. **133**(43): p. 17454-17462.

21. Valeria De Matteis, Mariafrancesca Cascione, Chiara Cristina Toma, Stefano Leporatti, *Sol–gel synthesis of nanosilver embedded hybrid materials using combined organosilica precursors.* Journal of sol-gel science and technology, 2012. **62**(3): p. 281-286.

22. Xu Shao, Shang-Ru Zhai, Bin Zhai, Qing-Da An, *Ag+/MPTMS/PMHS-mediated two-step acid–base synthesis of hybrid materials with embedded nanosilver.* Journal of sol-gel science and technology, 2013. **66**(2): p. 264-273.

23. Meier, M., V. Dubois, and S. Seeger, *Reduced bacterial colonisation on surfaces coated with silicone nanostructures.* Applied Surface Science, 2018. **459**: p. 505-511.

24. Colin R. Crick, Salim Ismail, Jonathan Pratten, Ivan P. Parkin, *An investigation into bacterial attachment to an elastomeric superhydrophobic surface prepared via aerosol assisted deposition.* Thin Solid Films, 2011. **519**(11): p. 3722-3727.

25. Benjamin J. Privett, Jonghae Youn, Sung A Hong, Jiyeon Lee, Junhee Han, Jae Ho Shin, Mark H. Schoenfisch, *Antibacterial fluorinated silica colloid superhydrophobic surfaces.* Langmuir, 2011. **27**(15): p. 9597-9601.

26. Arash Bahrami, Reza Rezaei Mokarram, Mahmoud Sowti Khiabani, Babak Ghanbarzadeh, Roya Salehi, *Physico-mechanical and antimicrobial properties of tragacanth/hydroxypropyl methylcellulose/beeswax edible films reinforced with silver nanoparticles.* International journal of biological macromolecules, 2019. **129**: p. 1103-1112.

27. Siddaramanna, A., N. Saleema, and D. Sarkar, *A versatile cost-effective and one step process to engineer ZnO superhydrophobic surfaces on Al substrate.* Applied Surface Science, 2014. **311**: p. 182-188.

28. Xiong, J., D.K. Sarkar, and X.G. Chen, *Ultraviolet-Durable Superhydrophobic Nanocomposite Thin Films Based on Cobalt Stearate-Coated TiO2 Nanoparticles Combined with Polymethylhydrosiloxane.* ACS Omega, 2017. **2**(11): p. 8198-8204.

29. Jizong Zhang, Xin Hu, Jian Zhang, Yushang Cui, Changsheng Yuan, Haixiong Ge, Yanfeng Chen, Wei Wu, Qiangfei Xia, *A fast thermal-curing nanoimprint resist based on cationic polymerizable epoxysiloxane.* Nanoscale research letters, 2012. **7**(1): p. 380.

30. D.K.Sarkar, D.Brassard, M.A. ElKhakanj, L.Ouellet, *Dielectric properties of sol–gel derived high-k titanium silicate thin films.* Thin Solid Films, 2007. **515**(11): p. 4788-4793.

31. Scheschkewitz, D. and U. Böhme, *Functional molecular silicon compounds*. 2014: Springer.

32. Corriu, R.J, *A new and mild access to N-functionalized formamido and thioformamido compounds using hypervalent silicon hydrides.* Tetrahedron Letters, 1990. **31**(18): p. 2585-2588.

33. Pope, E. and J. Mackenzie, *Sol-gel processing of silica: II. The role of the catalyst.* Journal of non-crystalline solids, 1986. **87**(1-2): p. 185-198.

34. Sharma, V.K., R.A. Yngard, and Y. Lin, *Silver nanoparticles: green synthesis and their antimicrobial activities.* Advances in colloid and interface science, 2009. **145**(1-2): p. 83-96.

35. Santipanusopon, S. and S.-A. Riyajan, *Effect of field natural rubber latex with different ammonia contents and storage period on physical properties of latex concentrate, stability of skim latex and dipped film.* Physics Procedia, 2009. **2**(1): p. 127-134.

36.   Momen, G., M. Farzaneh, and R. Jafari, *Wettability behaviour of RTV silicone rubber coated on nanostructured aluminium surface.* Applied Surface Science, 2011. **257**(15): p. 6489-6493.

37.   Alkire, R.C., Y. Gogotsi, and P. Simon, *Nanostructured materials in electrochemistry*. 2008: John Wiley & Sons.

38.   Tatsuya Kikuchi, Akimasa Takenaga, Shungo Natsui, Ryosuke O.Suzuki, *Advanced hard anodic alumina coatings via etidronic acid anodizing.* Surface and Coatings Technology, 2017. **326**: p. 72-78.

39.   Liou, T.-H., F.-W. Chang, and J.-J. Lo, *Pyrolysis kinetics of acid-leached rice husk.* Industrial & engineering chemistry research, 1997. **36**(3): p. 568-573.

40.   Brassard, J.-D., D.K. Sarkar, and J. Perron, *Synthesis of monodisperse fluorinated silica nanoparticles and their superhydrophobic thin films.* ACS applied materials & interfaces, 2011. **3**(9): p. 3583-3588.

41.   Masuda, H., H. Masuda, and K. Fukuda, *Ordered metal nanohole arrays made by a two-step replication of honeycomb structures of anodic alumina.* Science (New York, N.Y.), 1995. **268**(5216): p. 1466-1468.

42.   Wenzel, R.N., *Resistance of solid surfaces to wetting by water.* Industrial & Engineering Chemistry, 1936. **28**(8): p. 988-994.

43.   Cassie, A. and S. Baxter, *Wettability of porous surfaces.* Transactions of the Faraday society, 1944. **40**: p. 546-551.

44.   Jun Li,Lianhua Fan,Ching-Ping Wong,Franklin Cook Lambert, *Insulator coating and method for forming same*. 2010, Google Patents.

45.   Jean-Denis Brassard, Jean-Louis Laforte, Caroline Blackburn, Jean Perron, D.K.Sarkar, *Silicone based superhydrophobic coating efficient to reduce ice adhesion and accumulation on aluminum under offshore arctic conditions.* Ocean Engineering, 2017. **144**: p. 135-141.

46.   Poberžnik, M. and A. Kokalj, *Implausibility of bidentate bonding of the silanol headgroup to oxidized aluminum surfaces.* Applied Surface Science, 2019. **492**: p. 909-918.

47.   Milionis, A., E. Loth, and I.S. Bayer, *Recent advances in the mechanical durability of superhydrophobic materials.* Advances in colloid and interface science, 2016. **229**: p. 57-79.

48.   Pooi Leng Ho, Han Kee Ong, Jeanette Teo, Dave Siak-Wei Ow, Sheng-Hao Chao, *HEXIM1 peptide exhibits antimicrobial activity against antibiotic resistant bacteria through guidance of cell penetrating peptide.* Frontiers in microbiology, 2019. **10**: p. 203.

49.   Wayne, P., *Clinical and laboratory standards institute. Performance standards for antimicrobial susceptibility testing.* 2011.

50.   Banerjee, S.L., P. Potluri, and N.K. Singha, *Antimicrobial cotton fibre coated with UV cured colloidal natural rubber latex: A sustainable material.* Colloids and Surfaces A: Physicochemical and Engineering Aspects, 2019. **566**: p. 176-187.

51.   K Zheng,MI Setyawati,DT Leong, J Xie , *Antimicrobial silver nanomaterials.* Coordination Chemistry Reviews, 2018. **357**: p. 1-17.

52.   Percival, S.L., A.-M. Salisbury, and R. Chen, *Silver, biofilms and wounds: resistance revisited.* Critical reviews in microbiology, 2019: p. 1-15.

53.   P Sikder,SB Bhaduri,JL Ong, *Silver (Ag) doped magnesium phosphate microplatelets as next-generation antibacterial orthopedic biomaterials.* Journal of Biomedical Materials Research Part B: Applied Biomaterials, 2020. **108**(3): p. 976-989.

54.   Menagen, B., R. Pedahzur, and D. Avnir, *Sustained release from a metal-Analgesics entrapped within biocidal silver.* Scientific reports, 2017. **7**(1): p. 1-11.

55. Liuya Wei, Jingran Lu, Huizhong Xu, Atish Patel, Zhe-Sheng Chen, Guofang Chen, *Silver nanoparticles: synthesis, properties, and therapeutic applications.* Drug discovery today, 2015. **20**(5): p. 595-601.

56. Zhang, X., L. Wang, and E. Levänen, *Superhydrophobic surfaces for the reduction of bacterial adhesion.* Rsc Advances, 2013. **3**(30): p. 12003-12020.

57. Jafar Hasan, Hayden K Webb, Vi Khanh Truong, Sergey Pogodin, Vladimir A Baulin, Gregory S Watson, Jolanta A Watson, Russell J Crawford, Elena P Ivanova, *Selective bactericidal activity of nanopatterned superhydrophobic cicada Psaltoda claripennis wing surfaces.* Applied microbiology and biotechnology, 2013. **97**(20): p. 9257-9262.

58. Ferdi Hizal, Natthakan Rungraeng, Junghoon Lee, Soojin Jun, Henk J. Busscher, Henny C. van der Mei, Chang-Hwan Choi, *Nanoengineered superhydrophobic surfaces of aluminum with extremely low bacterial adhesivity.* ACS applied materials & interfaces, 2017. **9**(13): p. 12118-12129.

59. Eunmi Cho, Sung Hyun Kim, Mac Kim, Jin Seong Park, Sang Jin Lee, *Super-hydrophobic and antimicrobial properties of Ag-PPFC nanocomposite thin films fabricated using a ternary carbon nanotube-Ag-PTFE composite sputtering target.* Surface and Coatings Technology, 2019. **370**: p. 18-23.

60. Varun Sambhy, Megan M MacBride, Blake R Peterson, Ayusman Sen, *Silver bromide nanoparticle/polymer composites: dual action tunable antimicrobial materials.* Journal of the American Chemical Society, 2006. **128**(30): p. 9798-9808.

61. Dharm Raj Bhatta, Deependra Hamal, Rajani Shrestha, Supram Hosuru Subramanya, Nisha Baral, Rajesh Kumar Singh, Niranjan Nayak, Shishir Gokhale, *Bacterial contamination of frequently touched objects in a tertiary care hospital of Pokhara, Nepal: how safe are our hands?* Antimicrobial Resistance & Infection Control, 2018. **7**(1): p. 97.

62. Vincenzo Russotto, Andrea Cortegiani, Teresa Fasciana, Pasquale Iozzo, Santi Maurizio Raineri, Cesare Gregoretti, Anna Giammanco, and Antonino Giarratano, *What healthcare workers should know about environmental bacterial contamination in the intensive care unit.* BioMed research international, 2017. **2017**.

63. G Ramage, K Vande Walle, B L Wickes, J L López-Ribot, *Biofilm formation by Candida dubliniensis.* Journal of clinical microbiology, 2001. **39**(9): p. 3234-3240.

64. Ching-Yee Loo, Paul M Young, Wing-Hin Lee, Rosalia Cavaliere, Cynthia B Whitchurch, Ramin Rohanizadeh, *Superhydrophobic, nanotextured polyvinyl chloride films for delaying Pseudomonas aeruginosa attachment to intubation tubes and medical plastics.* Acta biomaterialia, 2012. **8**(5): p. 1881-1890.

65. Sara Naderizadeh, Silvia Dante, Pasquale Picone, Marta Di Carlo, Riccardo Carzino, Athanassia Athanassiou, Ilker S Bayer, *Bioresin-based Superhydrophobic Coatings with Reduced Bacterial Adhesion.* Journal of Colloid and Interface Science, 2020.

66. Lauren R. Freschauf, Jolie McLane, Himanshu Sharma, Michelle Khine, *Shrink-induced superhydrophobic and antibacterial surfaces in consumer plastics.* PLoS One, 2012. **7**(8): p. e40987.

CHAPTER 5

5   CHAPTER 5

This chapter has been published in Coating (*Coatings* 2020, *10*(10), 982), and was authored by Henry Agbe, Dilip Sarkar Kumar, and X-Grant Chen. As a first author, I designed and performed all experiments, analyzed, and interpreted the results, as well as wrote both initial and final manuscripts.

5.1   **Abstract.**

Surfaces in hygiene critical environment can become potential reservoir for transmission of pathogenic infections. Engineering surfaces with the tunable anti-biofouling and antibacterial properties could reduce infections particularly in hospitals and public transport hubs. In the present work, a facile two-step process has been deployed to fabricate superhydrophobic and antibacterial aluminum surface by chemical etching, followed by passivation with low surface energy octyltriethoxysilane (OTES) molecules. The wettability and antibacterial properties of the OTES passivated aluminum was monotonically tuned by adding quaternary ammonium (QUATs) molecules. An anti-biofouling property of 99.9, 99 and 99% against *Staphylococcus aureus*, *Pseudomonas aeruginosa and E. coli* bacteria respectively, was achieved.

5.2   **Introduction**

Antibacterial coatings for biomedical implant devices (such as catheters, artificial hip and knee joints, etc.) and high touch surface applications have gained much attention in recent times due to their ability to reduce the prevalence of nosocomial infections [1, 2]. Antibacterial coatings may not only prevent biofilm formation, medical impact device failure and post-operative bacterial

infections, but also reduce microbial bioburden in hygiene critical environment [2]. It is worthwhile mentioning that pathogenic microorganisms can survive on frequently touch surfaces in our daily life such as door knobs, push plates, etc. for days, weeks and months [1, 2]. Thus, surfaces act as hot-spots for transmission of pathogenic infections [2]. To this end, engineering surfaces with antibacterial property have now been acknowledged as important strategy for reducing microbial bioburden and the prevalence of infections [3]. Among surfaces with antibacterial properties, anti-biofouling and superhydrophobic surfaces seem desirable as they have the ability to inhibit bacterial attachment on surfaces.

Superhydrophobic surfaces possess a static water contact angle (CA) > 150° with a water roll-off property. In nature, scientists have discovered the unique water roll-off property in several plants, such as lotus leaf. Such superhydrophobic surface can be fabricated by patterning micro-nano structures, followed by passivation with low surface energy molecules. Various strategies such as photolithography [4], sol–gel [4], plasma etching [5], anodization [6] and chemical etching [7], have been deployed to fabricate superhydrophobic surfaces, which find applications as self-cleaning-fabrics, anticorrosion, drag reduction and anti-biofouling surface [8]. Though, superhydrophobic surfaces can repel bacterial adhesion, they fail under long-term exposure [9]. For example, Ivanova et al. [10], utilized femtosecond laser ablation process to fabricate superhydrophobic titanium coatings (with CA of 166°), and demonstrated their effectiveness at repelling *Pseudomonas aeruginosa* (P.A), (Gram −ve) bacterium attachment. However, over long-term exposure (~18 h), the water roll-off property was lost, subsequently leading to both *Staphylococcus aureus* (S.A), (Gram +ve) and P.A bacterial colonization. Thus, incorporating bactericides in superhydrophobic coating holds promise not only in inducing both anti-biofouling and antibacterial properties, but also for improving their longevity. Again, superhydrophobic

164

coating incorporated with bactericide could minimize uncontrolled bactericide release and subsequent toxicity concerns.

Therefore, designing surfaces with both superhydrophobic and antibacterial properties has recently gained significant interest [11-13]. For example, Chung et al. [12] fabricated a silver-perfluorodecanethiolate coatings on silicon wafer with both superhydrophobic and antibacterial coatings via precipitation method, using perfluorodecanethiol (PFDT) and silver as fluorinated and metal-thiolate complexes precursors, respectively. In a related work, Wang et al. [11] fabricated a superhydrophobic diamond films with both antibacterial and anti-biofouling properties using hot filament chemical vapor deposition and sol-gel perfluorodecyltrichlorosilane (PFTS) molecules passivation. Meanwhile, Zhang et al. [13] reported a Ag/Cu bimetallic coatings fabricated using a galvanic replacement reaction and thermal oxidation processes. This coating exhibited both superhydrophobic and antibacterial properties, but the bacterial repellent property was not reported. It is reported that fluorosilane molecules and leachable bactericides such as Ag and Cu may be toxic to the ecosystem [14]. For example, Ag and Cu at 6.1 ppm (56.5 μM) and 2.61 ppm (41.1 μM) were reported to be toxic to Zebrafish embryos [15]. Again, fluorinated compounds have been implicated in sporadic outbreaks of respiratory illness characterized by dyspnea, cough and chest pain [16]. Thus, there is an urgent need for alternative biocompatible low surface energy molecule and non-toxic bactericides (such as quaternary ammonium (QUATs) molecules commonly used as disinfectants for sanitizing hospital environment) to fabricate tunable superhydrophobic and antibacterial coatings

In the present work, a facile two-step process has been deployed to fabricate superhydrophobic and antibacterial aluminum surface by chemical etching, followed by passivation with low surface energy hydrocarbon of octyltriethoxysilane (OTES) molecules. To

165

the best of our knowledge, this is the first report on OTES-QUATs coatings with tunable antibacterial and bacterial repellent properties. While the water CA of most of the above-mentioned coatings [11-13] were well above 150° and the coatings exhibited bacterial repellent and antibacterial properties, their tunable properties have not been systematically studied yet. It should be mentioned that a tunable superhydrophobic coating could be tailored for some specific applications, such as hydrophobic and antibacterial coatings for medical implants or superhydrophobic and antibacterial coatings for cooling tower or frequently touch surfaces. Again, such coatings could improve the overall longevity of antibacterial properties even after the loss of superhydrophobicity. In the present study, the water roll-off property is monotonically tuned from superhydrophobic to hydrophilic surface by increasing the concentration of the QUATs. Furthermore, the excellent antibacterial and anti-biofouling properties, as well as their synergistic effects are demonstrated.

5.3 Experimental section

AA6061-T6 aluminum alloy of dimensions 2.54 cm x 5.08 cm was ultrasonically degreased in a soapy solution, followed by chemical etching in 30 wt. % HCl at 55 °C for 3 min. 50 ml ethanol was taken in a beaker and 1000 µL of 3.0 M OTES added while stirring using a magetic bar on a hot plat of temperuature of 25 °C to prepare the mixed solution of OTES. Furthermore 0.01 M QUAT were added drop by drop in the solution to obtain the mixed solution of OTES-QUAT. The amount of OTES was kept contant and the 0.01 M QUAT added in such as way that the molar ratio of QUAT/OTES varies between 0 to 54×10^{-4}, according to table S 5.1 (shown in the Supporting Information, Table S 5.1). The OTES-QUATs suspension was then

sonicated for 15 min for dispersion. Subsequently, the etched Al substrates were immersed in these solutions for 30 min for the passivation. Furthermore, the passivated aluminum substrates were dried in the oven 100 ˚C in the air atmosphere for 2 h to remove residual solvents.

Sample characterization. The morphological and elemental characterizations of the samples were analyzed using scanning electron microscopy (SEM, JEOL JSM-6480 LV), equipped with energy dispersive X-ray spectroscopy (EDS). The chemical compositions were analysed by Attenuated Total Reflection-Fourier Transform Infrared (ATR, Agilent Technologies Cary 630 FTIR). In addition, the wetting characteristics of the samples were determined by measuring both static and dynamic contact angles (CA) using a First Ten Angstrom Contact angle goniometer at five positions on each substrate using 10 µL deionized water drop. The dynamic contact angle was measured by holding the water droplet with a stationary needle in contact with the sample surface and moving the goniometer stage in one direction. The surface roughness of the coatings were measured using an optical profilometer (MicroXAM-100 HR 3D surface profilometer).

Antibacterial assay. Antibacterial activity was determined by both anti-biofouling and disk diffusion assays. Using bacterial repellent assay, bacterial strains: *Staphylococcus aureus* (ATCC 6538), *Escherichia coli* (ATCC 8739)*, and *Pseudomonas aeruginosa* (ATCC 9027)), were grown overnight from frozen (-80 °C) glycerol stock in Tryptic Soy Broth (TSB) (Hardy Diagnostics) at 37 °C, and then passaged on fresh TSB (37 °C) to obtain bacterial cell density of 10^8 colony forming units/ millilitre (CFU)/mL. Bacterial cell density was determined by measuring the optical density (OD) at 625 nm wavelength. Static bacterial adhesion experiments were conducted following a prescribed protocol elsewhere [17]. Briefly, two 250 mL sterile beakers were filled with 99 mL 10 mM Phosphate buffer solution (PBS) (pH 7.5 +/- 0.3 at 25°C.) and 1

mL bacterial culture. Subsequently, test samples, namely: 1-inche $\times$ 2 inches etched Al substrates (used as blank) and OTES-QUATs passivated Al substrates were placed separately in the beakers. Samples were then incubated for 3 h at 37 °C. Next, samples were rinsed in PBS to remove non-adherent bacteria, which were subsequently transferred into a set of 50 mL sterile beakers (containing PBS) and sonicated on ice for 10 min to remove adherent bacteria. Finally, the bacterial suspensions were serially diluted, and plated on tryptic soy agar TSA, followed by an aerobic incubation at 37 °C for 24 h. Positive controls were performed for t = 0 and t = 3 h to ascertain bacterial viability. All experiments were performed in triplicate and on fresh bacterial inoculum. Relative bacterial adhesion was calculated as: [(A-B)/A$\times$100%], where A = CFU/cm^2 of adherent bacteria on etched Al substrates and B = CFU/cm^2 of adherent bacteria on OTES-QUATs passivated sample

Regarding the disk diffusion assays, bacterial strains were grown overnight to obtain 10^8 CFU/mL as described above. Kirby Bauer disk diffusion assay was used as described elsewhere [18]. Briefly, sterile swab was used to inoculate Mueller Hinton Agar (Hardy Diagnostics) films by streaking to obtain a bacterial lawn. Subsequently, 20-µL QUATs soaked Whatman filter papers (6 mm diameter), were inserted on the agar media. Finally, the agar plates were aerobically incubated at 37 °C for 24 h. Experiments were repeated and in triplicate, on different days with fresh bacterial cell suspensions. All microbiology experiments related to the following bacterial cell culture: *Staphylococcus aureus*-(ATCC 6538), *Pseudomonas aeruginosa* (ATCC9027) and *Escherichia coli* (ATCC 8739) were obtained from Hardy Diagnostics and conducted at the microbiology laboratory of our industrial partner and commenced subject to the ethical approval of their ethics committee (https://a3surfaces.com/en/).

5.4 Results and discussion.

5.4.1 Morphological and chemical analysis

In Figure. 5.1 (a), I - III show the ATR-FTIR spectra of octyltriethoxysilane molecules passivated etched Al substrate (OTES/Al); octyltriethoxysilane and quaternary ammonium molecules passivated etched Al substrate (OTES-QUATs/Al); and quaternary ammonium molecules passivated etched aluminum (QUATs/Al), respectively. The peak at 3445 cm^{-1}, represents the O-H and N-H stretching modes [19]. While those at 2955 cm^{-1}, 2920 cm^{-1} and 2853 cm^{-1} can be assigned to asymmetric CH_3 groups; and symmetric CH_2 and asymmetric CH_2 vibration modes [20, 21]. Again, the asymmetrical stretching vibration of the Si−O−Si molecules are in the 1060-1100 cm^{-1} bands. Additionally, 1646-898 cm^{-1} can be assigned to the C-N and C-H stretching modes of QUATs [22, 23], (Supporting Information can be found in Figure. S 5-5). Finally, the 1080 cm^{-1} peak corresponds to the asymmetric $Si-O-CH_2CH_3$ mode of OTES-QUATs [20]. It is interesting to note that the increasing intensity of this peak of OTES-QUATs/Al compared to OTES/Al (Figure. 5.1(a)(II vs I)) is due to symmetric and asymmetrical stretching vibration overlaps from both the molecules of OTES and QUATs; and the resulting non-hydrolysable reaction [20]. It has been suggested that QUATs covalently bonds to alkyl chains of siloxane [19] through a non-hydrolysable Si-O-C bonding. Therefore, on the addition of QUATs, the alkyl group of nitrogen (N^+) - $(CH_3)_3$ covalently bonds with the octyl chains of the octyltriethoxysilane (OTES) molecules through a non-hydrolysable reaction. [24], as schematically modelled in Figure. 5.1 (b) (II).
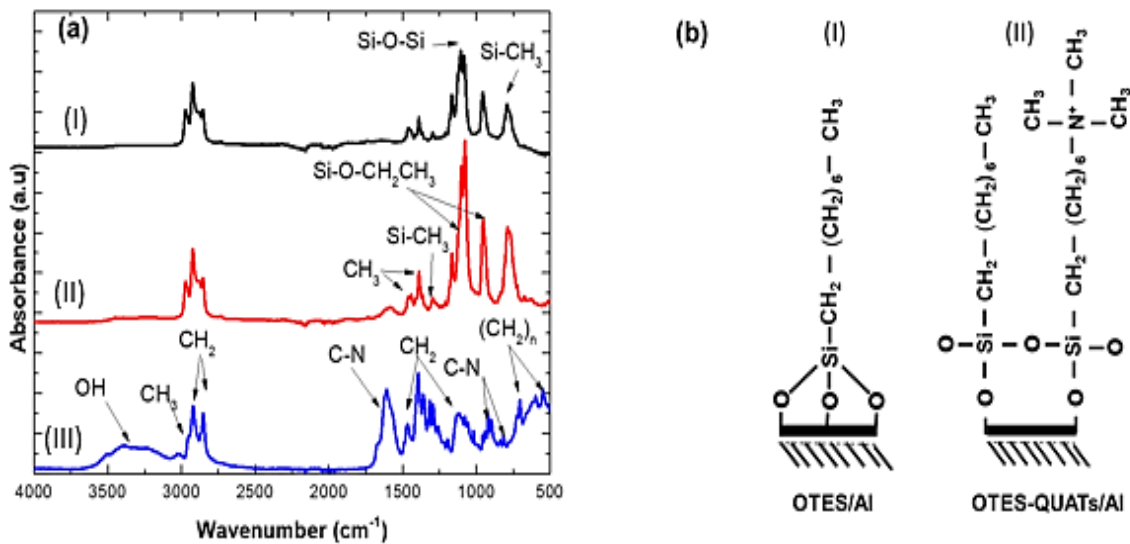
Figure 5-1. (a) ATR-FTIR spectra of: (I) Octyltriethoxysilane molecules passivated etched Al substrate (OTES/Al); (II) Octyltriethoxysilane and quaternary ammonium molecules passivated etched Al substrate (OTES-QUATs/Al); (III) Quaternary ammonium molecules passivated etched aluminum (QUATs/Al) and (b) Schematic model of: (I) OTES on etched aluminum (OTES/Al); (II) Formation of OTES-QUATs on etched Al, along with (OTES/Al). © Henry Agbe, 2021.

In addition to the FTIR, SEM and EDS (Figure. 5.2 (a-b) and (c-d)) were performed to study the morphological and the elemental composition of OTES-QUATs molecules passivated etched aluminum, respectively. EDS spectra show the presence of C, N, O, Al, Si and Cl, with their corresponding K_α peaks at 0.28, 0.39, 0.53, 1.49, 1.74 and 2.62 keV, respectively. As shown in the inset in Figure 5.2 (a), chemical etching results in a topologically terraced micro and nano-features with surface rms roughness and contact angle (CA) of 6.2 ± 1.5 µm and $16 \pm 0.2°$ (Supporting Information,Table S 5.2), respectively, which is similar to those previously reported

[25]. These small faceted and labyrinth micro-nano features, can trap air through the dispersed protrusions of asperities, reducing solid-droplet contact to repel droplet over the entrapped air layers [26]. However, OTES-QUATs/Al samples exhibited a roughness of 5.8 ± 0.5 µm and a CA of $153 \pm 3.7°$ (shown in the supporting information, Table S 5.2). Similarly, the OTES/Al samples showed a roughness of 6.5 ± 0.5 µm, and a CA of $161 \pm 2.3°$ (Supporting Information can be found in Table S 5.2). It can be noted that the roughness of the etched and passivated samples was around 6 µm.
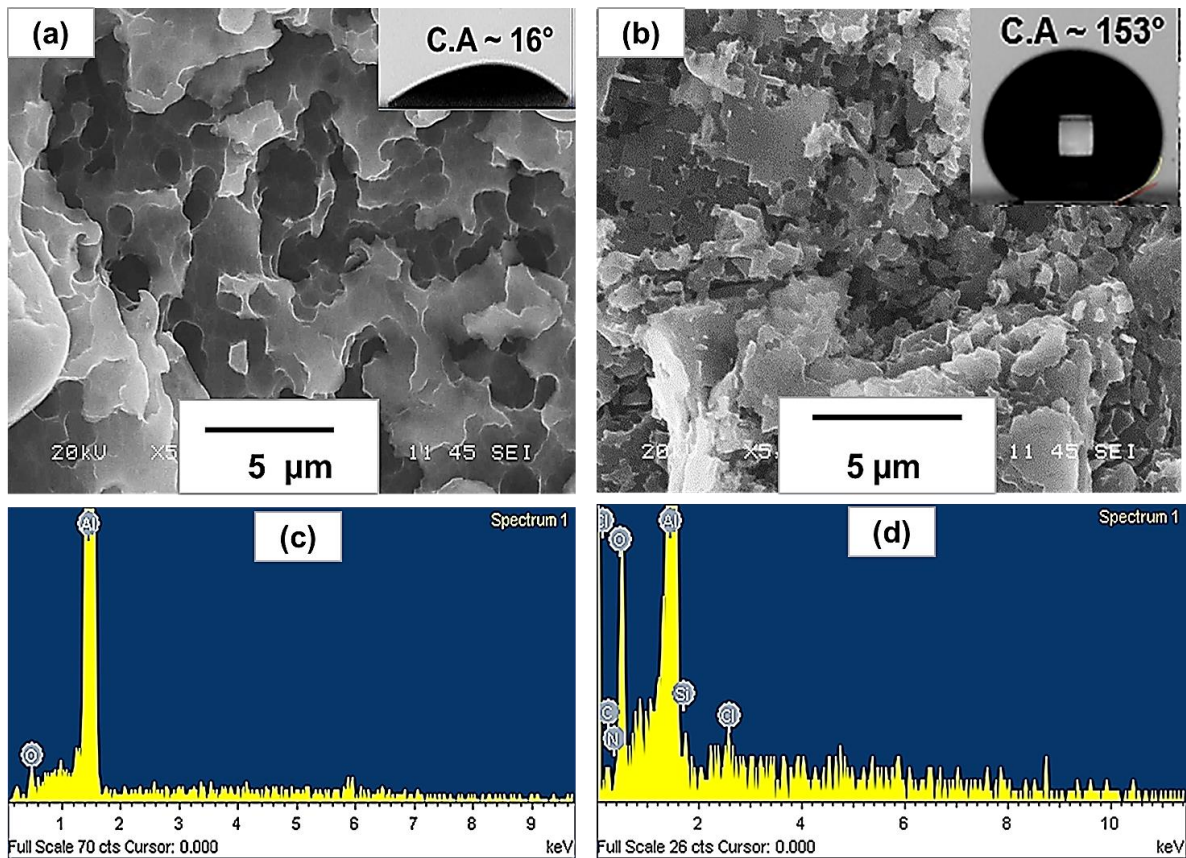
Figure 5-2. (a-b) and (c-d) SEM images and EDS spectra of etched Al substrate and OTES-QUATs/Al, respectively. X and Y-axes: Energy (keV) versus Intensity (a.u). The insets also show the images of water drop on the respective surfaces with their contact angles. © Henry Agbe, 2021.

Note that the superhydrophobicity is due to combined effects of low surface energy OTES molecules and nano−micro roughness of etched aluminum substrates. It is well known that the micro–nano pattern on the surface allows large amount of air to be entrapped into the pattern while the low surface energy molecules inhibits the interaction with water [27, 28]. Therefore, having a CA > 160°, it is reasonable to assume that water drops on OTES/Al samples would roll-off easily. However, by increasing molar ratio of QUATs/OTES, the wettability of OTES/Al sample was monotonically converted from superhydrophobic to hydrophilic. The trend continued with loss of superhydrophobicity (Figure 5.3). It should be mentioned that QUATs are amphiphilic surfactants having hydrophilic head groups (nitrogen and anion halide), covalently attached to four functional hydrophobic alkyl groups. At a high hydrophilic density (N^+-Cl^-, O^--H^+ etc.), surface chemistry is altered, decreasing OTES hydrophobic groups, thus lowering CA.

Compared to CA, contact angle hysteresis (CAH) exhibited a linear relationship with increasing molar ratio of [QUATs/OTES] (shown in the Supporting Information, Table S 5.2). OTES passivated Al showed a CAH of $9 \pm 3.6°$, where droplet becomes unstable and starts to roll-off on the surfaces. However, as molar ratio of [QUATs/OTES] increased, CAH gradually increased to $15 \pm 5°$ until droplet stuck on the surface with large values of CAH (Supporting Information, can be found in Table S 5.2).
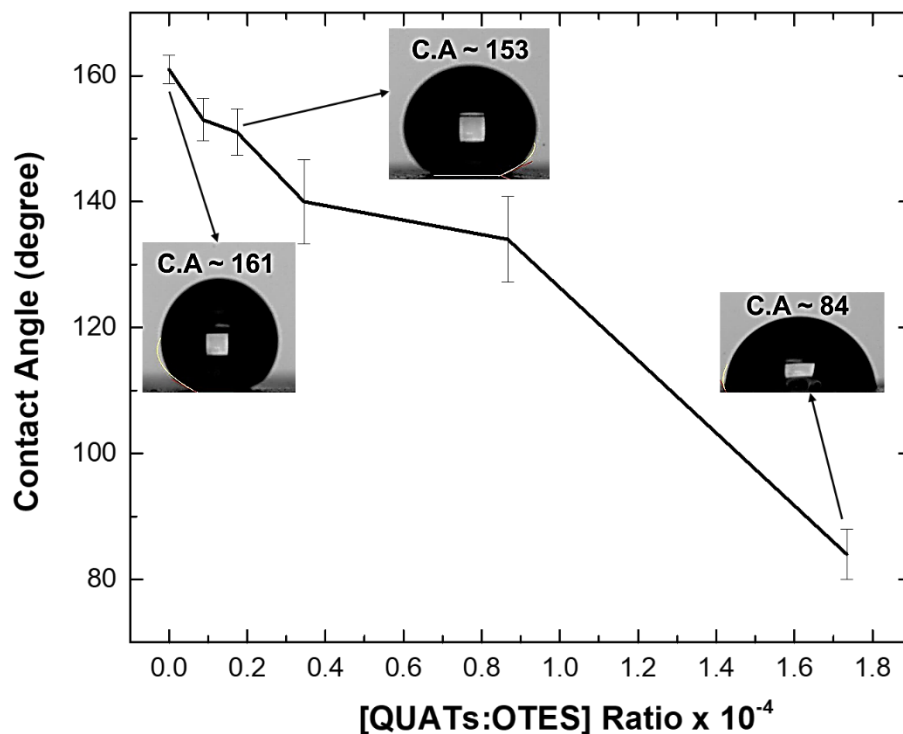
Figure 5-3. Variation in contact angle as a function of QUATs/OTES molar ratio. © Henry Agbe, 2021.

To further evaluate the durability of superhydrophobic OTES-QUATs/Al, UV accelerated weathering test was performed. It is interesting to note that the OTES-QUATs/Al coating was stable for 21 days with a CA > 150°; however, CA reduced gradually, until a lowest value of 121° after 35 days (Figure S 5-6).

5.4.2 Antibacterial activity

Antibacterial property was studied by both disk diffusion and bacterial adhesion assays. Note that disk diffusion describes antibacterial assay that utilizes the diffusion of antimicrobial agents to inhibit the growth of microorganisms. The region surrounding antimicrobial agent, where

microbial growth is inhibited is called the Zone of inhibition (ZOI). The larger the ZOI, the better and effective the antimicrobial agent. It should be mentioned that QUATs are membrane-active agents that interact with the cytoplasmic membrane of bacteria and lipids of viruses [29]. They are very effective antimicrobial agent and first-line defence disinfectants against a wide variety of pathogenic microorganisms, used generally for sanitizing hospital environment [30]. As shown in Figure 5.4 (a), the disk diffusion assay results for S.A showed a zone of inhibition (ZOI) of 39 ± 0.8, 34 ± 1.6, and 12.0 ± 0.5 for ethanoic QUATs, OTES-QUATs and OTES, respectively. Similar trends were also observed for the other bacteria, namely P.A and *E-Coli*, as given in Table 5.1. Note that the QUATs only partially bonded to the OTES, thus the remained QUATs could leached, forming the zone of inhibition. Again, it should be mentioned that the ZOI for OTES is due to the antibacterial effect of ethanol [31]. Though the antimicrobial mechanism for QUATs is unclear [32], it is generally believed that the electrostatic interaction between the positively charged nitrogen moiety (N^+) in QUATs and the negatively charged intracellular molecules (such as phospholipid bilayer, RNA and DNA), leads to cell membrane and cytoplasmic (lipid or protein) perturbation resulting in subsequent bacterial death [32, 33]. Again, due to its amphiphilic nature, hydrophobic tails can interact electrostatically with the hydrophobic groups of the phospholipid bilayer and in the process, disrupt bacterial membrane core, leading to bacterial death [34]
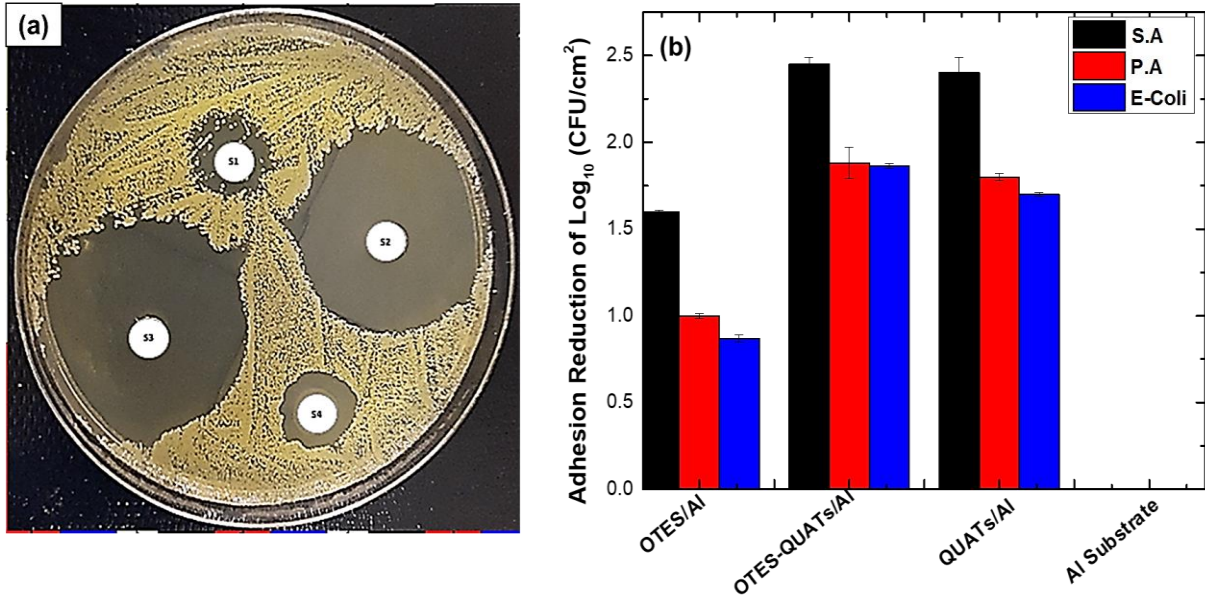
Figure 5-4. (a) Disk Diffusion assay of ethanoic solution of: OTES (Region S1); OTES-QUATs (region S2); (QUATs) (region S3) and Ethanol (region S4), treated against Staphylococcus aureus bacterium; and (b) Graphical representation of adhesion reduction of S.A, P.A and *E-coli* on OTES/Al, OTES-QUATs/Al, QUATs/Al and etched Al substrate. © Henry Agbe, 2021.

Table 5-1 Disk diffusion assay results of OTES-QUATs samples.

Agent	Mean diameter Zone of inhibition (ZOI)(mm)		
	Gram-positive bacterium	Gram-negative bacteria	
	Staphylococcus aureus (ATCC 6538)	*P. aeruginosa* (ATCC 9027)	*E. coli* (ATCC 7839)
OTES	12.0 ± 0.5	11.0 ± 1.0	11.0 ± 1.3
OTES-QUATs	34 ± 1.6	22 ± 1.4	25 ± 0.9
QUATs	39 ± 0.8	24 ± 1.2	27 ± 0.8
Ethanol	13 ± 0.8	12 ± 0.5	12 ± 0.5

Figure 5.4 (b) shows the graphical representation of bacterial adhesion reduction/cm^2 for the model bacteria under study (shown in the Supporting Information, Table S 5.3). OTES passivated aluminum sample showed a bacterial adhesion reduction factor of 1.6 (98%), 1.0 (90%) and 0.9 (87%) for S.A, P.A and *E-Coli* respectively, compared to etched Al substrate. Contrarily, OTES-QUATs/Al samples exhibited a log reduction of 2.45 (99.9%), 1.88 (99%) and 1.85 (99 %) for same bacteria respectively. Similarly, QUATs/Al sample, showed a 2.39 (99.6%), 1.79 (98.4%) and 1.69 (98.0%) log reduction. However, on etched Al substrate (used as control), there were no significant reduction in bacterial colony. Compared to OTES/Al samples, the OTES-QUATs/Al samples were superior and exhibited ~ two order of magnitude higher by reduction factor due to the synergistic effects of QUATs and OTES.

It is worthwhile mentioning that the OTES-QUATs passivated etched aluminum compares favourably to other superhydrophobic coatings/surfaces reported in the literature [11, 12]. For example, in the work of Chung et al [12], a silver-perfluorodecanethiolate superhydrophobic coatings on silicon wafer exhibited bacterial adhesion reduction factor of 77%. Also, in a related study by Wang et al [11] a perfluorodecyltrichlorosilane superhydrophobic diamond films showed a bacterial adhesion reduction of 90-99%. However, direct comparison of reported results in the literature must be treated with caution, due to possible different experimental conditions. In this study the superhydrophobic surfaces fabricated from a biocompatible siloxane precursor and a commonly used disinfectants (QUATs), which exhibits an excellent bacterial adhesion reduction factor of 99.9, 99 and 99 % against S.A, (Gram +ve) bacterium, and P.A and *E-Coli* (Gram −ve) bacterial, respectively, appears promising. In general, the OTES-QUATs on aluminum surface exhibits both anti-biofouling and antibacterial properties due to the combined effects of low energy OTES and nano−micro roughness and the presence of QUATs, respectively. As a further study, OTES-QUATs solution was dropped cast on cotton fiber and tissue paper and exhibited water roll-off property (Videos S5.1 & S5.2) suggesting that superhydrophobic OTES-QUATs could be explored in fabricating anti-biofouling healthcare consumables such as nose masks, bedsheets and medical scraps.

5.5   Conclusions

In this study, aluminum surfaces with tunable superhydrophobic, anti-biofouling and antibacterial properties have been described. These surfaces have been fabricated by chemical etching of aluminum substrates followed by passivation with OTES-QUATs molecules. The

OTES-QUATs solution exhibited excellent antibacterial activity with a ZOI of 34 ± 1.6, 22 ± 1.4, and 25 ± 0.9, against *Staphylococcus aureus*, *Pseudomonas aeruginosa and Escherichia coli,* respectively. Similarly, OTES-QUATs on aluminum surface showed superior anti-biofouling property of 99.9, 99 and 99% bacterial adhesion reduction for same bacteria respectively, due to both superhydrophobic nature of OTES and antibacterial nature of OUATs molecules. Overall, the antibacterial properties of the OTES-QUATs passivated aluminum looks promising and can be regarded as an adjunct to hand hygiene for reducing potential bacterial infections in hygiene critical environment.

5.6   **Supporting information**

Table S5-1 QUATs/OTES Molar ratio.

Samples	QUATs: OTES Molar Ratio $\times 10^{-4}$	Volume of Ethanol (mL)
1	0.000	50
2	0.087	50
3	0.174	50
4	0.360	50
5	1.737	50
6	8.682	50
7	54.000	50

Table S5-2 Variation of surface roughness, contact angle (CA), contact angle hysteresis, (CAH) and E-Coli adhesion reduction on etched Al; OTES/Al; OTES-QUATs/Al; and QUATs/Al samples.

Samples	Surface Roughness (rms)/μm	Contact Angles (°)	Contact Angle Hysteresis (°)	E-Coli Reduction (%)
OTES/Al	6.5 ± 0.5	161 ± 2.3	9 ± 3.6	87.0
OTES-QUATs/Al	5.8 ± 0.5	153 ± 3.7	15 ± 5	99.0
QUATs/Al	4.3 ± 0.4	40 ± 0.4	>	98.0
Etched Al Substrate	6.2 ± 1.5	16 ± 0.2	>	0
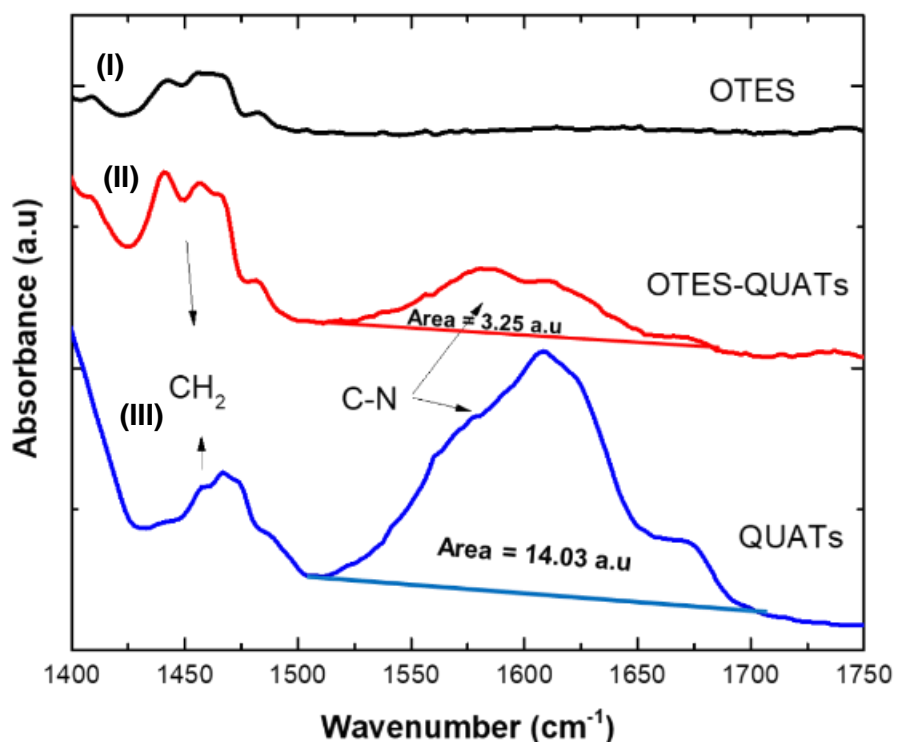
Figure S5-5. ATR-FTIR spectra showing no C–N region for (I) octyltriethoxysilane molecules passivated etched Al substrate (OTES/Al); and with selected region showing C–N vibration mode for (II) Octyltriethoxysilane and quaternary ammonium molecules passivated etched Al substrate (OTES-QUATs/Al); and (III) Quaternary ammonium molecules passivated etched aluminum (QUATs/Al). © Henry Agbe, 2021.
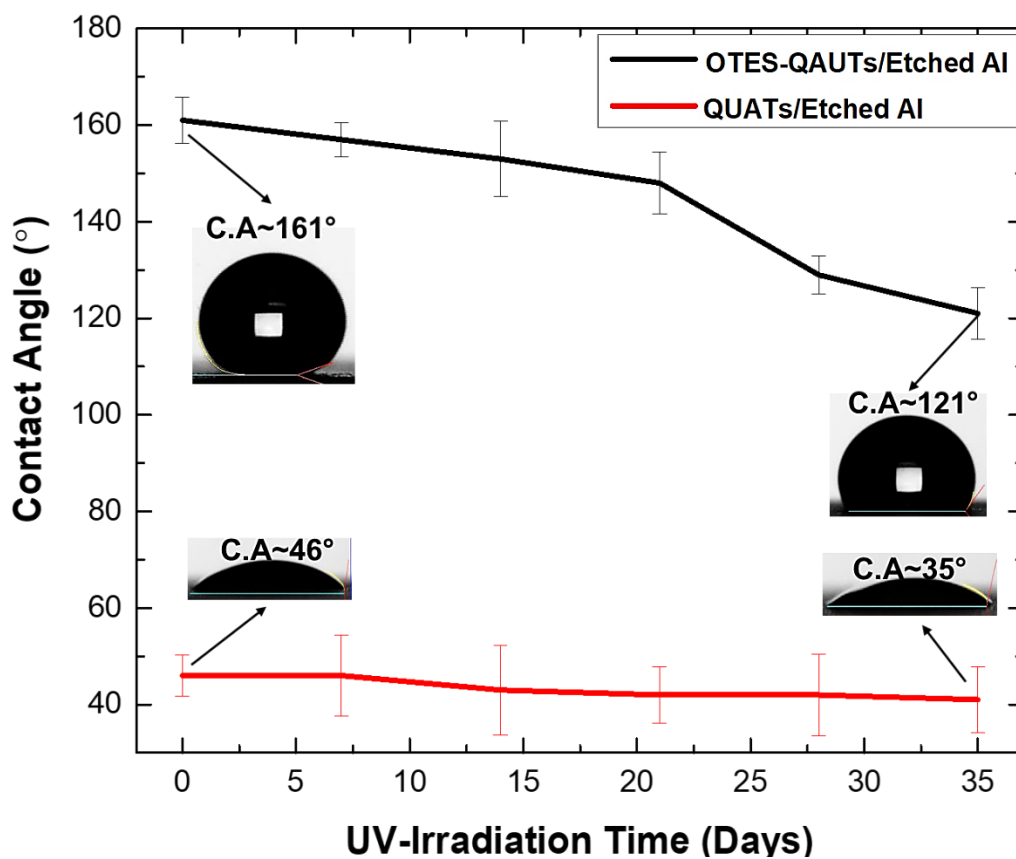
Figure S5-6. Variation of water contact angle as a function of UV irradiation time. © Henry Agbe, 2021.

Table S 5-3. Bacterial count on OTES-QUATs passivated aluminum and as-received Aluminum.

Model Bacterial Strain	-	Aluminum Substrate	OTES/Al	OTES-QUATs/Al	QUATs/Al
Staphylococcus aureus (ATCC 6538)	CFU/cm^2 after 3 h	43,333,333	1065833	153333.3	160,000
-	Reduction Rate [%]	0	97.5	99.7	99.6
-	Log 10 Reduction	-	1.6	2.45	2.39
Pseudomonas aeruginosa (ATCC 9027)	CFU/cm^2 after 3 h	16,250,000	1593333	234,166.7	255000
-	Reduction Rate [%]	0	89.7	98.7	98.4
-	Log 10 Reduction	-	1.0	1.88	1.79
Escherichia coli (ATCC 7839)	CFU/cm^2 after 3 h	16,250,000	2,193,333	222,500	322500
-	Reduction Rate [%]	0	86.5	98.6	98.0
-	Log 10 Reduction	-	0.87	1.85	1.69

Video
S1 OTES QUA

Video 5.S1. OTES-QUATs treated cotton fiber.

Video
S2 OTES QUA **Video 5.S2.** OTES-QUATs treated tissue paper.

5.7 References:

1. Vrana, N.E., *Biomaterials and Immune Response: Complications, Mechanisms and Immunomodulation*. 2018: CRC Press.
2. Walker, J., *Decontamination in Hospitals and Healthcare*. 2019: Woodhead Publishing.
3. Kramer, A., I. Schwebke, and G. Kampf, *How long do nosocomial pathogens persist on inanimate surfaces? A systematic review.* BMC infectious diseases, 2006. **6**(1): p. 130.
4. Öner, D. and T.J. McCarthy, *Ultrahydrophobic Surfaces. Effects of Topography Length Scales on Wettability.* Langmuir, 2000. **16**(20): p. 7777-7782.
5. M.B. Olde riekerink, J.G.A. Terlingen, J.G.A. Terlingen, G.H.M. Engbers, Jan Feijen, *Selective Etching of Semicrystalline Polymers: CF4 Gas Plasma Treatment of Poly(ethylene).* 1999: p. 4847-7463.
6. Momen, G., M. Farzaneh, and R. Jafari, *Wettability behaviour of RTV silicone rubber coated on nanostructured aluminium surface.* Applied Surface Science, 2011. **257**(15): p. 6489-6493.
7. Safaee, A., D.K. Sarkar, and M. Farzaneh, *Superhydrophobic properties of silver-coated films on copper surface by galvanic exchange reaction.* Applied Surface Science, 2008. **254**(8): p. 2493-2498.
8. Brassard, J.-D., D.K. Sarkar, and J. Perron, *Synthesis of monodisperse fluorinated silica nanoparticles and their superhydrophobic thin films.* ACS applied materials & interfaces, 2011. **3**(9): p. 3583-3588.
9. Shuhao Liu, Li Hao, Yagmur Yegin, Michael Bae, Beril Ulugun, Thomas Matthew Taylor, Ethan A. Scholar, Luis Cisneros-Zevallos, Jun Kyun Oh, Mustafa Akbulut, *Dual-Functional, Superhydrophobic Coatings with Bacterial Anticontact and Antimicrobial Characteristics.* ACS Applied Materials & Interfaces, 2020.
10. Elena Fadeeva, Vi Khanh Truong, Meike Stiesch, Boris N Chichkov, Russell J Crawford, James Wang, Elena P Ivanova, *Bacterial retention on superhydrophobic titanium surfaces fabricated by femtosecond laser ablation.* Langmuir, 2011. **27**(6): p. 3012-3019.
11. Tao Wang, Lei Huang, Yuzhi Liu, Xingxing Li, Chunhua Liu, Stephan Handschuh-Wang, Yang Xu, Ying Zhao, Yongbing Tang, *Robust Biomimetic Hierarchical Diamond Architecture with a Self-Cleaning, Antibacterial, and Antibiofouling Surface.* ACS applied materials & interfaces, 2020. **12**(21): p. 24432-24441.
12. Jae-Seung Chung, Byoung Gak Kim, Soojin Shim, Seong-Eun Kim, Eun-Ho Sohn, Jeyong Yoon, Jong-Chan Lee, *Silver-perfluorodecanethiolate complexes having superhydrophobic, antifouling, antibacterial properties.* Journal of colloid and interface science, 2012. **366**(1): p. 64-69.
13. Mei Zhang, Ping Wang, Hongyan Sun, Zuankai Wang, *Superhydrophobic surface with hierarchical architecture and bimetallic composition for enhanced antibacterial activity.* ACS applied materials & interfaces, 2014. **6**(24): p. 22108-22115.
14. Hays, H.L., D. Mathew, and J. Chapman, *Fluorides and Fluorocarbons Toxicity.* StatPearls [Internet], 2020.
15. Hsiu-Ju Yen, Jiun-Lin Horng, Ching-Hua Yu, Ching-Ya Fang, Ya-Hsin Yeh, Li-Yih Lin, *Toxic effects of silver and copper nanoparticles on lateral-line hair cells of zebrafish embryos.* Aquatic Toxicology, 2019. **215**: p. 105273.
16. Control, C.f.D. and Prevention, *Severe acute respiratory illness linked to use of shoe sprays--Colorado, November 1993.* MMWR. Morbidity and mortality weekly report, 1993. **42**(46): p. 885.

17. Meier, M., V. Dubois, and S. Seeger, *Reduced bacterial colonisation on surfaces coated with silicone nanostructures.* Applied Surface Science, 2018. **459**: p. 505-511.

18. Arash Bahrami, Reza Rezaei Mokarram, Mahmoud Sowti Khiabani, Babak Ghanbarzadeh, Roya Salehi, *Physico-mechanical and antimicrobial properties of tragacanth/hydroxypropyl methylcellulose/beeswax edible films reinforced with silver nanoparticles.* International journal of biological macromolecules, 2019. **129**: p. 1103-1112.

19. Kuo-Hui Wu, Je-Chuang Wang, Jo-Yu Huang, Chen-Yang Huang, Yi-Hui Cheng, Nien-Tung Liu, *Preparation and antibacterial effects of Ag/AgCl-doped quaternary ammonium-modified silicate hybrid antibacterial material.* Materials Science and Engineering: C, 2019. **98**: p. 177-184.

20. Hasan, A. and L.M. Pandey, *Kinetic studies of attachment and re-orientation of octyltriethoxysilane for formation of self-assembled monolayer on a silica substrate.* Materials Science and Engineering: C, 2016. **68**: p. 423-429.

21. Zhang, F. and M. Srinivasan, *Self-assembled molecular films of aminosilanes and their immobilization capacities.* Langmuir, 2004. **20**(6): p. 2309-2314.

22. Si-Dong Li, Pu-Wang Li, Zi-Ming Yang, Zheng Peng, Wei-Yan Quan, Xi-Hong Yang, Lei Yang, Jing-Jing Dong, *Synthesis and characterization of chitosan quaternary ammonium salt and its application as drug carrier for ribavirin.* Drug delivery, 2014. **21**(7): p. 548-552.

23. Kurrey, R., M.K. Deb, and K. Shrivas, *Surface enhanced infra-red spectroscopy with modified silver nanoparticles (AgNPs) for detection of quaternary ammonium cationic surfactants.* New Journal of Chemistry, 2019. **43**(21): p. 8109-8121.

24. Poberžnik, M. and A. Kokalj, *Implausibility of bidentate bonding of the silanol headgroup to oxidized aluminum surfaces.* Applied Surface Science, 2019. **492**: p. 909-918.

25. Escobar, A.M. and N. Llorca-Isern, *Superhydrophobic coating deposited directly on aluminum.* Applied surface science, 2014. **305**: p. 774-782.

26. Hosono E, Fujihara S, Honma I, Haoshen zhou, *Superhydrophobic perpendicular nanopin film by the bottom-up process.* Journal of the American Chemical Society, 2005. **127**(39): p. 13458-13459.

27. Wenjing Ma, Yichun Ding, Mengjie Zhang, Shuting Gao, Yuansheng Li, Chaobo Huang, Guodong Fu, *Nature-inspired chemistry toward hierarchical superhydrophobic, antibacterial and biocompatible nanofibrous membranes for effective UV-shielding, self-cleaning and oil-water separation.* Journal of hazardous materials, 2020. **384**: p. 121476.

28. Brassard, J.-D., D.K. Sarkar, and J. Perron, *Studies of drag on the nanocomposite superhydrophobic surfaces.* Applied Surface Science, 2015. **324**: p. 525-531.

29. Gerba, C.P., *Quaternary ammonium biocides: efficacy in application.* Appl. Environ. Microbiol., 2015. **81**(2): p. 464-469.

30. Megan C Jennings, Bettina A Buttaro, Kevin P C Minbiole, William M Wuest, *Bioorganic investigation of multicationic antimicrobials to combat QAC-resistant Staphylococcus aureus.* ACS infectious diseases, 2015. **1**(7): p. 304-309.

31. Batzing, B.L., *Microbiology: an introduction*. 2002: Brooks/Cole Pacific Grove, CA.

32. Gregory A. Knauf, Ashley L. Cunningham, Misha I. Kazi, Ian M. Riddington, Alexander A. Crofts, Vincent Cattoir, M. Stephen Trent, Bryan W. Davies, *Exploring the antimicrobial action of quaternary amines against Acinetobacter baumannii.* MBio, 2018. **9**(1): p. e02394-17.

33. Minghao Zeng, Jiayun Xu, Quan Luo, Chunxi Hou, Shanpeng Qiao, Shuang Fu, Xiaotong Fan, Junqiu Liu, *Constructing antibacterial polymer nanocapsules based on pyridine quaternary ammonium salt.* Materials Science and Engineering: C, 2020. **108**: p. 110383.

34.   Yang Jiao, Li-Na Niu, Sai Ma, Jing Li, Franklin R Tay, Ji-Hua Chen, *Quaternary ammonium-based biomedical materials: State-of-the-art, toxicological aspects and antimicrobial resistance.* Progress in Polymer Science, 2017. **71**: p. 53-90.

CHAPTER 6

CHAPTER 6

Chapter 6 is under peer review in the Journal of Materials Chemistry B, and authored by Henry Agbe, Dilip Sarkar Kumar, and X-Grant Chen. As a first author, I conceived, designed, and performed all experiments, analyzed and interpreted the results, as well as wrote both the original and final manuscript.

6   Abstract

A two-step electrochemical deposition process has been deployed to fabricate Ag_3PO_4 antibacterial coating on anodized aluminum surfaces. Structural, morphological, and chemical compositional analyses characterized by XRD, SEM and FTIR, confirm the formation of crystalline Ag_3PO_4 nanoparticles. The Ag_3PO_4 coated anodized aluminum resulted in 100% *Escherichia coli* (*E. coli*) bacteria inactivation. Furthermore, susceptibility and photocatalysis studies on powdered (5 µg/mL) Ag_3PO_4 nanoparticles showed excellent antibacterial properties with a zone of inhibition of 20 ± 1.3 mm and 100% *E. coli* inactivation under 15 min of visible-light irradiation. Additionally, the electrochemically synthesized Ag_3PO_4 coating on anodized aluminum exhibited a remarkably high adhesion.

6.1   **Introduction**

Silver is a metallic element of great value in human civilisation. It finds application in photography, catalysis and antimicrobial applications among many others [1]. In particular, antimicrobial property of silver has been known throughout history, and was used to fight

microbial infections until the discovery of penicillin in the 1940s [2]. However, the inherent ability of microorganisms to mutate, coupled with indiscriminate use of antibiotics has resulted in the development of antimicrobial resistant strains to conventional antibiotics, necessitating the need for novel antimicrobial solutions. In this regard, nanotechnology can serve as an important toolkit for synthesizing variety of promising antimicrobial materials such as antimicrobial silver phosphate nanoparticles.

Silver phosphate (Ag_3PO_4) is a high quantum yield visible-light active photocatalytic nanomaterial [3]. Since its discovery by Yi et a l [4] in 2010, various groups have reported on the excellent photocatalytic performance of Ag_3PO_4 for various applications, including water purification, environmental remediation, water splitting and most importantly, the antibacterial applications [3, 5, 6]. Xie X et al [7] demonstrated an antibacterial property of silver phosphate using the synergistic effect of Ag^+ ion and reactive oxygen species (ROS) in both vitro and in vivo systems [7]. They showed that by immobilizing polydopamine (PDA)/Ag_3PO_4/graphene oxide (GO) coatings on both titanium alloy and polyether ether ketone (*PEEK*), the hybrid coating could maintain a repeatable and sustained antibacterial efficacy against both *Staphylococcus Aureus* (gram +ve) and *E. coli* (gram –ve). Similarly, in the work of Yingde Xu et al [8], a synergistic antibacterial effects of nanospikes and Ag_3PO_4-TiO_2- photocatalyst was able to inactivate both *Staphylococcus Aureus* (gram +ve) and *E.coli* (gram –ve) bacteria under 20 min of visible light irradiation. Meanwhile, Zhang, C et al [9] showed that nanocomposite power of polyvinyl alcohol hydrogel (PAH), reduced graphene oxide (RGO), molybdenum disulphide (MoS_2) and silver phosphate (Ag_3PO_4), under co-irradiation of 660 nm (visible light) and 808 nm (near-infrared light) could inactivate both *Staphylococcus aureus* and *E.coli* bacteria [9]. Note that antibacterial property of Ag_3PO_4, can also be enhanced by the PO_4^{3-} groups, which can attract bacteria in a

"Trojan horse system", interfering with the Adenosine triphosphate/Adenosine diphosphate (ATP/ADP) interconversion cycle through competitive inhibition pathways to inactivate bacterial cell [10].

Conventionally, Ag_3PO_4 has been synthesized by ion exchange, precipitation and hydrothermal synthesis processes [11]. Hong L. et al, used hydrothermal method to fabricate a Bi_2S_3 nanorod (NR) arrays on titanium (Ti) implants, followed by a stepwise electrostatic adsorption of Ag_3PO_4 nanoparticles (NPs) [12]. While the coating demonstrated an excellent biocompatibility and antibacterial properties against both *Staphylococcus aureus* and *E. coli*, the adhesive property of the coating on the titanium implants was not reported. For application on frequently touched surfaces such as doorknobs and countertops, where coatings must adhere to underlying substrates, wet chemistry technique such as electrochemical deposition processes are desirable. , Yi *et al* [4] has reported Ag_3PO_4 synthesis by electrochemical process for deposition on indium tin-oxide (ITO)-coated glass substrate. However, their application was not focussed on antibacterial properties, and rather, on successful coating for water splitting application. Furthermore, electrochemical silver-phosphate synthesis has been limited to hydroxyapatite-based compounds [13-15], presumably due to their unique osseo-integration property as reported. Fu *et al* [13] deplored a two-step electrochemical process to fabricate a silver-hydroxyapatite (Ag-$Ca_{10}(PO_4)_6(OH)_2$) on titanium alloy surface for orthopaedics and dental implant applications. The titanium alloy was first coated with hydroxyapatite during the oxidation process, followed by silver nanoparticles deposition on the hydroxyapatite during the reduction process. Their silver-hydroxyapatite coated titanium alloy was effective in inhibiting the growth of gram (-) *E. coli* bacteria by 87% in a span of 8 h. In a similar study, Mokabber *et al* [14] used a pulsed

electrodeposition method to fabricate silver-calcium phosphate coatings on titanium substrates. The silver-calcium phosphate coatings exhibited an antibacterial efficiency between 76 to 99.7% for *Staphylococcus aureus* bacterium in 48 h. In a related study, Jianghong L. et al [16] fabricated a pyrrole/hydroxyapatite/ZnO-Ag-Cu nanocomposite coatings on Ti substrate using pulse electrochemical method. During the oxidation step, pyrrole was polymerized into polypyrrole, and then followed by nucleation and growth of hydroxyapatite (from PO_4^{3-}-based electrolyte) during the reduction step. This coating was not only effective in inactivating bacteria, but also in promoting growth and proliferation of both Vascular Endothelial Cells (VECs) and Bone Marrow Mesenchymal Stem Cells (BMSCs). From the foregoing, it is noticeable that reported work on electrochemical process has been limited to titanium alloys due to their biocompatibility [17-21]. However, as aluminum is a commonly used engineering material for general construction and fabrication of frequently touched surfaces, it is important the surface of aluminum be modified to exhibit antibacterial property via electrochemical process such as deposition of silver phosphate on the anodized aluminum oxide surfaces.

In the present work, a two-step electrochemical process has been deployed to fabricate Ag_3PO_4 nanoparticles on anodized aluminum oxide for antibacterial applications. Ag^+ ion was first reduced to Ag^0 metal at a reduction process, while the metallic Ag^0 was oxidized again into Ag^+ ion. Antibacterial properties of the Ag_3PO_4 coated anodized aluminum (Ag_3PO_4/AAO/Al) were studied by a novel dry seeding, Kirby Bauer disk diffusion and photocatalytic assays, showing promising results for application on frequently touched aluminum parts.

6.2   Experimental section

6.2.1   Anodization of aluminum

AA6061-T6 aluminum alloys of dimensions 2.54 cm x 5.08 cm were degreased under ultrasound washing in a diluted soap solution (LIQUINOX), followed by distilled water for 15 minutes. Next, 1 M NaOH (VWR) chemical etching at 55 °C was performed for 3 minutes to remove the weak native oxide layer from the clean Al surfaces. The etched Al substrates were then immersed in HNO_3 solution (10 wt. %, VWR) for desmutting, followed by rinsing in distilled water. Subsequently, etched and desmutted Al alloys were anodized in an acidic electrolyte of 3 wt.% H_3PO_4 (VWR) in galvanostatic mode at a constant current density of 40 mA/cm^2 for 120 minutes. The electrochemical cell was equipped with a 600 W direct current power supply (Ametek Sorensen DCS 100-12E, Chicoutimi, QC, Canada), a quartz-jacketed beaker with circulating cold water (5 °C), and a small magnetic Teflon stirrer, rotating at 2000 rpm. Finally, the anodized aluminum oxide (AAO/Al) samples were dried at 70 °C overnight in an electric oven (VWR). For quality control and reproducibility, each experiment was repeated in triplicate.

6.2.2   Electrochemical deposition of Ag₃PO₄ nanoparticles

A two-step redox electrochemical process was deployed to deposit Ag_3PO_4 nanoparticles in situ on anodized aluminum oxide layer (AAO/Al) in a regular two-electrode cell. In the first stage, AAO/Al and as-received aluminum (used as cathode and anode electrodes, respectively) were immersed in a 0.12 M $AgNO_3$ electrolyte solution under a -1.0 V DC potential and a

temperature of $65 \pm 1\,°C$, while stirring with a magnetic Teflon stirrer rotating at 500 rpm for 15, 30 and 60 minutes. In the second stage, electrodes were exchanged, where the Ag coated anodized aluminum oxide (Ag/AAO/Al) and as-received aluminum were used as anode and cathode, respectively. The electrodes were immersed in a 0.12 M sodium orthophosphate (Na_2HPO_4) electrolytic solution under a 10 V DC potential for 60 seconds at a temperature of $65 \pm 1\,°C$. During this process, metallic Ag^0 oxidizes to react with orthophosphate anions (PO_4^{3-}) to form the Ag_3PO_4 [4] in situ on anodized aluminum pores. To investigate antibacterial activity in aqueous conditions, powder form of Ag_3PO_4 was also prepared, by following a modified ion-exchange process described in our previous contribution [3]. Briefly, 0.12 M $AgNO_3$ was completely dissolved in 100 mL distilled water under constant magnetic stirring. Next 0.12 M of Na_2HPO_4 was added dropwise to above solution under continuous stirring for 15 minutes to form the Ag_3PO_4 deposits in the solution. The powdered Ag_3PO_4 was washed severally with deionised water, followed by drying at 70 ˚C overnight in an electric oven (VWR).

6.2.3 Sample characterization

The micro-nanostructure and morphological analyses were performed using Scanning Electron Microscopy (SEM, JEOL JSM-6480 LV, Pleasanton, USA). Elemental composition of the Ag_3PO_4 nanoparticles were further analyzed with the SEM equipped energy-dispersive spectroscopy (SEM/EDS). The crystalline structure and chemical composition were analyzed using X-ray powder diffraction (XRD) (a Bruker D8 Discover system) and attenuated total reflection-Fourier transform infrared (ATR, Agilent Technologies Cary 630 FTIR), respectively. The XRD data are collected in the 2θ range of $10-80°$ with a step size of $0.02°$, while the FTIR spectra were collected

191

in the range of 4000 – 500 cm^{-1}. Crosshatch Cutter, ASTM D-3359, (ASTM standard) was used to evaluate adhesion level of the Ag$_3$PO$_4$ coated anodized aluminum.

6.2.4   **Antibacterial assays.**

Antibacterial performances were determined by dry seeding, Kirby Bauer disk diffusion assays and photocatalysis. Dry seeding was performed as follows: The *E. coli* bacterium (ATCC 8739), was grown overnight from frozen (−80 °C) glycerol stock in tryptic soy broth (TSB) (Hardy Diagnostics) at 37 °C. A sub-culture was prepared on the fresh TSB (37 °C) to obtain bacterial cell density of 10^8 colony forming units/milliliter, (CFU)/mL. Cell density was determined at a wavelength of 625 nm at an absorbance of 0.1. Next, 5 µL of bacterial inoculum was seeded onto a sterile 2.54 cm x 2.54 cm Ag$_3$PO$_4$ coated anodized aluminum and control coupons. Coupons were incubated at ambient conditions of temperature (25 °C) and relative humidity (50 ± 10%) in a Class II Biological safety cabinet for a pre-determined contact time (0, 15, 60, 90, 240 and 1440 minutes). Sterile swab was then used to sample bacteria into a physiological saline (0.85 wt.% NaCl), followed by serial dilutions and plating on tryptic soy agar (TSA). Agar plates were then aerobically incubated at a temperature of 37 °C for 24 h to yield countable viable bacterial colonies (30–300 colonies per plate). Three independent experiments were performed from fresh culture and repeated to determine number of viable bacteria. Data were analyzed by a one-way analysis of variance (ANOVA) with the Tukey–Kramer multiple comparison test. Results were considered significant at $p < 0.05$. Antibacterial efficiency was calculated as: $[(A-B)]/A \times 100$ %, where A = colony-forming unit per cm^2 (CFU/cm^2) of viable bacteria on Ag$_3$PO$_4$ coated anodized aluminum coupon and B = CFU/cm^2 of viable bacteria on as-received aluminum coupon (as control).

The Kirby Bauer disk diffusion assay was prepared as described in our previous work [22]. Similar protocol described above was used to grow bacterial culture. For photocatalysis-mediated *E. coli* inactivation, 2g/L Ag_3PO_4 or commercially available TiO_2 anatase (positive control) powder were dispersed in physiological saline, containing *E. coli* inoculum. Next, the reactor flasks were exposed to either the visible light (25-watt table lamp, 17.3 W/m^2) or the UV-A light (30-watt UV-A lamp, 259 nm, 21 W/m^2) under constant stirring, with 1 ml aliquots withdrawn for pre-determined time of 0, 15, 30 and 60 minutes to determine bacteria concentration. This was determined by performing serial dilution, followed by streaking to obtain a bacterial lawn. After incubation at 37 °C for 24 h, the number of viable *E. coli* cells were counted. Bacterial inactivation rate was calculated using equation 3.8 as showed in chapter 3.

6.3   Results and discussion.

6.3.1   Deposition of Ag₃PO₄ on anodized aluminum oxide layer

A two-step redox electrochemical process was deployed to deposit Ag_3PO_4 in situ on an anodized aluminum oxide (AAO/Al) according to Equations 6.1 and 6.2.

Cathodic reaction:

$$Ag^+ + e \rightarrow Ag_s \tag{6.1}$$

Anodic reaction:

$$3Ag_S^0 + PO_4^{3-} \rightarrow Ag_3PO_4 \downarrow + 3e \tag{6.2}$$

During the reduction process, a -1.0V potential reduces Ag^+ ion into metallic Ag^0 in situ on AAO/Al (Figure. 6.1(A)). Evidently, this is a typical current-time transient curve for instantaneous

silver growth [23], where incoming silver atoms occupy all nucleation sites simultaneously at the instant of deposition [24]. As shown in Figure. 6.1(A), current density increased linearly with time and attained a maximum peak of 376 µA/cm^2 and 831 µA/cm^2 after 15 and 60 minutes of electrodeposition, respectively. It should be mentioned that the barrier oxide layer (~250 nm in thickness) of typical sulphuric acid anodized aluminum presents a challenge for metal electrodeposition [25]. Traditionally, two steps have been utilized for DC metal electrodeposition on anodized aluminum. These methods involve removal of base aluminum metal with saturated HgCl$_2$ solution in the first step, and metallization of the anodized alumina, prior to electrodeposition using high applied voltage (> 5V)[25]. However, this is not only cumbersome and time consuming, but also the high applied potential leads to hydrogen gas evolution from water splitting, and an unstable coating [25].

To circumvent this phenomenon, anodization of aluminum was performed with a 3 wt.% H$_3$PO$_4$ and the electrochemical silver reduction achieved at an optimal potential of -1.0V. The mass of silver determined from Equation 6.3 was found to increase linearly with deposition time (Figure. 6.1(B)), where M is the molar mass of deposited Ag^0 (107.87 g mol^{-1}), or PO$_4$ (94.97 g mol^{-1}), Z is the number of electrons transferred or accepted in the redox reaction, F is Faraday's C/mol), I, the current (A) and t, the time (s)

$$m = \frac{MIt}{ZF}$$
(6.3)

Calculated mass of silver was 0, 0.4, 1.6 and 3.4 mg for electrodeposition time of 0, 15, 30 and 60 minutes, respectively and equivalent mass of PO$_4$ of 0.3 mg. (Supporting Information, Table S6.1). After deposition of Ag in AAO/Al, this electrode was used in the solution of Na$_2$HPO$_4$ to deposit Ag$_3$PO$_4$. Figure. 6.1(C) shows the current-time (I-t) transient curve on the growth of

Ag$_3$PO$_4$ from the deposited Ag in the electrolyte of Na$_2$HPO$_4$, utilizing a constant voltage of +10 V.
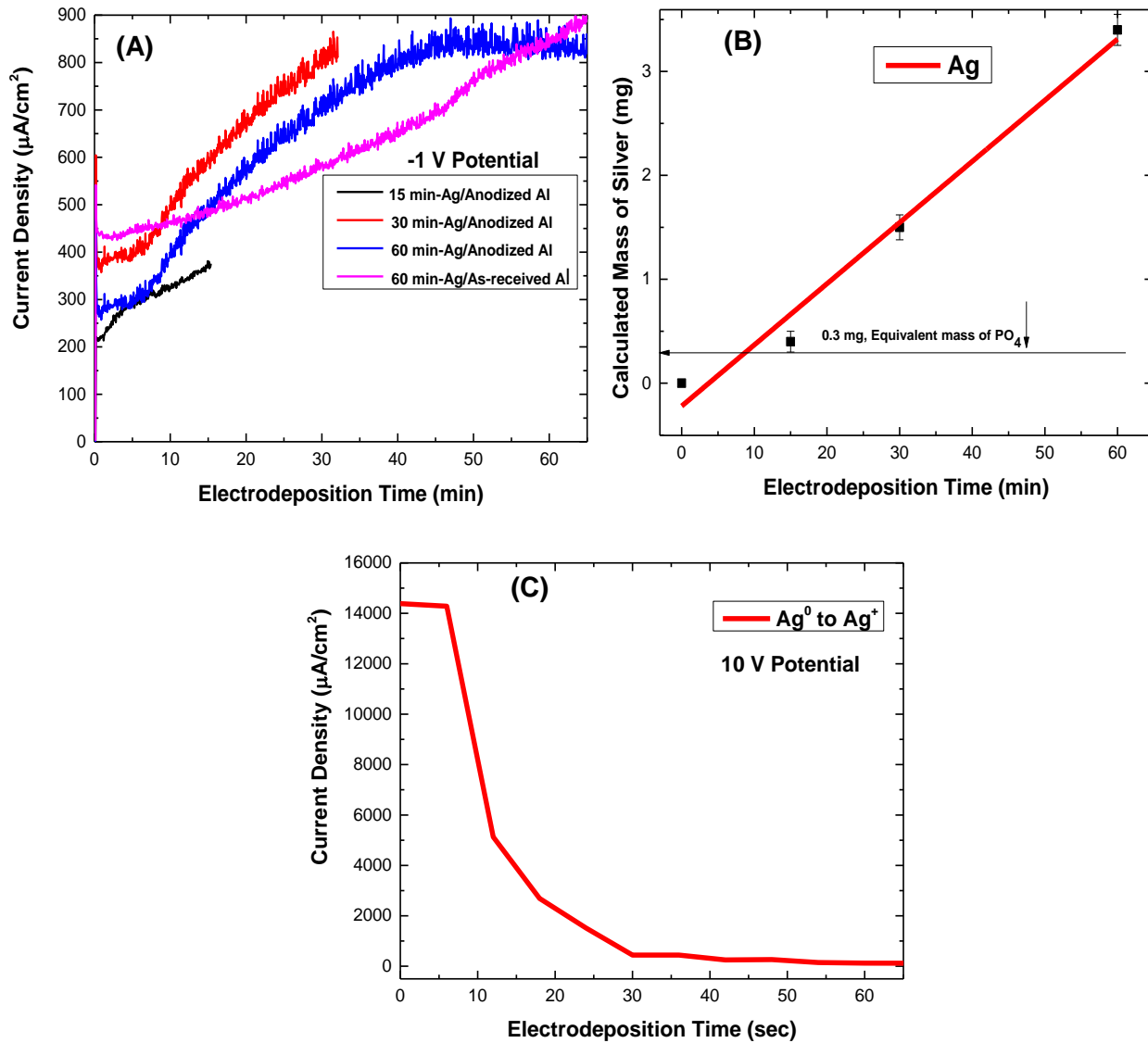
Figure. 6-1. Graphical representation of: (A) Current-time (I-t) transient curve of silver deposition on AAO/Al for 15, 30, and 60 minutes, (B) Calculated mass of Ag from (A); (C) Current-time (I-t) transient curve for electrodeposition of Ag$_3$PO$_4$ on AAO/Al. © Henry Agbe, 2021.

During the oxidation process, metallic Ag^0 oxidizes to Ag^+, which in turn reacts with Na_2HPO_4. Specifically, as metallic Ag^0 oxidizes, Ag^+ reacts with PO_4^{3-} to electrochemically precipitate Ag_3PO_4 [4] in situ on anodized aluminum (Ag_3PO_4/AAO/Al) according to Equation. 6.4

$$3AgNO_3 + Na_2HPO_4 \rightarrow Ag_3PO_4 \downarrow + 2NaNO_3 + HNO_3 \qquad (6.4)$$
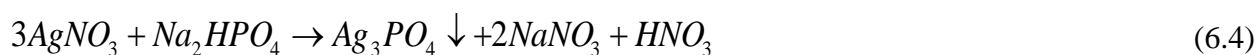
It is observed that this reaction occurred faster and completed in just one minute of +10V. The applied potential among other factors (concentration and pH of electrolyte) plays an important role in electrodeposition. This is due to the fact that the number of active nucleation sites and growth of metallic silver are proportional to applied potential [24].

Morphological analysis of both anodized aluminum oxide (AAO/Al) and Ag_3PO_4 coated anodized aluminum (Ag_3PO_4/AAO/Al) were characterized by SEM. Figure. 6.2(A) shows the SEM micrograph of AAO/Al, exhibiting typical porous morphological features [22]. Figure. 6.2(B), (C) and (D) show SEM micrographs of Ag_3PO_4 deposited electrochemically on anodized aluminum using deposited silver for 15, 30 and 60 minutes, respectively. Evidently, the number density of Ag_3PO_4 nanoparticles increased linearly with electrodeposition time, where 15 minutes led to a randomly distributed and fewer particles of average size, 33 ± 9 nm (Figure. 6.2 (B) and Supporting Information, Figure. S 6.1). However, as the electrodeposition time increased to 30 minutes, the number density of the particles increased accordingly, as characterized by few isolated uncoated areas (Figure. 6.2 (C)). With further increase in deposition time to 60 minutes, individual Ag_3PO_4 nanoparticles of size 91 ± 27 nm presumably merged to form nanoclusters, covering the entire area, (Figure. 6.2 (D) and Supporting Information, Figure. S 6.1). Nanoclusters of Ag_3PO_4 appears to be deposited in situ on AAO/Al pores of diameter of 151 ± 37 nm, as shown in Figures. 6.2.(E) and (F).
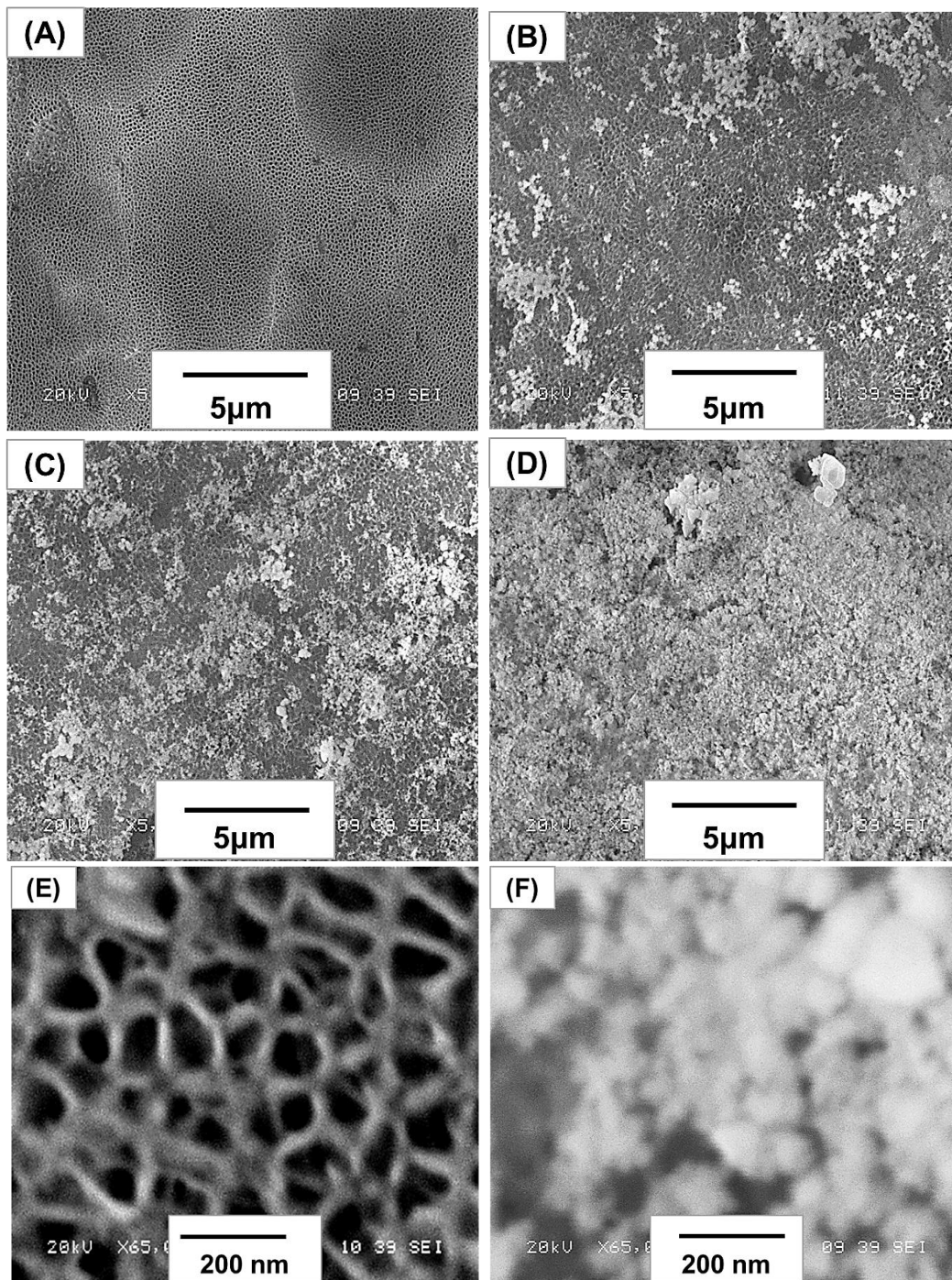
Figure. 6-2. SEM images of (A) AAO/Al; and electrodeposition of Ag_3PO_4 on AAO/Al using deposited silver for (B) 15 minutes; (C) 30 minutes; and (D) 60 minutes, respectively; and high magnification images of (E) AAO/Al and (F) Ag_3PO_4 on AAO/Al. © Henry Agbe, 2021.

Since chemical nature of Ag_3PO_4 coated anodized aluminum is important for determining Ag^+ release kinetics, a representative portion of Ag_3PO_4 coated anodized aluminum using 60 minutes deposited silver, was examined using EDS elemental mapping. Among serval locations of the elemental mapping, Fig. 6.3(A) shows the SEM micrograph of the representative site, while the Figures. 6.3 (B), (C), (D) and (E) show the elemental mapping of Al, O, Ag and P, respectively. Notably, Al and O, arising from porous oxide layer of AAO/Al covered the entire selected area (Figure. 6.3(B) and (C)), confirming the successful anodization. In addition, uniformly distributed patterns of Ag nanocluster are visibly distributed on entire selected area, as evident in Figure. 6.3 (D). A similar trend was observed for P, albeit a low mass (Figure. 6.3 (E)). It should be reiterated that a relative mass of 11.333 (Ag^+/PO_4) was observed for Ag_3PO_4 coated anodized aluminum. From both SEM micrograph and EDS elemental mapping, it is evident that Ag_3PO_4 nanoparticles was uniformly deposited on entire range of randomly selected area of the Ag_3PO_4 coated anodized aluminum. Additionally, EDS confirmed the elemental composition to consist of O, Al, and P with corresponding K_α peaks values at 0.52, 1.48, 2.01 keV respectively, and L_α peak of Ag at 2.98 keV (Figure. 6.3 (F) and Figure. 6.4).
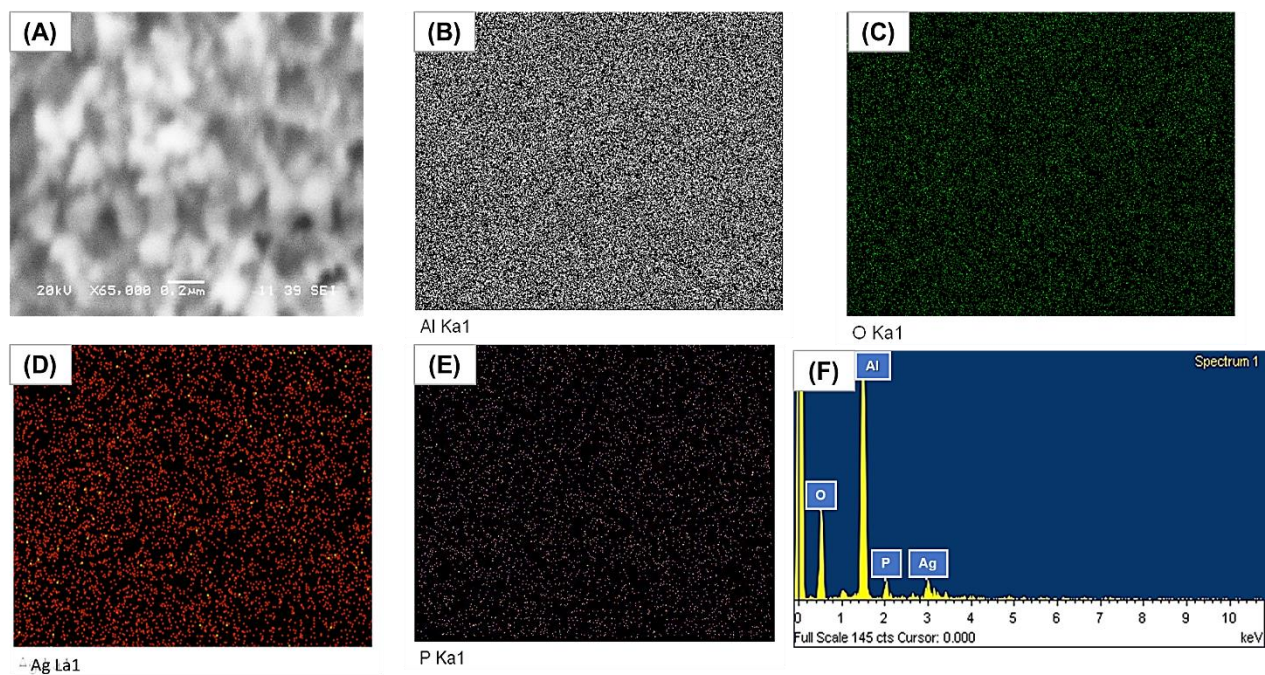
Figure.6-3. EDS mapping of electrodeposition of Ag_3PO_4 on AAO/Al: (A) SEM image; (B) Al; (C) O; (D) Ag; (E) P; and (F) Elemental composition. X and Y-axes: Energy (keV) versus Intensity (a.u). © Henry Agbe, 2021.

As a further study, X-ray diffraction (XRD) analysis was performed to confirm the crystal structure of the Ag_3PO_4 coated anodized aluminum. Figure. 6.5 (I-II)) shows the XRD spectra of body centered cubic (bcc) crystal structure of Ag_3PO_4 and the face centered cubic (fcc) structure of aluminum. All XRD patterns match well with standard data of Ag_3PO_4 with prominent peaks for 2θ at $20.8°$, $29.7°$, $33.3°$, $36.5°$, $42.4°$, $47.8°$ $52.6°$, $55.0°$, $57.2°$, $61.6°$, $70.0°$, $71.8°$ and $73.7°$, with corresponding planes (110), (200), (210), (211), (220), (310), (222), (320), (321), (400), (411), (420) and (421), respectively (JCPDS No. 06-0505) [3]. The 2θ for aluminum of planes (200), (220) and (311), corresponds to $38.75°$, $67.0°$ and 78.3, respectively (JCPDS file No. 04-0787)

[26]. These results show that the electrodeposited Ag_3PO_4 nanoparticles are of high crystallinity and purity.
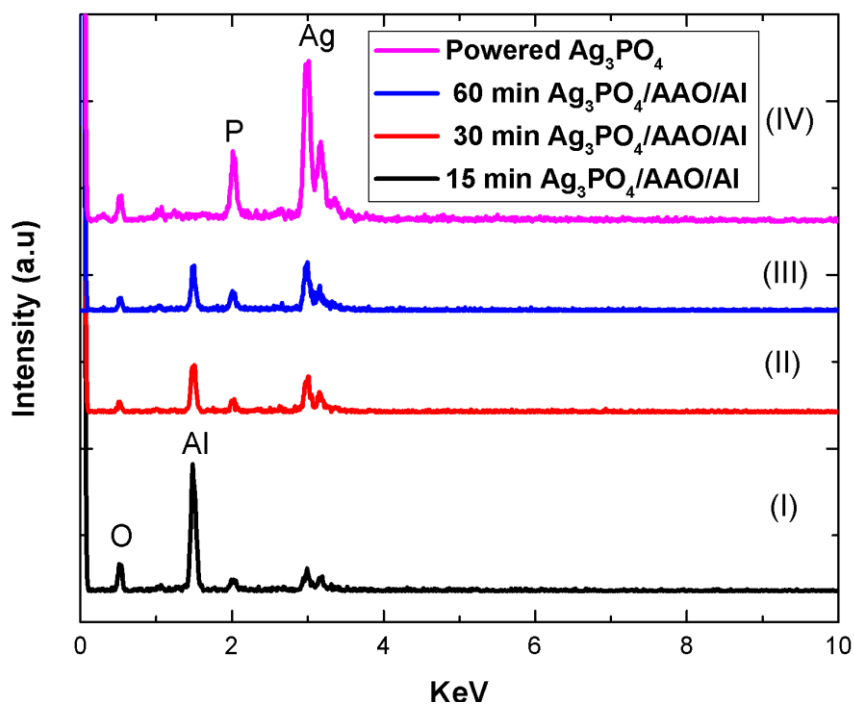
Figure. 6-4. EDS spectra of electrodeposition of Ag_3PO_4 on AAO/Al using deposited silver for (I) 15 minutes, (II) 30 minutes and (III) 60 minutes; and (IV) Powdered Ag_3PO_4, respectively.© Henry Agbe, 2021.
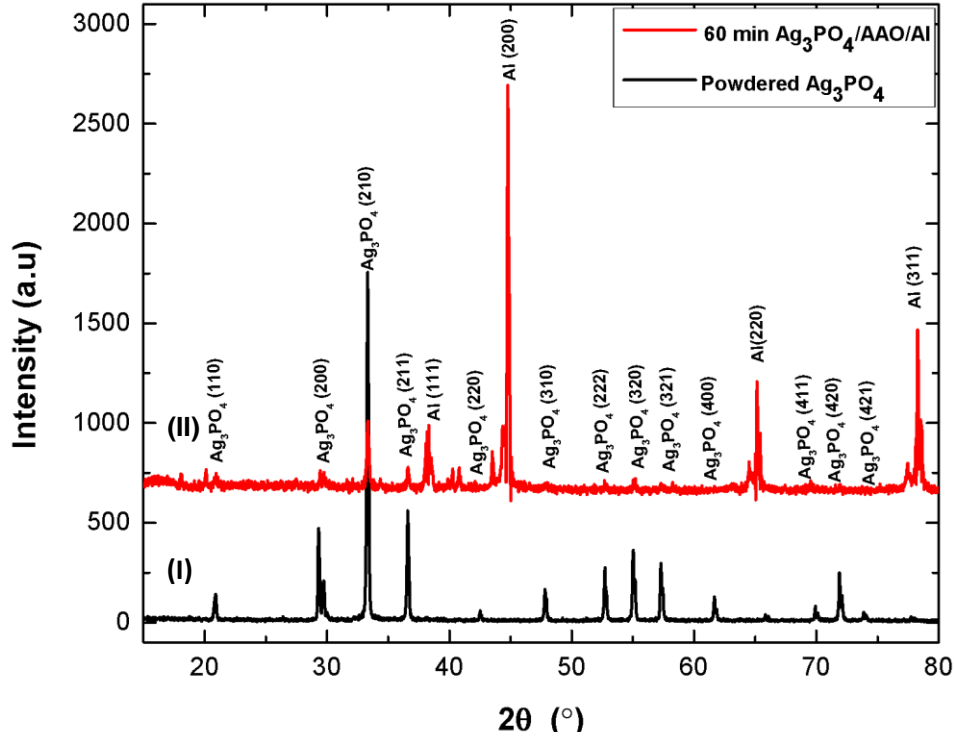
Figure.6-5. XRD spectra of (I) Powdered Ag_3PO_4; and (II) Electrodeposition of Ag_3PO_4 on AAO/Al. © Henry Agbe, 2021.

Figure. 6.6 (A) shows the ATR-FTIR spectra of electrodeposition of Ag_3PO_4 on AAO/Al using deposited silver for 15, 30 and 60 minutes; and powdered Ag_3PO_4 (I-IV), respectively. The broad absorption bands of 3400–3500 cm^{-1} located at the high-frequency region can be assigned to the stretching vibration of H−O−H [27]. The two absorption peaks at the lower frequency region centered at 1650 cm^{-1}, correspond to bending vibration bond of O−H of absorbed water molecules, while the 1353 cm^{-1} can be attributed to the Ag−O vibration bond [28] of electrodeposited silver. Similarly, peaks at low frequency regions at 930 cm^{-1} and 550 cm^{-1} can be ascribed to the molecular vibrations of PO_4^{3-} and Ag – O bonds, respectively [28]. As expected, increased electrodeposition time, such as 60 minutes, increases intensity of Ag-O absorption peaks at both

201

1353 cm^{-1} and 550 cm^{-1}. In addition, P-O peak appears to shift towards a lower frequency region as Ag-O peak increases. Contrarily to strong absorption peak associated with Ag-O vibration band at 1353 cm^{-1} for 60 minutes of electrodeposition, no signal was detected for the 15- and 30-minutes counterparts (Figure. 6.6 (A) (I and 1I)). Furthermore, analysis of selected region of interest (560-540 cm^{-1}), confirmed a linear relation between the integrated peak area and electrodeposition time (Figure. 6.6 (B). Thus, the coating obtained from 60 minutes of electrodeposition was selected for the remainder of the study.
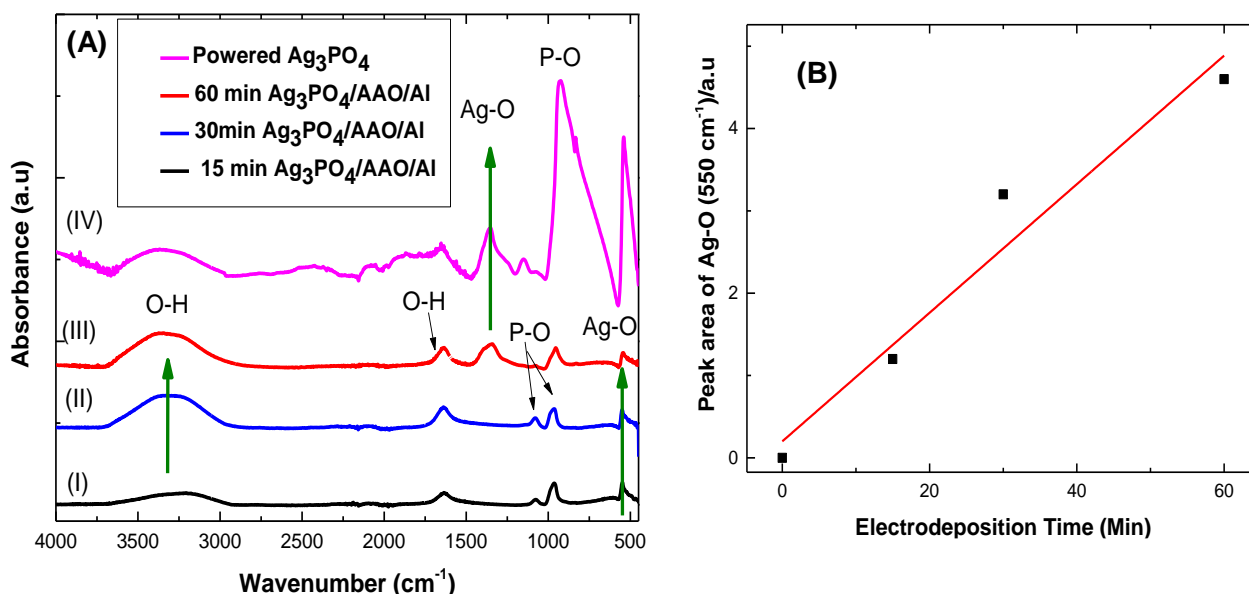
Figure. 6-6. (A) ATR-FTIR spectra of electrodeposition of Ag$_3$PO$_4$ on AAO/Al using deposited silver for (I) 15 minutes, (II) 30 minutes and (III) 60 minutes and (IV) Powdered Ag$_3$PO$_4$, respectively; and (B) Graphical representation of peak area with electrodeposition time. © Henry Agbe, 2021.

Since the Ag$_3$PO$_4$ coated anodized aluminum is intended for frequently touched surfaces application, stability of such coatings is important. Therefore, a crosshatch adhesion tester based on ASTM D-3359 standard was used to evaluate the adhesion level of the Ag$_3$PO$_4$ coating

with the anodized aluminum (Ag$_3$PO$_4$/AAO/Al). According to the ASTM standard, a grade 5B defines the highest level of adhesion of a coating with its substrate with the levels decreasing with lower grades, namely, 4B, 3B, 2B and 1B, while 0B defines the least adhesion level referring to very poor adhesion of the coating [29]. As evident from Figure. 6.7, electrodeposited Ag$_3$PO$_4$ on anodized aluminum (Ag$_3$PO$_4$/AAO/Al) exhibited the highest adhesion level of grade 5B, compared to electrodeposited Ag$_3$PO$_4$ on as-received aluminum with the lowest adhesion level of grade of 0B. The strong adhesion of Ag$_3$PO$_4$ coatings on anodized aluminum may be attributed to both anodization process and presence of P–O–P groups which interact covalently with Al$_2$O$_3$ to form P-O-Al via strong monodentate bonding [30]. Hence, Ag$_3$PO$_4$ coated anodized aluminum is found to be durable and therefore, ideal for practical applications.
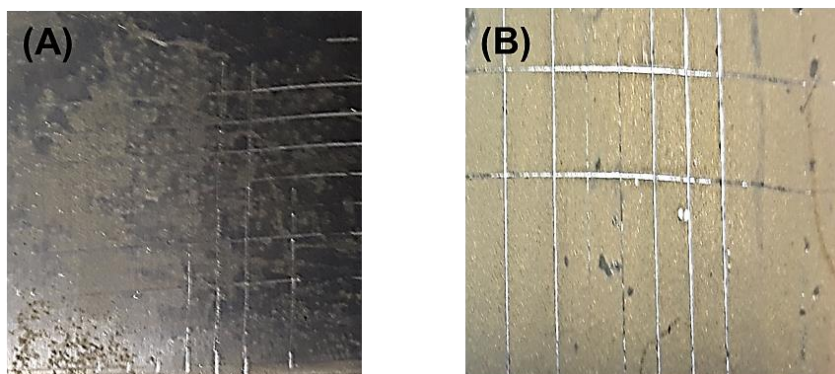
Figure. 6-7. Digital images of scratch test based on American Standard Test Method (ASTM D-3359) showing the adhesion of electrodeposited Ag$_3$PO$_4$ on (A) As-received aluminum and (B) AAO/Al. © Henry Agbe, 2021.

6.4   **Antibacterial assays**

Antibacterial activity was studied by a novel dry seeding assay, Kirby Bauer disk diffusion assay and photo-induce catalysis. The dry seeding assay was performed to mimic near-dry conditions of frequently touched surfaces in hospital environments. The antibacterial performance of Ag_3PO_4/AAO/Al obtained from 60 minutes deposited silver was compared with control coupons such as copper, anodized aluminum oxide (AAO/Al) and as-received aluminum (Figure. 6.8).
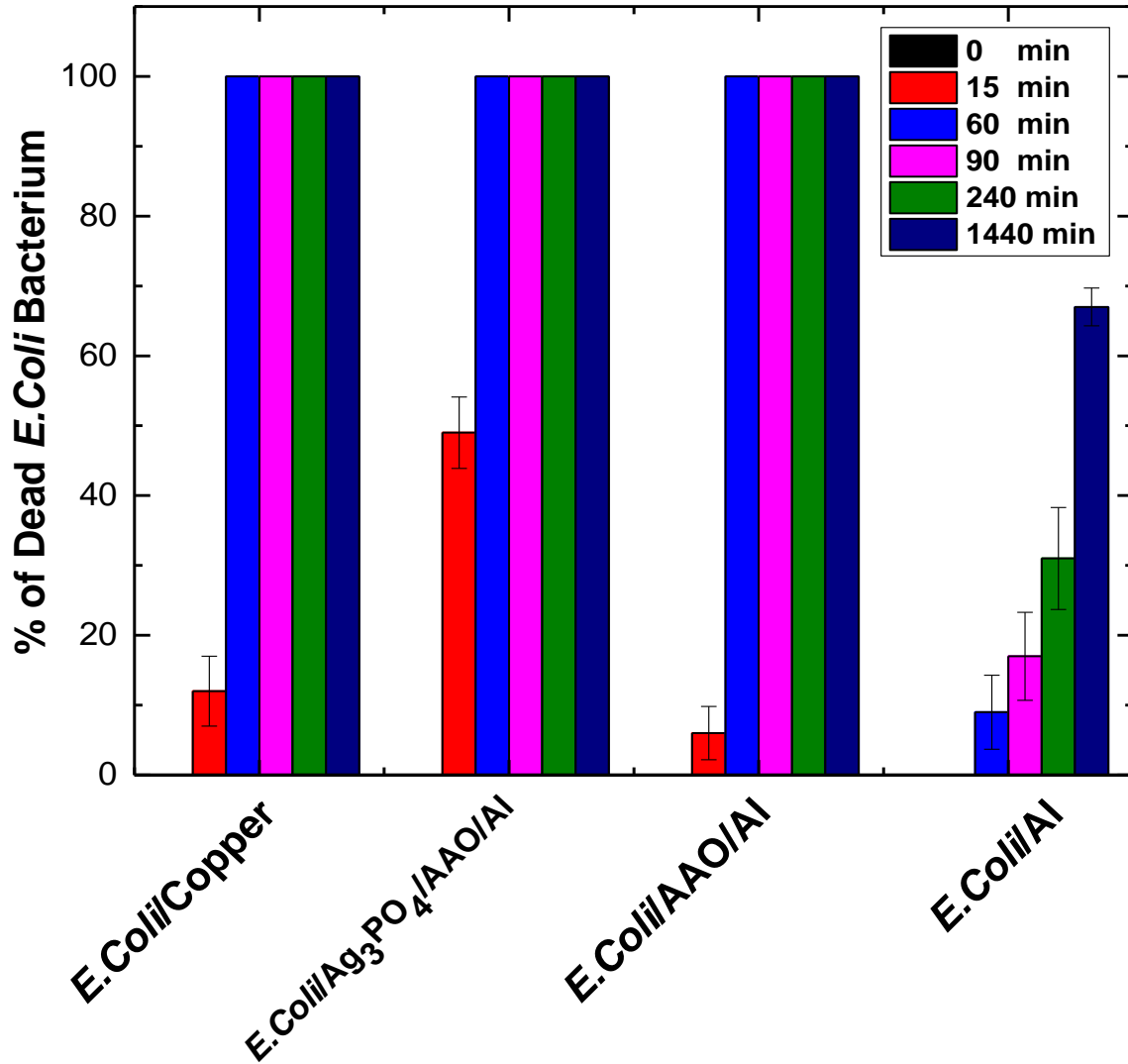
Figure. 6-8. Antibacterial activity of *E. coli* bacteria on Ag_3PO_4 coated anodized aluminum (Ag_3PO_4 /AAO/Al) compared to control samples (copper, AAO/Al and as-received aluminum) under different contact times. © Henry Agbe, 2021.

Compared to copper and AAO/Al surfaces, which resulted in 12% and 6% *E. coli* bacteria death, respectively, Ag_3PO_4/AAO/Al led to ~ 50% bacteria death in 15 minutes. However, after 60 minutes, a 100% bacteria killing was observed for all three conditions, which is consistent with other reports on copper [31, 32]. On the other hand, we found that AAO/Al is able to inactivate *E.*

coli bacteria after 60 minutes of contact, which is presumably due to nanoscale topographical features of pore diameter, surface roughness, and oxide layer thickness. Anodizing aluminum with 3wt.% H_3PO_4 at a current density of 40 mA/cm^2 and anodization time of 120 minutes, exhibits a pore diameter of 151 ± 37 nm, a cell dimeter of 239 ± 53 nm, an oxide layer thickness of 5.3 ± 0.4 nm, a rms roughness of $2.9 \pm 0.7\mu$m and antibacterial efficiency of 100%. It should be mentioned that since topography-mediated antibacterial cicada wings was first reported by Ivanova and co-workers [33] against *Pseudomonas aeruginosa* (gram -ve) bacterium, and their subsequent report on synthetic analogue, black silicon [34], these surfaces have attracted the interest of the scientific community due to their non-toxicity and durability. However, antibacterial mechanism of the topography-mediated antibacterial aluminum alloy is not provided here. Additionally, as can be seen, *E. coli* bacteria survived quite well on as-received aluminum. After 1440 minutes of bacterial contact, ~ 33% of *E. coli* bacteria was still persistent on as-received aluminum. This is worrisome; as such bacterial contaminated surface could lead to healthcare associated infections [35]. It has also been reported that multi-drug resistant (MDR) pathogens survived on inanimate dry high-touch surface for months [35-37]. Thus, our Ag_3PO_4/AAO/Al surfaces, which present better antibacterial effects, show sound promises to reduce both microbial burden and nosocomial infections in hygiene critical environment.

Antibacterial property of Ag_3PO_4 (5 µg/mL) was further analyzed using Kirby Bauer disk diffusion assay. Figure. 6.9 (A) and (B) show the zone of inhibitions (ZOI) of *E. coli* bacteria by Ag_3PO_4, under visible light and dark conditions, compared with commercially available antibacterial standard (as positive control) and deionized water (as negative control). The region surrounding an antibacterial agent where the growth of bacteria is inhibited or inactivated is called the zone of inhibitions (ZOI). The ZOI for Ag_3PO_4, under light and dark conditions were found to be 20 ± 1.3 mm and 15 ± 1.0 mm, respectively compared to 26 ± 1.7 mm for the commercially available standard, while the bacteria grew successfully around negative control sample. Antibacterial activity of Ag_3PO_4 in the dark conditions may be attributed to the presence of Ag^+. It should be mentioned that ~5 mm gain in ZOI by visible light activated Ag_3PO_4, is due to its photocatalytic nature.
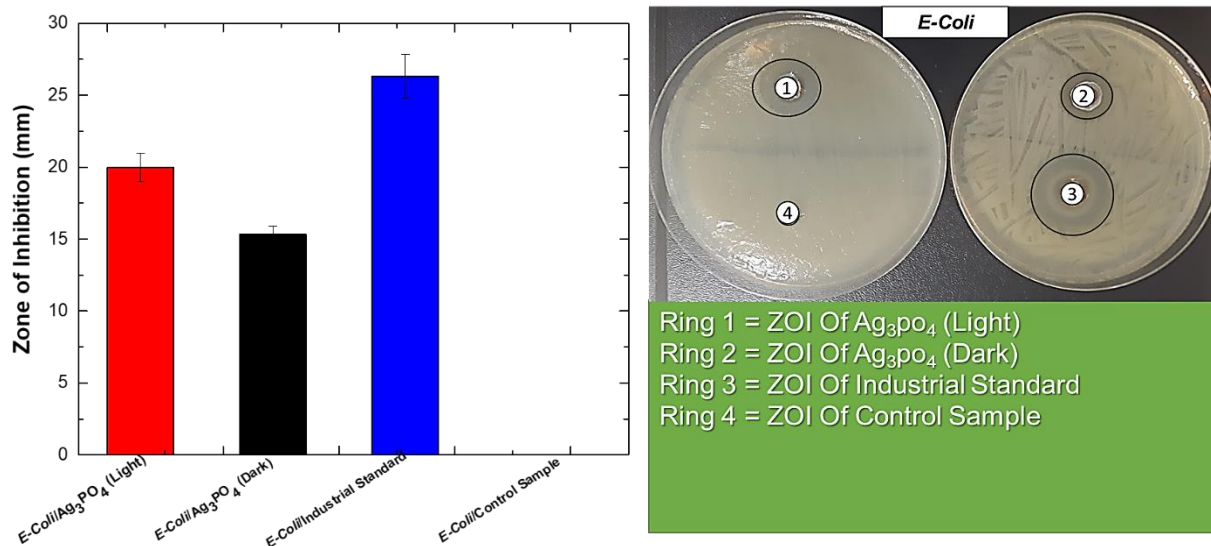
Figure. 6-9. (A). Antibacterial activity of powered Ag_3PO_4 nanoparticles against of *E. coli* (in both light and dark conditions) compared with controls (industrial standard and distilled water); and (B) Disk diffusion assay of Ag_3PO_4 nanoparticles: Ring 1 (Ag_3PO_4) (in light); Ring 2 (Ag_3PO_4) (in dark); Industrial standard: Ring 3; Distilled water Ring 4. Data represent three independent experiments. © Henry Agbe, 2021.

These ZOI compare favourably with those reported on free releasing silver or silver-impregnated polymer. For example, ZOI of 19.5 ± 0.71 was observed for $AgNO_3$ (15 µg/mL) whilst a ZOI of 15.5 ± 0.71 has been reported for Derris trifoliate-Ag-NPs (10 µg/mL)[38]. Ag_3PO_4 is a photocatalyst [3], as such can be activated by visible light to generate Reactive Oxygen Species (ROS) to inhibit bacterial growth. Specifically, upon visible light activation by photons of energy greater than the bandgap of Ag_3PO_4 (2.34 eV > E_g of wavelength 530 nm), exciton or electron-hole pairs are generated [3], leading to ROS ($^\bullet OH^-$, $^\bullet O_2^-$ radicals, H_2O_2 etc.), which can inactivate bacterial cells [5]. Again, phosphate-uptake by bacteria can lead to Ag^+ ions release to covalently bond with both purine and pyrimidine base pairs, rupturing the H-bonds, leading to Deoxyribonucleic acid (DNA) disruption [39], loss of DNA replications [40] and bacterial death [41][42]. Furthermore, Ag_3PO_4 is a slightly soluble in water (0.02 g/L 25 °C) and can release Ag^+ ions by sustained kinetic profile with oligodynamic effects [10]. Specifically, Ag_3PO_4 can dissociate gradually from $Ag_2PO_4^{1-}$ through $AgPO_4^{2-}$, to PO_4^{3-}. The PO_4^{3-} ions could then act as bait (in a "Trojan horse system") for targeting and interfering with ATP/ADP interconversion cycle to inactivate *E. coli* cell [10], (Figure. 6.10). Per the Clinical and Laboratory Standards Institute standards, ZOI values falling within 8–30 mm are considered as acceptable standards for inactivating MDR pathogens such as methicillin-resistant *Staphylococcus aureus* (MRSA), *Pseudomonas aeruginosa* and *E.coli* [43]. Therefore, Ag_3PO_4 proves to be an effective antibacterial agent, particularly for gram-negative bacteria, such as *E-coli.*

As factors such as humidity, temperature, concentration and light source, affect antibacterial property of Ag_3PO_4, further analysis was performed for Ag_3PO_4 in aqueous conditions under both ultraviolet (UV) and visible-light irradiation. Figure. 6.11 shows *E.coli* inactivation rate

under visible light, UV and dark conditions. As it is evident in Figure. 6.11 (A), Ag_3PO_4 under visible light proves to be very effective at inactivating *E.coli* bacteria.
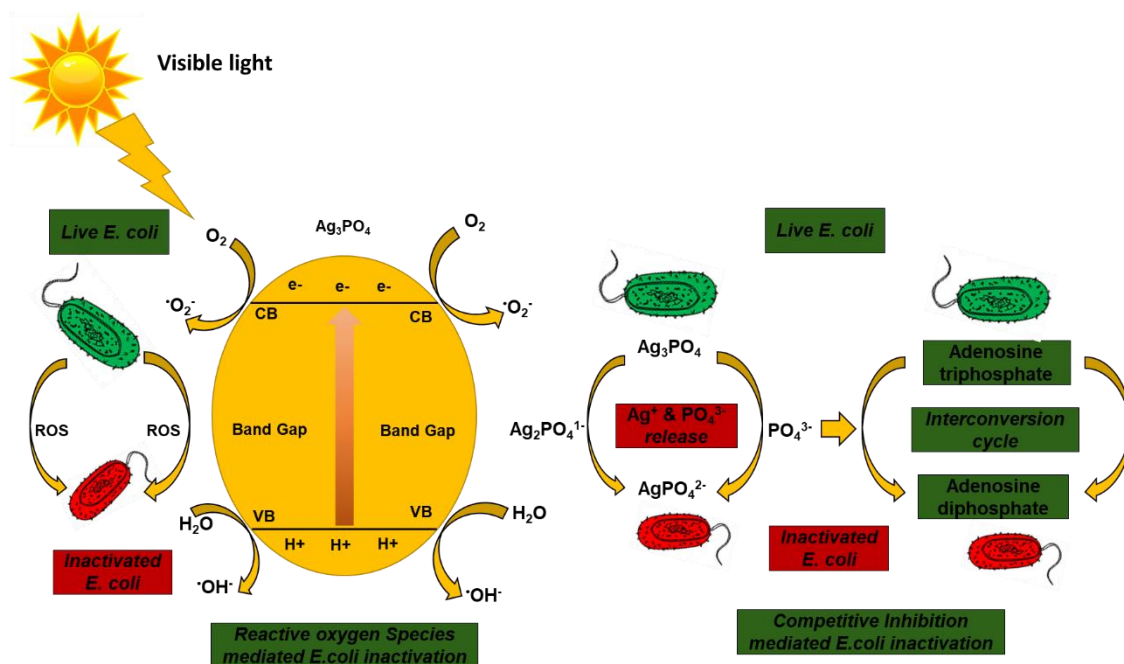
Figure 6-10. Schematic representation of proposed mechanisms of antibacterial Ag_3PO_4 nanoparticles. © Henry Agbe, 2021.

It achieved a 100% efficiency in 15 minutes compared to 44% by TiO_2 (titania), that was used as control (Supporting Information can be found in Table S 6.2). Note that the titania is regarded as standard photocatalyst against which other photo catalytic materials are evaluated [44]. After 60 minutes of the photocatalysis, only 48% of *E.coli* bacteria had been inactivated by titania. Similarly, under 60 minutes visible light irradiation (without a Titania and Ag_3PO_4), only 13% of *E.coli* bacteria was inactivated. This signifies the role of catalysts (Ag_3PO_4 and TiO_2) in photocatalysis. Figure. 6.11 (B), shows the effect of photocatalysis under UV light. Similar to visible light, irradiation of Ag_3PO_4 by UV light led to 100% inactivation efficiency in 15 minutes.

On the other hand, titania under same conditions, led to 70% inactivation efficiency. Increasing duration of irradiation of titania by UV light to 60 minutes, resulted in corresponding increase in , *E. coli* bacteria inactivation efficiency by ~85%   . This is ~100% increase in inactivation rate compared to titania under visible light conditions, which exhibited in an inactivation efficiency of 48% (Figure. 6.11 (A)). The high antibacterial performance of TiO_2 in the UV spectrum is presumably due to its high band gap range of 3.0–3.2 eV [45].

Thus, TiO_2 activation under UV light is much favourable than visible light. On the contrary, Ag_3PO_4 is photoactive in both UV and visible light spectra due to its low indirect and direct band gaps of 2.36 and 2.43 eV [3], hence, resulting in 100% efficiency very easily as compared to TiO_2. As expected, efficiencies in dark were rather low, particularly for TiO_2, which exhibited ~ 36% efficiency after 60 minutes (Figure. 6.11 (C)) whereas for the Ag_3PO_4 was 91%. The high *E. coli* inactivation rate for Ag_3PO_4 under same conditions can be attributed to the role of Ag^+ ions as explained above. While many reports exist in the literature relating to Ag_3PO_4 photocatalysis for water spitting and environmental degradation [4, 46-48], few reports are found on antibacterial application [49, 50] (Supporting information can be found in Table S 6.3).
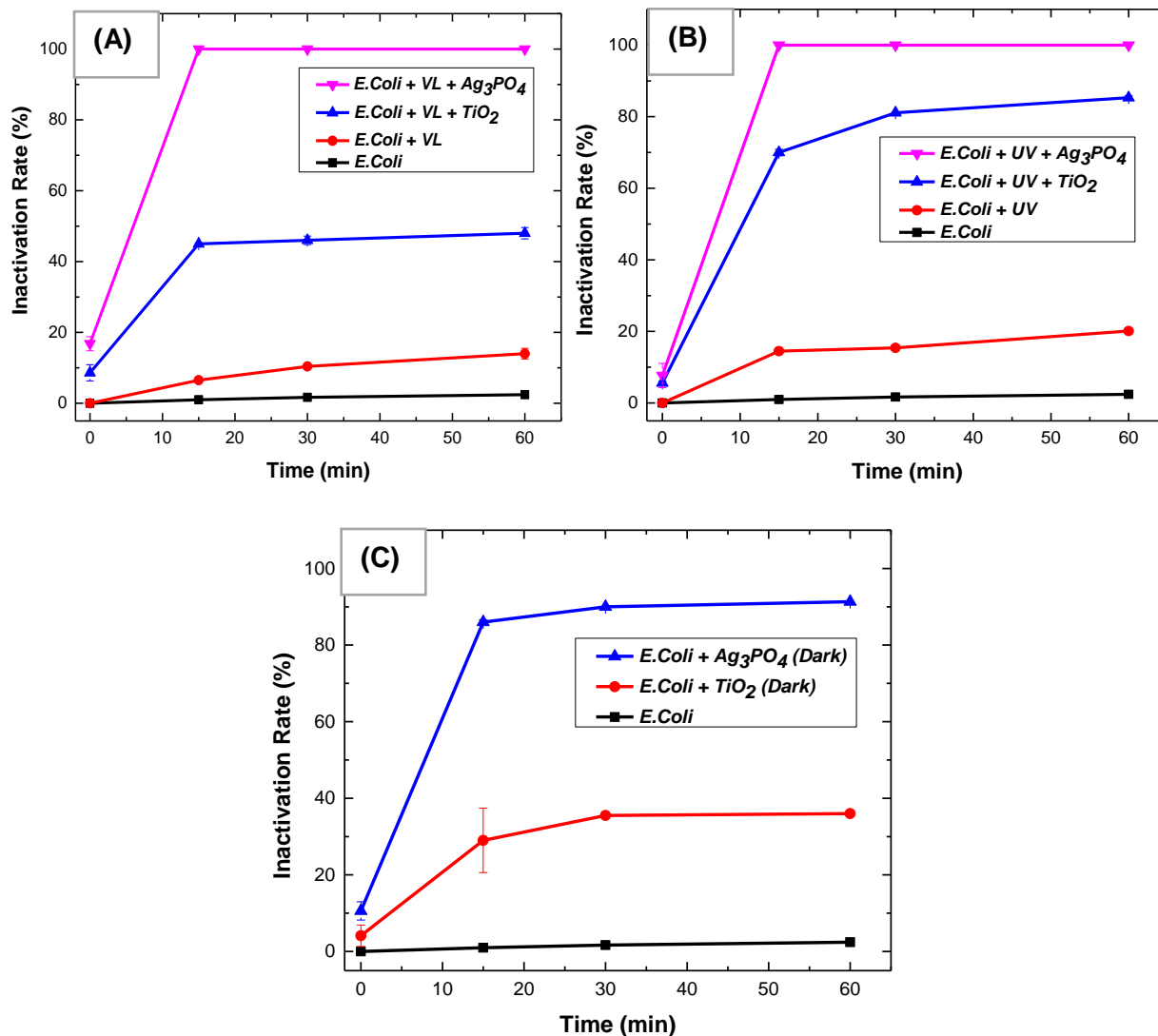
Figure. 6-11. *E. coli* bacterium inactivation by powdered Ag₃PO₄ nanoparticles under (A) Visible light irradiation; (B) UV-A irradiation; and (C) Dark condition. Data represent three independent experiments. © Henry Agbe, 2021.

In the work of Seo *et al.*[49] for example, Ag₃PO₄ synthesized by precipitation method, yielded ~ 50% *E.coli* bacteria inactivation after 16 h, compared to 100% inactivation under only 15 minutes

in our present study. In another work by Su *et al.*[50], a 99.91% *E.coli* bacteria inactivation was achieved by solvothermal synthesis of $Ag_3PO_4/\alpha\text{-}Fe_2O_3$ composites. However, given the different experimental conditions reported in the literature, direct comparisons must be treated with caution.

6.5   Conclusion

In the present study, Ag_3PO_4 was synthesized on anodized aluminum oxide (AAO/Al) by a two-step electrochemical process. Ag^+ ion was reduced to metallic Ag^0, followed by oxidation in sodium orthophosphate to form Ag_3PO_4 on AAO/Al. The Ag_3PO_4 coated anodized aluminum (Ag_3PO_4/AAO/Al) exhibited an excellent antibacterial efficiency of 100% for *E.coli* bacteria in 60 minutes. Both susceptibility and photocatalysis studies on Ag_3PO_4 showed excellent antibacterial properties, with ZOI value of 20 ± 1.3 mm and 100% *E.coli* inactivation under 15 minutes visible-light irradiation, respectively. Furthermore, the Ag_3PO_4 coated anodized aluminum, exhibited a remarkably high adhesion levels of Ag_3PO_4 with the anodized aluminum surfaces. Overall, the Ag_3PO_4 coated anodized aluminum has proven to be an excellent antibacterial material and a promising solution to be considered for use of frequently touched parts as adjunct to hand hygiene in reducing the potential threat of healthcare associated infections in hygiene critical environment.

6.6   Supporting information
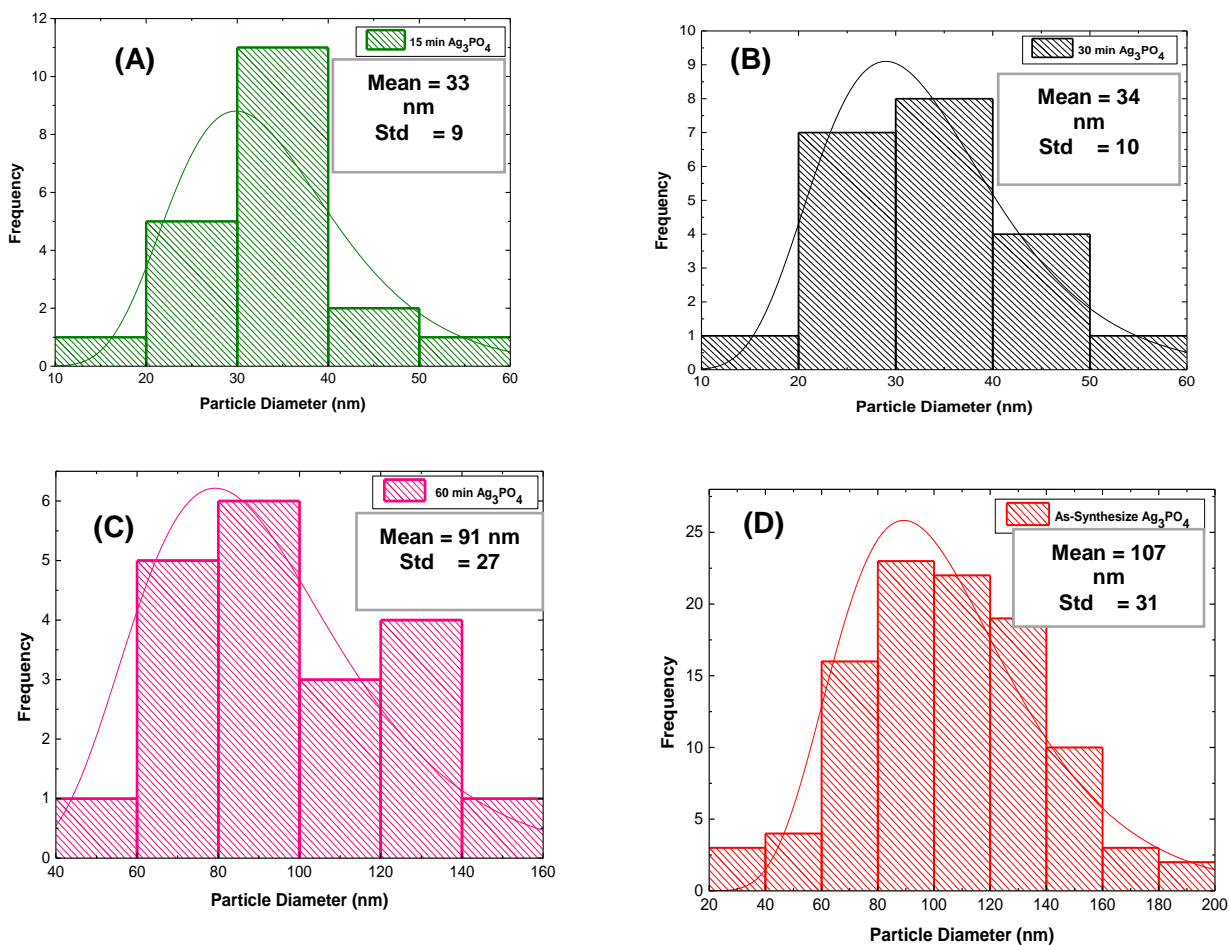
Figure S 6-12. Particle size distributions for electrodeposition Ag_3PO_4 on AAO/Al using deposited silver for (A) 15 minutes, (B) 30 minutes; (C) 60 minutes; and (D)Powered Ag_3PO_4 nanoparticles. © Henry Agbe, 2021.

Table S6-1. Calculated mass of silver and phosphate by electrodeposition process

Deposition Time (min)	Calculated mass of Ag (mg)	Calculated mass of Ag$_3$PO$_4$ (mg)	Factor
0	321,000	418,580	
15	0.4	0.52	1.30
30	1.6	2.08	1.30
60	3.4	4.42	1.30

Table S6-2. 1 % inactivation *E. coli* by Ag$_3$PO$_4$ under visible light, UV light and dark conditions

Samples	*E.coli* Bacterium inactivation Rate (%)			
	Photocatalysis Time (min)			
	0	15	30	60
E.coli	0	1.0	1.3	2.0
E.coli + Visible Light	0	7	10	13
E.coli + UV Light	0	14	15	20
E.coli + Visible Light + Ag$_3$PO$_4$	16	100	100	100
E.coli + Visible Light + TiO$_2$	8	44	46	48
E.coli + UV Light + Ag$_3$PO$_4$	8	100	100	100
E.coli + UV Light + TiO$_2$	5	70	81	85
E.coli + Ag$_3$PO$_4$ (Dark)	10	86	90	91
E.coli + TiO$_2$ (Dark)	4	29	35	36

Table S6-3 Comparison of current study with existing reports in the literature

Ag$_3$PO$_4$-Based Antibacterial Agent	Antibacterial Efficiency		Reaction Time (min)	Wavelength (nm)	Mechanisms	Reference
	S. A	E. coli				
Ag$_3$PO$_4$/AAO/Al (Coating)	--	100%	60	-	Photocatalysis	Current Study
Ag$_3$PO$_4$ (light) 5µg/mL –ZOI (mm)	--	20	1440	-	Photocatalysis/Diffusion	Current Study
Ag$_3$PO$_4$ (dark) 5µg/mL- ZOI (mm)		15	1440	-	Diffusion	Current Study
Ag$_3$PO$_4$ Suspension (Dark)	--	91%	60	-	Ag+ ion leaching	Current Study
Ag$_3$PO$_4$ Suspension (visible-light)	--	100%	15	-	Photocatalysis	Current Study
Ag$_3$PO$_4$ (visible-light) 125µg/mL-ZOI (mm)	9.2 --	10.00	1440	-	Photocatalysis/Diffusion	[51]
BU–TiO$_2$-X/Ag$_3$PO$_4$ (Suspension (visible light)	99.85% --	99.76%	20	750-1000	Photocatalysis	[8]
Bi$_2$S$_3$@Ag$_3$PO$_4$/Ti Suspension (visible light)	99.45% --	99.74%	15	808	Photocatalysis	[12]
RGO/MoS$_2$/Ag$_3$PO$_4$ composite	97.8% --	98.33%	10	660	Photocatalysis	[9]
PDA/Ag$_3$PO$_4$/GO hybrid (coating)	99.66%	99.53%	15	660	Photocatalysis	[7]

6.7 **Reference:**

1. Lansdown, A.B., *Silver in healthcare: its antimicrobial efficacy and safety in use*. 2010: Royal Society of Chemistry.

2. Huh, A.J. and Y.J. Kwon, *"Nanoantibiotics": a new paradigm for treating infectious diseases using nanomaterials in the antibiotics resistant era.* Journal of controlled release, 2011. **156**(2): p. 128-145.

3. Henry Agbe, Nadeem Raza, David Dodoo-Arhin, Aditya Chauhan, Ramachandran Vasant Kumar, *H2O2 rejuvenation-mediated synthesis of stable mixed-morphology Ag3PO4 photocatalysts.* Heliyon, 2018. **4**(4): p. e00599.

4. Zhiguo Yi, Jinhua Ye, Naoki Kikugawa, Tetsuya Kako, Shuxin Ouyang, Hilary Stuart-Williams, Hui Yang, Junyu Cao, Wenjun Luo, Zhaosheng Li, Yun Liu, Ray L Withers, *An orthophosphate semiconductor with photooxidation properties under visible-light irradiation.* Nature materials, 2010. **9**(7): p. 559-564.

5. Gopal Panthi, Rosa Ranjit, Hak-YongKim, Deependra DasMulmi, *Size dependent optical and antibacterial properties of Ag3PO4 synthesized by facile precipitation and colloidal approach in aqueous solution.* Optik, 2018. **156**: p. 60-68.

6. Yang-Sen Xu and Wei-De Zhan, *Morphology-controlled synthesis of Ag3PO4 nano/microcrystals and their antibacterial properties.* Materials Research Bulletin, 2013. **48**(9): p. 3043-3048.

7. Xianzhou Xie, Congyang Mao, Xiangmei Liu, Lei Tan, Zhenduo Cui, Xianjin Yang, Shengli Zhu, Zhaoyang Li, Xubo Yuan, Yufeng Zheng, Kelvin Wai Kwok Yeung, Paul K. Chu, Shuilin Wu, *Tuning the bandgap of photo-sensitive polydopamine/Ag3PO4/graphene oxide coating for rapid, noninvasive disinfection of implants.* ACS central science, 2018. **4**(6): p. 724-738.

8. Yingde Xu, Xiangmei Liu, Yufeng Zheng, Changyi Li, Kelvin WaiKwok Yeung, Zhenduo Cui, Yanqin Liang, Zhaoyang Li, Shengli Zhu, Shuilin, Wu, *Ag3PO4 decorated black urchin-like defective TiO2 for rapid and long-term bacteria-killing under visible light.* Bioactive materials, 2021. **6**(6): p. 1575-1587.

9. Chao Zhang, Jiameng Wang, Ruifang Chi, Jing Shi, Yongqiang, Yang, Xiangyu Zhang, *Reduced graphene oxide loaded with MoS2 and Ag3PO4 nanoparticles/PVA interpenetrating hydrogels for improved mechanical and antibacterial properties.* Materials & Design, 2019. **183**: p. 108166.

10. Jin-Ku Liu, Chong-Xiao Luo, Jian-Dong Wang, Xiao-Hong Yang Xin-Hua Zhong, *Controlled synthesis of silver phosphate crystals with high photocatalytic activity and bacteriostatic activity.* CrystEngComm, 2012. **14**(24): p. 8714-8721.

11. Xiaopei Li, Piao Xu, Ming Chen, Guangming Zeng, Dongbo Wang, Fei Chen, Wangwang Tang, Changya Chen, Chen Zhang, Xiaofei Tan, *Application of silver phosphate-based photocatalysts: Barriers and solutions.* Chemical Engineering Journal, 2019. **366**: p. 339-357.

12. Li Hong, Xiangmei Liu, Lei Tan, Zhenduo Cui, Xianjin Yang, Yanqin Liang, Zhaoyang Li, Shengli Zhu, Yufeng Zheng, Kelvin Wai Kwok Yeung, Doudou Jing, Dong Zheng, Xianbao Wang, Shuilin W, *Rapid Biofilm Elimination on Bone Implants Using Near-*

Infrared-Activated Inorganic Semiconductor Heterostructures. Advanced healthcare materials, 2019. **8**(19): p. 1900835.

13. Cong Fu, Xuefei Zhang, Keith Savino, Paul Gabrys, Yun Gao, Wanaruk Chaimayo, Benjamin L. Miller, Matthew Z. Yates, *Antimicrobial silver-hydroxyapatite composite coatings through two-stage electrochemical synthesis.* Surface and Coatings Technology, 2016. **301**: p. 13-19.

14. T. Mokabber, H. T. Cao, N. Norouzi, P. van Rijn, Y. T. Pei, *Antimicrobial electrodeposited silver-containing calcium phosphate coatings.* ACS applied materials & interfaces, 2020. **12**(5): p. 5531-5541.

15. Sanja Eraković, Ana Janković, Djordje Veljović, Eriks Palcevskis, Miodrag Mitrić, Tatjana Stevanović, Djordje Janaćković, Vesna Mišković-Stanković, *Corrosion stability and bioactivity in simulated body fluid of silver/hydroxyapatite and silver/hydroxyapatite/lignin coatings on titanium obtained by electrophoretic deposition.* The Journal of physical chemistry B, 2013. **117**(6): p. 1633-1643.

16. Jianghong Luo, Bakri Mamat, ZhihaoYue, NaiyinZhang, XiaojunXu, YunlingLj, Zhi Su, Chuang Ma, Fazhi Zang, Yingbo Wang, *Multi-metal ions doped hydroxyapatite coatings via electrochemical methods for antibacterial and osteogenesis.* Colloid and Interface Science Communications, 2021. **43**: p. 100435.

17. Sepideh Minagar, Christopher C Berndt, James Wang, Elena Ivanova, Cuie Wen, *A review of the application of anodization for the fabrication of nanotubes on metal implant surfaces.* Acta biomaterialia, 2012. **8**(8): p. 2875-2888.

18. Livia Visai, Luigi De Nardo, Carlo Punta, Lucio Melone, Alberto Cigada, Marcello Imbriani, Carla Renata Arciola, *Titanium oxide antibacterial surfaces in biomedical devices.* The International journal of artificial organs, 2011. **34**(9): p. 929-946.

19. Domenico Regonini, A Satka, A Jaroenworaluck, Duncan W E Allsopp, Christopher R Bowen, R Stevens, *Factors influencing surface morphology of anodized TiO2 nanotubes.* Electrochimica Acta, 2012. **74**: p. 244-253.

20. Urvashi Fowdar Gunputh, Huirong Le, Richard D Handy, Christopher Tredwi, *Anodised TiO 2 nanotubes as a scaffold for antibacterial silver nanoparticles on titanium implant.* Materials Science and Engineering: C, 2018.

21. Nithideth Somsanith, Yu-Kyoung Kim,Young-Seok Jang, Young-Hee Lee, Ho-Keun Yi,Jong-Hwa Jang, Kyoung-A Kim, Tae-Sung Bae, and Min-Ho Lee, *Enhancing of Osseointegration with Propolis-Loaded TiO2 Nanotubes in Rat Mandible for Dental Implants.* Materials, 2018. **11**(1): p. 61.

22. Henry Agbe, Dilip Kumar Sarkar, X.-Grant Chen, Nathalie Faucheux, Gervais Soucy, Jean-Luc Bernier, *Silver–Polymethylhydrosiloxane Nanocomposite Coating on Anodized Aluminum with Superhydrophobic and Antibacterial Properties.* ACS Applied Bio Materials, 2020. **3**(7): p. 4062-4073.

23. Stanley C. S. Lai, Robert A. Lazenby, Paul M. Kirkman, Patrick R. Unwin, *Nucleation, aggregative growth and detachment of metal nanoparticles during electrodeposition at electrode surfaces.* Chemical science, 2015. **6**(2): p. 1126-1138.

24. D. K. Sarkar, X. J. Zhou, A. Tannous, and K. T. Leung, *Growth mechanisms of copper nanocrystals on thin polypyrrole films by electrochemistry.* The Journal of Physical Chemistry B, 2003. **107**(13): p. 2879-2881.

25. Nasirpouri, F., *Electrodeposition of nanostructured materials.* Vol. 62. 2017: Springer.

26. Narayanasamy, R., T. Ramesh, and M. Prabhakar, *Effect of particle size of SiC in aluminium matrix on workability and strain hardening behaviour of P/M composite.* Materials Science and Engineering: A, 2009. **504**(1-2): p. 13-23.

27. Huang, G. and Y. Zhu, *Enhanced photocatalytic activity of ZnWO4 catalyst via fluorine doping.* The Journal of Physical Chemistry C, 2007. **111**(32): p. 11952-11958.

28. C.Piccirillo, R.A.Pinto, D.M.Tobaldi, R.C.Pullar, J.A.Labrincha, M.M.E.Pintado, P.M.L.Castro, *Light induced antibacterial activity and photocatalytic properties of Ag/Ag3PO4-based material of marine origin.* Journal of Photochemistry and Photobiology A: Chemistry, 2015. **296**: p. 40-47.

29. Milionis, A., E. Loth, and I.S. Bayer, *Recent advances in the mechanical durability of superhydrophobic materials.* Advances in colloid and interface science, 2016. **229**: p. 57-79.

30. Xiaohua Chen,Yong Zheng,Yelin Chen,Yalan Xu,Fulan Zhong,Wen Zhang,Yihong Xiao,Ying Zheng, *Improved methane oxidation activity of P-doped γ-Al2O3 supported palladium catalysts by tailoring the oxygen mobility and electronic properties.* International Journal of Hydrogen Energy, 2019. **44**(51): p. 27772-27783.

31. Noyce, J., H. Michels, and C. Keevil, *Use of copper cast alloys to control Escherichia coli O157 cross-contamination during food processing.* Applied and environmental microbiology, 2006. **72**(6): p. 4239-4244.

32. Grass, G., C. Rensing, and M. Solioz, *Metallic copper as an antimicrobial surface.* Applied and environmental microbiology, 2011. **77**(5): p. 1541-1547.

33. Jafar Hasan, Hayden K Webb, Vi Khanh Truong, Sergey Pogodin, Vladimir A Baulin, Gregory S Watson, Jolanta A Watson, Russell J Crawford, Elena P Ivanova, *Selective bactericidal activity of nanopatterned superhydrophobic cicada Psaltoda claripennis wing surfaces.* Applied microbiology and biotechnology, 2013. **97**(20): p. 9257-9262.

34. Elena P. Ivanova, Jafar Hasan, Hayden K. Webb, Gediminas Gervinskas, Saulius Juodkazis, Vi Khanh Truong, Alex H.F. Wu, Robert N. Lamb, Vladimir A. Baulin, Gregory S. Watson, Jolanta A. Watson, David E. Mainwaring, Russell J. Crawford , *Bactericidal activity of black silicon.* Nature communications, 2013. **4**(1): p. 1-7.

35. Kramer, A., I. Schwebke, and G. Kampf, *How long do nosocomial pathogens persist on inanimate surfaces? A systematic review.* BMC infectious diseases, 2006. **6**(1): p. 130.

36. Weinstein, R.A. and B. Hota, *Contamination, disinfection, and cross-colonization: are hospital surfaces reservoirs for nosocomial infection?* Clinical infectious diseases, 2004. **39**(8): p. 1182-1189.

37. Vincenzo Russotto, Andrea Cortegiani, Teresa Fasciana, Pasquale Iozzo, Santi Maurizio Raineri, Cesare Gregoretti, Anna Giammanco, Antonino Giarratano, *What healthcare workers should know about environmental bacterial contamination in the intensive care unit.* BioMed research international, 2017. **2017**.

38. Neethu Cyril,James Baben George,Laigi Joseph,A C Raghavamenon,Sylas V P, *Assessment of antioxidant, antibacterial and anti-proliferative (lung cancer cell line A549) activities of green synthesized silver nanoparticles from Derris trifoliata.* Toxicology research, 2019. **8**(2): p. 297-308.

39. Banerjee, S.L., P. Potluri, and N.K. Singha, *Antimicrobial cotton fibre coated with UV cured colloidal natural rubber latex: A sustainable material.* Colloids and Surfaces A: Physicochemical and Engineering Aspects, 2019. **566**: p. 176-187.

40. Kaiyuan Zheng, Magdiel Inggrid Setyawati, David Tai Leong, Jianping Xie, *Antimicrobial silver nanomaterials.* Coordination Chemistry Reviews, 2018. **357**: p. 1-17.

41. Percival, S.L., A.-M. Salisbury, and R. Chen, *Silver, biofilms and wounds: resistance revisited.* Critical reviews in microbiology, 2019: p. 1-15.

42. Lukas C. Gerber, Fabian M. Koehler, Robert N. Grass, and Wendelin J. Stark, *Incorporation of reactive silver-tricalcium phosphate nanoparticles into polyamide 6 allows preparation of self-disinfecting fibers.* Polymer Engineering & Science, 2011. **51**(1): p. 71-77.

43. Wayne, P., *Clinical and laboratory standards institute. Performance standards for antimicrobial susceptibility testing.* 2011.

44. Henry Agbe, Emmanuel Nyankson, Nadeem Raza, David Dodoo-Arhin, Aditya Chauhan, Gabriel Osei, Vasant Kumar, Ki Hyun Kim, *Recent advances in photoinduced catalysis for water splitting and environmental applications.* Journal of Industrial and Engineering Chemistry, 2019. **72**: p. 31-49.

45. Ryu Abe, Koujirou Hara, Kazuhiro Sayama, Kazunari Domen, Hironori Arakawa, *Steady hydrogen evolution from water on Eosin Y-fixed TiO2 photocatalyst using a silane-coupling reagent under visible light irradiation.* Journal of Photochemistry and Photobiology A: Chemistry, 2000. **137**(1): p. 63-69.

46. Raeisi-Kheirabadi, N. and A. Nezamzadeh-Ejhieh, *A Z-scheme g-C3N4/Ag3PO4 nanocomposite: Its photocatalytic activity and capability for water splitting.* International Journal of Hydrogen Energy, 2020. **45**(58): p. 33381-33395.

47. Hongfei Yin, Ying Cao, Tianle Fan, Min Zhang, Jiacheng Yao, Pengfei Li, Shenming Chen, Xiaoheng Liu, *In situ synthesis of Ag3PO4/C3N5 Z-scheme heterojunctions with enhanced visible-light-responsive photocatalytic performance for antibiotics removal.* Science of The Total Environment, 2021. **754**: p. 141926.

48. Altan, O. and Ö. Metin, *Boosting formic acid dehydrogenation via the design of a Z-scheme heterojunction photocatalyst: The case of graphitic carbon nitride/Ag/Ag3PO4-AgPd quaternary nanocomposites.* Applied Surface Science, 2021. **535**: p. 147740.

49. Youngsik Seo, Byul-Ee Yeo, Young-Sik Cho, Heonyong Park, Chian Kwon, Young-Duk Huh, *Photo-enhanced antibacterial activity of Ag3PO4.* Materials Letters, 2017. **197**: p. 146-149.

50. Wenting SuXiangmei Liu, Lei Tan, Zhenduo Cui, Yanqin Liang, Zhaoyang Li, Shengli Zhu, Shuilin Wu, *Rapid Sterilization by Photocatalytic Ag3PO4/α-Fe2O3 Composites Using Visible Light.* ACS Sustainable Chemistry & Engineering, 2020. **8**(6): p. 2577-2585.

51. Karim Dânoun, Rida Tabit, Abdelaziz Laghzizil, Mohamed Zahouily, *A novel approach for the synthesis of nanostructured Ag3PO4 from phosphate rock: high catalytic and antibacterial activities.* BMC chemistry, 2021. **15**(1): p. 1-12.

CHAPTER 7

7   CHAPTER 7

This final contribution is currently under peer review in ACS Biomaterial Science and Engineering. Henry Agbe, Dilip Sarkar Kumar, and X-Grant Chen authored it. As a first author, I conceived, designed, and performed all experiments, analyzed, and interpreted the results, as well as wrote both the original and final manuscript.

7.1   Abstract

Topography-mediated antibacterial surfaces that inactivate bacteria by physical contact are gaining attention in recent times. Contrary to conventional antibacterial coatings, topography-mediated antibacterial surfaces do not suffer from coating instability and possible toxicity problems. In this study, a one-step hard anodization process has been deployed to fabricate a topography-mediated antibacterial aluminum surface. By optimizing anodization parameters, such as concentration of electrolyte, current density and anodization time, desirable features of micro-nanoscale morphology were achieved. The optimum condition of anodized aluminum that provided pores of diameter of 151 ± 37 nm effectively killed 100% *E. coli* bacteria.

7.2   Introduction

Many organisms such as cicada, dragonfly and damselfly use their micro-nanoscale surface structures to adapt, fight colonization or as evolutionary surviving strategy [1]. These micro-nanostructures on the wings of most insects and plant parts such as lotus leaves are composed of natural long chain palmitic (hexadecanoic) and stearic (octadecanoic) fatty acids [2], rendering them

superhydrophobic. Superhydrophobic surfaces are known to exhibit water contact angle (WCA) > 150° and a tilting angle < 10° [3]. Due to their ability to inhibit initial bacterial attachment and subsequent biofilm formation, superhydrophobic coatings are considered important strategy for designing anti-biofouling surfaces [3]. However, they lose their water roll-off property over time [4] due to coating instability. Hence, novel antibacterial strategies that kill bacteria on contact via surface topography have become an area of intense scientific focus in recent times [1, 5-7]. These novel antibacterial strategies herein referred as topography-mediated antibacterial surfaces exhibit antibacterial property by inducing mechanical stresses to damage cell membrane, leading to bacterial cell death [6, 8, 9].

Since topography-mediated antibacterial cicada wings was first reported by Ivanova and co-workers [5] against *Pseudomonas aeruginosa* (P.A) (gram -ve) bacterium, and their subsequent report on synthetic analogue, black silicon [10], various artificial antibacterial surfaces, mediated by micro-nanoscale patterns, such as nanocones, nanofibers and nanopillars have been fabricated on metals, ceramics and polymers [11-13]. These approaches provide a paradigm shift in fabrication of the next generation novel antibacterial surfaces. Contrary to conventional antibacterial coatings, such as leachable antibacterial agents (metallic silver and copper), these do not suffer from coating instability, possible toxicity and antibacterial resistance problems [6]. Thus, they are more eco-sustainable, have great potential for medical implant prostheses and devices, and frequently touched surface applications. These could be useful as antibacterial touched surfaces, in support of existing hand hygiene, masking and social distancing protocols aimed at curbing both community and healthcare spread of the *severe acute respiratory syndrome coronavirus 2* (SARS-CoV-2) infections. Surfaces in frequently touched areas can become potential reservoir for transmission of various pathogens making it a serious infection prone health risk. For example, SARS-CoV-2, methicillin-

resistant *Staphylococcus aureus* (MRSA), *Escherichia coli* (*E. coli*), *Pseudomonas aeruginosa* (P.A)

and *Clostridium difficile* spores can survive on inanimate environmental surfaces for days, weeks and

months [14-16]. Thus, commonly touched inanimate environmental surfaces such as elevator buttons,

doorknobs, handrails, faucet handles, light switches, medical equipment etc., should be rendered

antibacterial to limit the spread of pathogenic infections.

Aluminum is a very attractive material for engineering constructions and many aluminum

components are widely used in medical devices [17] and in frequently touched surfaces [18].

Aluminum can be transformed into antibacterial surface via low-cost wet chemistry surface

modification. Surprisingly, only few studies have reported on antibacterial aluminum modified by

wet chemistry [17-19]. Hasan et al [19], recently fabricated antiviral aluminum surface using

chemical etching process. The aluminum surface was effective against the current SARS-CoV-2. In

a related study [18], they demonstrated the antimicrobial activity of a topography-mediated

aluminum, fabricated by chemical etching against common multi-drug resistant (MDR) pathogens

such as *Pseudomonas aeruginosa* (P.A) and *Staphylococcus aureus* (S.A), and on respiratory viruses

such as *respiratory syncytial virus* (RSV) and *rhino virus* (RV). While desirable nanoscale

topography are achievable by chemical etching, mechanical property of nanoscale features are rather

weak [20]. An alternative surface treatment process resulting in aluminum surfaces with excellent

anti-corrosive, tribological and mechanical properties such as anodization [21] appears promising in

terms of robustness.

Considering the importance of the microstructural stability of the surface for a long-term

service life and protection, we report novel topography-mediated antibacterial aluminum surfaces,

fabricated via anodization. In this study, parameters of anodization such as electrolyte types, current

density and anodization time have been systematically varied for obtaining optimal topography that

showed the best antibacterial performance. The results of the optimization process and the antibacterial properties have been demonstrated. It has been shown that the excellent antibacterial performance was purely driven by the surface topography of the anodized aluminum.

7.3   Experimental section

Pre-treatment of aluminum. AA6061-T6 aluminum sheets of dimensions $1'' \times 2''$ were ultrasonically degreased (Branson® Ultrasonic Bath, 230 Vac, 50 Hz) in a diluted soap solution for 15 minutes. The cleaned Al substrates were immersed in 1 M NaOH (VWR) etchant for 3 minutes at 55 °C to remove a superficial oxide layer. Subsequently, etched Al substrates were immersed in HNO_3 solution (10 wt. %, VWR) for desmutting, followed by further rinsing thoroughly in distilled water. Finally, etched Al substrates were dried at 70 ˚C in an oven overnight.

Anodizing in acid electrolyte. Etched and as-received AA6061-T6 aluminum sheets were used as anode and cathode, respectively, in different acidic electrolytes of H_2SO_4 and H_3PO_4 (VWR) and 3 wt. %, 15 wt. % and 45 wt. % concentration. The anodization process was performed by optimizing current density from 7 to 40 mA/cm^2 and time from 30 to 120 minutes in a galvanostatic 600 W direct current power system (Ametek Sorensen DCS 100-12E, Chicoutimi, QC, Canada). To ensure uniform heat distribution and prevent burning, the electrochemical cell was equipped with a cold-water circulating coolant bath (5 °C) and a Teflon stirring magnetic unit, rotating at 2000 rpm throughout the anodization process. During anodization, the two electrodes were separated in parallel by 1.5 cm. Anodized coupons were finally sonicated for 30 minutes in distilled water to remove residual electrolytes, followed by drying at 70 ˚C in an electric oven (VWR) over night. For quality control and reproducibility, each experiment was repeated in triplicate.

Sample characterization: The surface morphological and elemental analyses of anodized samples were performed using scanning electron microscopy (SEM, JEOL JSM-6480 LV) equipped with energy dispersive X-ray spectroscopy (EDS). High-resolution SEM micrographs were analyzed in a Java-based image-processing program-Image J (http://rsbweb.nih.gov/ij/), to determine the morphological features. A minimum of 30 different SEM micrographs were taken from each sample for analysis. Approximately 1,000 independent measurements were analysed. Prior to SEM analysis, anodized samples were metalized with gold coating (~8 nm) using an Edwards Scancoat Six Sputter Coater. The surface roughness of anodized samples was studied using an optical profilometry (MicroXAM-100 HR 3D surface profilometer, *NANOVEA*, Irvine, USA). Antibacterial property was studied by a novel dry seeding assay, described in both Chapters 3 and 6.

7.4   Results and discussions

7.4.1   Effect of H_3PO_4 concentration and current density

Figure 7.1. (A) and (B) show the potential-time (V-t) transient curve for the anodization process. As typical for galvanostatic anodization, potential increases sharply at the initial stage and reduces gradually with steady state oxide growth and dissolution over anodization time [22]. The sharp increase in potential is due to high resistance imposed by the compact barrier oxide layer. It should be mentioned that barrier oxide results from egressing Al^+ ion (from the metal/oxide interface) and ingress O^{2-} ion (from the oxide/metal interface), following local electrolytic water splitting [23].

As the anodization continues, potential increases linearly with time until it reaches a local maximum called the breakdown potential.
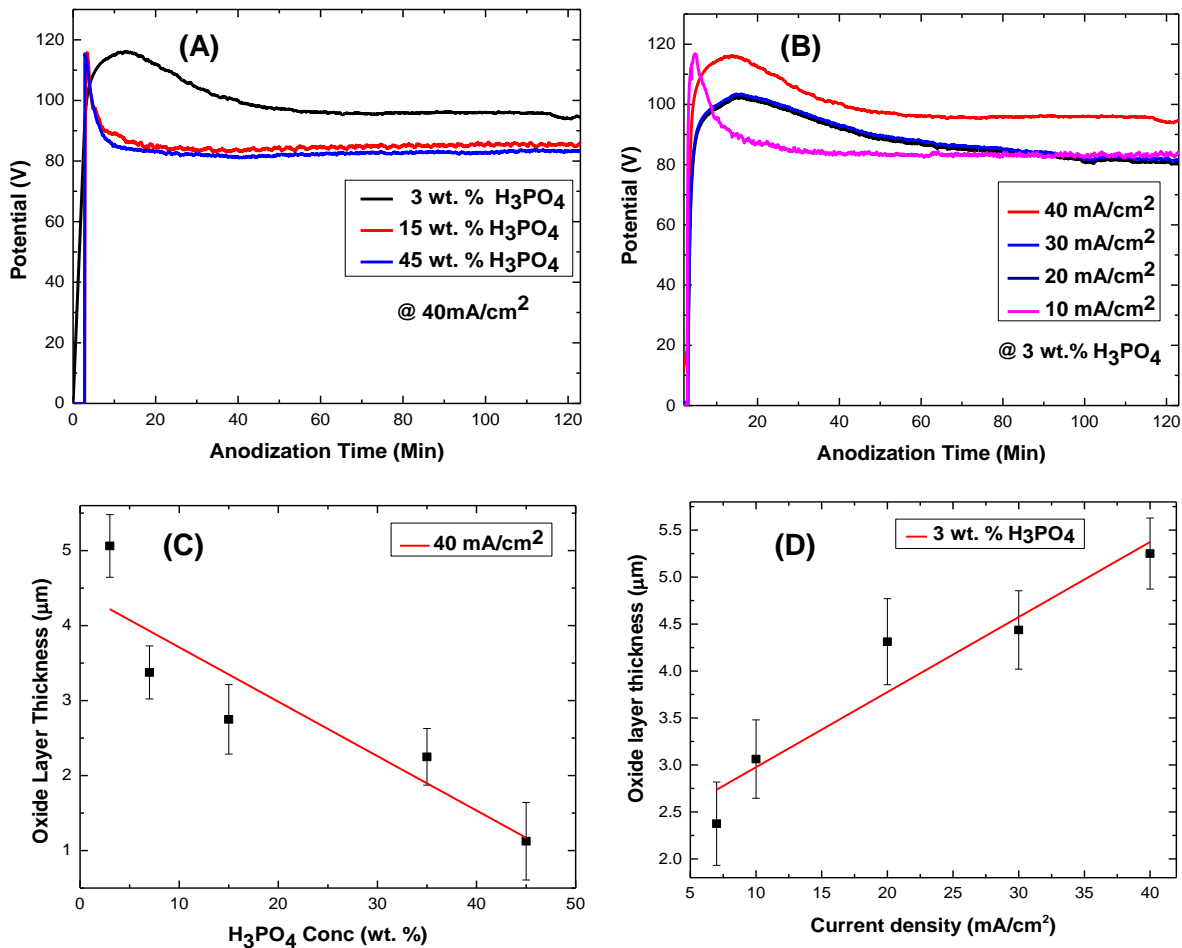
Figure 7-1. Parameters of anodization process: (A) Voltage-time (V-t) transient curve as a function of concentration of H_3PO_4 acid; (B) Voltage-time (V-t) transient curve as a function of current density; (C) Thickness of anodized alumina oxide layer as a function of concentration of H_3PO_4 acid; and (D) Thickness of anodized alumina oxide layer as a function of current density. © Henry Agbe, 2021.

Beyond the breakdown potential, it decreases gradually until it reaches a steady state-forming potential [22]. For a 3 wt. % H₃PO₄, a steady state-forming potential of 96 V was attained after 60 minutes. Beyond this, the potential remains constant for an equilibrium oxide layer growth and dissolution, which leads to a complete formation of porous oxide after 120 minutes. Similar trend was observed for the other H₃PO₄ concentrations such as 15 and 45 wt. %. For example, a steady state-forming potential of 82 V was attained for 45wt. % H₃PO₄ after 50 minutes, which led to complete anodization after 120 minutes. Notably, steady state-forming potential decreased with increasing H₃PO₄ concentration. This may be due to the inverse relation between steady state-forming potential and acid concentration, which is commonly explained by the oxygen bubble growth model [24]. According to this model, total anodizing current (J_{total}) contributing to oxide layer growth and dissolution, consists of both ionic current (J_{ion}) and electronic current (J_e) as shown in Equation 7.1 [25]

$$J_{Total} = J_{ion} + J_e \tag{7.1}$$

where J_{Total}, is the total current, J_{ion}, the ionic current, and J_e, the electronic current. The ionic current contributing to migration of anions and cations at the anode can be expressed as Equation 7.2.

$$2Al^{3+} + 3O^{2-} \rightarrow Al_2O_3 \tag{7.2}$$

similarly, the electronic current leading to oxygen evolution at the anode can be expressed as Equation 7.3.

$$4O^{2-} \rightarrow 2O_2 \uparrow + 8e \tag{7.3}$$

However, since ionic current dominates at the initial stage of anodization, the requisite net current for overcoming the resistance of the compact barrier oxide layer is induced by ionic current [25].

Contrarily, beyond the breakdown potential, electronic current increases at the expense of ionic current. Resulting in a decrease in total current J_{ion} and potential, leading to oxygen evolution and a lower porous oxide growth [24, 25]. Hence, high acid concentration such as 45 wt. % H_3PO_4 resulted in a lower steady state-forming potential of 82V. On the other hand, a low acid concentration such as 3 wt. % H_3PO_4 led to higher steady state-forming potential of 96V. A similar observation was made by Zhang et al [24] on anodized Titanium alloy using NH_4F acid as electrolyte. They demonstrated that NH_4F concentration of 0.5 wt. % resulted in a low steady state-forming potential of 55V compared to 0.1 wt. % NH_4F acid, with a high steady state-forming potential of 95V. As shown in Figure 7.1 (B), steady state-forming potential increased with increased current density. As a result, a steady state-forming potential of 96V was achieved for 40mA/cm^2, compared to 78 V for 10mA/cm^2. Similarly, current density increased linearly with oxide layer thickness. Consequently, 10 mA/cm^2 resulted in oxide layer thickness of 3.1 ± 0.4 µm. On the other hand, 40 mA/cm^2 led to a thickness of 5.3 ± 0.4 µm (Figure 7.1. (C)). Contrarily, as acid concentration increased, oxide layer thickness decreased. Thus, a porous oxide thickness of 1.1 ± 0.5 µm was obtained for 45 wt. % H_3PO_4 concentration, as opposed to a thickness of 5.3 ± 0.4 µm for 3 wt. % H_3PO_4 (Figure 7.1 (D)).

Since topographical features such as pore diameter, cell diameter or pitch, oxide thickness and roughness are important for antibacterial activity [6], topographical features were analyzed using Equations 7.4, 7.5 and 7.6 [22].

$$n = \frac{10^{14}}{P_h} = \frac{2.10^{14}}{\sqrt{3}*D_c^2} \tag{7.4}$$

$$W = \frac{Dc-Dp}{2} \tag{7.5}$$

$$\alpha = \frac{\pi}{2\sqrt{3}}\left(\frac{D_p}{D_c}\right)^2 = 0.907\left(\frac{D_p}{D_c}\right)^2 \tag{7.6}$$

where η is the pore density, P_h is the surface area of a single hexagonal cell, D_p, is the pore diameter and D_c, is the cell diameter in nm. Generally, phosphoric acid with low acid concentration, such as 3% H_3PO_4 and a high current density such as 40 mA/cm^2, led to a large pore diameter, a large cell diameter, a high surface roughness and efficient bactericidal property, compared to 45wt. % H_3PO_4 at a low current density such as 10 mA/cm^2. The low acid concentration leading to increased potential and larger morphological features can be explained by oxygen bubble growth model [25]. By contrast, the classical field-assisted growth model explains the reason for increased current density resulting in larger morphological features. Thus, 3 wt. % H_3PO_4 (herein referred as 3HP40), exhibited a pore a diameter of 151 ± 37 nm, a cell diameter of 239 ± 53 nm, a roughness (rms) of 2.9 ± 0.7 μm and bactericidal efficiency of 100%. Contrarily, 45wt. % H_3PO_4 (herein referred as 45HP40) showed a low pore diameter of 55 ± 12 nm, a cell diameter of 115 ± 16 nm, a roughness (rms) of 0.8 ± 0.1 μm and a bactericidal efficiency of 90%. (Details can be found in Supplementary data, Table S7.1).

7.4.2 Effect of H_2SO_4 concentration and anodization time

Figure 7.2. (A) and (B) show the potential-time (V-t) transient curve at constant current for H_2SO_4 acid anodization. Like H_3PO_4, potential decreased with increasing H_2SO_4 concentration (Figure 7.2. (A)), which can be explained by the oxygen bubble growth model [25]. In addition, potential increased linearly with anodization time. While incomplete anodization was observed for both 30 min and 60 min anodization times, 15wt. % H_2SO_4 anodized at 120 min resulted in complete anodization process (Figure 7.2. (B)). Figure 7.2 (C) shows the graphical representation of H_2SO_4 concentration relative to porous oxide thickness. Notably, a 45 wt. % H_2SO_4 concentration, resulted

in decreased thickness of porous oxide growth compared to that obtained for a low concentration such as 3 wt. % H_2SO_4. However, 15 wt. % H_2SO_4 concentration was deemed optimal for its bioactivity (see section 7.3).
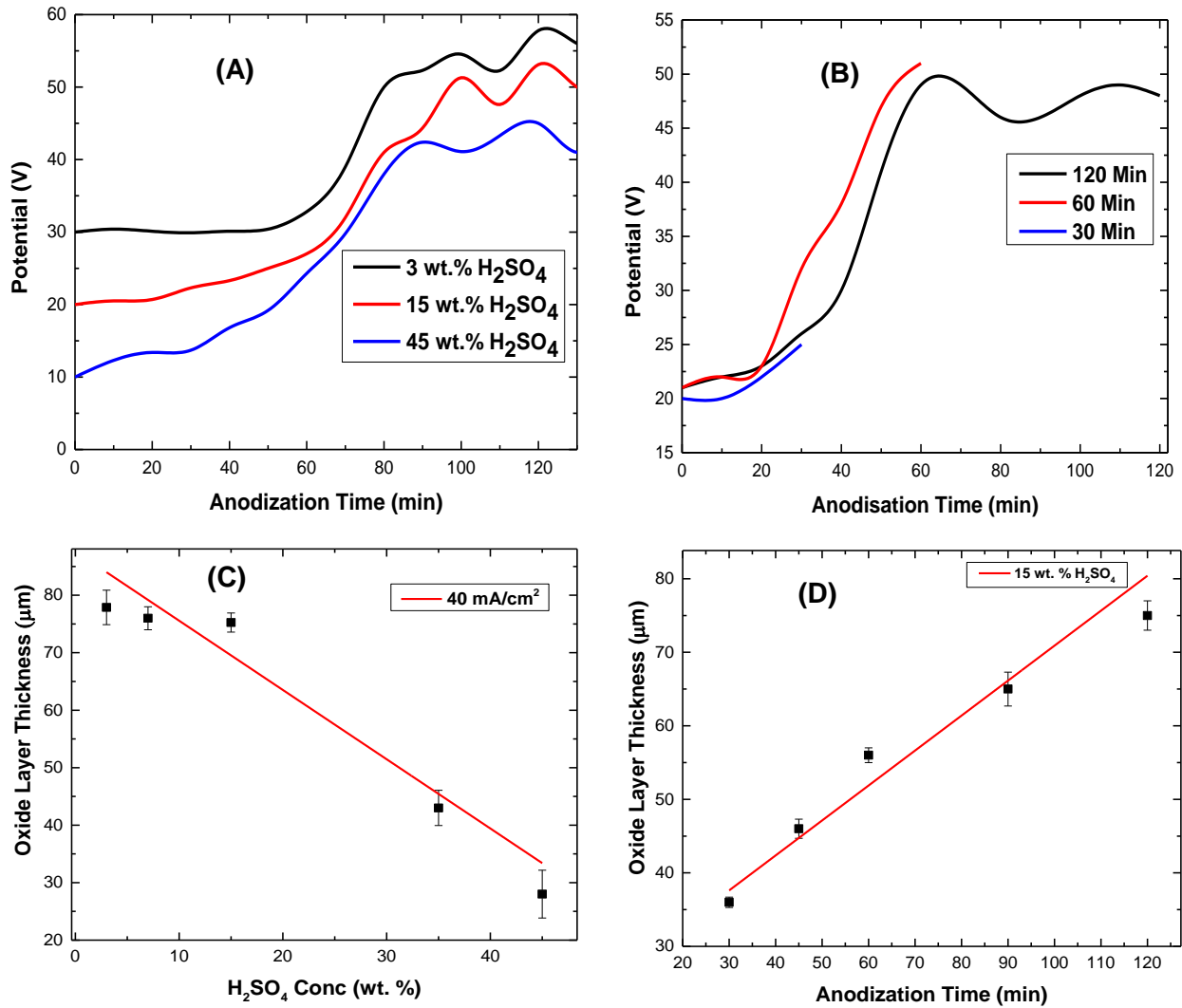
Figure 7-2. Parameters of anodization process: (A) Voltage-time (V-t) transient curve as a function of concentration of H_2SO_4 acid; (B) Voltage-time (V-t) transient curve as a function of anodization time; (C) Thickness of anodized alumina oxide layer as function of concentration of H_2SO_4 acid; (D) Thickness of anodized alumina oxide layer as a function of anodization time. © Henry Agbe, 2021.

As shown in Figure 7.2 (D), porous oxide growth increased linearly with anodization time. Thus, porous oxide increased from 36 ± 0.7 μm to 75 ± 2.0 μm, for anodization time of 30 min and 120 min, respectively. Also, 15 wt. % H_2SO_4 (herein referred as 15HS40) concentration produced a pore diameter of 60 ± 11 nm, a cell diameter of 121 ± 19 nm, a roughness (rms) of 9.2 ± 0.6 μm and 100% antibacterial performance. In contrast, 45 wt. % H_2SO_4 concentration (herein referred as 45HS40) produced a pore diameter of 27 ± 13 nm, a cell diameter of 60 ± 20 nm, a roughness (rms) of 5.0 ± 0.7 μm and a 79% antibacterial performance. (Details can be found in Supplementary data in Table S 7.2 and Figure S7-7). However, since phosphoric acid anodization is more advantageous compared to sulphuric acid, in terms of cost and environmental friendliness [23], phosphoric acid anodization was selected for the remainder of the study involving antibacterial activities.

7.5 Antibacterial activity

Antibacterial activity was studied by a novel dry seeding assay against E. coli bacterium on both test and control coupons. The objective here was to mimic a real-world scenario. Thus, we inoculated test coupons with *E. coli* inoculum at ambient conditions of 25 °C and relative humidity of $50 \pm 10\%$ in a cell culture plate for pre-determined contact time of 1-4h. Figure 7.3 shows the effects of morphological features on *E.coli* bacterial killing. Generally, antibacterial efficiency of anodized coupon increased linearly with increased pore diameter, cell diameter, oxide layer thickness and root mean square roughness. Anodized coupon having a lower H_3PO_4 concentration such as 3

wt. %. and a high current density such as 40 mA/cm^2, exhibited a high antibacterial efficiency compared to anodized coupon with a high H$_3$PO$_4$ concentration such as 45wt. %.
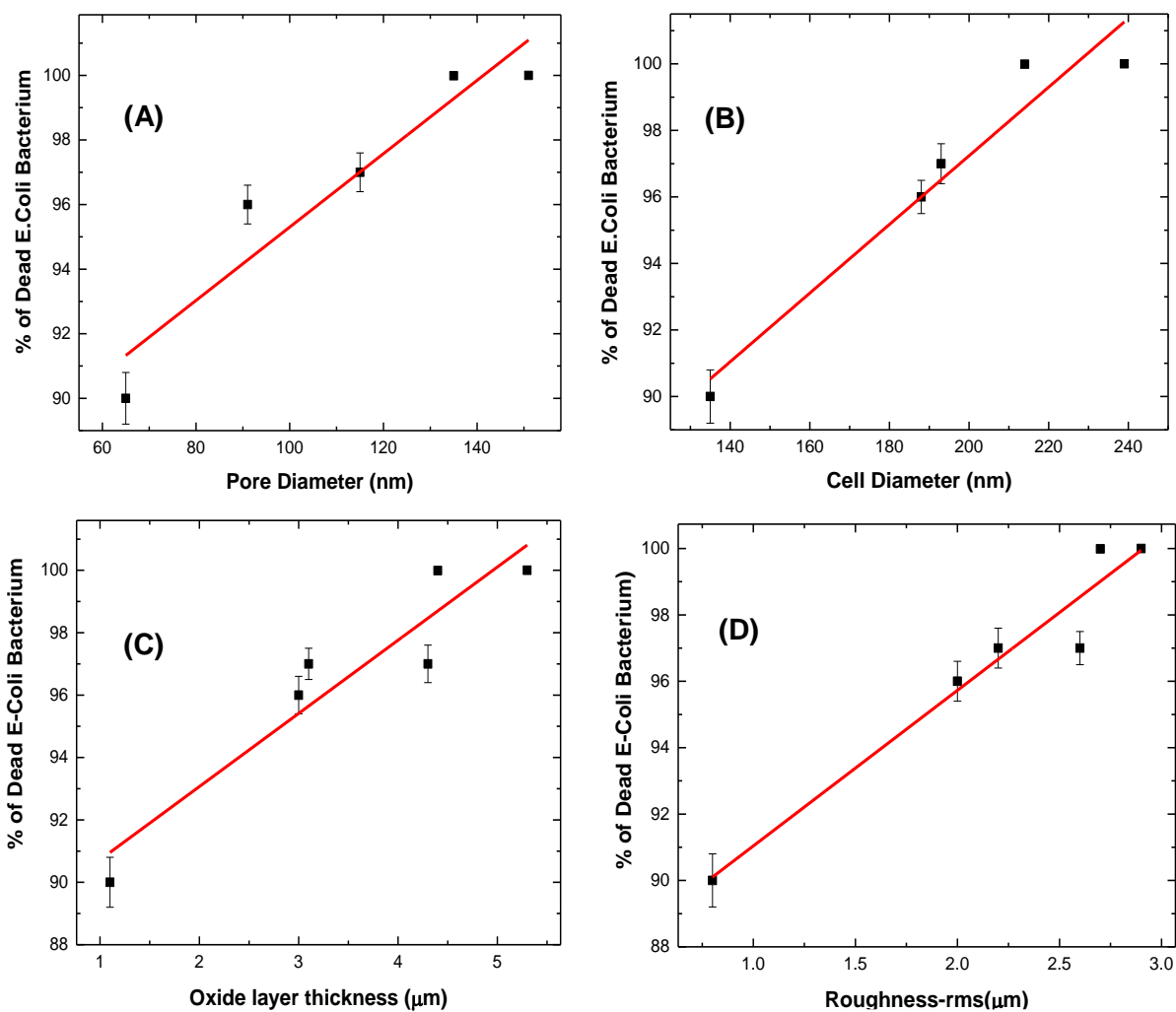
Figure 7-3. Effects of morphological features resulted from different anodization parameters on *E. coli* bacteria killing efficiency: (A) pore diameter, (B) cell diameter, (C) oxide thickness, (D) surface roughness (rms). © Henry Agbe, 2021.

In particular, for 3wt.% H_3PO_4, increasing the current density from 10 mA/cm^2 to 40 mA/cm^2, led to increase in both pore and cell diameters with a corresponding increase in bactericidal performance (Details can be found in Supplementary data, Table S7.1 and Figure S7.8). For instance, the pore diameter increased from 65 ± 15 μm to 151 ± 37 μm for current densities of 7 to 40 mA/cm^2, corresponding in an increase of antibacterial activity from 90 to 100%, (Figure 7.3 (A)). Similarly, the cell diameter or pitch increased from 135 ± 10 μm to 239 ± 53 μm for same current densities with a corresponding increase in antibacterial activity from 90 to 100% (Figure 7.3 (B)). As would be expected, the current density also increased linearly with porous oxide thickness and hence antibacterial activity. Oxide thickness of 1.1 ± 0.5 μm and 5.3 ± 0.4 μm, were obtained for current densities of 7 and 40 mA/cm^2, respectively, resulting in 90% and 100% antibacterial efficiency (Figure 7.3 (C)), respectively. Similar trend was observed for the surface roughness and bacterial efficiency (Figure 7.3 (D)). It should be mentioned that exact antibacterial mechanism for 3 wt. % H_3PO_4 anodized coupon-3HP40, was not fully elucidated here. Bacterial attachment on both biotic and abiotic substratum surfaces is a complex phenomenon, involving surface chemistry and substratum surface morphology, bacterial cell type and adhesion, Van der Waals interactions, extra polymeric substance (EPS) and quorum sensing molecules [26]-[27] etc,. However, we hypothesize that the micro-nanoscale topography features, characterized as pore diameter, cell diameter (pitch) and roughness (rms) may be responsible for the excellent bactericidal activity. It should be mentioned that previous reports have confirmed a topography-mediated antibacterial surface [5]. In fact, Ivanova et al.[5] first reported on topography-mediated bactericidal effects on *Psaltoda claripennis* cicada wings. In their work, they demonstrated that by pure physical contact of *Pseudomonas aeruginosa* (P.A) (gram -ve) bacterium on micro-nanoscale patterns cicada wings, P.A died in 30 minutes. These

nanoscale pillar arrays were hexagonal and conical shapes, with spherical caps of diameter ~ 60 nm, pitch of 170 nm and height of 200 nm [5]. Similarly, in a recent work by Hasan, et al [17, 18], a 3 h NaOH and KOH chemical etching of wrought aluminum alloys (Al 5052, Al 1200 and Al 6063) resulted in a 5 to 97% antibacterial efficiency. However, by using gold sputtering to alter surface chemistry, they confirmed antibacterial activity of the etched aluminum alloys was purely mediated by topography [17]. Also, Kelleher, S.M. et al [9] showed that nano-pillar array of diameters ranging from 156 ± 29 nm to 207 ± 62 nm and pitch ranging from 165 ± 8 nm to 251 ± 31 nm, could effectively kill *Pseudomonas fluorescens* bacterium. However, direct comparison of reported results in the literature must be treated with caution as the difference may arise due to different experimental conditions. In the present report, 3 wt. % H_3PO_4 anodized coupon-3HP40 was compared with the control coupons of as-received aluminum and of antibacterial solid copper (C11000 of 99.9% Cu) in a novel dry seeding assay. It is worthy to note that since 2008, copper has been registered by the United States Environmental Protection Agency (US-EPA) as an antimicrobial touched surface and regarded as gold standard for comparing other non-porous antimicrobial touched surfaces [28-30]. Also note that existing protocols such as the ASTM E 2180 [31], the Japanese Standard JIS Z2801 [32] or the ISO 22196 [33] stipulate conditions of high liquid medium and temperature of ~37°C. While these protocol might be ideal for biomedical implant applications, they do reflect the near dry conditions of inanimate environmental surfaces in close proximity to patients, typified by a comfortable humidity and temperature [34]. Thus, these protocols may not truly predict the efficacy of antibacterial surfaces under realistic conditions [34].

Figure 7.4 shows representative images of *E. coli* bacterium colonies on 3HP40 test coupon, relative to the control coupons. Compared to anodize aluminum coupon-H3P40, as-received aluminum displayed a confluent bacterial growth with evenly spread colonies on TSA media even

after 4 h *E. coli* bacterium contact. On the contrary, it is noticeable that 3 wt.% H_3PO_4 anodized aluminum coupon-3HP40 killed virtually all bacteria under 1 h of *E. coli* bacterium contact. The number of colonies on as-received aluminum at time 0 h, 1 h, and 4 h were 4.5×10^7, 4.207×10^7 and 2.24×10^7, respectively. These represent a 6.6% or 0-log reduction, 39% or 0.2 log reduction and 51% or 0.3 log reduction, respectively (see Table S 7-3 of supplementary data). In contrast, the 3 wt.% H_3PO_4 anodized aluminum coupon-3HP40 achieved a bactericidal efficiency of 99.99998% or 6.5 log reduction after 1 h of contact.
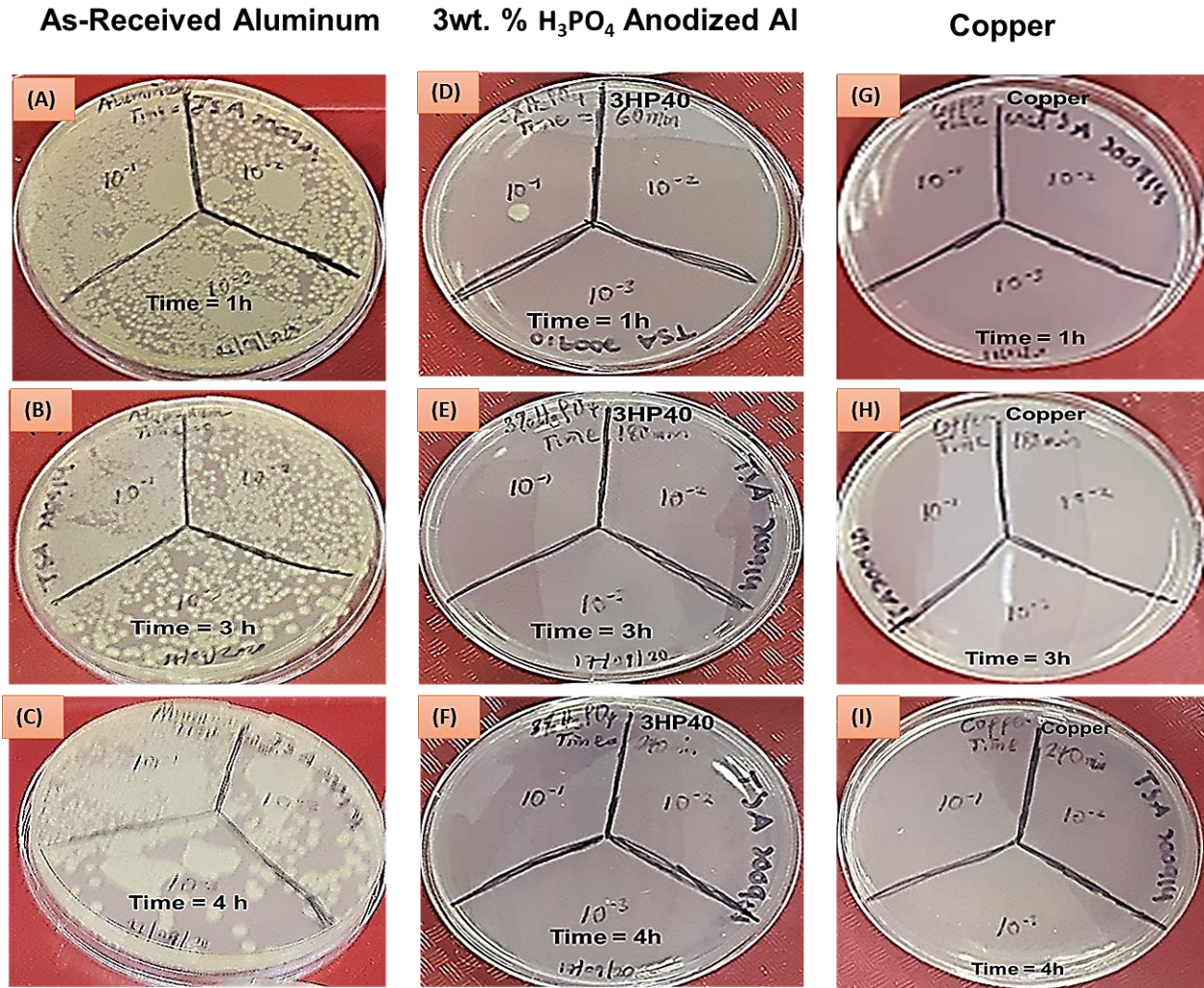
Figure 7-4. Representative images of colonies of *E. coli* in contact with as-received aluminum coupon from 1- 4 h (A)-(C); 3 wt.% H_3PO_4 anodized aluminum coupon-3HP40 from 1- 4 h (D)-(F); and copper coupon from 1- 4 h (G)-(I). © Henry Agbe, 2021.

The results of 3 wt.% H_3PO_4 anodized aluminum are very comparable with the commercially available antimicrobial copper, of which both exhibited a 100% bactericidal efficiency after 1 h under same conditions (Figure 7.5). It must be noted that minimum microbiologic bacterial loads acceptable in hospital inanimate environmental surfaces is 2.5 cfu/cm^2. Thus, bacterial colonies of 2.24×10^7 on

as-received aluminum could be regarded worrisome; since such surface contamination could be a potential reservoir for spread of nosocomial infection.
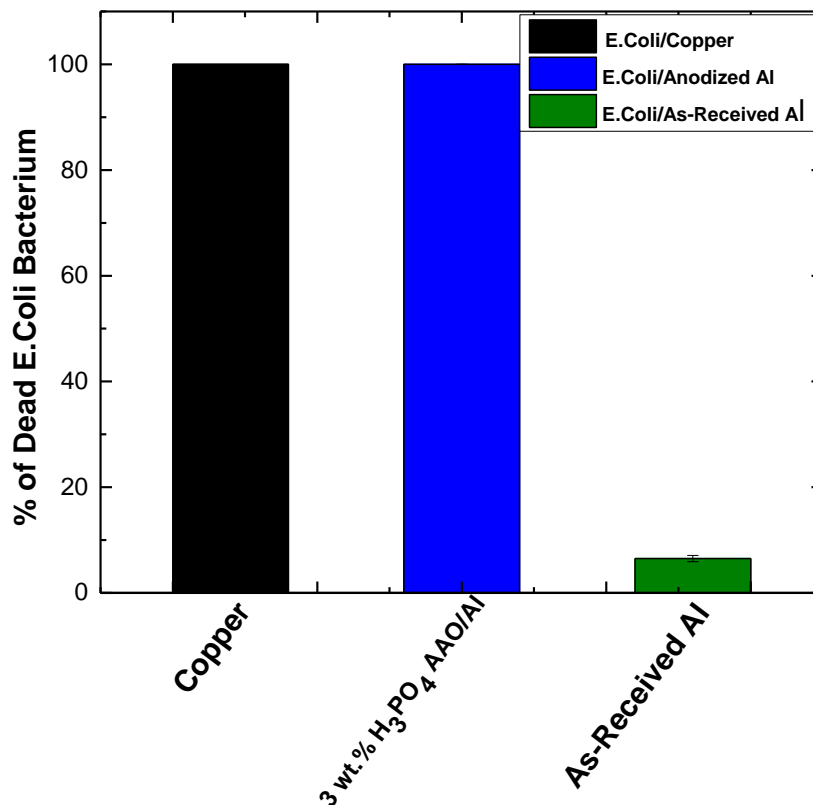
Figure 7-5. Bactericidal efficiency of *E. coli* bacteria on 3 wt.% H_3PO_4 anodized aluminum coupon-3HP40 compared to control samples (as-received aluminum and copper) under 1 h of contact. Data represent three independent experiments. © Henry Agbe, 2021.

According to the US-EPA, touched surfaces with the claim of antibacterial property ought to kill or inhibit the growth of bacteria to a minimum of 3-log reduction or 99.9 % [35]. Thus, the 3 wt.% H_3PO_4 anodized aluminum is very promising and shows great potentials as the ideal condition for practical antibacterial touched surface applications.

Figure 7.6 (A) and (B) show the SEM micrographs of as-received aluminum and 3 wt.% H_3PO_4 anodized aluminum coupon-3HP40, respectively. Notably, rod shaped *E. coli* bacteria (green arrows) are clearly seen on as-received aluminum (Figure 7.6 (A). In contrast, live *E. coli* bacteria cells are not seen on 3 wt.% H_3PO_4 anodized aluminum coupon-3HP40, except for cytoplasmic material (shown in the region in red) (Figure 7.6 (B)), which leaked out from bacteria after they were deformed and sunk into the nanopores [8]. In fact, the antibacterial mechanism for topography-mediated antibacterial surfaces such as cicada wings has been attributed to the self-induced shear stresses on bacterial cell membrane in contact with nano-pillars [1, 5, 36, 37]. Specifically, higher surface roughness, coupled with micro-nanoscale patterns increases surface area for attachment from multiple focal points and overall bacterial-substratum interaction. A stronger bacterial-substratum interaction would presumably enhance the tendency for bacterial membrane to be stretched out, leading to an irreversible rupture and death [32]. However, in the present work, a micro-nanoscale pattern was achieved by nano-pore arrays, different from other nanostructures such as nanopillars reported previously [5-7]. Thus, we hypothesize that upon bacterial attachment on the surface of the anodized aluminum (3HP40), *E. coli* bacteria become suspended under gravity within nano-pore arrays of anodized surface, where the suspended regions of anodized pores induce shear stresses on *E. coli* cell membrane. In their attempt to avoid uncomfortable suspended regions, *E. coli* bacteria release extra polymeric substance (EPS), which further enhance bacterial attachment on nano-pores of anodized aluminum surface (3HP40). Consequently, this leads to membrane deformation, cytoplasmic material leakage, failure of cell membrane integrity [8] and bacterial death.
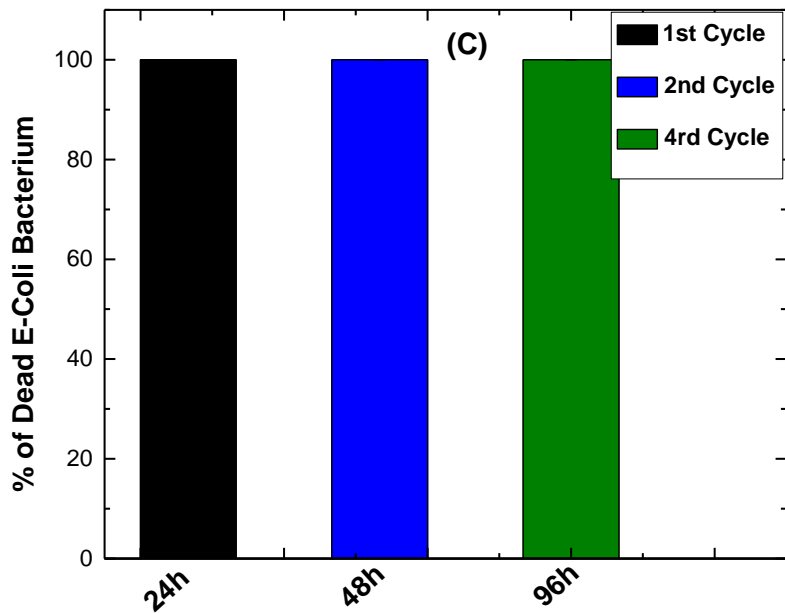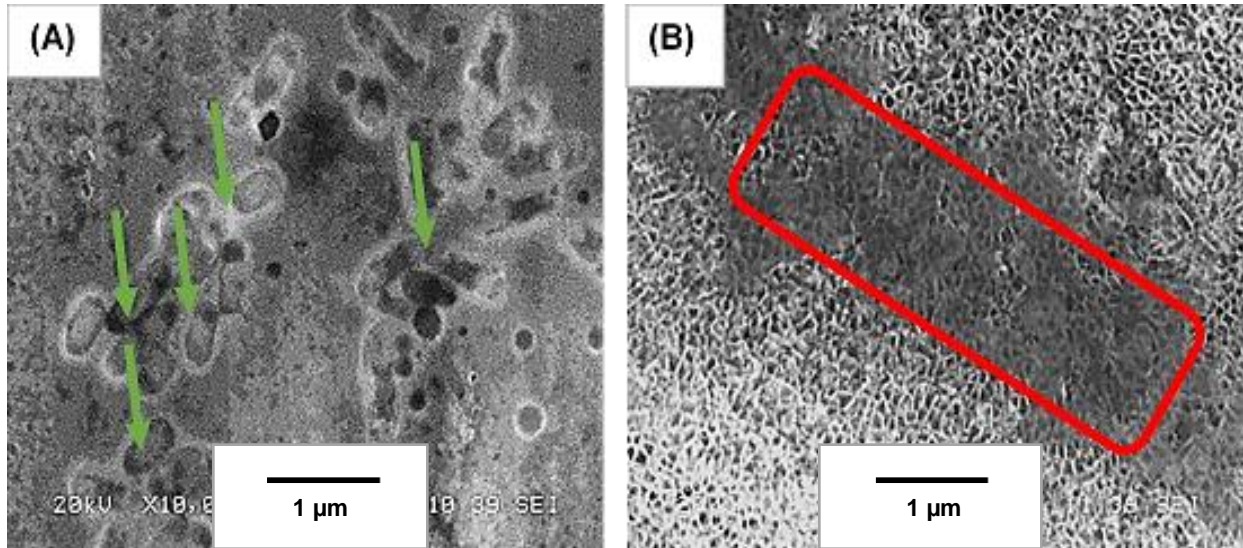
Figure 7-6. Representative SEM microimages of colonies *E-Coli* bacteria on: (A) As-received aluminum coupon; (B) 3 wt.% H_3PO_4 anodized aluminum coupon-3HP40; and (C) Graphical representation of 96 h *E. coli* bacteria continuous loading on 3 wt.% H_3PO_4 anodized aluminum coupon-3HP40. The green arrows in (A) show live *E. coli* bacteria and the region in red in (B) indicates dead *E. coli* bacteria, respectively. Data represent three independent experiments. © Henry Agbe, 2021.

Figure 7.6 (C) shows a graphical representation of a 96-h continuous *E. coli* bacterial loading study on the 3 wt.% H_3PO_4 anodized aluminum coupon-3HP40. The samples were monitored at 24 h interval within cycles to evaluate the long-term activity of the anodized aluminum surface. Interestingly, even after 96 h *E. coli* bacteria continuous loading cycles, the 3 wt.% H_3PO_4 anodized aluminum coupon-3HP40 was still bioactive with a 100% bactericidal efficiency. Thus, this anodized aluminum surface with excellent bactericidal efficiency and durability looks promising for antibacterial touched surface applications and an adjunct to hand hygiene for reducing potential bacterial infections in hygiene critical environments.

7.6   Conclusions

In the present study, a topography-mediated novel antibacterial aluminum surface was fabricated using a one-step hard anodization process. Anodization parameters such as electrolyte concentration, time and current density were optimized. 3wt.% H_3PO_4 anodized aluminum at current density of 40 mA/cm^2 and anodization time of 120 minutes exhibited a larger pore diameter (151 ± 37 nm), larger cell dimeter (239 ± 53 nm), higher oxide layer thickness (5.3 ± 0.4 nm) and higher *rms* roughness (2.9 ± 0.7μm), compared to 45 wt.% H_3PO_4 anodized aluminum at same conditions. Furthermore, 3wt.% H_3PO_4 anodized aluminum at current density of 40 mA/cm^2 compared favourably with antibacterial solid copper with 100% bactericidal efficiency after 1 h *E. coli* bacterium contact. Overall, the fabrication of topography-mediated antibacterial aluminum presents a novel approach to be considered for the use of the next generation frequently touched surfaces.

7.7 Supporting information

Table S7-1. Effect of H$_3$PO$_4$ acid concentration and current density on morphological features of as received aluminum coupon and various anodized aluminum coupons under different conditions.

Samples	Pore Diameter: Dp (nm)	Cell Diameter Pitch (P) (nm)	Wall Thickness: W (nm)	Oxide Thickness (μm)	Pore Density: η (pore/cm^2)	Porosity: α (%)	Roughness: Rq (um)	Bactericidal activity against E. coli (%)
As Received Al	Nii	Nii	Nii	Nii	Nii	Nii	0.5 ± 0.1	50
Varied H$_3$PO$_4$ concentration (3%, 15% and 45%) @ constant current density of 40 mA/cm^2 and time = 120 min								
3HP40 (3% H$_3$PO$_4$)	151 ± 37	239 ± 53	44 ± 8	5.3 ± 0.4	2.0 x 10^9	57	2.9 ± 0.7	100
15HP40 (15% H$_3$PO$_4$)	119 ± 30	188 ± 41	35 ± 5.5	3.0 ± 0.5	3.2 x 10^9	27	1.6 ± 0.1	97
45HP40 (45% H$_3$PO$_4$)	55 ± 12	115 ± 16	30 ± 2	1.1 ± 0.5	8.7 x 10^9	21	0.8 ± 0.1	85
Varied current density (10, 20, 30 and 40 mA/cm^2) @ constant H$_3$PO$_4$ concentration (3%) and time = 120 min								
3HP10 (10 mA/cm^2)	91 ± 35	188 ± 37	49 ± 1	3.1 ± 0.4	3.3 x 10^9	21	2.0 ± 0.7	99
3HP20 (20 mA/cm^2)	115 ± 30	193 ± 41	39 ± 6	4.3 ± 0.4	3.0 x 10^9	32	2.2 ± 0.6	99.4
3HP30 (30 mA/cm^2)	135 ± 29	214 ± 37	43 ± 3	4.4 ± 0.4	2.9 x 10^9	45	2.7 ± 0.8	99.99
3HP40 (40 mA/cm^2)	151 ± 37	239 ± 53	44 ± 8	5.3 ± 0.4	2.0 x 10^9	57	2.9 ± 0.7	100
Anodization Time (120 min) @ constant C$_2$H$_2$O$_4$ concentration (10%) and current density of 40 mA/cm^2								
10CH40 (40 mA/cm^2)	45 ± 7	93 ± 10	24 ± 2	3.2 ± 0.7	5.7 x 10^9	21	2.3 ± 0.6	96

Table S7-2. Effect of H_2SO_4 acid concentration and anodization time on morphological features of various anodized aluminum coupons under different conditions

	Pore Diameter: Dp (nm)	Cell Diameter (Pitch (P)) (nm)	Wall Thickness: W (nm)	Oxide Thickness (μm)	Pore Density: n (pore/cm²)	Porosity: α (%)	Roughness: Rq (um)	Bactericidal activity against E. coli (%)
Varied H_2SO_4 concentration (3%, 15% and 45%) @ constant current density of 40 mA/cm² and time = 120 min								
3HS40 (3% H_2SO_4)	30 ± 19	62 ± 19	16 ± 0.1	78 ± 3.0	3.0×10^{10}	21	11.2 ± 0.9	80
15HS40 (15% H_2SO_4)	60 ± 11	121 ± 19	31 ± 4	75 ± 1.7	7.9×10^{9}	22	9.2 ± 0.6	100
45HS40 (45% H_2SO_4)	27 ± 13	60 ± 20	20 ± 7	28 ± 4.2	3.2×10^{10}	18	5.0 ± 0.6	79
Varied Anodization Time (30, 60 and 120 min) @ constant H_2SO_4 concentration (15%) and constant current density of 40 mA/cm²								
15HS120 (120 min)	60 ± 11	121 ± 19	31 ± 4	75 ± 2.0	7.9×10^{9}	22	9.2 ± 0.6	100
15 HS60 (60 min)	39 ± 18	90 ± 20	26 ± 2	56 ± 1.0	1.4×10^{10}	17	5.0 ± 0.4	70
15HS30 (30 min)	26 ± 6	59 ± 14	17 ± 4	36 ± 0.7	3.3×10^{10}	18	3.0 ± 0.2	68

.
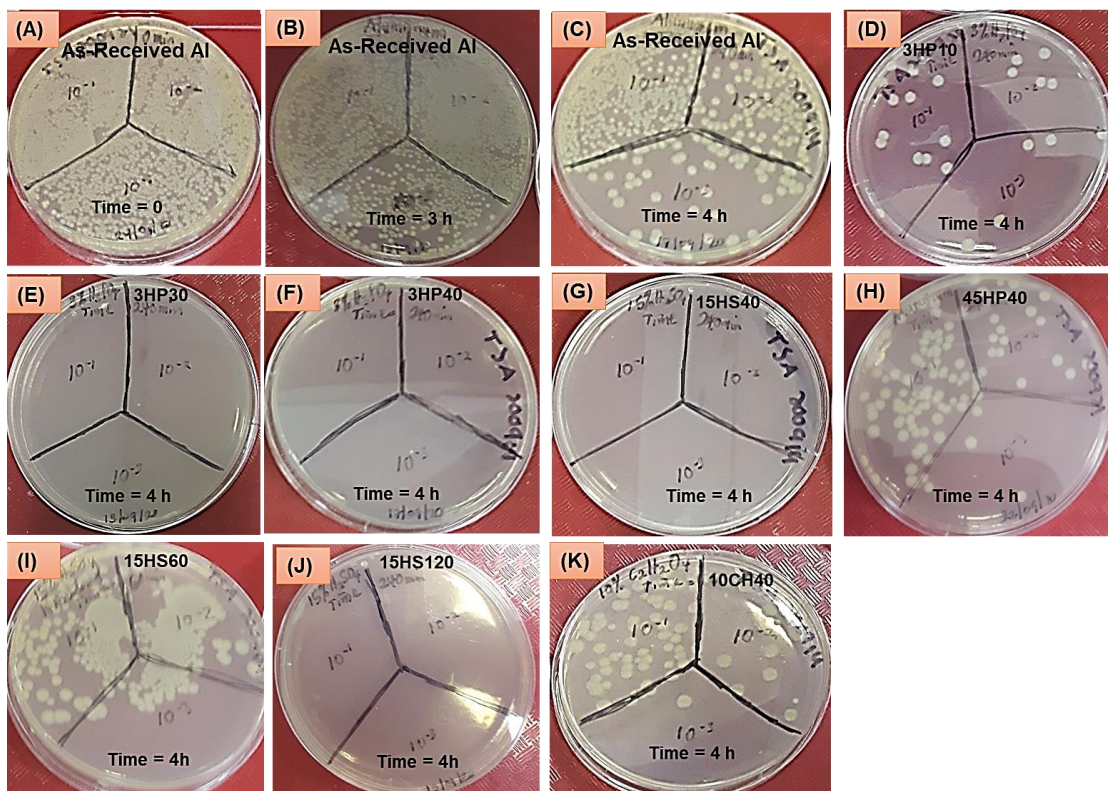
Figure S7-7. Representative images of colonies of *E. coli* bacterium in contact with: as-received aluminum for 0 h (A), 3 h (B) and 4 h (C); 3 wt.% H_3PO_4 anodized aluminum for 4 h at 10mA/cm^2 (3HP10) (D), at 30mA/cm^2 (3HP30) (E) and at 40mA/cm^2 (3HP40) (F); 15 wt.% H_2SO_4 anodized aluminum for 2 h at 40mA/cm^2 (15HS40) (G); 45 wt.% H_3PO_4 anodized aluminum for 2 h at 40mA/cm^2 (45HP40) (H); 15 wt.% H_3PO_4 anodized aluminum for 1 h at 40mA/cm^2 (15HS60) (I); 15 wt.% H_3PO_4 anodized aluminum for 2 h at 40mA/cm^2 (15HS120) (J); and 10 wt.% $C_2H_2O_4$ anodized aluminum at 40mA/cm^2 (10CH40) (K). © Henry Agbe, 2021.
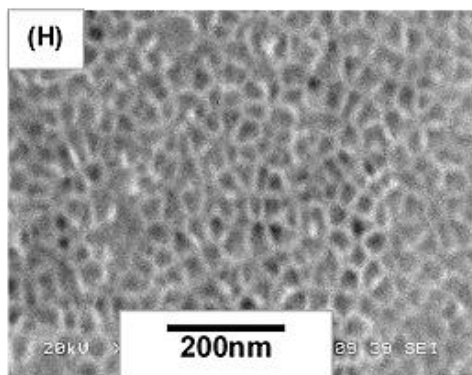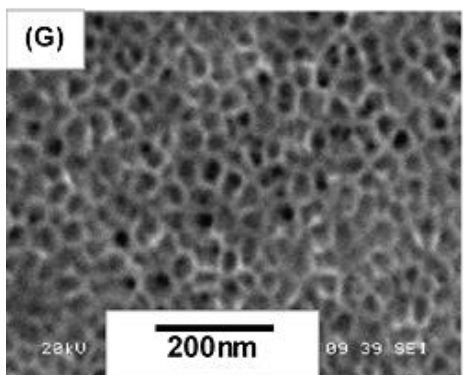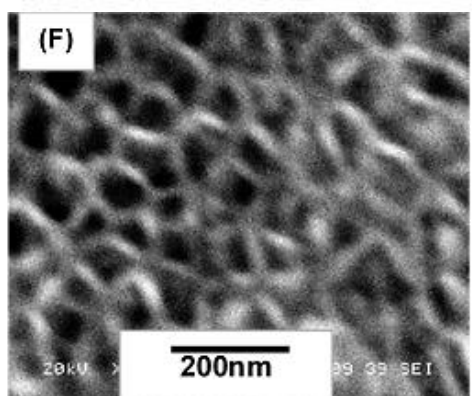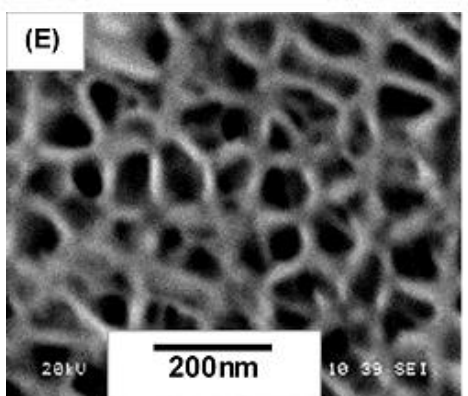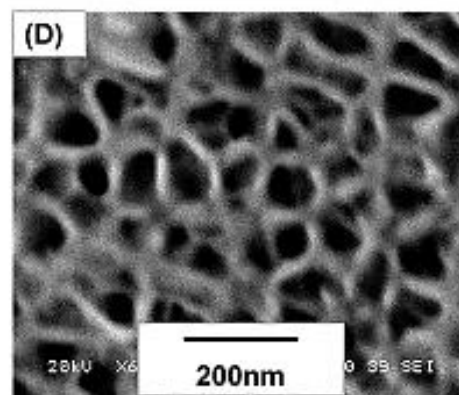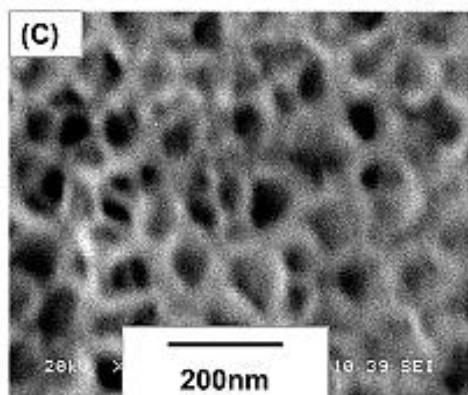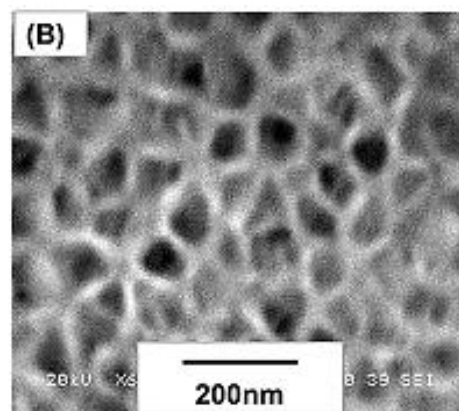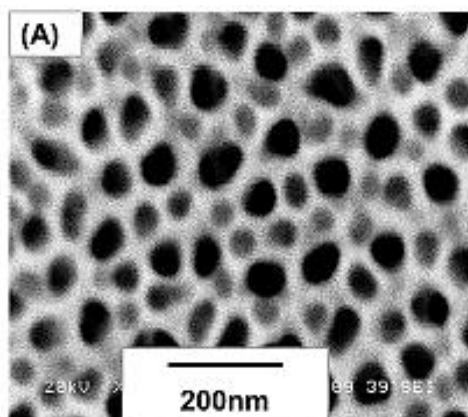
Figure S7-8. Representative SEM micro images of anodized aluminum coupons using 3 wt.% H_3PO_4 at a current density of: (A) 10 mA/cm^2, (B) 20 mA/cm^2, (C) 30 mA/cm^2 and (D) 40 mA/cm^2; and at a constant current density of 40 mA/cm^2 and varied phosphoric acid concentrations of: (E) 3 wt.% H_3PO_4, (F) 15 wt.% H_3PO_4, (G) 35 wt.% H_3PO_4 and (H) 45 wt.%. H_3PO_4. © Henry Agbe, 2021

Table S7-3. Bactericidal performance of 3 wt. % H_3PO_4 anodized coupon-3HP40 compared to control samples (as-received aluminum and copper).

Bacterial Strain		As-Receive Aluminum	3HP40	Copper
	Time 0	45,000,000	-	-
Escherichia coli (ATCC 7839)	CFU/cm^2 after 1 h	42,075,000	< 10	0
	Reduction Rate [%]	6.5	99.99998	100
	Log 10 Reduction	0.0	6.7	7.7
Escherichia coli (ATCC 7839)	CFU/cm^2 after 3 h	27,333,333	0	0
	Reduction Rate [%]	39.3	100	100
	Log 10 Reduction	0.2	7.7	7.7
Escherichia coli (ATCC 7839)	CFU/cm^2 after 4 h	22,000,000	0	0
	Reduction Rate [%]	51	100	100
	Log 10 Reduction	0.3	7.7	7.7

7.8 **Reference:**

1. Jafar Hasan, Anindo Roy, Kaushik Chatterjee**,** Prasad K. D. V. Yarlagadda, *Mimicking insect wings: The roadmap to bioinspiration.* ACS Biomaterials Science & Engineering, 2019. **5**(7): p. 3139-3160.
2. Elena P. Ivanova, Song Ha Nguyen, Hayden K. Webb, Jafar Hasan, Vi Khanh Truong, Robert N. Lamb, Xiaofei Duan, Mark J. Tobin, Peter J. Mahon, Russell J. Crawford, *Molecular organization of the nanoscale surface structures of the dragonfly Hemianax papuensis wing epicuticle.* PLoS One, 2013. **8**(7): p. e67893.
3. Crawford, R.J. and E.P. Ivanova, *Superhydrophobic surfaces.* 2015: Elsevier.
4. Henry Agbe, Dilip Kumar Sarkar**,** X.-Grant Chen, Nathalie Faucheux, Gervais Soucy, Jean-Luc Bernier, *Silver–Polymethylhydrosiloxane Nanocomposite Coating on Anodized Aluminum with Superhydrophobic and Antibacterial Properties.* ACS Applied Bio Materials, 2020. **3**(7): p. 4062-4073.
5. Jafar Hasan, Hayden K Webb, Vi Khanh Truong, Sergey Pogodin, Vladimir A Baulin, Gregory S Watson, Jolanta A Watson, Russell J Crawford, Elena P Ivanova, *Selective bactericidal activity of nanopatterned superhydrophobic cicada Psaltoda claripennis wing surfaces.* Applied microbiology and biotechnology, 2013. **97**(20): p. 9257-9262.
6. Elena P. Ivanova, Jafar Hasan, Hayden K. Webb, Vi Khanh Truong, Gregory S. Watson, Jolanta A. Watson, Vladimir A. Baulin, Sergey Pogodin, James Y. Wang, Mark J. Tobin, Christian Löbbe, Russell J. Crawford, *Natural bactericidal surfaces: mechanical rupture of Pseudomonas aeruginosa cells by cicada wings.* Small, 2012. **8**(16): p. 2489-2494.
7. Elena P. Ivanova, Denver P. Linklater, Marco Werner, Vladimir A. Baulin, XiuMei Xu, Na, *The multi-faceted mechano-bactericidal mechanism of nanostructured surfaces.* Proceedings of the National Academy of Sciences, 2020. **117**(23): p. 12598-12605.
8. Chaturanga D. Bandara, Sanjleena Singh, Isaac O. Afara᾽ Annalena Wolff, Tuquabo Tesfamichael, Kostya Ostrikov, Adekunle Oloyede, *Bactericidal effects of natural nanotopography of dragonfly wing on Escherichia coli.* ACS applied materials & interfaces, 2017. **9**(8): p. 6746-6760.
9. S M Kelleher, O Habimana, J Lawler, B O' Reilly, S Daniels, E Casey, A Cowley, *Cicada wing surface topography: an investigation into the bactericidal properties of nanostructural features.* ACS applied materials & interfaces, 2016. **8**(24): p. 14966-14974.

10. Elena P. Ivanova, Jafar Hasan, Hayden K. Webb, Gediminas Gervinskas, Saulius Juodkazis, Vi Khanh Truong, Alex H.F. Wu, Robert N. Lamb, Vladimir A. Baulin, Gregory S. Watson, Jolanta A. Watson, David E. Mainwaring, Russell J. Crawford, *Bactericidal activity of black silicon.* Nature communications, 2013. **4**(1): p. 1-7.

11. Mary Nora Dickson, Elena I Liang, Luis A Rodriguez, Nicolas Vollereaux, Albert F Yee, *Nanopatterned polymer surfaces with bactericidal properties.* Biointerphases, 2015. **10**(2): p. 021010.

12. Chris M. Bhadra, Vi Khanh Truong, Vy T. H. Pham, Mohammad Al Kobaisi, Gediminas Seniutinas, James Y. Wang, Saulius Juodkazis, Russell J. Crawford, Elena P. Ivanova, *Antibacterial titanium nano-patterned arrays inspired by dragonfly wings.* Scientific reports, 2015. **5**(1): p. 1-12.

13. Xuewen Wang, Chris M. Bhadra, Thi Hoang Yen Dang, Ričardas Buividas, James Wang, Russell J. Crawford, Elena P. Ivanova, Saulius Juodkazis, *A bactericidal microfluidic device constructed using nano-textured black silicon.* RSC advances, 2016. **6**(31): p. 26300-26306.

14.   Van Doremalen, N, *Aerosol and surface stability of SARS-CoV-2 as compared with SARS-CoV-1.* New England Journal of Medicine, 2020. **382**(16): p. 1564-1567.

15.   Walker, J., *Decontamination in Hospitals and Healthcare.* 2019: Woodhead Publishing.

16.   Kramer, A., I. Schwebke, and G. Kampf, *How long do nosocomial pathogens persist on inanimate surfaces? A systematic review.* BMC infectious diseases, 2006. **6**(1): p. 130.

17.   Jafar Hasan, Shubham Jain, Rinsha Padmarajan, Swathi Purighalla, Vasan K. Sambandamurthy, Kaushik Chatterjee, *Multi-scale surface topography to minimize adherence and viability of nosocomial drug-resistant bacteria.* Materials & design, 2018. **140**: p. 332-344.

18.   Jafar Hasan, Yanan Xu, Tejasri Yarlagadda, Michael Schuetz, Kirsten Span, Prasad KDV Yarlagadda, *Antiviral and antibacterial nanostructured surfaces with excellent mechanical properties for hospital applications.* ACS Biomaterials Science & Engineering, 2020.

19.   Jafar Hasa, Alyssa Pyke, Neelima Nair, Tejasri Yarlagadda, Geoffrey Will, Kirsten Spann, Prasad K.D.V. Yarlagadda, *Antiviral Nanostructured Surfaces Reduce the Viability of SARS-CoV-2.* ACS Biomaterials Science & Engineering, 2020.

20.   Kathrin Schwirn, Woo Lee, Reinald Hillebrand, Martin Steinhart, Kornelius Nielsch, Ulrich Gösele, *Effect of alkaline etching on microstructure and anticorrosion performance of anodic film on Al-Mg-Si alloy.* Corrosion Science, 2020. **169**: p. 108642.

21.   Rungsinee Canyook, Phakaphol Seubsom, JatupumSang-ngean, Thotsaphon Trirujirapapong, Kattareeya Taweesup, *Influences of sealing solutions on anodized layer properties of 7075 aluminium alloy.* Materials Today: Proceedings, 2018. **5**(3): p. 9483-9488.

22.   Alkire, R.C., Y. Gogotsi, and P. Simon, *Nanostructured materials in electrochemistry.* 2008: John Wiley & Sons.

23.   Lee, W. and S.-J. Park, *Porous anodic aluminum oxide: anodization and templated synthesis of functional nanostructures.* Chemical reviews, 2014. **114**(15): p. 7487-7556.

24.   Zhaoying Zhang, Qianqian Liu, Mingfei He, Fengrui Tang, Zongrong Ying, Haoqing Xu, Ye Song, Junwu Zhu and Xufei Zhu, *Quantitative Analysis of Oxide Growth During Ti Galvanostatic Anodization.* Journal of The Electrochemical Society, 2020. **167**(11): p. 113501.

25.   Xu-Fei Zhu, Ye Song, Lin Liu, Chen-Yu Wang, Jie Zheng, Hong-Bing Jia, Xin-Long Wang, *Electronic currents and the formation of nanopores in porous anodic alumina.* Nanotechnology, 2009. **20**(47): p. 475303.

26.   Sara Naderizadeh, Silvia Dante, Pasquale Picone, Marta Di Carlo, Riccardo Carzino, Athanassia Athanassiou, Ilker S Bayer, *Bioresin-based Superhydrophobic Coatings with Reduced Bacterial Adhesion.* Journal of Colloid and Interface Science, 2020.

27.   Humberto Palza, Mauricio Nuñez, Roberto Bastías, Katherine Delgado, *In situ antimicrobial behavior of materials with copper-based additives in a hospital environment.* International journal of antimicrobial agents, 2018. **51**(6): p. 912-917.

29.   Schmidt, M. *Copper surfaces in the ICU reduced the relative risk of acquiring an infection while hospitalized.* in *BMC proceedings.* 2011. BioMed Central.

30.   Warnes, S.L., C.J. Highmore, and C.W. Keevil, *Horizontal transfer of antibiotic resistance genes on abiotic touch surfaces: implications for public health.* MBio, 2012. **3**(6): p. e00489-12.

31.   ASTM, E. *2180-07.".* in *ASTM E.* 2012.

32.   Association, J.S., *Antimicrobial products: test for antimicrobial activity and efficacy.* Japanese Industrial Standard 2000; JIS Z 2801, 2000.

33.   Cornelia Wiegand, Andrea Völpel, Andrea Ewald, Markko Remesch, Jan Kuever, Janine Bauer, Stefanie Griesheim, Carolin Hauser, Julian Thielmann, Silke Tonndorf-Martini, Bernd W Sigusch, Jürgen Weisser, Ralf Wyrwa, Peter Elsner, Uta-Christina Hipler, Martin Roth, Carolin

Dewald , Claudia Lüdecke-Beyer , Jörg Bossert , *Critical physiological factors influencing the outcome of antimicrobial testing according to ISO 22196/JIS Z 2801.* PloS one, 2018. **13**(3): p. e0194339.

34.   Johannes Karl-Mark Knobloch, Sabrina Tofern, Wladimir Kunz, Sara Schütze, Michael Riecke, Werner Solbach, Thomas Wuske, *"Life-like" assessment of antimicrobial surfaces by a new touch transfer assay displays strong superiority of a copper alloy compared to silver containing surfaces.* Plos one, 2017. **12**(11): p. e0187442.

35.   Timothy   M.   Gross, Joydeep   Lahiri, Avantika   Golas, Jian   Luo, Florence   Verrier, Jackie   L. Kurzejewski, David E. Baker, Jie Wang, Paul F. Novak, Michael J. Snyder, *Copper-containing glass ceramic with high antimicrobial efficacy.* Nature communications, 2019. **10**(1): p. 1979.

36.   Sergey Pogodin , Jafar Hasan, Vladimir A Baulin, Hayden K Webb, Vi Khanh Truong, The Hong Phong Nguyen, Veselin Boshkovikj, Christopher J Fluke, Gregory S Watson, Jolanta A Watson, Russell J Crawford, Elena P Ivanova, *Biophysical model of bacterial cell interactions with nanopatterned cicada wing surfaces.* Biophysical journal, 2013. **104**(4): p. 835-840.

37.   Nicholas Lin, Paula Berton, Christopher Moraes , Robin D. Rogers, Nathalie Tufenkji, *Nanodarts, nanoblades, and nanospikes: Mechano-bactericidal nanostructures and where to find them.* Advances in colloid and interface science, 2018. **252**: p. 55-68.

CHAPTER 8

CONCLUSIONS AND FUTURE RECOMMENDATIONS

8   CHAPTER 8: CONCLUSIONS AND FUTURE RECOMMENDATIONS

8.1   Transversal discussions of contributing chapters

This chapter provides brief discussions on findings of the contributing chapters, how they compare with requirements of ideal antibacterial coatings, and originality in relation to existing works in the field of surface engineering and antibacterial surfaces. Table 8.1 shows a summary of comparison of contributing chapters to an ideal antibacterial coating.

Table 8-1. A summary of contributing chapters in relation to an ideal antibacterial coating

Item	Requirement of Antibacterial Coating	Ideal situation	Contributing chapters			
			Chapter 4	**Chapter 5**	**Chapter 6**	**Chapter 7**
1	Simple fabrication	Yes	Yes	Yes	Yes	Yes
2	Biocide property of morphological features	Yes	No	No	No	Yes
3	Durability and mechanical stability	Yes	Yes	Yes	Yes	Yes
4	Broad spectrum effectiveness	Yes	Yes	Yes	Yes	Not studied
5	Environmental friendliness	Yes	Yes	Yes	Yes	Yes
	Non-toxicity	Yes	Not studied	Not studied	Not studied	Not studied
6	Adaptability to large scale production	Yes	Yes	Yes	Yes	Yes
7	Cost effectiveness	Yes	Yes	Yes	Yes	Yes
8	Antibacterial resistance	Yes	Not studied	Not studied	Not studied	Not studied

8.1.1 **Chapter 4**

Chapter 4 described the fabrication of superhydrophobic antibacterial aluminum surfaces using a biocompatible polymethylhydrosiloxane (PMHS) and silver nanoparticles (Ag-NPs) on anodized aluminum via a simple sol-gel process. Morphological features of Ag-PMHS nanocomposite coating observed by scanning electron microscopy showed heterogeneous micro–nanostructures. The chemical compositions of these coatings were characterized using X-ray diffraction and attenuated total reflection-Fourier Transform infrared spectroscopy, which indicated the presence of silver and low-energy PMHS polymer. Optimal micro-nano topographical features such as surface roughness of 9.7 ± 1.0 µm, pore diameter of 60 ± 11 nm and cell diameter of 121 ± 19 nm were observed. The micro-nano topography, resulting from both silver nanocluster and anodized nano pores, was passivated with the low energy PMHS to fabricate a superhydrophobic coating. This strategy induced both anti-bacterial and anti-biofouling character, not from micro-nano topographical features per say, but from silver nanocluster and superhydrophobicity. This is very pertinent, considering the shortcomings associated with existing antibacterial surfaces, in terms of instability of superhydrophobicity and uncontrolled release of leachable bactericidal silver, (the latter, which has implication for toxicity concerns). Thus, PMHS polymer firstly, served as a reducing agent for synthesizing Ag-NPs in situ within the polymeric matrix, secondly, for anchoring the Ag-NPs within an anodized Al oxide (AAO) substrate, and thirdly, for enhancing the adhesion, durability, and stability of superhydrophobic Ag-PMHS nanocomposites, as confirmed by both chemical and mechanical stability studies. It should be mentioned that given the highly multidisciplinary nature of this project, bactericidal leachable ion release kinetics (silver, aluminum, and quaternary ammonium salt) and both in-vitro and in vivo

cytotoxic impact studies, were investigated by collaborators at Sherbrook University. Thus, the scope of the current research was limited to the fabrication of a novel and durable aluminum surfaces, and validation of their antibacterial properties.

Though silicone-based superhydrophobic antibacterial surface are common in the literature due to their biocompatibility nature, their ability to repel bacterial adhesion has been rather low (79 - 95 %)[1, 2]. In this contributing chapter, the antibacterial property of the reported silicone-based superhydrophobic antibacterial surface, enhanced by Ag-NPs, resulted in an excellent performance, with anti-biofouling property or bacterial adhesion reductions of 99.0 %, 99.5 %, and 99.3 % for *P. Aeruginosa*, *E. coli*, and *S. Aureus*, respectively. Again, anti-biofilm assay studied by scanning electron microscopy, demonstrated that the superhydrophobic Ag–PMHS nanocomposite coated aluminum inhibited initial bacterial attachment and subsequent biofilm formation. This is particularly important given that biofilm on both animate and inanimate surfaces is known to represent a potential reservoir for the spread of nosocomial infections. The excellent anti-biofilm performance was due to combined effects of silver and superhydrophobicity, which exhibited a water CA of $159 \pm 0.5°$.

Furthermore, as the lack of mechanical robustness of a micro-nanoscale architecture and stability of surface chemistry affect durability of superhydrophobic coating, the chemical stability of Ag–PMHS nanocomposite was investigated. UV-accelerated weathering and 0.85 wt. % saline immersion studies were performed. The former simulates natural solar irradiation to quantify the effects of weathering conditions (UV irradiation) on the coating's degradability, while the latter simulates ability to inhibit bacterial initial attachment, particularly for cooling towers applications. Cooling towers are known to transmit *Legionella pneumophila* and *P. Aeruginosa* bacterial infections in hospital environment.

The surface chemistry is altered as a coating is exposed to harsh environmental conditions of different pH, humidity and UV-outdoor environmental conditions, whereas mechanical stability is affected by delamination of coating from underlying substrate over time. Interestingly, the mechanical stability of Ag–PMHS nanocomposite studied with the American Standard Test Method (ASTM D-3359) showed remarkably high coating adhesion. In addition, superhydrophobicity was stable with water contact angle (WCA) > 150° after 35 days of UV irradiation and 90 days 0.85 wt. % saline immersion studies, respectively. The 35 days of UV irradiation, represents a continuous UV irradiation, which overestimates the typical UV irradiation conditions in an indoor healthcare environment, typified by sporadic and intermittent irradiation. In a recent UV-accelerated weathering study by Xianai Huang [3], it predicted a relation between an artificial UV and natural UV irradiation in Canada. The study revealed that a1500h continuous UV irradiation of coatings corresponds to a 6 years and 4 months coating stability. Thus, in principle, the Ag–PMHS nanocomposite, subjected to similar conditions (but (840h)) can achieve long-term durability and stability for years.

Overall, chapter 4 met most requirements of antibacterial coating in terms of ease of sol-gel synthesis, durability and mechanical stability, broad-spectrum effectiveness, environmental friendliness, low-cost and adaptability to large-scale production. However, toxicity and antibacterial resistance investigations were not performed. In addition, morphological features in terms of roughness of $9.7 \pm 1.0\,\mu m$ could be optimized to produce nanoscale roughness that targets pathogens in the nano to few micro scale dimensions.

Chapter 5 dealt with the fabrication of superhydrophobic surface with tunable antibacterial and anti-biofouling properties. These properties were achieved by chemical etching of aluminum followed by passivation with octyltriethoxysilane (OTES)–quaternary ammonium salt (QUATs) molecules in a facile chemical bath process. The wettability and antibacterial properties of the OTES passivated aluminum was monotonically tuned by optimizing QUATs/OTES molar ratio. This is very pertinent as an ability to tune superhydrophobicity opens room for designing tailored antibacterial-anti-biofouling coatings for specific applications. It should be mentioned that this contribution was the first report on the use of a biocompatible low surface energy OTES molecule and a non-toxic QUATs to fabricate a tunable superhydrophobic and antibacterial coating. The micro and nano-topological roughness of 5.8 ± 0.5 µm, observed by scanning electron microscopy was passivated with the low surface energy OTES molecules to generate the superhydrophobicity, whilst the bactericidal property was induced by QUATs.

An antibacterial property, with a zone of inhibition of 34 ± 1.6, 22 ± 1.4, and 25 ± 0.9 against *S. Aureus, P. Aeruginosa* and *E. coli,* respectively, were obtained for the solution form of OTES-QUATs. Conversely, anti-biofouling property of 99.9, 99 and 99% were obtained for same bacteria respectively, on the OTES-QUATs coated aluminium surface. As durability and chemical stability of coatings are important for practical application, a 35-day UV-accelerated weathering study was performed to investigate the stability of the OTES-QUATs coating. Interestingly, the superhydrophobic OTES-QUATs coating was stable with a water contact angle (WCA) > 150° after 21 days, which showed the ability of OTES-QUATs coating to repel bacterial attachment. However, the WCA reduced gradually to a value of 121° after 35 days of UV irradiation.

Nonetheless, theoretically, the presence of QUATs could offer extended bactericidal properties to guarantee long-term antibacterial activity.

In summary, chapter 5 met the requirements of antibacterial coating by way of facile chemical bath synthesis, long-term bactericidal performance, broad-spectrum effectiveness, environmental friendliness, low-cost production, and adaptability to large-scale production. However, toxicity and antibacterial resistance investigations were not performed.

8.1.3   Chapter 6

Chapter 6 shed light on a facile two-step electrochemical synthesis process to deposit Ag_3PO_4 nanoparticles on anodized aluminum surfaces for obtaining durable antibacterial properties. Ionic silver (Ag^+ ion) was first reduced to metallic Ag^0 on anodized aluminum, followed by oxidation of the metallic silver (Ag^0) in an electrolyte of sodium orthophosphate to electrochemically precipitate Ag_3PO_4 in situ on anodized aluminum surface. These were achieved by applying an optimized reduction potential of -1.0V and oxidation potential of 10V; respectively on a 3 wt. % H_3PO_4 anodized aluminum. This strategy is very innovative and promising as it enabled the use of direct current (DC) to electrochemically synthesis silver phosphate on anodized aluminum, without the need for high-cost alternative current (AC) electrodeposition process or the time-consuming process of removing anodic aluminum oxide layer, required for typical electrodeposition of metals on H_2SO_4 anodized aluminum.

The characterization by X-ray powder diffraction, attenuated total reflection-Fourier transform infrared spectroscopy, energy-dispersive spectroscopy and scanning electron

microscopy confirmed the formation of Ag_3PO_4 nanoparticles. Furthermore, mechanical stability study on the Ag_3PO_4 coated anodized aluminum using the American Standard Test Method (ASTM D-3359), revealed a remarkably high resistance against scratch and a very high coating adhesion. Additionally, antibacterial property of the Ag_3PO_4 coated anodized aluminum was excellent, with 100% efficiency in 60 minutes of contact with *E. coli* bacteria. Again, both susceptibility and photocatalysis studies on Ag_3PO_4 showed superior antibacterial properties with a zone of inhibition (ZOI) value of 20 ± 1.3 mm and 100% *E. coli* inactivation in 15 min of visible-light irradiation.

In chapter 6, antibacterial-coating requirements such as use of simple and scalable electrochemical synthesis process, durable and stable coating, broad-spectrum antibacterial effectiveness, low-cost fabrication process and environmental friendliness were achieved. Nonetheless, ion releasing, its evolution with time, safety concerns on touchers, long-term toxicity and antibacterial resistance concerns were not addressed.

8.1.4 **Chapter 7**

In chapter 7, the serendipitous discovery of a topography-mediated antibacterial aluminum surface, fabricated by a one-step hard anodization process was discussed. Anodization parameters such as electrolyte, concentration, time, and current density were optimized to induce micro-nanoscale topographical features, composed of pore diameter, cell diameter, surface roughness, and oxide layer thickness among others. These features characterized by scanning electron microscopy, energy dispersive X-ray spectroscopy and surface profilometry were found to be

responsible for antibacterial performance. Phosphoric acid electrolyte produced better topographical features compared to sulphuric acid. In general, phosphoric acid with low acid concentration, such as 3% H_3PO_4 and a higher current density such as 40 mA/cm^2 led to a large pore diameter, a large cell diameter, a high surface roughness and excellent antibacterial property, compared to higher acid concentration such as 45wt. % H_3PO_4 under similar conditions. Thus, 3 wt. % H_3PO_4, exhibited a pore diameter of 151 ± 37 nm, a cell diameter of 239 ± 53nm, a roughness (rms) of 2.9 ± 0.7μm and bactericidal efficiency of 100%. Contrarily, 45wt. % H_3PO_4 showed a lower pore diameter of 55 ± 12 nm, a cell diameter of 115 ± 16, a roughness (rms) of 0.8 ± 0.1μm and a bactericidal efficiency of 85%. In addition, the 3 wt. % H_3PO_4 anodized at 40 mA/cm^2 compared favourably with a commercially available antibacterial copper (C11000 of 99.9% Cu), having a 100% bactericidal efficiency after 1h *E. coli* bacterial contact. Furthermore, after 96 h of *E. coli* bacterial continuous loading cycles, the 3 wt.% H_3PO_4 anodized aluminum coupon still exhibited a superior antibacterial property, having 100% efficiency. On the contrary, as-received aluminum killed only 6.6% of *E. coli* bacteria after 1h of contact.

This novel antibacterial strategy represents a very innovative and promising solution to overcome the issues with existing antibacterial coatings, characterized by coating instability, toxicity, and antibacterial resistance problems. The fact that topography-mediated antibacterial aluminum surface requires no coating, but mainly the outermost interface needs to be engineered to induce micro-nanoscale topographical patterns to modulate antibacterial activity represents a paradigm shift in antibacterial surface technology. Thus, these surfaces represent a more eco-sustainable solution to both implant devices prostheses and frequently touched surfaces-mediated healthcare associated infections. The originality of this contributing chapter consists of the fact that, theoretically, topography-mediated antibacterial aluminum surface could offer a more durable

and long-lasting antibacterial surface in term of bioactivity, for months and years of repeated touches.

Another important contribution to knowledge was the development of the novel dry seeding protocol that simulated the near dry conditions of typical frequently touched surface of hygiene critical environment. Existing antibacterial protocols are limited to immersion and wet condition studies, (which is typical for medical implant device prostheses applications). However, protocols intending to assess antibacterial effectiveness of inanimate frequently touched areas in hospital environment ought to mimic and model the near dry conditions, characterized by very thin aqueous films or local droplets of fingerprint-contact of indoor inanimate surfaces. In this regard, the novel dry seeding protocol described in chapter 7, attempted to achieve such realistic conditions by utilizing maximum recovery diluent (MRD) load to simulate soiling condition of vomit, blood or faeces spread on inanimate frequently touched areas. As noted earlier, result of this novel dry seeding protocol, conducted on both commercially available antibacterial copper and the 3 wt.% H_3PO_4 anodized aluminum coupon-3HP40, was excellent with 100% bactericidal efficiency after 1h *E. coli* bacteria contact.

In summary, requirements of antibacterial coating in terms of simple fabrication process, adaptability to large-scale production, non-toxicity, environmental friendliness, low-cost production, durability, and long-term stability of topographical features were achieved. However, long-term antibacterial performance and bioactivity in contaminated environment could have been further explored.

8.2 Conclusions

Multidrug resistance pathogens such as *S. Aureus, P. Aeruginosa* and *E. coli* can survive on frequently touched surfaces. These surfaces can become potential reservoirs for transmission of both community and healthcare associated pathogenic infections. As a common engineering material having easy fabrication process for such applications, aluminum alloy has been used and transformed into antibacterial surfaces *by: (i) anodization process to create a nano-porous topographical pattern, which kill bacteria on contact; (ii) as well as passivating the nano-porous topographical pattern to create superhydrophobic properties to repel the initial attachment of bacteria; or (iii) immobilizing antibacterial agents on anodized aluminum to kill bacteria on contacts*.

Through the existence of the extensive literature and experimental investigations in the field of antibacterial materials and surfaces, this research, as apart of doctoral studies, has successfully demonstrated the potential use of AA6061-T6 aluminum alloy as the antibacterial surfaces via the following original contributions:

1. Fabrication of a novel topography-mediated antibacterial aluminum surface via a one-step constant current hard anodization.

2. Designing a novel dry seeding protocol that simulate near dry condition of typical frequently touched surfaces.

3. Fabrication of silver-polymethylhydrosiloxane (Ag-PMHS) nanocomposite coating on anodized aluminum with superhydrophobic and antibacterial properties.

4. Fabrication of a tunable superhydrophobic aluminum surface with anti-biofouling and antibacterial properties.

5. Electrochemically synthesized silver phosphate coating on anodized aluminum with superior antibacterial properties.

Overall, in this research, different methods have been utilized to fabricate the novel antibacterial aluminum surfaces. Typically, utilization of surface engineering strategies such as anodization, low surface energy passivation and electrochemical surface immobilization of photocatalysts, prove to be sufficient to transform AA6061-T6 aluminum alloy into antibacterial surfaces capable of reducing microbial burden of clinically relevant pathogens such as *S. Aureus, P. Aeruginosa* and *E. coli*.

8.3 **References:**

1. Meier, M., V. Dubois, and S. Seeger, *Reduced bacterial colonisation on surfaces coated with silicone nanostructures.* Applied Surface Science, 2018. **459**: p. 505-511.
2. Colin R. Crick, Salim Ismail, Jonathan Pratten, Ivan P. Parkin, *An investigation into bacterial attachment to an elastomeric superhydrophobic surface prepared via aerosol assisted deposition.* Thin Solid Films, 2011. **519** (11): p. 3722-3727.
3. Huang, X., *Study on the degradation mechanism of heat-treated wood by UV light*. 2012: Université du Québec à Chicoutimi.

8.4   Recommendations and future work

While this study has demonstrated different experimental process for transforming AA6061-T6 aluminum alloy used in our daily life, for the potential use as antibacterial surface, there are still opportunities to improve the limitations and unanswered questions worthy of consideration for further studies:

1. In this research project, antibacterial performance of the fabricated aluminum surfaces was evaluated by in-vitro assays. However, this may not replicate the real sites of intended applications such as healthcare facility, long-term care homes, outpatient surgical centres and other hygiene critical environment. Hence, future work should focus on evaluating the antibacterial activity of the AA6061-T6 aluminum surfaces in real life settings.

2. To improve longevity of antibacterial properties even after eventual possible loss of superhydrophobicity in the long-term, silver and quaternary ammonium salt (QUATs) were incorporated in polymethylhydrosiloxane (PMHS) polymeric matrix and octyltriethoxysilane molecules, respectively. As future recommendation, release kinetics of these antimicrobial materials and cytotoxic impact studies (for example on fibroblasts cell lines) and possible resistance to bacteria could be investigated.

3. While anti-biofilm study was conducted on Ag–PMHS nanocomposite aluminum, most bactericidal assays were performed on one planktonic bacteria cell at time. However, it is common knowledge that bacteria attach and develop in colonies of biofilms. Hence, further investigation could be investigated using a high throughput Calgary Biofilm Device

(CBD). The CBD is a very versatile Biofilm culturing device that can provide information not only on the minimal inhibitory concentration, the minimal biocidal concentration, the minimal biofilm eradication concentration (ability to kill existing biofilms), the minimal biofilm prevention concentration (ability to prevent attachment and biofilm initiation) but also the minimal biofilm growth inhibition concentration (ability to prevent biofilm proliferation).

4. In addition, the excellent performance of the topography-mediated antibacterial aluminum surface was studied under near dry conditions to simulate conditions of typical frequently touched surface. However, it would be interesting also to evaluate the antibacterial performance in wet conditions. In addition, studies with gram-positive bacteria could be investigated. Furthermore, detailed mechanism of the topography-mediated antibacterial aluminum surfaces could be investigated. Furthermore, while maximum recovery diluent (MRD) load was utilized to simulate soiling condition of vomit, blood or faeces, alternative organic soil such as Bovine Serum Albumin could be further explored. In addition, long-term bioactivity in contaminated environment could be studied.

5. Finally, regarding the study on electrochemically synthesized Ag_3PO_4 coating on aluminum, it is unclear whether the nucleation and growth of the Ag_3PO_4 occurred within the anodized aluminum pores. Thus, anodization parameters such as concentration of different electrolytes, temperature and applied potential or current, could be optimized to produce larger pores to incorporate Ag_3PO_4 nanoparticles. Again, morphological surface roughness could be optimized to produce nanoscale feature that targets pathogens in the nano to few micro scale dimensions.

9   LIST OF PUBLICATIONS OF CANDIDATE

Journal articles

1. <u>Henry Agbe</u>, Dilip. Kumar. Sarkar, X.Grant. Chen, Nathalie Faucheux, Gervais Soucy and Jean-Luc Bernier, Silver-polymethylhydrosiloxane nanocomposite coating on anodized aluminum with superhydrophobic and antibacterial properties, ACS Appl. Bio Mater., 3, 7 (2020) 4062–4073.

2. <u>Henry Agbe</u>, Dilip. Kumar. Sarkar, and X.Grant. Chen, Tunable Superhydrophobic Aluminum surfaces with Anti-biofouling and Antibacterial Properties, *Coatings* 2020, *10*(10), 982.

3. <u>Henry Agbe</u>, Dilip. Kumar. Sarkar, and X. Grant. Chen, Anodized aluminum surface with topography-mediated antibacterial properties. **Revision (ASC Biomaterial Science and Engineering)**.

4. <u>Henry Agbe</u>, Dilip. Kumar. Sarkar, and X. Grant. Chen, electrochemically synthesized silver phosphate coated anodized aluminum with superior antibacterial properties**. Revision (RSC Material Chemistry B).**

5. <u>Henry Agbe</u>, Dilip. Kumar. Sarkar, X. Grant. Chen and Saleema Noormohammed. Antibacterial aluminum surfaces for curbing the prevalence of healthcare-associated infections (HCAI): Prospects and Challenges**. In preparation.**

6. <u>Henry Agbe</u>, Dilip. Kumar. Sarkar, and X. Grant. Chen, Onion-extract mediated silver synthesis on aluminum with antibacterial and self-disinfection properties. **In preparation.**

7. <u>Henry Agbe</u>, Dilip. Kumar. Sarkar, and X. Grant. Chen, Silver- polymethylhydrosiloxane-quaternary ammonium on anodized aluminum with excellent self-disinfection property. **In preparation.**

8. <u>Henry Agbe</u>, Dilip. Kumar. Sarkar, and X. Grant. Chen, Silver- based nanocomposite coatings on aluminum with tunable antibacterial and anti-biofouling properties. **In preparation.**

Conference articles:

1. <u>Henry Agbe</u>, Dilip. Kumar. Sarkar, and X. Grant. Chen, (May. 2018). Synthesis of Ag-Based Nanocomposites on Anodic Aluminum Oxide Templates- A Review. Oral presentation at 7th International Conference & Exhibition on Advanced & Nano Materials. Montreal, QC.

2. <u>Henry Agbe</u>, Dilip. Kumar. Sarkar, and X. Grant. Chen, (2019, August). Tunable superhydrophobic Ag-based nanocomposite coatings on Aluminum with enhanced antibacterial and anti-fouling properties. Oral presentation presented at the 8th International Conference & Exhibition on Advanced & Nano Materials. Quebec QC.

3. <u>Henry Agbe</u>, Dilip. Kumar. Sarkar, X.Grant. Chen, Nathalie Faucheux, Gervais Soucy and Jean-Luc Bernier, (2019, October) Silver-based nanocomposite coatings on anodized aluminium with excellent antibacterial properties. Oral presentation presented at journée international des étudiants du REGAL, Quebec QC.

4. <u>Henry Agbe</u>, Dilip. Kumar. Sarkar, X.Grant. Chen, Nathalie Faucheux, Gervais Soucy and Jean-Luc Bernier, (2020, October), Superhydrophobic coatings on Aluminum with anti-biofouling and antibacterial properties, *Oral* presentation at Canadian Biomaterials Society, Seminar series, student chapter-Laval University, QC.

Posters:

1. Henry Agbe, Dilip. Kumar. Sarkar, and X.Grant. Chen (2018, June), Synthesis of Ag-based nanocomposites on anodic aluminium oxide templates. Poster session presented at La Journée des étudiants du REGAL. Montreal QC.

2. <u>Henry Agbe</u>, Dilip. Kumar. Sarkar, X.Grant. Chen, Nathalie Faucheux, Gervais Soucy and Jean-Luc Bernier, (2019, October), Silver-based nanocomposite coatings on aluminium with tunable antibacterial and anti-fouling properties, poster presentation at journée international des étudiants du REGAL, Quebec QC.

3. Henry Agbe, Dilip. Kumar. Sarkar, and X. Grant. Chen, (2020, October), Superhydrophobic coatings on Aluminum with anti-biofouling and antibacterial properties, poster presentation at journée international des étudiants du REGAL, Quebec QC.